TECHNISCHE UNIVERSITÄT MÜNCHEN
Lehrstuhl für Raumfahrttechnik

Analytical and Experimental Characterization of a Liquid Crystal based Phased Array

Dipl.-Ing. Univ. Matthias Tebbe

Vollständiger Abdruck der von der Fakultät für Maschinenwesen der Technischen Universität München zur Erlangung des akademischen Grades eines

Doktor-Ingenieurs (Dr.-Ing.)

genehmigten Dissertation.

Vorsitzender:		Prof. Dr. rer. nat. Tim C. Lüth
Prüfer der Dissertation:	1.)	Prof. Prof. h.c. Dr. rer. nat. Dr. h.c. Ulrich Walter
	2.)	Prof. Dr.-Ing. Georg Strauß, Hochschule für Angewandte Wissenschaften München

Die Dissertation wurde am 28.06.2018 bei der Technischen Universität München eingereicht und durch die Fakultät für Maschinenwesen am 10.12.2018 angenommen.

Acknowledgments

I thank Professor Walter for the opportunity to write this thesis and for the freedom at work during the last five years at the LRT. I would also like to thank Professor Strauß for many helpful discussions and the opportunity to perform several measurements at your institute.

Alex Hoehn thank you for not only offering the position in the LISA-ES project to me, but also for the enjoyable cooperation in several other projects (LISA-MS+, CopKa and CFRM-HF). You motivated me to keep on going, even if the manufacturing resulted in many scrap parts and our discussions always helped me to focus on the essential parts of this work.

Martin Rott and Petra Lochner thank you for the support in financial and organizational issues and for helping me understand the bureaucratic hurdles of the university.

Thank you, Tobias Abstreiter, for your support in many projects with your expertise and manufacturing skills.

A good working atmosphere is always a key factor and I can definitely say, that the atmosphere at the LRT was superb over the last years (and still is). For this I have to thank my former and current colleagues, in particular the ones working in the same projects and with whom I share unforgettable conference trips.

Especially I would like to thank Philipp Reiß, not only for the corporate rebuild of the thermal vacuum chamber, but also for sharing the interest in outdoor activities, many craft projects and music, thanks mate!

I would also like to thank Norbert Nathrath and Christian Weickhmann for introducing me to the exotic field of antenna functionality and radio frequency measurement and *Airbus DS* (Michael Schneider, Ralf Gehring, Christian Pflügler, Andreas Schinagl-Weiß) for helping me with measurement equipment, time and knowledge.

But without my great family and friends, I would not have finished this dissertation.

Abstract

This dissertation analyzes the suitability of liquid crystal based phase shifters in a waveguide design for the use in a phased array antenna on a relay satellite in a geostationary orbit.

Four key issues are addressed:

1) The influence of the phase shifters on the array performance in a realistic use scenario. Simulations evaluate the influence of the slow reaction time and the insufficient phase range of liquid crystal phase shifters for the desired application.

It is shown that even for a worst-case scenario, the performance-reducing of slow phase shifters can be minimized to acceptable levels.

2) The envisioned manufacturing method for an integrated phase shifter.

The manufacturing method proved to be difficult to handle and therefore error-prone. Several integrated phase shifters were built, but only one could be used in the intended way. For further developments, alternative methods are proposed.

3) The characterization of the phase shifter performance with different manufacturing techniques and under different temperatures.

The envisioned integrated manufacturing techniques show higher losses compared to a split block laboratory setup. The temperature dependency is as expected and does not present a problem for space applications.

4) The calibration of the phase shifters and the characterization of a 4x1 array in a static and a dynamic environment.

The calibration could be performed successfully and could be used for the array measurements. The experimental array performance correlates well to analytical model predictions and demonstrated good performance in static and dynamic steering scenarios.

Analytical and experimental characterizations showed suitable applications for the proposed liquid crystal phase shifters, despite the high transmission losses for the intended applications.

Zusammenfassung

Diese Dissertation analysiert die Eignung von flüssigkristallbasierten Phasenschiebern in Hohlleiterbauweise welche in einer Phased-Array-Antenne auf einem geostationären Satelliten eingesetzt werden sollen.

Vier Hauptpunkte werden hierbei adressiert:

1) Der Einfluss der Phasenschieber auf die Arrayperformanz in einem realistischen Anwendungsszenario. Simulationen sollen den Einfluss von langsam reagierenden Flüssigkristallphasenschiebern mit unzureichendem Phasenbereich in der angestrebten Anwendung evaluieren.

Es wird gezeigt, dass der negative Einfluss von langsamen Phasenschiebern auch für den schlimmsten Extremfall auf ein akzeptables Niveau reduziert werden kann.

2) Die angedachte Fertigungsmethode für einen integrierten Phasenschieber.

Die Fertigungsmethode stellte sich als schwierig handzuhaben heraus und war daher fehleranfällig. Mehrere integrierte Phasenschieber wurden gebaut, aber nur einer konnte in der geplanten Art genutzt werden. Für zukünftige Entwicklungen werden alternative Fertigungsmethoden vorgeschlagen.

3) Die Charakterisierung der Phasenschieberperformanz von verschiedentlich gefertigten Phasenschiebern und bei verschiedenen Temperaturen.

Die angedachte integrierte Fertigungsmethode zeigte, verglichen mit einem Halbschalen-Laboraufbau, höhere Verluste. Die Temperaturabhängigkeit ist wie erwartet und stellt kein Problem für eine Anwendung im Weltraum dar.

4) Die Kalibrierung der Phasenschieber und die Charakterisierung eines 4x1 Arrays in einer statischen und einer dynamischen Umgebung.

Die Kalibrierung konnte erfolgreich durchgeführt werden und wurde danach für die Arraymessungen genutzt. Die experimentelle Performanz des Arrays korreliert gut mit den analytischen Vorhersagen und zeigte eine gute Performanz in statischen und dynamischen Szenarien.

Analytische und experimentelle Charakterisierungen zeigten, abgesehen von den hohen Transmissionsverlusten, passende Anwendungen für die vorgeschlagenen Flüssigkristallphasenschieber.

Contents

Abbreviations & Acronyms

ABS	Acrylonitrile butadiene styrene
AC	Alternating current
AESA	Active electronically scanned array
AFR	Array fed reflector
AGIPA	Advanced / Adaptive ground implemented phased array
AWG	American wire gauge
BFN	Beam forming network
C-band	Frequency band - 4 GHz to 8 GHz, (IEEE Aerospace & Electronic Systems Society, 2002)
CAD	Computer aided design
CCR	Compensated compact range
CPW	Coplanar waveguide
CW	Continuous wave
DC	Direct current
DLR	German aerospace center (Deutsches Zentrum für Luft- und Raumfahrt)
DOF	Degree(s) of freedom
DRA	Direct radiating array
ETS-VI	Engineering test satellite - VI
ETS-VIII	Engineering test satellite - VIII
FET	Field-effect transistor
FPGA	Field-programmable gate array
GEO	Geostationary orbit
H	Horizontal (electric field)
HRM	Hold-down release mechanism
HEMT	High-electron-mobility transistor
HPA	High power amplifier
IL	Insertion loss
IMSL	Inverted micro stripline
IPA	Imaging phased array
ISL	Inter-satellite link
JAXA	Japan aerospace exploration agency
K-band	Frequency band - 18 GHz to 27 GHz, (IEEE Aerospace & Electronic Systems Society, 2002)
Ka-band	Frequency band - 27 GHz to 40 GHz, (IEEE Aerospace & Electronic Systems Society, 2002)
Ku-band	Frequency band - 12 GHz to 18 GHz, (IEEE Aerospace & Electronic Systems Society, 2002)
L-band	Frequency band - 1 GHz to 2 GHz, (IEEE Aerospace & Electronic Systems Society, 2002)
LC	Liquid crystal
LCPS	Liquid crystal phase shifter
LEO	Low earth orbit
LHCP	Left-handed circular polarization
LIDAR	Light detection and ranging (‘Light radar’)
LIQUIDA	Liquid crystal antenna array
LISA-ES	Lightweight inter-satellite link antenna – electronically steerable
LISA-MS	Lightweight inter-satellite link antenna – mechanically steerable
LNA	Low noise amplifier
LOS	Loss of signal
LRT	Institute of Astronautics (Lehrstuhl für Raumfahrttechnik)

LTCC	Low temperature cofired ceramics
MEMS	Micro-electro-mechanical systems
MESFET	Metal–semiconductor field-effect transistor
MMIC	Monolithic microwave integrated circuit
MPA	Multiport power amplifier
NASA	National aeronautics and space administration
NASDA	National space development agency (now JAXA)
NICT	National institute of information and communications technology
PAE	Power added efficiency
PCB	Printed circuit board
PESA	Passive electronically scanned array
PET	Polyethylene terephthalate
PI	Polyimide
PIN	Positive intrinsic negative (diode)
PT100	Platinum thermistor with a resistance of 100 Ω at 0 °C
PTFE	Polytetrafluoroethylene
PVC	Polyvinyl chloride
RADAR	Radio detection and ranging
RF	Radio frequency
RHCP	Right-handed circular polarization
RL	Return loss
RX	Receiver exchange
S-band	Frequency band - 2 GHz to 4 GHz, (IEEE Aerospace & Electronic Systems Society, 2002)
S-CPW	Slow-wave coplanar waveguide
SANTANA	Smart antenna terminal
SIW	Structure integrated waveguide
SL	Stripline
SOLT	Short-Open-Load-Thru (calibration standard)
SSPA	Solid state power amplifier
TDRS	Tracking and data relay satellite
TE	Transverse electric
TEM	Transverse electromagnetic
TM	Transverse magnetic
TRL	Thru-Reflect-Line (calibration standard)
TWTA	Traveling-wave tube amplifier
TX	Transmitter exchange
V	Vertical (electric field)
WINDS	Wideband internetworking engineering test and demonstration satellite
WR34	Waveguide rectangular, width: 0.34 inch, height: 0.17 inch (=1/2 width)
X-band	Frequency band - 8 GHz to 12 GHz, (IEEE Aerospace & Electronic Systems Society, 2002)

Symbols & Indices

Symbols:		SI-units:
a	Semi-major axis or	m
	Width of waveguide	
b	Height of waveguide	m
c	Speed of light	m/s
d	Element spacing	m
e	Eccentricity	-
f	Frequency	Hz
i	Inclination	rad
k	Wavenumber	rad/m
n	Mean motion	rad/s
$\vec{n}$	Director of liquid crystal	-
p	Phase	rad
p_0	Phase offset	rad
$\dot{p}$	Phase change rate / phase velocity	rad/s
v	Velocity	m/s
z	Position of an array element	m
A_{mn}	Amplitude	A/m
B	Beam pattern	-
B_{mn}	Amplitude	V/m
$\vec{D}$	Displacement (el. Field)	C/m²
E	Eccentric anomaly or	rad
	Transverse component of electric Field	V/m
$\vec{E}$	Electric field vector	V/m
F_{FoM}	Figure of Merit, phase shifting	rad
G	Gain (factor)	dB
H	Transverse component of magnetic Field	A/m
$L_{\mathrm{gain,para}}$	Loss due to paraphases	dB
$L_{\mathrm{IL,max}}$	Maximum insertion loss	dB
L_{LOS}	Figure of Merit, loss of signal	s
M	Mean anomaly	rad
N	Number of array elements	-
T	Orbital period or	s
	Temperature	K
U	Voltage	V
Z	Impedance	Ω
$\alpha_1 to\ \alpha_6$	Leslie coefficients	Pa·s
β	Propagation constant	rad/m
γ_1	Rotational viscosity	Pa·s
γ_2	Torsion coefficient	Pa·s
δ_{s}	Skin depth	m
$\delta_{\alpha\beta}$	Kronecker delta	-
ε	Permittivity	F/m
ε_{r}	Relative permittivity	-
θ	Pattern angle	rad
θ_0	Incident angle	rad
λ	Wavelength	m
λ_{g}	Guide wavelength	m
μ	Permeability	H/m
μ_{r}	Relative permeability	-
ν	True anomaly	rad
σ	Electric conductivity	S/m
τ	Time delay	s
ϕ	Phase lag (rot. viscosity)	rad
χ	Magnetic susceptibility	-

ω	Argument of periapsis or	rad
	Angular rate of rotation	rad/s
Ω	Longitude of ascending node	rad

Constants:

c_0	Speed of light in vacuum $299\,792\,458\ \mathrm{m/s}$
$M_\oplus$	Earth mass $5.975 \times 10^{24}\,\mathrm{kg}$
G	Gravitational constant $6.6726 \times 10^{-11}\,\mathrm{m^3 kg^{-1} s^{-2}}$
ε_0	Vacuum permittivity $\frac{1}{c_0 \cdot \mu_0} \approx 8.854\,187\,817 \cdot 10^{-12}\,\mathrm{F/m}$
μ_0	Vacuum permeability $4\pi \cdot 10^{-7}\,\mathrm{H/m}$
$\mu_\oplus$	Earths standard gravitational parameter $M_\oplus \cdot G \approx 3.9869 \times 10^{14}\ \mathrm{m^3/s^2}$

Indices:

$1\mathrm{dB}$	Parameter at 1 dB loss
$3\mathrm{dB}$	Parameter at 3 dB loss
$6\mathrm{dB}$	Parameter at 6 dB loss
a	Anisotropy
c	Cutoff
$diagonal$	Diagonal of the Array
g	Group
GEO	Geostationary orbit
i	Array element number
LEO	Low earth orbit
m	First number of mode definition or Side / grating lobe number
max	Maximum value
min	Minimum value
n	Last number of mode definition or Number of horns in paraphase
nom	Nominal
p	Phase
$para$	Paraphase
$parallel$	Parallel to the main axes of the array
TE	Transverse electric wave
TM	Transverse magnetic wave
var	Variable
x	In direction of the x-axis
y	In direction of the y-axis
var	Variable
θ	Pattern angle
$\parallel$	Parallel
$\perp$	Perpendicular

1 Introduction

This thesis examines the feasibility of a new type of phase shifter for the application in a satellite based phased array communication antenna. One intended application is a tracking antenna on a relay satellite in geostationary orbit (GEO) that tracks a satellite in a low earth orbit (LEO). This is taken as a use case for performance requirements and to analyze the dynamic behavior of the antenna. The new type of phase shifter is based on a waveguide design and uses liquid crystal (LC) to manipulate the phase of the radio frequency (RF) signal that is transmitted.

Chapter 1 comprises the scope of this work, the state of the art and the knowledge gap analysis.

The scope includes the motivation to develop a phased array based on liquid crystal phase shifters (LCPSs), the problem statement and hypothesis and the structure of this thesis.

The state of the art part is divided in subchapters to distinguish between the state of the art in phased array technologies, phase shifter technologies and LCPSs. It also includes an overview of the project LISA-ES (lightweight inter-satellite link antenna – electronically steerable) with a description of the overall scenario on which the antenna development is based, the horn antenna array design, the LCPS functionality and the control of the phased array.

The knowledge gap analysis is divided into the gap identification and the thesis objectives derived from the identified gaps.

1.1 Scope of this work

1.1.1 Motivation

Phased arrays can be seen as an alternative to mechanically steered antennas, which are common in space communication systems. Phased arrays in satellite applications have some potential advantages compared to mechanically steered antennas. The critical points of mechanical antenna systems in space applications can be summarized in the following keywords:

- Failure probability and consequences in mechanisms
- Induced disturbing moments and jitter
- Necessity of rotary joints

The motivation for the research in phased array technology stems from these critical points and the vision that an electronically steered phased array can provide alternative solutions improving on the critical points of mechanical systems.

A failure of a mechanism does not start with a failure during operation. For the launch, each degree of freedom of the mechanism has to be blocked by a hold-down release mechanism (HRM) to reduce the relative movement during the launch and thus undesired loads on the gearboxes or electric motors (e.g., *TiNi Frangibolt*, see for instance Gabriel et al. (2016)). These hold-down release mechanisms are often a single point of failure and therefore have to be very reliable.

If the hold-down release mechanism works properly, most mechanisms still only have one set of bearings (normally two or three) and one electric motor per axis. If one of these components fails, the entire antenna system might be unusable. Since a steering mechanism for antennas often consists of two axes (two degrees of freedom, 2-DOF), a failure of one component in one of those axes could lead to a failure of the entire antenna system.

Mechanically moving parts are often seen as critical for space applications. The reasons are the difficulty of ensuring a constant lubrication of the bearings (e.g., dry lubrication or *Braycote*) over the entire lifetime in a space environment and the use of different materials, often necessary to meet the weight restrictions, in combination with large temperature gradients. The last point can lead to locked bearings because of different coefficients of thermal expansion. This is often counteracted with an increased bearing clearance. In addition, potential cold welding between some material combinations also has to be taken into account.

In comparison, for a direct radiating array (DRA) that is mounted on the earth deck of a GEO satellite, no mechanical movement and thus no hold-down release mechanism is necessary. During operation, the failure of a single phase shifter in an array with many array elements only has a small impact on the overall array performance. Even if the failure probability of a single phase shifter within the array would be slightly higher than the failure probability of an electric motor or bearing, the consequences of a failure are less severe.

If the mechanism works nominally, it still causes disturbances such as torques, vibration and jitter. Each relative movement of the antenna causes a counter-reaction of the satellite since the entire satellite (with antenna) is free-floating. Therefore, if the antenna moves, the attitude control system of the satellite has to counteract this movement, or the satellite will change its attitude.

If the attitude is controlled with reaction or momentum wheels, the steering of the antenna will, over time, lead to a saturation of the wheels. The desaturation is often performed with a chemical propulsion system which has limited fuel and thus limits the lifetime of the satellite.

In addition, the torque to steer the antenna is also limited (by the motor and by the attitude control system) and therefore the maximum tracking velocity is restricted. For a phased array antenna, this restriction comes from the phase change rate of the phase shifters which, in the case of switches in MEMS (micro-electro-mechanical systems) or transistor architecture, can change their state (and thus the beam direction) in a fraction of a second.

For some satellites with sensitive optical payloads, such as telescopes, the jitter imposed by the mechanical movement of the antenna (motor and bearings) can be a source of degradation of the optical resolution (see for instance Kozilek et al. (2013)). In some of these cases a phased array antenna might be easier to implement than the dampening or prevention of the vibration in a mechanical system.

Depending on the angular range of the axes and the radiated RF power, rotary joints (coax or waveguides) are necessary in mechanically steered systems (see for instance Gabriel et al. (2016)). If the radiated power and the frequency is high, waveguides have to be used to transmit the signal to the antenna. Waveguides have no or very little flexibility and therefore rotary joints have to be used even for a small angular range. For applications with less RF power, limited range moving coaxial cables can be used for the transmission which are more flexible, but limited in allowable bend cycles and angular range. For the azimuth rotation, more than 360° or infinite rotation is a desired specification which is only possible with rotary joints even for other signal and power lines within the mechanism. These rotary joints can be expensive and the contact points between the two moving parts are critical for wear.

In addition to the before mentioned prevention of critical points in mechanical systems, a phased array can also be used to form several beams with a reduced gain instead of one high gain main lobe (assuming an adjusted distribution network). The ability to track several satellites or other objects (e.g., ships and planes) at the same time with reduced data rate or change the shape of footprints on the ground is interesting especially for GEO applications. This flexibility is not only required by the military (*Wideband Global SATCOM)* - (Roper *et al.*, 2003; Kumar *et al.*, 2005; Cook, 2010), but also commercial operators have an increasing demand for flexible satellites (Fenech *et al.*, 2015; Gatti, 2015).

“Beam-shape flexibility greatly reduces the business-plan risk associated with a satellite, as it is possible to reconfigure the coverage area to respond to changing markets” (Jacomb-Hood and Lier, 2000, p. 41).

“Whereas commercial Ku-band [12 GHz to 18 GHz] satellites have seen significant technological developments at equipment level, the transponder concept remains unchallenged. Payloads have increased in size, leading to increased equipment count. Additionally, operator quest to improve efficiency and a high fill-factor has increased the importance of flexibility” (Fenech *et al.*, 2015, p. 1). The flexibility is not limited to the antenna system, but it plays an important role.

The need to develop more flexible GEO satellites is also increased due to several companies that are planning to build satellite constellations in LEO to enable broadband communication via LEO satellites (*OneWeb*, *SpaceX*, *Boeing* and others). These LEO constellations could be strong competitors on the GEO communication market with the benefit of lower latency and smaller ground terminals or high bandwidth (in this case with the disadvantage of a steerable ground terminal, even for non-moving applications, e.g. *Kymeta Corporation*, *Wafer LLC*, *ALCAN Systems GmbH*).

In current satellite applications, traveling wave tube amplifiers (TWTAs) are commonly used, especially in the K/Ka-band (about 18 GHz to 40 GHz). Solid state amplifiers (SSPAs) are used for satellite applications at lower frequency bands but cannot yet compete with the efficiency of TWTAs at higher frequency bands (Table 2).

For an active array (see Chapter 1.2.1) with one power amplifier per array element, TWTAs get too bulky for high frequency bands, since the element spacing is dependent on the frequency (higher frequency leads to smaller spacing) due to the grating lobe restrictions (see Chapter 2.1.1). Therefore, it is challenging or even impossible to use bulky TWTAs in high frequency active arrays (especially DRAs), and SSPAs at each array element might be the only option. In active arrays, the phase shift is performed before the signal is amplified (for the transmitting case) and therefore, the transmission losses of the phase shifters play a minor role. The *Quantum* class satellites will use TWTAs in a Ka-band (27 GHz to 40 GHz) phased array, but the antenna design is an array-fed reflector and not a DRA (Gatti, 2015). Therefore, the grating lobe restrictions might be different when compared to DRAs.

A passive array (see Chapter 1.2.1) with only one power amplifier for the entire array, but low-loss phase shifters before each array element can be an alternative. Low-loss phase shifters are crucial for this design, since the phase shift is performed in the already amplified path of the array (for the transmitting case). With relatively small phase shifters (compared to the size of a TWTA) and the use of one TWTA for the array, this design could reduce the cost (less amplifiers) and increase the efficiency (TWTA instead of SSPA) compared to an active array.

First experiments with different designs of LCPSs showed lower losses compared to other phase shifting technologies used until now (Jakoby *et al.*, 2004). Therefore, use of LCs for phase shifting applications seems promising. For a low-loss transmission of high frequency signals, waveguides are commonly used. An LCPS in a waveguide design therefore could lead to a low-loss phase shifter for passive arrays that could be used on GEO satellites with high transmit power and high bandwidth (Gaebler, Goelden, *et al.*, 2009). This was the starting hypothesis for the LISA-ES project.

1.1.2 Problem Statement and working Hypothesis

Within the LISA-ES project, the design of the LCPS proposed by Gaebler, Goelden, et al. (2009) has been optimized to get a better phase shifting performance and less transmission losses. The resulting LCPS and thus the phased array is still based on several compromises regarding phase range, dynamic behavior, manufacturability and operability (see Chapter 1.3). Because of these compromises, the feasibility of such a satellite based phased array for static and dynamic steering applications is put into question.

The working hypothesis of this work is:

Liquid crystal phase shifters based on a waveguide design are feasible for passive phased array antennas in a geostationary relay application.

1.1.3 Structure of this Thesis

The thesis is structured as follows:

In Chapter 1, the scope of this work is shown followed by the current state of the art starting with phased array technologies for satellite communication antennas followed by phase shifter technologies and liquid crystal phase shifters and a description of the project LISA-ES. The knowledge gap analysis with the gap identification and the resulting thesis objectives concludes this chapter.

In Chapter 2, the fundamentals for the functionality of the phased array antenna are described starting with general characteristics of phased arrays. This is followed by a brief description of the characteristics of liquid crystals and basics of wave propagation in rectangular waveguides.

The simulation and phase jump optimization of the proposed antenna array with 16x16 horns is shown in Chapter 3. The necessity of phase jumps is described, followed by a simplified calculation of the worst case gain reduction through paraphases. A baseline simulation for different orbit scenarios is performed to evaluate this problem in a realistic environment. This baseline is used to propose an optimization method which is then evaluated on a worst-case scenario of the baseline simulation.

Chapter 4 shows the developed manufacturing process and the encountered problems. First, different designs of the LCPS parts are presented to show the development during the project and some of the encountered problems at this stage are described. Then, the internal structure and the process sequence are shown including the solutions to the encountered problems. At last, alternative manufacturing methods are proposed and first results are shown.

The LCPS characterization is shown in Chapter 5. It is divided into the description of the experimental setup, the comparison of different manufacturing techniques, the temperature dependency of the LCPS's properties and the phase over voltage calibration of the LCPSs.

The experimental measurements of a 4x1 horn antenna array is shown in Chapter 6. It starts with a description of the experimental setup in the compensated compact range, followed by the static measurements of the array. At last the dynamic behavior of the array at a constant steering velocity is shown.

The conclusion and outlook of this work are given in Chapter 7.

1.2 State of the Art

This subchapter shows the state of the art in phased array technologies for communication antennas with the focus on phase shifting technologies. Chapter 1.2.1 gives an overview of different phased array technologies and a typical classification before several applications with the focus on satellite communication are introduced. Chapter 1.2.2 shows different phase shifting technologies that are used or under development, not only for space but also for terrestrial applications. In Chapter 1.2.3 different uses of LC for phase shifting technologies are shown.

1.2.1 Phased Array Technologies for Satellite Communication

A phased array consists of several radiating elements or array elements that are, in most cases, connected through a distribution network or feed network (Table 1, left and middle). If the network itself is used to control the beam formed by the array it is sometimes also referred to as a beam forming network (BFN).

Phased arrays are commonly divided into two groups, passive and active arrays, shown in Table 1 on the left side and in the middle (Parker and Zimmermann, 2002b). Passive arrays (also PESA, passive electronically scanned array) are defined to have only one high power amplifier (HPA, transmitter exchange (TX) case) or low noise amplifier (LNA, receiver exchange (RX) case) for all array elements. For the TX case, the amplification of the signal is done before the signal is split up and phase shifted. In the RX case, the phase shifting is performed before the LNA. Active arrays (also AESA, active electronically scanned array) have one HPA and one LNA for each array element. In the TX case, the phase shift is performed before the signal is amplified and in the RX case the LNA amplifies the signal before the phase is shifted.

Digital beamforming, shown in Table 1 on the right side, can be seen as a special form of an active array since each radiating element has an HPA / LNA (Parker and Zimmermann, 2002a). The difference of the 'normal' active array to the active array with digital beamforming is the absence of a phase shifter. For the TX case, the signal is generated for each array element separately (in baseband-, intermediate- or carrier frequency). The signal consists of a digital waveform that is generated by, for instance, a field-programmable gate array (FPGA). This allows to shift the signal in time thus creating a true time delay phase shifter.

Since active antennas need several amplifiers (one for each radiating element), a small amplifier would be desirable. The use of solid state power amplifiers (SSPA) would reduce the size of such arrays, but the power dissipation of SSPAs is still significantly higher than the dissipation in common traveling-wave tube amplifiers (TWTA) especially at high frequencies (Yüceer, 2012). Table 2 shows some efficiency values for TWTAs and SSPAs (PAE – power added efficiency). Despite the disadvantage in efficiency at high frequencies, the SSPAs offer an advantage in mass and complexity. Reliability data for TWTAs and SSPAs can be found in Strauss (1994); Weekley and Mangus (2005); Nicol, Mangus and Grebliunas (2008).

For the 'normal' active array and the passive array, phase shifters are a key component. "In passive phased arrays, low-loss feed networks are essential and usually waveguides are used. In active arrays, some loss in the feed network can be tolerated and stripline or air-stripline medium is used to reduce array depth, weight and cost" (Parker and Zimmermann, 2002a, p. 690).

Table 1: Overview phased arrays

Passive array	**Active array**	Digital Beamforming
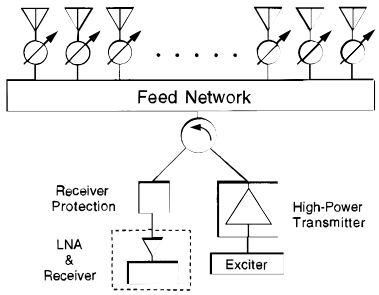	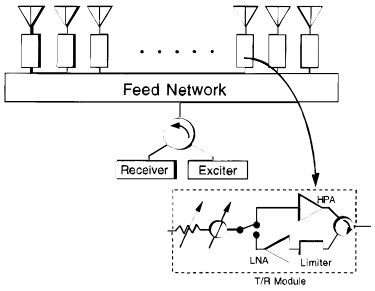	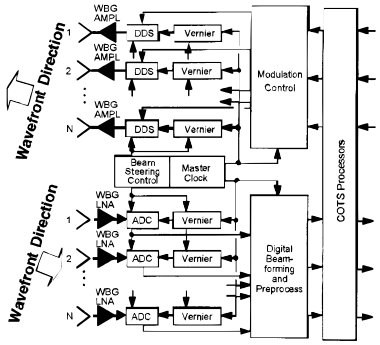
(Parker and Zimmermann, 2002b)	(Parker and Zimmermann, 2002b)	(Parker and Zimmermann, 2002a)

Table 2: Efficiencies of high power amplifiers

	TWTA	**SSPA**
L-band	60 %-65 % (Thales, 2012b)	65.8 % PAE (Katz *et al.*, 2017)
S-band	64 %-66 % (Thales, 2012b)	48 % PAE (Darbandi *et al.*, 2008)
X-band	46 % (Sharma *et al.*, 2017) for deep space 59 %-66 % (Thales, 2012c)	37.5 % (Sharma *et al.*, 2017) for deep space
Ku-band	65 %-70 % (Thales, 2012a)	45 % PAE (Kaper, Harris and Kessler, 2017)
K-band	52 %-65 % (Thales, 2013)	29 % PAE (Kaper, Harris and Kessler, 2017) 30 % PAE (Noh and Yom, 2016) 34 % PAE (Friesicke *et al.*, 2013) 48 % PAE (Campbell *et al.*, 2012)
Ka-band	55.2 % (Simons *et al.*, 2010) 50 %-55 % (Thales, 2013)	27 % PAE (Fujii, 2015) 30 % PAE (Campbell *et al.*, 2013) 34 % PAE (Campbell *et al.*, 2013)

There are several possibilities to change the phase of an incoming signal. The technologies differ in the usable bandwidth, the insertion loss (IL), the return loss (RL) and usable frequencies. Thus, not all of these technologies are useful for all types of applications and not all of them are feasible in both groups of arrays.

For phased arrays in space communication, different configurations can be found. If there is only free space between the array elements and the receiving antenna in a transmitting case, the array is often referred to as a DRA. In some cases, a reflector is inserted into the propagation path to increase the gain of the antenna. This configuration is also referred to as an array-fed reflector (AFR). An AFR with a confocal reflector optic (two confocal reflectors within the propagation path) is referred to as imaging phased array (IPA). All of these options have in common that the phase shifting is performed by the feed array (Rutledge and Muha, 1982; Stirland, Scouarnec and Wolf, 2013; Wolf *et al.*, 2014; Cooley, 2015).

In contrast to these technologies that use a phased array as a feed, an antenna referred to as reflectarray is fed by a single horn and the phase control is performed by the reflector (Huang and Encinar, 2007; Yüceer, 2012). The reflector consists of several metal patches on a dielectric substrate instead of one solid piece of metal or carbon fiber. In some cases, the properties of the dielectric substrate can be dynamically controlled and thus the antenna beam can be steered. This technology has been realized with liquid crystals (Moessinger *et al.*, 2006; Hu *et al.*, 2007, 2008; Marin *et al.*, 2007; Bildik *et al.*, 2011, 2015, Perez-Palomino *et al.*, 2013, 2015).

Phased arrays with fixed beams are widely used in GEO relay satellites. The footprints are shaped with a BFN to distribute the information depending on, for example, linguistic borders (Schneider, Hartwanger and Wolf, 2011; Wolf *et al.*, 2014). Designs for a BFN are, for example, the *Butler Matrix* or the *Rotman Lens*.

The *Iridium* and *Globalstar* satellites in LEO are using BFNs to create multiple beams (Metzen, 2000; Rohwer *et al.*, 2010). *Iridium* uses active phased arrays with *Butler Matrices* to produce 16 beams in the L-band (1 GHz to 2 GHz) with 80 radiating elements per panel. Each satellite carries three of these active phased array panels resulting in 48 beams per satellite. The amplification of the signal at each array element is performed by a gallium arsenide pseudomorphic high-electron-mobility transistor (HEMT) *Doherty* power amplifier (also SSPA). *Globalstar* provides 16 beams per satellite and uses SSPAs, pseudomorphic HEMT and field-effect transistor (FET) in a monolithic microwave integrated circuit (MMIC), to amplify the signal. It uses 91 array elements for the transmission in S-band (2 GHz to 4 GHz) and 61 array elements for the reception in L-band (1 GHz - 2 GHz).

Another interesting new field for fixed beam phased array antennas is the application on *CubeSats*. Hodges, Hoppe, et al. (2015), and Hodges, Radway, et al. (2015) describe the development of an AFR on the back of a solar panel that is mounted on a three unit *CubeSat*. A refined version of this antenna (X-band, 8 GHz to 12 GHz) is mounted on the first deep space *CubeSat* mission *MarCO* which successfully operated close to Mars (Klesh and Krajewski, 2015; Asmar and Matousek, 2016; Hodges *et al.*, 2017).

Besides the use of fixed beams (that only allow minor adjustments), some applications need beam steering capability to be able to change their service area (footprint) or even offer the continuous tracking of an object (e.g., plane, satellite in LEO).

Begovich et al. (1966) describe the idea of using self-phased arrays (*Van Atta* arrays) as retrodirective arrays on a relay satellite. Thereby, the retrodirective array is used to forward the signal from the relay satellite to the receiving station (satellite or ground station). The receiving station has to send a continuous wave (CW) signal to the array. This signal is then modulated with the signal send from the transmitting station and is automatically returned in the direction of the CW signal. The modulated signal of the transmitting station is received by another antenna on the relay satellite.

In Kampinsky and Kummer (1970), two beam steering (scanning) applications for space applications with ferrite phase shifters are described. The first is a variable coverage communication antenna using nonreciprocal ferrite phase shifters and the second is an antenna for radiometric measurements with *Spencer-Reggia* type phase shifters (payload name *Nimbus D*). The second antenna array was originally developed for a jet aircraft (bandwidth 300 MHz, frequency 19 GHz).

After these early applications, phased array antennas are in use on several communication satellites.

The *Tracking and Data Relay Satellites* (TDRS) of the National Aeronautics and Space Administration (NASA) use phased arrays as their multiple access antenna (Schwartz *et al.*, 1970; Teles, Samii and Doll, 1995). However, for a receive case the signal of each array element is transmitted to the ground and the array pattern is generated in the ground station. The system is called adaptive ground-implemented phased array (AGIPA) - (Spearing, 1973; Schwartz and Smith, 1975; Avant *et al.*, 1992). The ground link of each TDRS has to have the bandwidth of the number of array elements times the bandwidth of each element.

The MESSENGER Deep Space Mission uses a X-band phased array with MMIC phase shifters and SSPAs (Wallis and Cheng, 2001).

The *Engineering Test Satellite VI* (ETS-VI) of the national space development agency (NASDA, now Japan Aerospace Exploration Agency - JAXA) uses an S-band phased array antenna with 4-bit PIN (positive intrinsic negative diode) phase shifters and an on-orbit phase calculation (Tanaka *et al.*, 1994, 1997, 1998). The tracking range (field of view) is ±10° to enable the relay of data for LEO satellites up to 1 000 km orbit altitude. The antenna system is capable to form multiple beams and the tracking error is given with less than ±1.1°. It is an active array with an LNA and an HPA for each array element. The LNA and the HPA are based on a gallium arsenide FETs.

Engineering Test Satellite VIII (ETS-VIII) uses two AFRs with active phased arrays and MMIC beamformers (including MESFET-based phase shifters, metal-semiconductor field effect transistor). Each of the two antennas works in S-band and consists of a 19x17 m reflector that is fed by 31 radiating elements (Ohira, 1997; Suzuki *et al.*, 2000; Suzuki, Imaizumi and Ohata, 2008). The BFN is based on a *Butler Matrix*.

Another Japanese satellite (JAXA & National Institute of Information and Communications Technology, NICT) *Wideband InterNetworking engineering test and Demonstration Satellite* (WINDS) carries an active phased array with digital phase shifters (MMIC, 5 bit) that works in the Ka-band (Masanobu *et al.*, 2007). The antenna consists of two direct radiating arrays, one for receiving and one for transmitting signals. Each array has 128 elements and supports two beams. The target maximum data rate is 1.2 Gbps.

The *Wideband Global SATCOM* satellites system of the United States Department of Defense use X-band phased arrays (Roper *et al.*, 2003; Kumar *et al.*, 2005; Cook, 2010).

The British *Skynet 5* satellites (Ministry of Defense) also have an active X-band receive array with up to 50 independent gain areas (Stirland, Scouarnec and Wolf, 2013; Airbus, 2014).

Besides these governmental satellites, commercial satellite providers are also interested in the gain in flexibility due to steerable phased arrays.

The *Inmarsat 4* satellites use digital beamforming via an on-board processor (Stirland and Brain, 2006; Stirland, Scouarnec and Wolf, 2013). The main antenna is an array-fed mesh reflector with a diameter of 9 m. The array consists of 120 LHCP (left-handed circular polarization) helix radiators and is working in the L-band. The reflection changes the polarization to right-handed circular polarization (RHCP). The signal amplification is performed by a multiport power amplifier (MPA) consisting of 150 SSPAs (120 are active) (Angeletti and Lisi, 2008). The antenna can synthesize more than 200 beams.

The *Eutelsat Quantum* class satellites will use a reflector fed by two active arrays (horn antenna arrays) with one traveling wave tube amplifier (TWTA) for each horn. “Eutelsat Quantum class of satellites is the first fully flexible software-defined Ku-band geostationary satellite for the commercial telecommunication market. […] The composite signal for each beam is generated at low power level and amplified just behind the array, via a dedicated HPA per array element. The low-power BFN is located before the amplification section and includes all the control functions to reconfigure each single beam, i.e., a Variable Phase-Shifter and a Variable Attenuator for each radiating element.” (Gatti, 2015, pp. 2–4)

1.2.2 Phase Shifter Technologies

There are many options to build a phase shifting device. Some of the technologies can be combined to enhance the performance which makes it even more difficult to get an overview of the different options.

In Koul and Bhat (1991, 1992) phase shifters are divided into the following types shown in Table 3. They describe five subtypes of mechanical phase shifters whereby the last subtype only discusses the use of the before mentioned techniques as fixed phase shifters.

Linear phase shifters use a linear motion to control the length of the section responsible for the phase shift. A rotary vane phase shifter uses a rotary motion to change the rotation angle of a circular waveguide relative to the beginning / end piece of the waveguide (a linearly polarized TE_{10} mode is converted into a TE_{11} mode that is affected by the relative angle between a half-wave plate and two quarter-wave plates). Dielectric-insert phase shifter use a linear or rotary motion to insert / extract dielectric material into / out of the transmission path. Dielectric-slab-loaded waveguide phase shifter use a linear motion to change the position of dielectric material within the waveguide (along the broad side of the cross-section).

The second type of phase shifters described by Koul and Bhat (1991, 1992) are ferrite phase shifters. According to Parker and Zimmermann (2002a) and Romanofsky (2007) ferrite phase shifters are common in radar technology and a comparison of PIN diode and ferrite phase shifters can be found in Parker and Zimmermann (2002a). Further information about ferrite phase shifters can be found in the following publications: Dionne, Oates and Temme (1995); Oates et al. (1997); Dixit and Pourush (2000); Yang et al. (2013); Deng et al. (2017). According to Yüceer (2012, p. 31) the “Ferrite phase shifter technology is a mature technology widely used in US military communication satellites, and selected for its low loss characteristics”. Some early ideas for ferrite phase shifters in space applications are shown in Backus (1965) and Kampinsky and Kummer (1970).

A third type of phase shifters are called switch-type phase shifters which are typically manufactured in MMIC technology (Parker and Zimmermann, 2002b, 2002a). The switches can be realized as MEMS, PIN diode, FET/MESFET and (pseudomorphic) HEMT. These phase shifters are sometimes referred to as digital phase shifters since the phase can only be influenced in steps (e.g., 4 or 5 bit) and not continuously. In addition to the switches, varactor diodes can influence the phase between the switched states leading to an analog (or continuous) phase shifter with more than just the phase states defined by the switches (Koul and Bhat, 1991, 1992). Roederer (2005) describes a phase shifting application with MEMS and Parker and Zimmermann (2002a) show different circuits for switch type phase shifters.

The surface acoustic phase shifter uses the piezo electric effect to shift the phase and the magnetostatic phase shifter uses ferrimagnetic materials to shift the phase.

The losses / figure of merit of the FET and MEMS technology for different frequencies have been compared in Romanofsky et al. (2000) and Rebeiz, Tan and Hayden (2002). Pillans et al. (1999, 2000) show the RF-performance of MEMS in the Ka-band.

In addition to the types defined in Table 3, there are some other technologies available or under development:

Christodoulou et al. (2012) mention the option of using photoconductive elements as switches and calls the antennas optically reconfigurable antennas. Additional possibilities for optically reconfigurable antennas are described in Frankel et al. (1998) and Meijerink et al. (2007).

True time delay phase shifters based on optical systems are introduced in Ng et al. (1991); Ackerman et al. (1992); Esman et al. (1993); Soref (1996); Anderson and Liddle (2002); Chen et al. (2004); Davis et al. (2013); Rotman, Tur and Yaron (2016); Anzalchi et al. (2017). The length of the optical path is controlled by optical switches and thus the time delay of the signal can be controlled. Most of these systems have a finite number of states and are therefore digital phase shifters.

Another option are ferroelectric materials. They are fast, but need a strong electric field in the order of 10^3 V/mm (Romanofsky, 2007). A comparison between ferroelectric phase shifters and other types of phase shifters (ferrite, MEMS, semiconductor-MMIC and LC) can be found in Jakoby et al. (2004) and Romanofsky (2007). In Weil, Mueller, Scheele, Kryvoshapka, et al. (2003), both LC and ferroelectric phase shifters are tested. Further information about ferroelectric materials can be found in Romanofsky and Qureshi (2000); Romanofsky et al. (2000); Miranda et al. (2000); Acikel et al. (2001, 2002b, 2002a); Vélu et al. (2007); Romanofsky and Toonen (2018).

Table 3: Types of phase shifter technologies

Type:	Subtype:	Sub-Subtype:	Additional information:
Mechanical	Linear		
	Rotary-Vane		
	Dielectric-Insert		
	Dielectric-Stab-Loaded		
	Fixed		
Ferrite	Waveguide geometry	Nonreciprocal	
		Reciprocal	
	Strip-Line	Nonreciprocal	
		Reciprocal	
	Microstrip-Line	Nonreciprocal	
		Reciprocal	
	Slot-Line	On Dielectric Substrate	
		On Coplanar-Line on Ferrite Substrate	
		Multilayered	
	Coplanar-Line	On Ferrite Substrate	
		Multilayered	
	Fin-Line	On Ferrite Substrate	
		On Ferrite-Dielectric Substrate	
Switch	Reflection-type	Circulator coupled	Digital, Analog with Voltage variable control devices (e.g., varactor diode)
		Hybrid coupled	Digital, Analog with Voltage variable control devices (e.g., varactor diode)
	Transmission-type	Switched line	Digital
		Loaded line	Digital, Analog with Voltage variable control devices (e.g., varactor diode)
		High-pass low-pass	Digital
		Switched network	Digital
Surface Acoustic	Surface Acoustic Wave Delay-Line (SAW)		Piezoelectric
Magnetostatic	Magnetostatic Wave Delay-Line (MSW)		Ferrimagnetic medium

1.2.3 Liquid Crystal Phase Shifters

Liquid crystals (see Chapter 2.2) can be used in different ways for phase shifting applications. Based on the structure proposed by Koul and Bhat (1991, 1992) shown in Table 3, Table 4 and Table 5 show a similar structure applied to LCPSs.

Many of the subtypes of the LCPSs in Table 5 can also be found for ferrite phase shifters (Table 3). The effect used in ferrite phase shifters is mainly the change in the permeability whereas the LCPSs use the change in the permittivity. Since permeability and permittivity are connected through the speed of light in the material ($c = 1/\sqrt{\mu\varepsilon}$) the effect on the RF-signal is similar.

The sub-subtypes show some additional ideas to optimize the performance. If the field sub-subtype in Table 5 is left blank, the subtype can be seen as the reference.

The use of liquid crystals in switch type phase shifters is limited to the use in varactor diodes. In Koul and Bhat (1992) the option of using varactor diodes for some of the switch type phase shifters from Table 3 to enable a refined tuning of the phase ('analog' instead of 'digital') is mentioned. Table 4 lists two publications that examine the use of LC in varactor diodes which could be used in switch type phase shifters.

In addition to the structure proposed in Koul and Bhat (1991, 1992), Strunck et al. (2013) describe three different phase shifting options for LC:

1. Loaded line with varactor (Atwater, 1985; Ellinger, Vogt and Bachtold, 2001)
2. Resonant type (Moessinger *et al.*, 2010)
3. Transmission type (Goelden *et al.*, 2009)

This description is not based on the component or material that is mainly responsible for the phase shift, but on the circuit design that is used to get a phase shifting effect.

The examples for the waveguide topology in Table 5 also show publications from the project LISA-ES and its predecessor. First measurements of the current LCPS waveguide design with regard to its performance at room temperature can be found in Weickhmann (2017).

Since LC is commonly known in optical applications, McManamon et al. (1996), Anderson and Liddle (2002) and Davis et al. (2013) also describe the option of using LC in optical phase shifters for phased arrays.

The uses of LC mentioned here are all aiming for a phase shifting device used in a phased array. A reflectarray is another possible option to realize the beam steering (Chapter 1.2.1). This technology, together with the use of LC is described in Moessinger et al. (2006); Hu et al. (2007); Marin et al. (2007); Gaebler, Moessinger, et al. (2009); Doyle et al. (2016).

Table 4: Switch-type phase shifter extendable with liquid crystal based varactor diodes

Type:	Subtype:	Sub-Subtype:	Publications:	Additional information:
Switch	Reflection-type	Circulator coupled	(Goelden *et al.*, 2008; Karabey *et al.*, 2011)	Analog with Voltage variable control devices (e.g., **varactor diode**)
		Hybrid coupled		Analog with Voltage variable control devices (e.g., **varactor diode**)
	Transmission-type	Loaded line		Analog with Voltage variable control devices (e.g., **varactor diode**)

Table 5: Phase shifter technologies using liquid crystals

Type:	Subtype:	Sub-Subtype:	Publications:	Additional information:
Liquid Crystal	Waveguide geometry		(Gaebler *et al.*, 2008a; Gaebler, Goelden, *et al.*, 2009; Jost *et al.*, 2013; Weickhmann, Gaebler, *et al.*, 2013; Weickhmann, Nathrath, *et al.*, 2013; Jost, Weickhmann, *et al.*, 2015; Weickhmann, 2017) Project LISA-ES and predecessor	
		Substrate-integrated waveguide (SIW)	(Strunck *et al.*, 2013, 2015) Project Liquida 2 (using low temperature cofired ceramics, LTCC)	
	Strip-Line		(Jost, Strunck, *et al.*, 2015)	
	Microstrip-Line		(Dolfi *et al.*, 1993)	
		Meander Delay Line	(Kuki, Fujikake and Nomoto, 2002), (Deo *et al.*, 2013)	
		Microstrip Patch Array	(Liu and Langley, 2008)	
	Inverted Microstrip-Line (IMSL)		(Weil, Luessem and Jakoby, 2002; Martin *et al.*, 2003; Weil, Mueller, Scheele, Best, *et al.*, 2003; Jakoby *et al.*, 2004; Muller *et al.*, 2004; Gaebler *et al.*, 2008b; Gaebler, Goelden, *et al.*, 2009; Karabey *et al.*, 2011) (Sanadgol, Holzwarth and Kassner, 2009; Strunck *et al.*, 2013) Project *Liquida* (in LTCC)	
		Spiral Delay Line	(Karabey *et al.*, 2012)	
		Ring Filter	(Moessinger *et al.*, 2010)	Resonant type
	Coplanar-Line (Coplanar Waveguide, CPW)		(Goelden *et al.*, 2009)	Transmission type
	Slow-Wave Coplanar-Line (Coplanar Waveguide, S-CPW)		(A.-L. Franc *et al.*, 2013)	
	Fin-Line		(Mueller, Felber, *et al.*, 2005)	

1.2.4 Project LISA-ES

LISA-ES was funded by the German Aerospace Center (DLR) *Space Administration* and developed by the *Technical University of Munich*, the *TU Darmstadt*, *NTP GmbH*, *University of Applied Sciences Munich*, *IMST GmbH, Ingenieurbuero Letschnik – IBL and Astrium GmbH (now Airbus DS).*

The aim of this project was to develop the idea of a waveguide-based phase shifter with liquid crystal to a point where the functionality of a phased array with these phase shifters could be demonstrated. The project is based on an antenna design and manufacturing method developed in the project LISA-MS (lightweight inter-satellite link antenna – mechanically steerable, also LISA-2). Both antennas are designed for inter-satellite link (ISL) frequencies in the K/Ka-band since, compared to S- or X-band, higher bandwidths are available.

1.2.4.1 Scenario

The basis for the development of the LISA-ES antenna is an on-orbit servicing scenario. A servicing satellite in a LEO chases a target satellite and aims to catch it / dock with it. A controller on the ground monitors the situation or even controls the servicing satellite. The situational awareness of the controller is a key factor for this scenario. Several vision/optical sensors (cameras) and sensors such as range finders (LIDAR – light detection and ranging or RADAR – radio detection and ranging), force sensors, or tactile sensors can improve this situational awareness (Wilde *et al.*, 2015), but they also produce a large amount of data that has to be transmitted to the ground station. According to Harder et al. (2009) at least 10 Mbps are necessary.

The reason to use a relay satellite in a GEO is the need for a close to real-time and continuous data link capability despite the limited duration where a LEO satellite is visible from the ground station. Even for LEO satellites in high altitudes (1 000 km to 2 000 km), the visibility, and thus the communication link, lasts for 18 to 22 minutes (minimal elevation angle of 10°), and this only for an optimal pass. For lower orbits, such as for instance the Hubble Space Telescope with an orbit height of about 570 km, the best case acquisition time would be 12 minutes (Stoll *et al.*, 2012). A GEO relay satellite can increase the time without the need for several ground stations to slightly more than half the orbit period (52 to 64 minutes) for small inclination angles. For inclination angles around 90°, the link time can, for certain constellations, be extended up to an entire orbit period of the LEO satellite (Lundin and Stoll, 2006; Stoll *et al.*, 2012).

A continuous communication between the operator and the servicing satellite during the docking is essential for a tele-commanded servicing mission (Harder *et al.*, 2009). Even for an automated mission with an observer on the ground, it would be desirable to have a continuous link, to be able to abort the docking process if necessary.

The advantage of the GEO relay satellite for this type of missions comes at the cost of a much longer minimum signal traveling time of 0.24 s for one way and 0.48 s for a roundtrip compared to less than 0.03 s for a roundtrip with a direct downlink from LEO. Experimental measurements showed time delays between 0.56 s and 0.70 s for the roundtrip including delays caused by local and wide area networks (Stoll *et al.*, 2009, 2012). Furthermore, the antenna size on the servicing satellite has to be increased compared to a direct downlink to the ground station if the power consumption and the data rate are fixed.

The motivation to develop this antenna system (LISA-ES and LISA-MS/MS+) lies in the combination of the signal traveling time, the large amount of data produced on the servicing satellite and the situational awareness of the controller. Long contact times are desired for the operation, but the controllability decreases with increasing time delay (Wilde *et al.*, 2015). Since the time delay is critical and high compression rates tend to increase the time delay, the idea is to go to higher bandwidths and low compression rates to keep the time delay at a minimum.

For a high data rate communication, a high gain antenna on the GEO satellite is needed. Besides using a low loss waveguide distribution network for the amplified signal, the directivity of the antenna is the main driver to increase the gain. A high directivity results in a narrow beam which makes a beam steering necessary.

The angular range to track a LEO satellite from a satellite in GEO is about ±11° (from boresight). This covers LEO satellites with a maximum orbit height of 1 500 km. Since this angular range is relatively small, phased antenna arrays can cope with it without losing much of their gain due to the influence of the element patterns. The element patterns and the element spacing of the LISA-ES array are designed to comply with these specifications (see Chapter 1.2.4.2).

In contrast, the LISA-MS/MS+ antenna and mechanism are specially designed for the application on the more agile servicing satellite (compact antenna design with an agile mechanism) and act as a counterpart to the LISA-ES antenna. The development of the mechanically steered LISA-MS antenna started prior to LISA-ES. However, at the start of the LISA-MS development, the idea of an electronically steered antenna already existed as a long-term goal. The first idea was to combine the manufacturing technology with a digital beam forming technology for a GEO application which was also funded by the DLR *Space Administration* (Smart Antenna Terminal / SANTANA developed by *IMST GmbH, Institute of High Frequency Technology – Hamburg University of Technology, Institute of Communications and Navigation* - DLR *in Oberpfaffenhofen, EADS Astrium GmbH*).

Besides the mentioned application as a relay antenna for on-orbit servicing missions, LISA-ES could also be used as a relay antenna for earth observation missions where the data has to be transmitted in close to real time or data storage is difficult / the amount of data produced in one orbit is too large for a single data downlink dump to a single ground station (Harder *et al.*, 2009).

1.2.4.2 Antenna

The LISA-MS/MS+ antenna is manufactured in an electroplating technique, using lost aluminum cores. After the copper is electro-deposited on the core, the aluminum is etched out to create a hollow waveguide with a thin copper wall, whose inner surface is a close negative replica of the lost aluminum core.

The idea of LISA-ES is to combine this LISA manufacturing technique and the phase-shifting technology developed in the project LIQUIDA (liquid crystal antenna array, LIQUIDA 2) funded by the DLR *Space Administration* and developed by *IMST GmbH, W.C. Heraeus GmbH, BAM Bundesanstalt für Materialforschung und -prüfung, Merck KGaA* and the *TU Darmstadt*.

The development of an integrated waveguide phase shifter with an electroplated copper wall, filled with liquid crystal, is an objective of the LISA-ES project. This phase shifter has to be tested together with the electroplated array to demonstrate the functionality as a phased array system.

The LISA-ES antenna can be seen as the counterpart of the LISA-MS antenna within the ISL network. LISA-ES is therefore designed for ISL frequencies in the K/Ka-band and the application on a GEO relay satellite (lower band: 23.0 GHz to 23.5 GHz, upper band: 27.0 GHz to 27.5 GHz).

The design of the LISA-ES array is a trade-off between the grating lobe requirements and the increasing complexity due to an increasing number of horns, phase shifters and levels / branches in the distribution network. For the same aperture size, more horns would result in a larger offset of the grating lobes to the main lobe up to the point where they disappear from the visible region (wavelength equals element spacing). However, this increases the complexity of the antenna and leads to problems accommodating the LCPSs. Fewer horns decrease the complexity, but, at a certain element spacing, the grating lobes occur within the desired steering region of the array which has to be avoided.

Therefore, the horn design from LISA-MS (transmitting from LEO to GEO) has to be modified to meet the requirements of the GEO application. The horns have a smaller diameter to be able to minimize the spacing

(from 50 mm to 25 mm) to avoid grating lobes within the desired steering region of the main lobe / in the vicinity of the earth. For 23 GHz, the grating lobes occur at about ±30° and for 27.5 GHz the grating lobes occur at about ±25° from boresight. With a desired steering angle of ±11°, the grating lobes are moving equally to the main lobe and therefore can get close to ±19° / ±14° from boresight of the antenna.

The antenna array for a GEO application comparable to LISA-MS (400 mm x 400 mm) would thus consist of 256 horn antennas (16x16) with two polarizations (RHCP & LHCP). Due to limited funding, in LISA-ES, only a 4x4 demonstrator was built to demonstrate the general functionality of a 2D electronically steerable antenna with LCPSs. Figure 1 shows this demonstrator without the LCPSs.

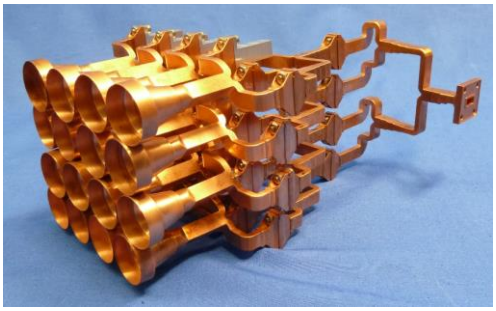

Figure 1: LISA-ES antenna, horns and waveguide distribution network, without LCPSs

1.2.4.3 Liquid Crystal Phase Shifter Control Functionality

The cross section in Figure 2 shows a simplified version of the phase shifter. The yellow lines are the striplines (titanium) that generate the electric field over the length of the LC cavity. The striplines are connected by a resistor network to ensure the even distribution of the voltages at minimized electric current (resistor values >1 MΩ between the striplines). The voltages at the upper left and lower right corner are constant (±164 V chosen for the demonstrator). The voltages at the lower left and upper right corner are variable between ±164 V, but $U_{1,\mathrm{var}} = -U_{2,\mathrm{var}}$ (see also Figure 3).

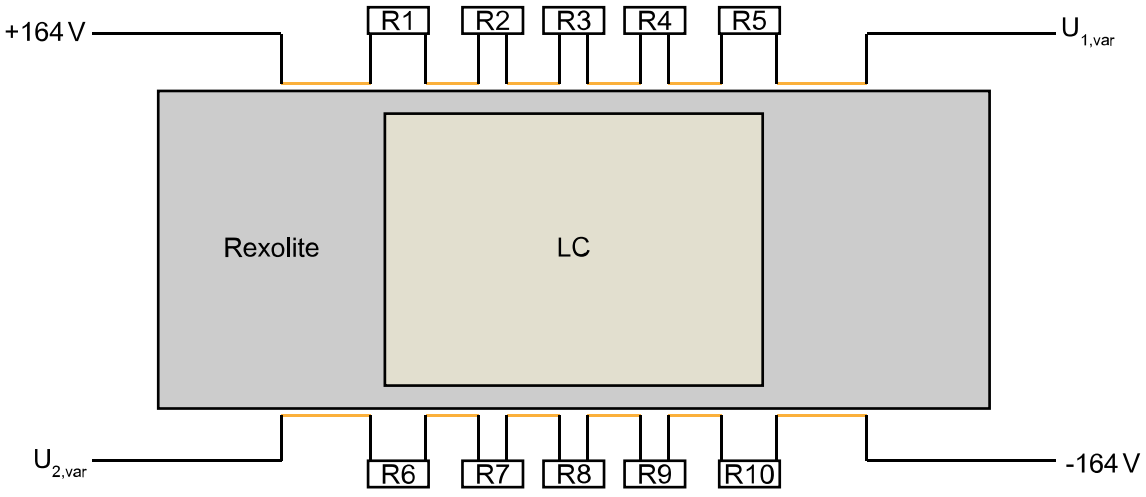

Figure 2: Cross section of the LISA-ES phase shifter

Figure 3 shows three different orientations of the electric biasing field in a cross section of the LCPS. The color represents the voltages between -164 V (blue) and +164 V (red). The black lines within the colored area are voltage level curves.

For the left orientation, the commanded voltage is -164 V and the case is referred to as the horizontal (H) case. The right orientation is the vertical (V) case and the commanded voltage for this case is +164 V. The orientation in the middle shows a state in between the two extreme states V and H. The variable voltages at the upper right and lower left corner can be controlled in steps of 1 V.

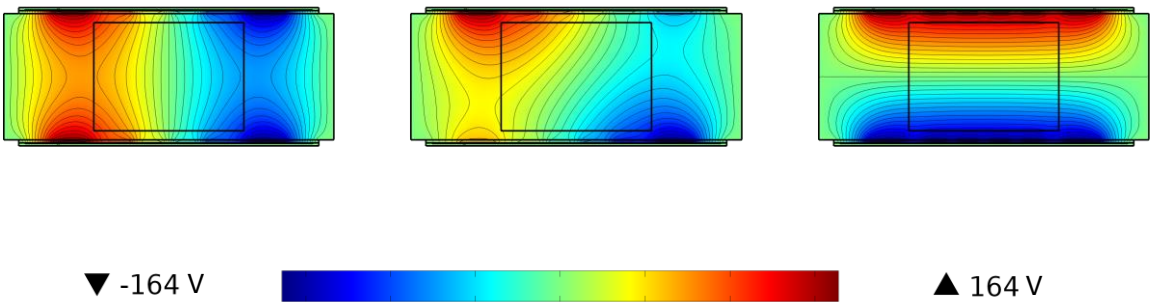

Figure 3: Horizontal case (left), an intermediate case (middle) and vertical case (right)

The illustrated voltage differentials (Figure 3) are constant for each commanded voltage (direct current, DC), but for practical purposes, an alternating current (AC) field with a square wave voltage is used (Chapter 2.2) to mitigate potential ionic migration within the LC to one electrode. Therefore, the voltages of the corner electrodes are switched crosswise, so that the direction of the resulting electric field is switched by 180°, which is deemed irrelevant for the LC orientation.

1.2.4.4 Phased Array Control

The control of the phased array consists of a hardware and a software part. The control electronics hardware is built by *IMST GmbH* and is able to supply each of the planned 16 LCPSs with four different voltages (2x constant ±164 V, 2x variable between ±164 V). For the chosen voltages, commercial of the shelf hardware parts are available. Higher voltages would be desirable and would improve the dynamic behavior of the LC. However, the cost for these parts would increase significantly and for a demonstration of the applicability, the commercial of the shelf hardware is sufficient.

A basic version of the software is also developed by *IMST GmbH* and is able to control the voltages at each channel (or LCPS) of the control electronic. The software communicates with the control electronic through *USB* with a serial communication protocol. On-board communication between the digital to analog converters is by *I²C* serial communication protocols.

The original rudimentary electronics control software is extended at the LRT (Institute of Astronautics, by Ventura and Hannon) to be able, as an integrated system software, to calculate the phases for the 16 LCPSs of the 4x4 array.

Figure 4 shows the control electronics hardware on the left side and the control software on the right side.

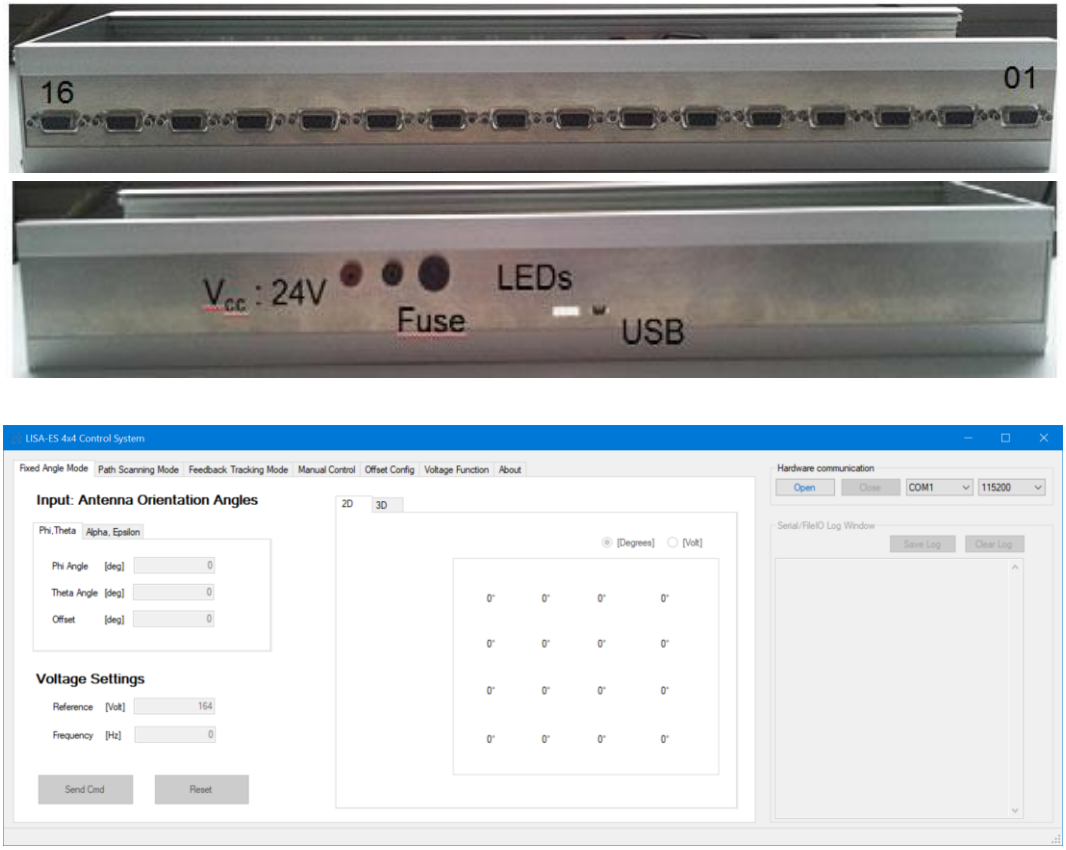

Figure 4: Hardware (top) and software (bottom) of the phased array control

1.3 Knowledge Gap Analysis

1.3.1 Gap Identification

In the development of the LISA-ES LCPSs several compromises are necessary concerning phase range (400°-500° instead of >3 000°), dynamic behavior (electric field strength, only ±164 V due to commercial of the shelf parts), manufacturability (minimum wall thickness) and operability (thermal stability and impermeability). These compromises have a strong influence on the LCPS performance which makes it necessary to characterize the resulting performance and analyze the usability for the desired application.

The wall thickness on the top and the bottom of the LCPS is limited due to the milling process. This limits the minimum distance between the LC and the film electrode which has an influence on the dynamic behavior of the LC.

The thermal expansion of the LC leads to increasing pressure within the LC cavity. The pressure can be reduced with bellows outside the waveguide that enable the expansion of the LC volume. The ‘chimneys’ extend the LC volume from inside the waveguide and lead through the waveguide wall to enable the mounting of bellows on the outside (see Chapter 4.2). This however has a negative effect on the RF-performance.

The design of the body (two plastic parts that build the LC-cavity) and the used glue (see Chapter 4.1.1) had to be changed due to leaks in the body. The thin film electrodes are very sensitive to mechanical damage and therefore the latest design allows for the use of solder pads within the waveguide (see Chapter 4.1.2). Cables can be soldered to these pads and lead through the waveguide wall. Both changes also have an effect on the RF-performance.

For a space application additional challenges arise that could lead to a non-functioning LCPS. Analyses on the behavior of different LCs regarding the space environment have shown, that LCs are not sensitive to radiation and have a relatively low vapor pressure (see Chapter 2.2). Due to the low vapor pressure, the mechanical stability and the gas permeability of the body encapsulating the LC cavity (LC-container) have been assessed as non-critical for first feasibility studies, even including short-term vacuum exposure.

To ensure a long-term functioning LCPS under space conditions, some analyses and experimental characterizations for this LCPS design are still necessary.

The following four knowledge gaps can be identified:

1) The design of the LCPS (bulky LC cavity and relatively large distance between the film electrodes) and the use of commercial of the shelf parts for the control electronics (max. ±164 V) lead to a small electric field strength and thus to a slow dynamic behavior (depending on the LC). The length of the LCPS is chosen to enable a phase range of >360° but is still too short for the desired steering range. This leads to lower transmission losses but the desired steering range of ±11° can only be reached by using different wavenumbers in a 'saw tooth' pattern over the entire array (see Chapter 3). With this pattern, instantaneous phase changes during the dynamic steering process are necessary. Since a dynamic tracking of a LEO satellite is one envisioned application for such an antenna, the effects of the dynamic behavior of the LCPS on the antenna performance have to be analyzed and characterized. It is essential to simulate the satellite orbits to get a realistic relative motion requirement and thus meaningful data regarding the antenna performance in real-life applications.

2) It has not been proven, that the envisioned manufacturing process (electroplated LCPS) can lead to a functional integrated LCPS. Since a light weight, small and rugged LCPS is critical for the integrated system and a planned application in space, the development of a manufacturing methodology and the verification of the manufacturing process is also critical and important for this type of LCPS.

The functionality of the integrated LCPS is not only dependent on the phase shift but also on the transmission losses and the reflection within the phase shifter. It is important to evaluate the manufacturing method also on the impact on these RF parameters.

3) Temperature environment compatibility and control in space applications is often critical. Therefore, it is essential to know the temperature-dependent behavior of the LCPS. The behavior is primarily determined by the temperature behavior of the LC. For the functionality of the LCPS, it is crucial that the temperature of the LC is within the limits of the nematic phase (clearing point *GT3-23002*: +153 °C, courtesy *Merck KGaA*) (see Chapter 5.5.2).

4) Due to the current design, the phase of the LCPS cannot be measured within the antenna assembly. It is necessary to calibrate each LCPS by measuring the relative phase over the commanded voltage to be able to steer the antenna beam. The verification of this method has not been performed with this LCPS design and is also critical for the functionality of the antenna.

The intended application involves a dynamic beam steering. The ability to dynamically control the phases of several phase shifters simultaneously is not yet proven.

1.3.2 Thesis' Objectives

From the identified knowledge gaps, the following thesis objectives can be derived:

Objective 1: Analysis of the influence of phase jumps during the dynamic tracking of the antenna

- Phase jump distribution for realistic LEO orbits (realistic relative motion)
- Different control options for the LCPSs (pivot point in the array center or at one corner horn)
- Jump optimization for a worst-case scenario

Objective 2: Documenting the preceding LCPS designs and challenges to be able to establish a functioning manufacturing process based on the latest design to get a fully integrated and functional LCPS

- Review of the preceding designs
- Process assurance of the LCPS core assembly
- Adaptation of the core assembly through additional steps, tools and changes in the process sequence where necessary
- Performance measurements of the manufactured LCPSs

Objective 3: Temperature dependent measurements of the static and dynamic behavior of the LCPS

- Measurement of the relative phase, transmission and reflection values (static)
- Measurement of the relative phase during phase jumps to get the time dependent behavior

Objective 4: Measurement of a phased array assembly with LCPSs to prove the static and dynamic functionality

- Calibration of each LCPS (Phase over voltage)
- Static measurement of the array pattern under different commanded angles
- Measurement of the array pattern with paraphases (static)
- Dynamic measurement of the array tracking

Not part of this work are measurements of the sensitivity of the used LCs to radiation and thermal vacuum testing of the LCPS. Since several publications have shown that the examined LCs have a low sensitivity to radiation, this influence is not seen critical and therefore not regarded in this work (see Chapter 2.2).

The vapor pressure that has been measured for several other LCs is low, and it is assumed that the vapor pressures for the LCs in this work are not significantly higher (see Chapter 2.2). Due to the fact that the mechanical stability of the LCPS body is not seen critical and the thermal expansion problem has not been solved sufficiently for a space application (despite the idea of using bellows) a thermal vacuum test is not performed within this work.

Therefore, neither radiation nor thermal-vacuum compatibility appear to be road-blocks for the implementation phase, should the fundamental functionality of the LC-based phase shifter be feasible and beneficial for the intended application.

2 Fundamentals

This chapter comprises the fundamentals that are necessary for this work. It is divided into three sections with the fundamentals for phased arrays, liquid crystals and waveguides.

2.1 Phased Array

“Phased arrays scan the beam by controlling the relative phasing between the elements. […] [Figure 5] shows the results of adding a series of time delays to equalize the path lengths in the lines where the position z_i along the axis determines the time delay τ_i for incident angle θ_0 [$i = 1,2, \ldots$]:

$$\tau_i = \frac{z_i}{c} \cos\theta_0 + \tau_0 \qquad \textbf{(2-1)}$$

This feed network is frequency independent, as we vary the progression of time delays to scan the beam.

Phase shifters replace the time-delay networks in phased arrays. They provide equivalent beam scanning at a single frequency.” (Milligan, 2005, pp. 115–116)

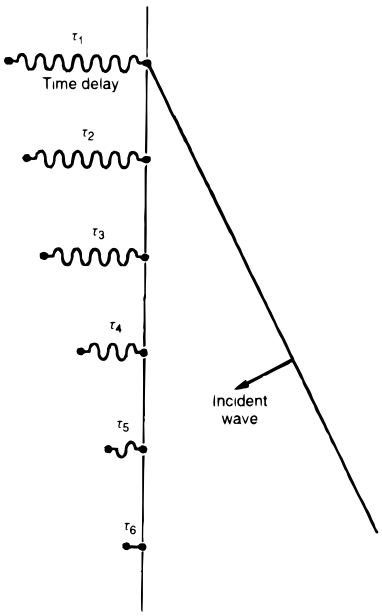

Figure 5: Linear array with time delay networks (Milligan, 2005)

It is important to keep in mind that the time delay is the decisive variable and this variable is frequency independent. Phase shifters are one option to control this time delay, but this control is (in most cases) frequency dependent, resulting in a reduced bandwidth or beam squint.

2.1.1 Beam Pattern

The following equations and descriptions are an adapted and shortened version from Van Trees (2002). For a linear array with isotropic elements, the element number N and the element spacing d, the beam pattern can be written as:

$$B_\theta(\theta) = \frac{1}{N}\frac{\sin\left(\frac{N}{2}\frac{2\pi}{\lambda}\cos\left(\theta+\frac{\pi}{2}\right)d\right)}{\sin\left(\frac{1}{2}\frac{2\pi}{\lambda}\cos\left(\theta+\frac{\pi}{2}\right)d\right)} \quad \textbf{(2-2)}$$

with $-\pi/2 \leq \theta \leq \pi/2$ (pattern angle).

Besides the main lobe, the array pattern has side lobes with nulls between them. These nulls occur when (2-3) and (2-4) apply ($m = 1,2, \dots$):

$$\cos\left(\theta+\frac{\pi}{2}\right) = m\frac{\lambda}{Nd} \quad \textbf{(2-3)}$$

$$\cos\left(\theta+\frac{\pi}{2}\right) \neq m\frac{\lambda}{d} \quad \textbf{(2-4)}$$

For arrays with an element spacing d larger than the wavelength λ grating lobes occur in the visible region of the pattern $(-\pi/2 \leq \theta \leq \pi/2)$. With $d \leq \lambda/2$, grating lobes can be entirely avoided. For isotropic elements, these grating lobes have the same gain as the main lobe and therefore are to avoid in the desired steering region.

The position of the grating lobes can be calculated with ($m = 1,2, \dots$):

$$\cos\left(\theta+\frac{\pi}{2}\right) = m\frac{\lambda}{d} \quad \textbf{(2-5)}$$

2.1.2 Phase Calculation

The blue marks on the blue line in Figure 6 show the center points of each radiating element of the 4x1 array, measured in Chapter 6, to scale. The blue horizontal line is thereby the maximum width of the aperture. The number of each radiating element is equal to the number of the phase shifter it is attached to (LCPS 1 to 4). The green line represents a planar wave (points of equal phase) that is to be generated by the radiating elements in the far field of the array. The pivot point of this line is in the center of the array.

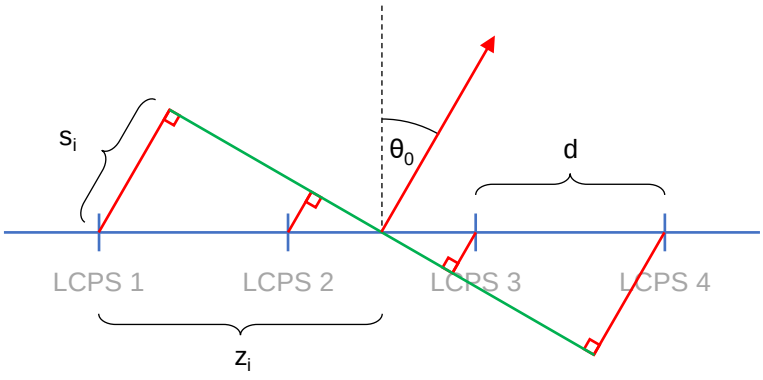

Figure 6: Phase calculation

The distance of each array element to the pivot point is given with z_i. With this distance, the spatial offsets s_i necessary for a constructive interference of the radiated signals in the desired direction are (similar to equation (2-1)):

$$s_i = z_i \cdot \sin\theta_0 \tag{2-6}$$

With the assumption that the signals propagate with the speed of light in vacuum (c_0) the time delay for each radiating element (LCPS) is:

$$\tau_i = \frac{s_i}{c_0} \tag{2-7}$$

The desired phase shift in degrees for a frequency f is thereby:

$$p_i = f \cdot \tau_i \cdot 360° + p_0 \tag{2-8}$$

Assuming that p_0 is zero, the phases for LCPS 3 & 4 in the case shown in Figure 6 are positive whereas the phases for LCPS 1 & 2 would be negative (as are the desired time delays). In reality, there are no negative time delays or phase shifts. The absolute phase shift level can be freely selected (p_0) since only the relative phases between the radiating elements have an influence on the behavior of the antenna. Therefore, the negative relative phase shift represents a phase shift level below the chosen absolute phase level ($p_0 \geq |p_{i,\mathrm{min,rel}}|$).

This also means, that the pivot point that is used to calculate the phases does not necessarily have to be in the center of the array but can also be at one of the radiating elements as shown in Chapter 3.

Table 6 shows the values of the 4x1 array (used in this work) for a steering angle of 11° at a frequency of 23 GHz. The desired time delay for each radiating element is in the range of picoseconds.

Table 6: Desired values for a steering angle of 11° at 23 GHz

	LCPS 1	LCPS 2	LCPS 3	LCPS 4
s	$-7.155 \cdot 10^{-3}\,\mathrm{m}$	$-2.385 \cdot 10^{-3}\,\mathrm{m}$	$+2.385 \cdot 10^{-3}\,\mathrm{m}$	$+7.155 \cdot 10^{-3}\,\mathrm{m}$
τ	$-23.867 \cdot 10^{-12}\,\mathrm{s}$	$-7.756 \cdot 10^{-12}\,\mathrm{s}$	$+7.756 \cdot 10^{-12}\,\mathrm{s}$	$+23.867 \cdot 10^{-12}\,\mathrm{s}$
p	$-197.624°$	$-65.875°$	$+65.875°$	$+197.624°$

The overall phase range of the case shown in Table 6 is more than 360°. Depending on the phase shifter design, this phase range might be larger than the phase range of the phase shifter. For some cases and under certain assumptions, this problem can be solved as described in Chapter 3.

2.1.3 Figure of Merit

The figure of merit for phase shifters is a measure used in several publications to compare the quality of different phase shifters. It relates the measured differential phase to the maximum insertion loss for a fixed frequency or small frequency range. For LCPSs the insertion loss is at a maximum when the loss tangent $\tan\delta$ is at a maximum. For the LCs used in the measurements, the loss tangent is at a maximum for the perpendicular biasing state / vertical electric field (see Appendix G for Figures of Merit of other LCPSs).

$$F_{\mathrm{FoM}} = \frac{p_{\max} - p_{\min}}{L_{\mathrm{IL}_{\max}}} \tag{2-9}$$

2.2 Liquid Crystal

Besides the three states of matter that we observe in our environment (solid, liquid, gaseous), some materials show more than three states. These organic materials are called liquid crystals (mesomorphic phases) and show several transitions between solid and liquid (de Gennes and Prost, 1995).

The states in-between solid and liquid can be defined by their positional order. In de Gennes and Prost (1995, p. 2) three states are defined:

a. Nematics
   - No positional order
   - Not isotropic
   - Two or more length scales, parallel ($\xi_{\parallel}$) and perpendicular ($\xi_{\perp}$) to a macroscopically defined direction
   - Often elongated molecules, but also disk-like molecules

b. Smectics
   - Ordered in one dimension
   - Often elongated molecules

c. Columnar phases
   - Ordered in two dimensions
   - Often disk-like molecules

The possible states are dependent on the molecule structure / shape but also on the temperature.

For the investigated application only the nematic phase is of use. Therefore, only liquid crystals with a nematic phase at, or close to room temperature are of interest. For space applications a wide temperature range for the nematic phase would be desirable to simplify the temperature control of the LCPS.

For uniaxial nematics de Gennes and Prost (1995, pp. 10–11) describes the features as follows:

1. No long-range order (similar to liquids)
2. The direction of the molecules is parallel to a director $\vec{n}$ (or close to parallel)
3. Arbitrariness of the director $\vec{n}$, can be affected by small forces (e.g., Frederiks Transition)
4. Indistinguishable directors $\vec{n}$ and $-\vec{n}$
5. Occurrence of a nematic phase is only possible when:
   a. All molecules are achiral (identical to their mirror image)

   or

   b. The mixture is racemic (1:1 mixture of both chiral species)

Figure 7 shows LC molecules, simplified as black lines, with their current direction and their preferred orientation or director.

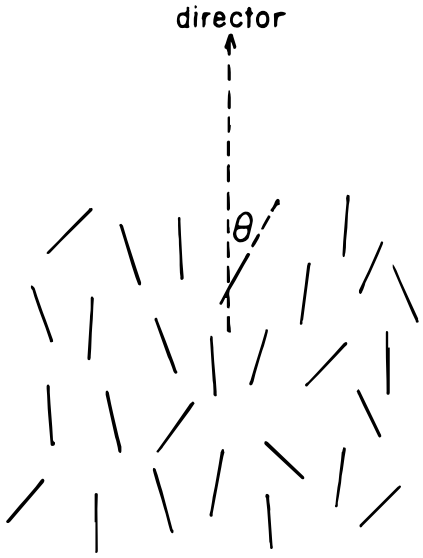

Figure 7: LC molecules with director / direction of preferred orientation (Collings, 1990, p. 10)

The direction of LCs can be manipulated by magnetic and electric fields. The magnetic manipulation is based on the diamagnetism of LCs and is particularly strong for aromatic molecules (de Gennes and Prost, 1995). More relevant for a lightweight phase shifter is the electric manipulation because electrodes for electrical biasing can be thin and therefore lightweight.

An external electric field imposes many effects on a nematic LC. In the following, only the effect due to the dielectric anisotropy is regarded since this is the most important one for the phase shift application. The equations and descriptions are taken from de Gennes and Prost (1995, p. 133).

Since the anisotropy of the nematic LC has an influence on the (static) dielectric constant the two extreme values can be defined as $\varepsilon_{\parallel}$ - parallel and $\varepsilon_{\perp}$ - perpendicular dielectric constant relative to the director. The difference between these two extreme values can be defined as the dielectric anisotropy:

$$\varepsilon_a = \varepsilon_{\parallel} - \varepsilon_{\perp} \tag{2-10}$$

The electric displacement within an electric field $\vec{E}$ can be written as:

$$\vec{D} = \varepsilon_{\perp}\vec{E} + (\varepsilon_{\parallel} + \varepsilon_{\perp})(\vec{n} \cdot \vec{E})\vec{n} \tag{2-11}$$

“1. If each molecule carries a permanent dipole moment parallel (or nearly parallel) to its long axis, the dipole can be oriented efficiently by a field $\vec{E}$ along the nematic axis […]. But a field $\vec{E}$ normal to $\vec{n}$ has only weak effects. Thus, in this case we have $\varepsilon_{\parallel} > \varepsilon_{\perp}$. […].

2. If there is a permanent dipole moment which is more or less normal to the long axis, the situation is reversed and $\varepsilon_{\parallel} < \varepsilon_{\perp}$.” (de Gennes and Prost, 1995, p. 134)

Figure 8 shows these two cases, on the left side the dipole is parallel to the long axis of the molecule and on the right side the dipole is perpendicular to the long axis of the molecule.

Due to the dielectric anisotropy, the molecules can be aligned by an electric field. This field contributes to the thermodynamic potential as follows:

$$-\frac{1}{4\pi}\int \vec{D}\cdot d\vec{E} = -\frac{\varepsilon_\perp}{8\pi}E^2 - \frac{\varepsilon_\mathrm{a}}{8\pi}\left(\vec{n}\cdot\vec{E}\right) \qquad \textbf{(2-12)}$$

Only the second term depends on the director $\vec{n}$. If ε_a is larger than zero, the contribution is larger for a director parallel to the electric field and if ε_a is less than zero, the contribution is larger for a director perpendicular to the electric field.

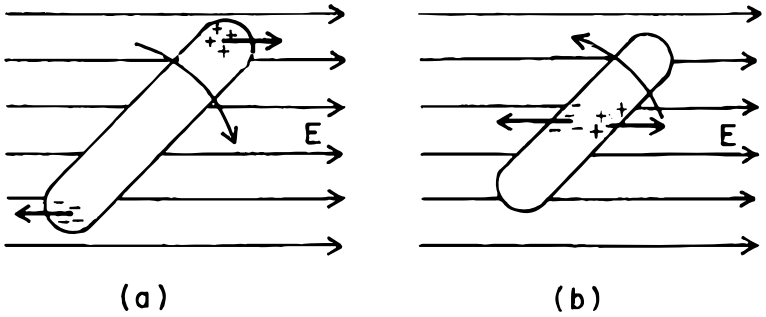

Figure 8: Influence of an electric field on an electric dipole, dipole along the long axis of the LC molecule (a) and across the long axis (b) (Collings, 1990, p. 40)

Since the relative permittivity $\varepsilon_\parallel$ - parallel and $\varepsilon_\perp$ - perpendicular to the director differ, a tensor for the permittivity can be written as (de Gennes and Prost, 1995, p. 144):

$$\varepsilon_{\alpha\beta} = \varepsilon_\perp\delta_{\alpha\beta} + (\varepsilon_\parallel - \varepsilon_\perp)n_\alpha n_\beta \qquad \textbf{(2-13)}$$

Or also as:

$$\overleftrightarrow{\varepsilon} = \begin{bmatrix} \varepsilon_\mathrm{a}n_\mathrm{x}^2 + \varepsilon_\perp & \varepsilon_\mathrm{a}n_\mathrm{x}n_\mathrm{y} & \varepsilon_\mathrm{a}n_\mathrm{x}n_\mathrm{z} \\ \varepsilon_\mathrm{a}n_\mathrm{x}n_\mathrm{y} & \varepsilon_\mathrm{a}n_\mathrm{y}^2 + \varepsilon_\perp & \varepsilon_\mathrm{a}n_\mathrm{y}n_\mathrm{z} \\ \varepsilon_\mathrm{a}n_\mathrm{x}n_\mathrm{z} & \varepsilon_\mathrm{a}n_\mathrm{y}n_\mathrm{z} & \varepsilon_\mathrm{a}n_\mathrm{z}^2 + \varepsilon_\perp \end{bmatrix} \qquad \textbf{(2-14)}$$

Further experiments on the behavior of LCs in an electric field can be found in Meier and Saupe (1966); Carr (1969); Deuling (1972).

The use of a constant (DC) field might cause long-term problems with the manipulation of the LC direction:

“While space charge injection is indispensable in the electrohydrodynamics of isotropic liquids, its importance in nematic phases relative to charge segregation seems not yet clear. Injection can be suppressed by the use of ac fields. A frequency of some 10 Hz is usually large enough to prevent both the transit of ions and the collapse of the deformation during one half period. Since the lifetime of electro-optical devices is longer with ac than with dc, ac is at present used in most applications.” (Helfrich, 1973, pp. 193–195; and similar in: De Vleeschouwer *et al.*, 2001).

A section regarding this topic can also be found in de Gennes and Prost (1995, pp. 232–233). Because of this problem, an AC field with a square wave voltage and a frequency of 50 Hz is used for the LISA-ES measurements (see also Chapter 1.2.4.3).

The liquid crystals used for the experiments are provided by *Merck KGaA*. Their relative permittivity and loss-tangent at +20 °C are shown in Table 7.

Table 7: Permittivities and loss tangents of the liquid crystals used in this thesis at +20 °C Weickhmann (2017) and courtesy *Merck KGaA*

Name	Frequency	$\varepsilon_{r,\parallel}$	$\varepsilon_{r,\perp}$	$\tan\delta_{\parallel}$	$\tan\delta_{\perp}$
GT5-26001	19 GHz	3.27	2.39	$2.2 \cdot 10^{-3}$	$7.0 \cdot 10^{-3}$
	30 GHz	3.27	2.51	$34.1 \cdot 10^{-3}$	$24.1 \cdot 10^{-3}$
GT3-23002	19 GHz	3.02	2.36	$3.5 \cdot 10^{-3}$	$12.8 \cdot 10^{-3}$

The relative permeability is not given for the two LCs. However Penirschke et al. (2004) showed for two other LC mixtures that $\mu_r \approx 1$ is a good assumption. Therefore, this assumption is now also applied to *GT5-26001* and *GT3-23002*.

Because the phase changes (switching times) for the LISA-ES LCPSs are slow compared to the ones seen in liquid crystal displays (LCDs), the dynamic behavior of the LC is of special interest. The LCs used in the LCPS have higher rotational viscosities than the ones used in LCDs. In Weickhmann (2017, p. 17), two LCs for phase shifting applications are compared with a generic display LC. For the generic display LC, the rotational viscosity is about a factor 10 smaller.

The three following equations for the rotational viscosity are taken from de Gennes and Prost (1995, p. 206 ff.):

$$\gamma_1 = \alpha_3 - \alpha_2 \tag{2-15}$$

$$\gamma_2 = \alpha_2 + \alpha_3 = \alpha_6 - \alpha_5 \tag{2-16}$$

with the *Leslie coefficients* α_1 to α_6 (incompressible nematics).

For rotating fields, in this example a magnetic field, and a bulk LC sample where the boundary effects of the rigid walls can be neglected, the friction torque can be written as:

$$\gamma_1 \omega = \frac{1}{2} \chi_a H^2 \sin 2\phi \tag{2-17}$$

(in centimeter–gram–second system of units; magnetic susceptibility $\chi_a = \chi_{\parallel} - \chi_{\perp}$; phase lag ϕ; rotation rate ω; rotational viscosity γ_1)

One assumption for this equation is that there is no hydrodynamic flow within the cavity. This method is suggested as a measuring technique for the rotational viscosity, and the left side of equation (2-17) shows the friction torque. The phase lag value is such that both torques (friction and magnetic) are equal.

For space applications the environment limits the use of some materials. Therefore, it is important to know the sensitivity of LC to the most hazardous environmental factors:

- Radiation
- Temperature
- Vacuum

In general, the more a material can withstand the lesser the provisions against these hazards have to be and the more likely it will be used in a space application.

Radiation: The sensitivity to radiation is very important especially for long term space missions. GEO satellites often have a lifetime of about 15 years and the malfunction of an antenna would cause a considerable loss of profit. The following publications show results for different radiation tests Berghmans et al. (1996); Graham et al. (1996); DeWalt, Miller and Stockley (2004); Stockley et al. (2006); Uber et al. (2008); Lane et al. (2009); Follmann et al. (2013); Dixit and Manohar (2015); Doyle et al. (2016); Woehrle et al. (2016). Follmann et al. (2013) probably used similar LCs to this work since the LIQUIDA project has some similarities to the LISA-ES project. The measurements included a total dose test and a proton test, and no influence was measured.

Vacuum: In space applications the LC will probably not be exposed directly to the vacuum. Most applications will store the LC in some kind of containment to hold it in place. For this containment the pressure difference necessary for the LC to be stable (in the nematic phase) is an important parameter. Measurement data for the vapor pressure of different LCs at different temperatures can be found in Deschamps, Trusler & Jackson (2008); Heath and Tumlinson (1986); Hiro and Wada (2011). Table 8 shows the vapor pressure for some LCs at potential working temperatures of the LCPS whereby all LCs measured in this publication are in the isotropic state at these temperatures. The minimum pressure measurable by the experimental setup is 0.1 Pa.

Table 8: Vapor pressure for some thermotropic LCs (isotropic phase) (Deschamps, Trusler and Jackson, 2008)

LC	Temperature	Vapor pressure
5CB	89.93 °C	0.23 Pa
CCH-5CF_3	54.50 °C	0.63 Pa
BCH-5F.F.F	85.78 °C	0.19 Pa
CCH-3CF_3	49.51 °C	1.24 Pa
BCH-3F.F.F	55.80 °C	0.13 Pa
MBBA	96.94 °C	0.25 Pa

Temperature: The temperature range of the nematic phase is the one of interest for the application because it defines the range in which the antenna can be used. For an extreme hot or cold case, where the antenna is not in use, a phase change of the LC might be tolerable. In this case it is important that the LC returns to the nematic phase in the entire volume as soon as the temperatures normalize. Otherwise the properties of the LCPSs might change. Measurements of the LC behavior over temperature can be found in Maier and Saupe (1958, 1959, 1960); Penirschke et al. (2004); Mueller, Penirschke, et al. (2005).

Furthermore, the phase change rate is dependent on the temperature. The change of the elastic constants causes the LCPS to be slower at lower temperatures (see Chapter 5.3.5). Measurements of elastic constants of LCs at different temperatures can be found in Gruler, Scheffer and Meier (1972); Gruler and Meier (1973); Srivastava and Singh (2004). Especially the rotational viscosity has a strong influence on the behavior of a bulk LC sample, where the effect of the boundary walls is negligible. The rotational viscosity over temperature for some LCs is shown in Kneppe, Schneider and Sharma (1982); Imai et al. (1994); Kim et al. (2011).

However, the LCs that are optimized for the use in RF-systems have larger rotational viscosities and therefore have slower reaction times (Weickhmann, 2017).

2.3 Waveguide

The fundamentals for rectangular waveguides are taken from Collin (1992) and Pozar (2011). Figure 9 shows a rectangular waveguide with the two dimensions a and b of the cross-section.

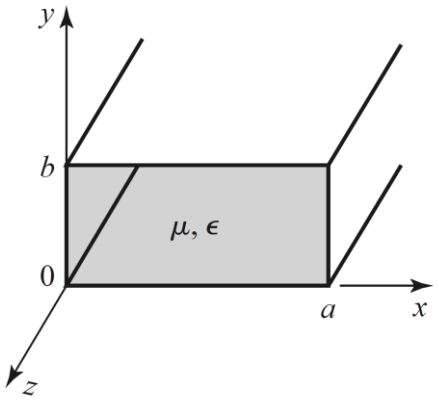

Figure 9: Rectangular waveguide (Pozar, 2011)

Wave propagation in transmission lines can be split in three mode types:

1. Transverse electromagnetic (TEM) waves, no longitudinal field components ($H_z = 0$, $E_z = 0$)
2. Transverse electric (TE), or H-waves, longitudinal magnetic field components ($H_z \neq 0$, $E_z = 0$)
3. Transverse magnetic (TM), or E-waves, longitudinal electric field components ($H_z = 0$, $E_z \neq 0$)

TEM waves need two or more conductors to exist (e.g., coaxial cable). Since waveguides only consist of one conductor only TE and TM waves are supported.

The transverse field components for TE-modes (TE_{mn}) in a rectangular waveguide ($m = 0,1,2, \ldots$; $n = 0,1,2, \ldots$) are:

$$E_x = \frac{j\omega\mu n\pi}{k_c^2 b} A_{mn} \cos\frac{m\pi x}{a} \sin\frac{n\pi y}{b} e^{-j\beta z} \quad \textbf{(2-18)}$$

$$E_y = \frac{-j\omega\mu m\pi}{k_c^2 a} A_{mn} \sin\frac{m\pi x}{a} \cos\frac{n\pi y}{b} e^{-j\beta z} \quad \textbf{(2-19)}$$

$$H_x = \frac{j\beta m\pi}{k_c^2 a} A_{mn} \sin\frac{m\pi x}{a} \cos\frac{n\pi y}{b} e^{-j\beta z} \quad \textbf{(2-20)}$$

$$H_y = \frac{j\beta n\pi}{k_c^2 b} A_{mn} \cos\frac{m\pi x}{a} \sin\frac{n\pi y}{b} e^{-j\beta z} \quad \textbf{(2-21)}$$

(cutoff wave number k_c, these expressions are all zero for $m = n = 0$)

The propagation constant (phase constant) is:

$$\beta = \sqrt{k^2 - k_c^2} = \sqrt{k^2 - \left(\frac{m\pi}{a}\right)^2 - \left(\frac{n\pi}{b}\right)^2} \quad \textbf{(2-22)}$$

(wave number $k = \omega\sqrt{\mu\varepsilon}$ of the material filling the waveguide; β is real when $k > k_c$)

The cutoff frequency is given by:

$$f_{c_{mn}} = \frac{k_c}{2\pi\sqrt{\mu\varepsilon}} = \frac{1}{2\pi\sqrt{\mu\varepsilon}}\sqrt{\left(\frac{m\pi}{a}\right)^2 + \left(\frac{n\pi}{b}\right)^2} \tag{2-23}$$

The lowest cutoff frequency is called dominant mode. With $a > b$, the lowest frequency is $f_{c_{10}}$ with $m = 1$ and $n = 0$.

Wave impedance:

$$Z_{TE} = \frac{E_x}{H_y} = \frac{-E_y}{H_x} = \frac{k\eta}{\beta} = \frac{k\sqrt{\mu/\varepsilon}}{\beta} \tag{2-24}$$

Guide wavelength:

$$\lambda_g = \frac{2\pi}{\beta} > \frac{2\pi}{k} = \lambda \tag{2-25}$$

Phase velocity:

$$v_p = \frac{\omega}{\beta} > \frac{\omega}{k} = \frac{1}{\sqrt{\mu\varepsilon}} \tag{2-26}$$

(The speed of light in the medium / plane wave: $1/\sqrt{\mu\varepsilon} = c$, angular frequency: ω)

Group velocity (of a narrowband signal):

$$v_g = \left(\frac{d\beta}{d\omega}\right)^{-1}\Bigg|_{\omega=\omega_0} \tag{2-27}$$

(Center angular frequency ω_0)

Transverse field components for TM-modes in a rectangular waveguide ($m = 1,2,3,\ldots$; $n = 1,2,3,\ldots$):

$$E_x = \frac{-j\beta m\pi}{k_c^2 a} B_{mn} \cos\frac{m\pi x}{a} \sin\frac{n\pi y}{b} e^{-j\beta z} \tag{2-28}$$

$$E_y = \frac{-j\beta n\pi}{k_c^2 b} B_{mn} \sin\frac{m\pi x}{a} \cos\frac{n\pi y}{b} e^{-j\beta z} \tag{2-29}$$

$$H_x = \frac{j\omega\varepsilon n\pi}{k_c^2 b} B_{mn} \sin\frac{m\pi x}{a} \cos\frac{n\pi y}{b} e^{-j\beta z} \tag{2-30}$$

$$H_y = \frac{-j\omega\varepsilon m\pi}{k_c^2 a} B_{mn} \cos\frac{m\pi x}{a} \sin\frac{n\pi y}{b} e^{-j\beta z} \tag{2-31}$$

These expressions are all zero for if either $m = 0$ or $n = 0$.

The formula for the propagation constant and the formula for the cutoff frequencies are equal to the ones of the TE-modes. The lowest order TM-mode to propagate is TM_{11}. Table 9 shows the cutoff frequencies and relative cutoff frequencies for different TE- and TM-modes.

Table 9: Cutoff frequencies

Mode	m	n	Cutoff frequency	Relative cutoff frequency
TE	1	0	$\frac{1}{2a\sqrt{\mu\varepsilon}}$	1
TE	2	0	$\frac{1}{a\sqrt{\mu\varepsilon}}$	2
TE	0	1	$\frac{1}{2b\sqrt{\mu\varepsilon}}$	$\frac{a}{b}$
TE, TM	1	1	$\frac{\sqrt{\frac{1}{a^2}+\frac{1}{b^2}}}{2\sqrt{\mu\varepsilon}}$	$\sqrt{1+\frac{a^2}{b^2}}$
TE, TM	2	1	$\frac{\sqrt{\frac{4}{a^2}+\frac{1}{b^2}}}{2\sqrt{\mu\varepsilon}}$	$\sqrt{4+\frac{a^2}{b^2}}$

Most waveguides are designed to enable the dominant mode to propagate (TE_{10}, Figure 10) and have an aspect ratio of 2:1 ($a = 2b$). To ensure that only one mode propagates the frequency range of a waveguide is normally defined to be between the cutoff frequencies of the TE_{10}-mode and the TE_{20}-mode.

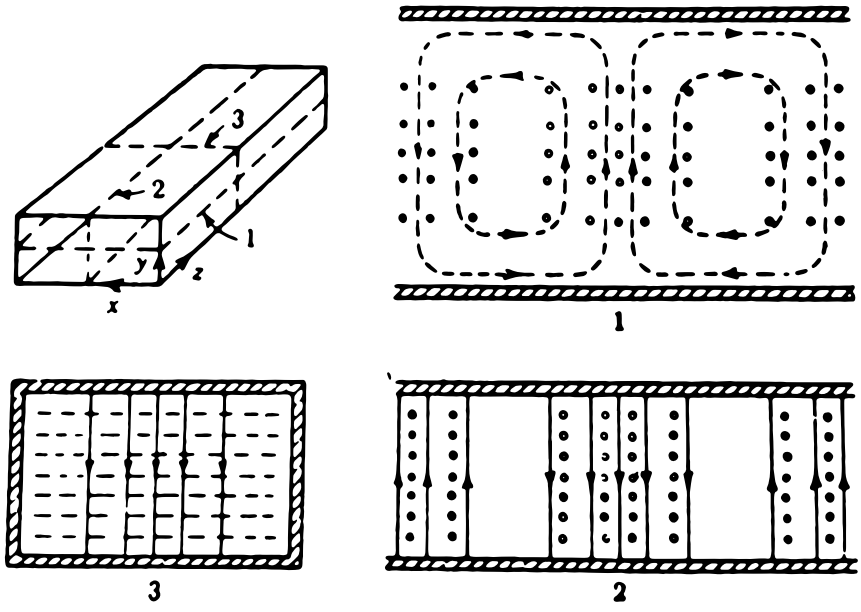

Figure 10: TE_{10}-mode, electric field lines – solid, magnetic field lines – dashed (Ramo, Whinnery and Van Duzer, 1994, p. 420)

The phase shifters developed in the project LISA-ES have the following dimensions: $a = 5.5\,\text{mm}$, $b = 2.3\,\text{mm}$. The cutoff frequencies are dependent on the filling of the waveguide. The filling is not homogeneous but for a first estimation, the parameters are calculated for each material as a homogeneous filling (see Table 10).

Table 10: LISA-ES phase shifter parameters
Permittivity data from Weickhmann (2017), courtesy *Merck KGaA* and *C-Lec Plastics* (2015)

Material	ε_r	f_{c10}	f_{c20}	v_{p10}@23 GHz	λ_{g10}@23 GHz	v_{g10}@23 GHz
Rexolite	2.53 (1 MHz – 500 GHz)	17.13 GHz	34.27 GHz	$188 \cdot 10^6 \frac{m}{s}$	8.2 mm	$125.7 \cdot 10^6 \frac{m}{s}$
GT5-26001 $\varepsilon_{r,\perp}$	2.39 (19 GHz) 2.51 (30 GHz)	17.63 GHz ($\varepsilon_{r,\perp}$ @ 19 GHz)	34.40 GHz ($\varepsilon_{r,\perp}$ @ 30 GHz)	$194 \cdot 10^6 \frac{m}{s}$ ($\varepsilon_{r,\perp}$ @ 19 GHz)	8.4 mm ($\varepsilon_{r,\perp}$ @ 19 GHz)	$124.5 \cdot 10^6 \frac{m}{s}$ ($\varepsilon_{r,\perp}$ @ 19 GHz)
GT5-26001 $\varepsilon_{r,\parallel}$	3.27 (19 GHz/30 GHz)	15.07 GHz	30.14 GHz	$166 \cdot 10^6 \frac{m}{s}$	7.2 mm	$125.2 \cdot 10^6 \frac{m}{s}$
GT3-23002 $\varepsilon_{r,\perp}$	2.36 (19 GHz)	17.74 GHz	35.48 GHz	$195 \cdot 10^6 \frac{m}{s}$	8.5 mm	$124.2 \cdot 10^6 \frac{m}{s}$
GT3-23002 $\varepsilon_{r,\parallel}$	3.02 (19 GHz)	15.68 GHz	31.37 GHz	$173 \cdot 10^6 \frac{m}{s}$	7.5 mm	$126.2 \cdot 10^6 \frac{m}{s}$

The waveguide dimensions before and after the LCPS are 7.30 mm x 3.35 mm. Since the wave impedance Z_{TE} is dependent on ε, a and b, the impedance has to be matched to the waveguide before and after the LCPS. Since the phase change is performed with a change of the relative permittivity within the LCPS an ideal matching for all phase shifting states is not possible.

In Chapter 5.2 one LCPS has only a thin conducting layer of silver (no copper layer on top) to measure the influence of the subsequent electroplating process. Therefore, the thickness of the conducting layer has to be sufficient to enable a low loss transition of the RF wave. The skin depth (characteristic depth of penetration) of the RF wave can be calculated with (Pozar, 2011):

$$\delta_S = \sqrt{\frac{2}{\omega \cdot \mu \cdot \sigma}} \tag{2-32}$$

The calculated depth defines the distance from the inner wall surface where the fields are decayed by e^{-1}.

3 Simulation of a Phased Array with Liquid Crystal Phase Shifters

The following chapter is an updated and extended version of the publication Tebbe et al. (2016).

Simulation of an electronically steerable horn antenna array with liquid crystal phase shifters

2016 IEEE Aerospace Conference, March 2016

In this chapter the simulation of a phased array antenna with liquid crystal phase shifters is shown. The simulation aims to quantify the effect of phase jumps on the antenna performance during the tracking of a LEO satellite. Thereby, the losses of the LCPSs and a potential coupling between the radiating elements are disregarded.

3.1 Background

As mentioned in Chapter 1.2.4.1, the reference scenario for this LC phased antenna array is an ISL between a GEO satellite and a LEO satellite, with the LC phased array antenna mounted on the GEO satellite. To cover most LEO orbits, the maximum steering angle required for the LC phased antenna array is approximately ±11°, which corresponds with an orbit altitude of 1 500 km for the LEO satellite. For the planned flight model of the high gain antenna array (375 mm x 375 mm array, center to center of each horn, for 36 dB gain), a maximum total phase shift of >3 000° is required over the entire array (at 27.5 GHz, diagonal steering case). An LCPS that could perform such a large phase shift would have to be significantly longer than the current LCPS design and therefore would cause unacceptably high losses.

However, it is possible to achieve the same effect on the array by influencing different wavenumbers with the LCPSs, even if each LCPS only has a limited phase shift capacity of only 360°. Within a certain limit of about 11 wavenumbers, there should be no noticeable effect on the modulated signal itself. By manipulating different wavenumbers of the signal, a ‘saw tooth’ pattern of phase jumps distributed across the whole array is generated. This approach can also be found in Koul and Bhat (1991, p. 51). Figure 11 shows the emitted waves from each horn in the desired direction. The part of the wave that is below the green line is equal to the phase of each phase shifter and equal distances between the upper end of each wave package (light blue) and the red line (wave front) represent wave packages with equal wavenumbers.

This approach, however, comes with one drawback for the dynamical steering process. As LCPSs have to change the wavenumber during the dynamic beam steering, they have to ideally change their phase by 360° (up or down) instantaneously (‘jump’). The actual phase change rate for the developed LCPSs with electric field orientation is very slow (see Weickhmann (2017) and Chapter 5.3.5), in the order of one to several minutes (with *GT5-26001*), causing ‘jumping’ LCPS to be out-of-phase.

An out-of-phase LCPS causes a drop in the antenna gain in the desired direction. Dependent on the steering angle, several LCPSs have to jump at the same time. First studies on this problem and possible solutions have been conducted at *TU Darmstadt* (Hu, 2011). The work presented here developed a dynamic simulation tool to further investigate the influence of these jumps on the communication link and compares different LCPS control and optimization techniques used in the distribution of phase jumps over time. A figure of merit for the link is defined to characterize mitigation methods across an orbit of the LEO satellite to minimize the effects of out-of-phase LCPSs. The various mitigation methods to be characterized with the software tool could aim at reducing the magnitude (optimized, staggered jumps) and/or duration of losses (faster LCPSs through faster LC or stronger electric field). None of these investigated mitigation

methods are expected to avoid the loss in gain entirely. Once validated, the software tool should then enable detailed parametric studies of phase shift speed and strategy to find an optimum of minimal loss of signal (LOS), which could either be minimal duration of LOS or minimal magnitude during a communication link over half an orbit.

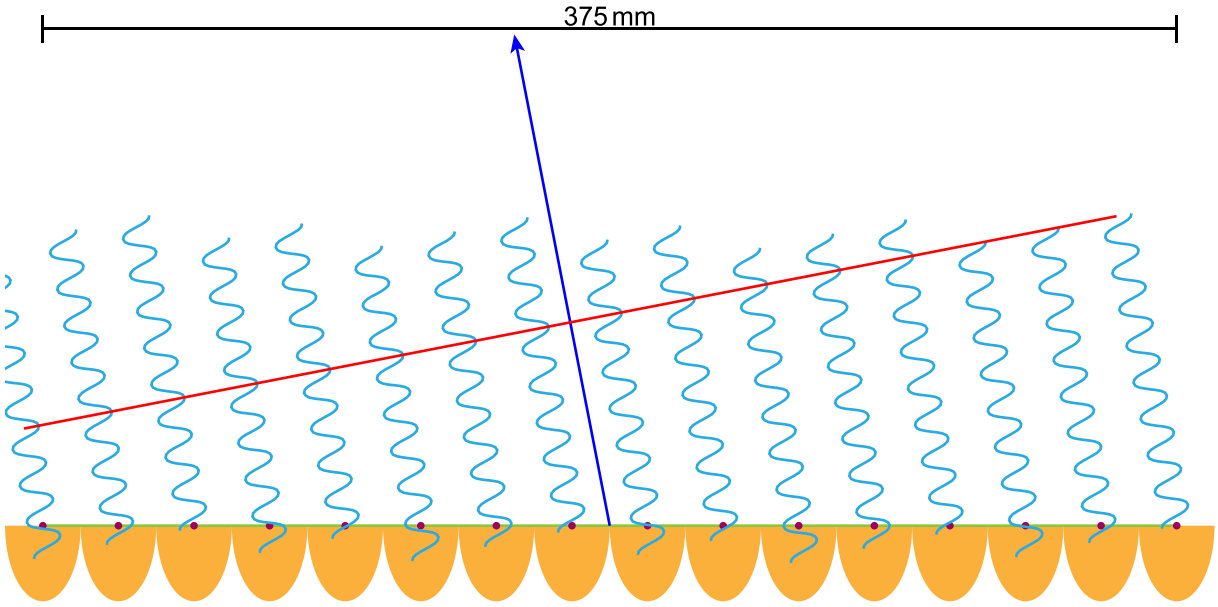

Figure 11: Phase distributions across array

3.2 Model

The software environment shall be able to investigate a variety of GEO-LEO orbit scenarios, have adjustable phase change rates for the LCPS based on the experimental results achieved to date, as well as support various loss mitigation methods such as time of phase jumps and distribution of phase jumps across the array. For comparison of methods, the resulting link performances for each orbit and method shall be characterized using a common metric, or figure of merit.

An evaluation on the basis of a worst-case scenario is not advisable, since this scenario only applies for isolated steering angles. Therefore, the actual use case during an orbit is a much better way to evaluate the performance and it might show that the influence of the out-of-phase LCPS during jumps is not as dramatic as in the worst case.

The calculations are performed in *MATLAB.*

3.2.1 Figure of Merit

The simulation with different use cases creates results with various dependencies which make it difficult to evaluate the performance of the antenna array over the entire simulation time. The introduced figure of merit should allow to evaluate the cumulative usability of the link as a function for different defined link margins during dynamic steering cases. Since a drop of gain during jumps can only be minimized but not avoided, the total timespan in which the gain drops under a certain threshold level during the steering process is summed up. Assuming an LOS during that time, the parameter is called L and represents the cumulative time of LOS during one orbit. Since a LOS is dependent on the entire link margin, three different L-parameters were defined relative to the maximum gain of the antenna array to accommodate different scenarios ($L_{1\mathrm{dB}}$, $L_{3\mathrm{dB}}$ and $L_{6\mathrm{dB}}$).

3.2.2 Orbit Simulation

The goal of this work is to simulate the phased array in a realistic space environment with regard to the relative motion, e.g., the angular steering velocity that the phased array has to achieve at each time step.

A simplified space environment is implemented to calculate the relative motion of a LEO and a GEO satellite. The total timespan for the simulation is chosen to be half of the LEO's orbital period. In the simulation, both satellites pass the same latitude (0°) at half of the simulation time. The simplified orbit calculation is based on Vallado (2013). The orbital parameters for this simulation are shown in Table 11 and Table 12.

Table 11: LEO satellite orbit parameters

Parameter	Value
Ω_{LEO}	$0°, -90°$
ω_{LEO}	$-90°, 0°, 180°$
a_{LEO}	$7\,878\ km\ (h\ \approx\ 1\,500\,\mathrm{km})$
i_{LEO}	$0°\ to\ 180°\ (stepsize\ 15°)$
e_{LEO}	$0\ (circular)$
n_{LEO}	$\sqrt{\mu_{\oplus}/a^3} = 9.03 \cdot 10^{-4}\ \mathrm{rad/s}$
$M_{\mathrm{LEO}} = E_{\mathrm{LEO}} = \nu_{\mathrm{LEO}}$	$n \cdot t$
T_{LEO}	$2\pi \cdot \sqrt{a^3/\mu_{\oplus}} = 6\,958.03\,\mathrm{s}$

Table 12: GEO satellite orbit parameters

Parameter	Value
Ω_{GEO}	$0°$
ω_{GEO}	$-7.27°$
a_{GEO}	$\sqrt[3]{(T^2 \cdot \mu_{\oplus})/(4 \cdot \pi^2)} = 42\,167.33\,\mathrm{km}$
i_{GEO}	$0°$
e_{GEO}	$0\ (circular)$
n_{GEO}	$\sqrt{\mu_{\oplus}/a^3} = 7.29 \cdot 10^{-5}\ \mathrm{rad/s}$
$M_{\mathrm{GEO}} = E_{\mathrm{GEO}} = \nu_{\mathrm{GEO}}$	$n \cdot t$
T_{GEO} = Sidereal day	$86\,164\,\mathrm{s}$ (Aoki *et al.*, 1982)

Case 1 and 2, shown in Table 13, are families of orbits that differ in their inclination angle. The rotation axis of the inclination angle in case 2 is turned by 90° with regard to case 1, as can be seen in Table 13. Since the orbits are circular, ω_{LEO} is used to define the starting point of the simulation. In Table 13 the starting points of the LEO and GEO satellites are marked with a red dot and the end points are marked with a green dot. The simulation time correlates with half of the orbit period of the LEO satellite ($T_{\mathrm{LEO}}/2 = 3\,479.015\,s$)

The simulation is performed with the *Phased Array System Toolbox* in *MATLAB* (*2014b* and *2015a*). The toolbox is based in large parts on Van Trees (2002). It considers the phase vectors of each horn to calculate the antenna gain in the desired direction. The decrease of the horn pattern from boresight is therefore also taken into account (cosine horn pattern), but the influence of the array environment on the horn pattern is not taken into account.

For this simulation, however, the toolbox had to be modified to be able to simulate a dynamic steering process with 'slow' LCPSs. Furthermore, the simulation has to support a phase angle range of more than 360° to investigate various jump optimization methods, as the designed LCPS can, based on their length, achieve 400° – 500° phase shifts with still acceptable losses.

The calculation of the antenna gain is performed for every time step of the simulation and is therefore equal to a static calculation for each time step. The dynamic calculation is accomplished by calculating realistic phase distributions over the array (including paraphases) using a more realistic jump behavior for each ideal jump within the array.

To determine a suitable resolution for the simulation, an inclination of 0° and orbit case 1 were chosen for an analysis. Both antenna arrays (4x4 demonstrator horn array and 16x16 flight horn array) were simulated and the results show that for resolutions of 1 000 steps to 3 000 steps, the results in $L_{1\mathrm{dB}}$ differed in <2 %, and $L_{3\mathrm{dB}} < 2{,}5\ \%$. For $L_{6\mathrm{dB}}$, the differences were larger, but not more than 3.479 s which is equal to the time step at 1 000 simulation steps. Since 1 000 steps is a good compromise between calculation time and resolution, all calculations were performed with this step count.

Table 13: Orbit case 1 (left) and cases 2a&b (right)

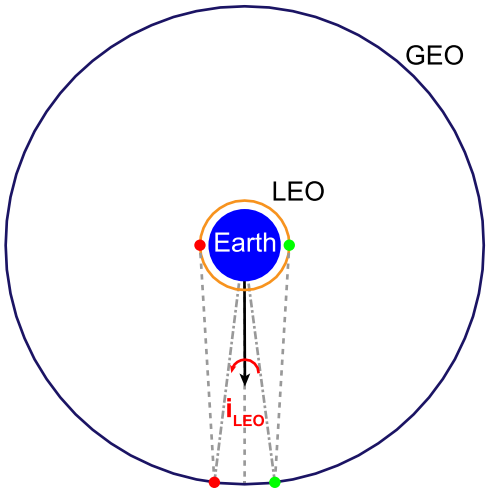

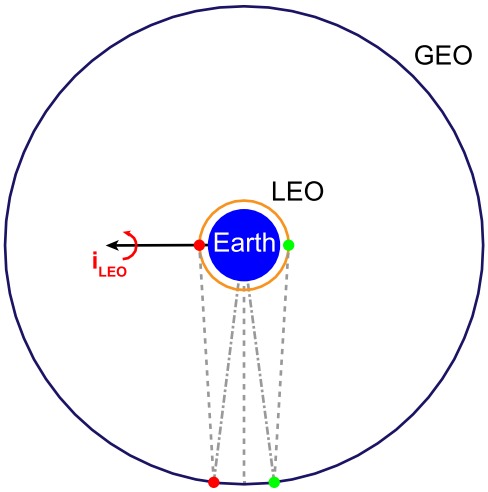

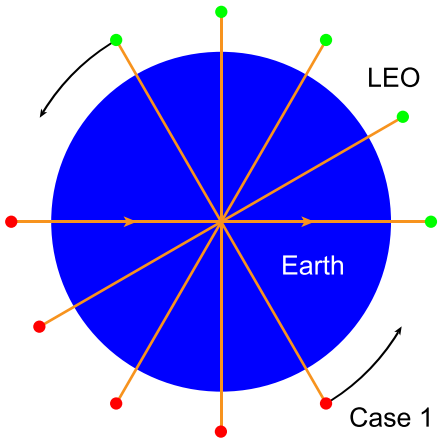

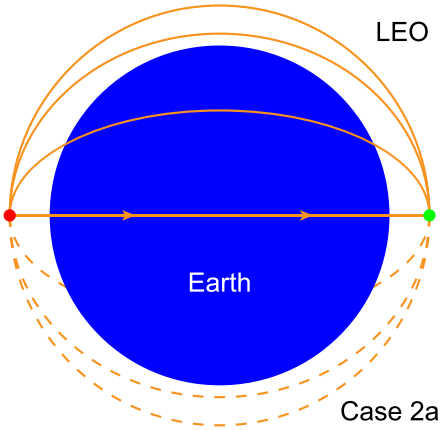

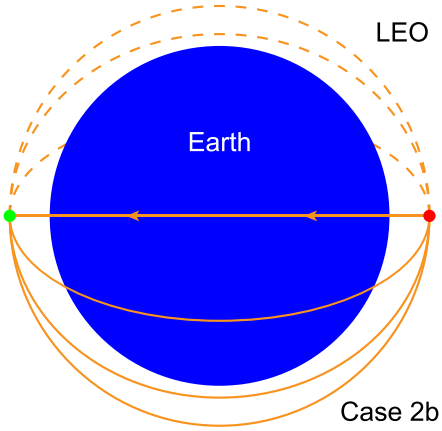

Case 1	Case 2a	Case 2b
$\Omega_{\mathrm{LEO}} = 0°$	$\Omega_{\mathrm{LEO}} = -90°$	$\Omega_{\mathrm{LEO}} = -90°$
$\omega_{\mathrm{LEO}} = -90°$	$\omega_{\mathrm{LEO}} = 0°$	$\omega_{\mathrm{LEO}} = 180°$
$i_{\mathrm{LEO}} = 0° \; to \; 180°$	$i_{\mathrm{LEO}} = 0° \; to \; 90°$	$i_{\mathrm{LEO}} = 90° \; to \; 180°$

3.2.3 Antenna Array

As introduced in Chapter 1.2.4.1, the LISA-ES project was funded to demonstrate the concept of an electronically steered phased array antenna using waveguide LCPSs for continuous beam steering in geostationary space applications. For cost and complexity reasons, the manufactured demonstrator array consists of only 4x4 horns (see Chapter 1.2.4.2) instead of a more realistic 16x16 horn high gain antenna (Figure 12) for spaceflight applications. The first simulations are therefore also based on this smaller 4x4 demonstrator to simulate the effects that will occur during the planned antenna tests in the compensated compact range (CCR). The basic parameters of both antenna arrays are shown in Table 14.

The antenna works in two frequency bands, 23.0 GHz to 23.5 GHz and 27.0 GHz to 27.5 GHz. Since the desired phase shift increases linearly with the frequency, the simulations were all conducted with a frequency of 27.5 GHz to simulate the maximum phase shift necessary.

Table 14: Array parameters

Parameter	Value
Element spacing	0.025 m
Array size (demonstrator)	4x4
Array size (flight model)	16x16
Simulated frequency	27.5 GHz

Figure 12 shows a top view onto the aperture of the horn antenna array. The orientation of the antenna aboard the satellite is chosen as follows: The Y-axis is within the equatorial plane pointing westwards, the Z-axis is pointing northwards and the X-axis (boresight) is always directed towards earth's center. The antenna horns are simulated as a cosine antenna element (*MATLAB Phased Array System Toolbox*).

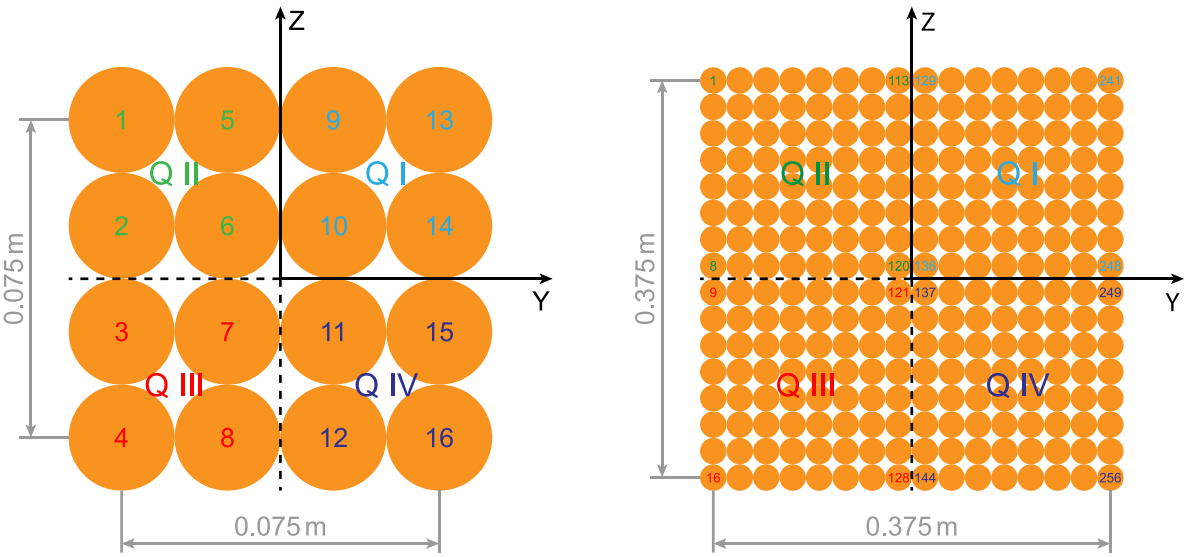

Figure 12: Top view of the 4x4 horn array demonstrator (left) and the 16x16 horn flight model (right)

3.2.4 Simulated Liquid Crystal Phase Shifter

Except for the slow phase change rate, the LCPSs are assumed to be ideal (have no losses). The maximum phase change rate of the LCPS for this simulation is chosen as constant over the entire phase range of the LCPS, though the simulation environment would also support a phase dependent phase change rate for future simulations. Because of the design of the LCPS biasing field, the phase change rate is dependent on the jump direction (Goelden *et al.*, 2006). For example, a phase change from +180° to -180° (H to V) will be faster than a phase change from -180° to +180° (V to H) due to the difference in the electric field strength of the biasing field (vertical field V is stronger than the horizontal field H). First measurements at *TU Darmstadt* showed that a phase change over the entire range takes about two minutes (*GT5-26001* at room temperature). Since the phase shift range for the currently implemented phase shifters is about 510° at 27.5 GHz (Weickhmann, Nathrath, *et al.*, 2013), phase change rates of 5 °/s for H to V (equal to 102 s for 510°) and 3 °/s for V to H (equal to 170 s for 510°) were chosen. During a jump, the LCPS is out of phase, meaning that it cannot provide the phase shift that is needed within the array, and even passes through a phase of 180° off phase compared to the actual phase shift needed. This point is called 'paraphase' and is particularly critical because it briefly causes the highest losses during the jump.

3.2.5 Control Methods

In a phased antenna array, the main lobe is determined by the phase front over the array. This phase front is defined by the relative phase shift of the LCPSs. Therefore, one degree of freedom is still available, allowing to choose the absolute phase at a certain point freely. This point becomes the pivot point (point with constant phase) for the phase front. For this simulation, three different methods, with different positions of this pivot point, were analyzed (see Table 15). The antenna is split into quadrants as defined in Figure 13. The red arrow marks the projection of the desired steering direction on the aperture. For this case the constant horn for cHornQ would be the one in the upper right corner (blue dot). It is in the same quadrant as the projection of the steering vector of the antenna array. The constant horn for cHornOQ is in the lower left corner (red dot). For cOffset, the center of the array is held constant at an offset of 180° (green dot).

Table 15: Control methods

Method	Pivot point	Constant phase	Phase range
cOffset	Center of the array	0°	$-180° \; to \; +180°$
cHornQ	Corner horn in the quadrant	360°	$0° \; to \; 360°$
cHornOQ	Corner horn opposite to the quadrant	0°	$0° \; to \; 360°$

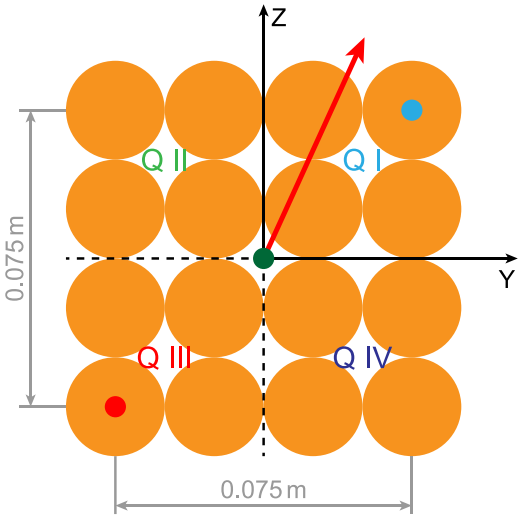

Figure 13: Quadrant definition for 'constant horn'

3.3 Baseline Simulation Results

3.3.1 Demonstrator Array without Jump Optimization

The demonstrator array represents one-sixteenth of the flight model (4x4 horns), built to demonstrate the general viability of an electronically steerable horn antenna array with LCPSs. As mentioned before, the dynamic steering over an angular range of ±11° requires jumps in some of the LCPSs. Since the LCPSs will pass through the paraphase, the antenna gain will always drop during jumps. More precisely, the antenna far field is the vector sum of all radiator contributions and the field vector of the jumping horn rotates by 360° during a jump whereby the worst case is at a phase shift of 180° compared to the desired phase (paraphase). For a first estimate, this worst case can be calculated with equation (3-1), where N represents the total number of horns in the antenna array, and n represents the number of simultaneous paraphases (jumps). The gain of the nominal case corresponds with nominal phase shifts for N horns ($n = 0$) and for the paraphase gain n horns are in paraphase. Value n is multiplied by 2, because the field vectors of one horn in paraphase and one ideal horn are canceled out and therefore, two horns have no contribution to the radiated field in the desired direction. Table 16 shows the total loss as a function of number of horns in paraphase. The position of the horn(s) in paraphase is assumed to be negligible, as we are only interested in the far field of the antenna array.

$$L_{\text{gain,para}} = G_{\text{nom}} - G_{\text{para}} = -20 \cdot \log_{10}(1 - 2 \cdot n/N) \quad \textbf{(3-1)}$$

Table 16: Paraphase influence, demonstrator array

Paraphase horn count (n)	Lost horn count $(2 \cdot n)$	$L_{\text{gain,para}}$
1	2	1.15984 dB
2	4	2.49877 dB
4	8	6.02060 dB
8	16	∞ dB

Figure 14 shows the L-values over the inclination angle of case 1. Maximum losses occur at 0°, 90° and 180° inclination angle which can be seen at $L_{3\mathrm{dB}}$ and $L_{6\mathrm{dB}}$. This is caused by the orientation of the antenna main axes because for these inclination angles entire rows of LCPSs are forced to jump at the same time, also leading to a shorter $L_{1\mathrm{dB}}$ time. The total jump count in Figure 16 however differs between the constant horn methods (cHornQ, cHornOQ) and the constant offset method (cOffset). Especially the drops at 0°, 90° and 180° inclination for the constant horn methods is interesting, since this antenna array is only just small enough that eight jumps are sufficient. A slightly larger element spacing (0.03 m instead of 0.025 m) would cause eight more jumps with these methods.

The 90° case is less severe compared to the 0° and 180° case as the relative motion between the two satellites results in an angular velocity vector that is not exactly parallel to one of the antenna's main axes. In the 0° and 180° cases, the velocity vectors of the two satellites are within one plane which results in an angular velocity vector that is parallel to the antenna's Z-axis.

Since one LCPS in paraphase results in a gain loss of already more than 1 dB (Table 16), an even distribution of jumps over time will lead to a larger $L_{1\mathrm{dB}}$ value.

The general statement is the same for cases 2a&b (see Appendix C). The rasterization causes some minor effects on the jump distribution and therefore the antenna gain. A general statement is not possible since it is highly dependent on the relative motion and the array design and size.

3.3.2 Flight Model Results without Jump Optimization

The high gain antenna flight model so far is just a theoretical antenna array that would be mounted on a geostationary satellite. The array consists of 16x16 horns of the same size as the ones of the demonstrator array. Table 17 shows the losses due to simultaneous paraphases in some of the LCPSs ($N = 256$).

Table 17: Paraphase influence, flight model (16x16 horns)

Paraphase horn count (n)	Lost horn count $(2n)$	$L_{\mathrm{gain,para}}$
1	2	0.06812 dB
16	32	1.15984 dB
32	64	2.49877 dB
64	128	6.02060 dB
128	256	∞ dB

The simulation results in Figure 15 show a similar behavior for the cOffset method for the demonstrator array and for the flight model, but the behavior of the constant horn methods (cHorn and cHornOQ) show increasing LOS times for $L_{3\mathrm{dB}}$ and $L_{1\mathrm{dB}}$. The results for cases 2a&b can be found in Appendix C.

This can be explained with the maximum phase change rates that were considered for this simulation. The phase change rates are dependent on the relative angular velocity of the two satellites and on the pivot point from where the phases are calculated.

Figure 18 shows the maximum angular velocity (ω) during the satellite pass for different inclination angles (angular velocities over the simulation time can be found in Appendix B). This is the same for all methods used to calculate the antenna steering. The maximum distance of one horn to the pivot point however is different between the methods. For the constant horn methods (cHornQ and cHornOQ), the maximum distances between the center of the corner horns in diagonal and in parallel to the main axes are given in Table 18 ($z_{\mathrm{max,diagonal}}$, $z_{\mathrm{max,parallel}}$). With these parameters, the maximum phase change rate can be calculated according to equation (3-2).

$$\dot{p}_i = 2\pi \cdot \frac{\omega \cdot z_i}{\lambda} \tag{3-2}$$

The results can be seen in Figure 19. The two purple lines mark the assumed maximum phase change rates of the simulated LCPSs (V to H / H to V). The maximum phase change rate (V to H) of the simulated LCPSs is in-between the values calculated for a diagonal and parallel steering process.

Table 18: Calculation parameter

Parameter	Value
$z_{\mathrm{max,parallel}}$	$375.0\,\mathrm{mm}$
$z_{\mathrm{max,diagonal}}$	$\approx 530.3\,\mathrm{mm}$
$\lambda(27.5\,\mathrm{GHz})$	$\approx 10.9\,\mathrm{mm}$

For cases that are close to a diagonal steering process, nominal phase changes (not only jumps) from V to H would have to be performed faster than the maximum change rate allows. This results in a lag of some of the LCPSs and therefore in a decrease of gain for the antenna array.

The total jump count for the second half of the simulation time in Figure 17 is also higher, because the phase of the next time step cannot be reached and this is counted as a jump. This especially occurs when close to the diagonal steering case (approximately at 135° inclination).

Since the pivot point for the cOffset method is in the middle of the antenna array, the distances are only half as large as the ones shown in Table 18. The required maximum change rates are therefore also halved, and the available phase change rates of the LCPSs are sufficient for all cases.

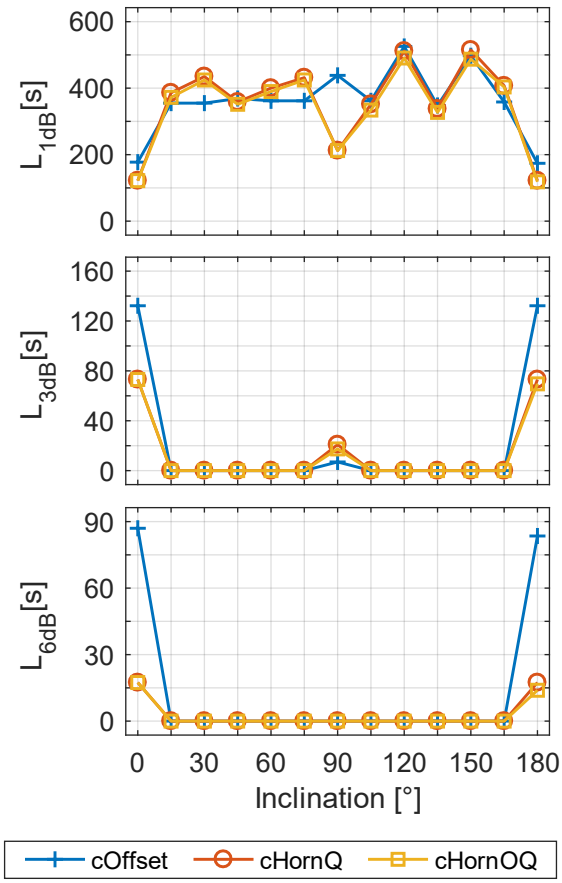

Figure 14: LOS of demonstrator array, case 1

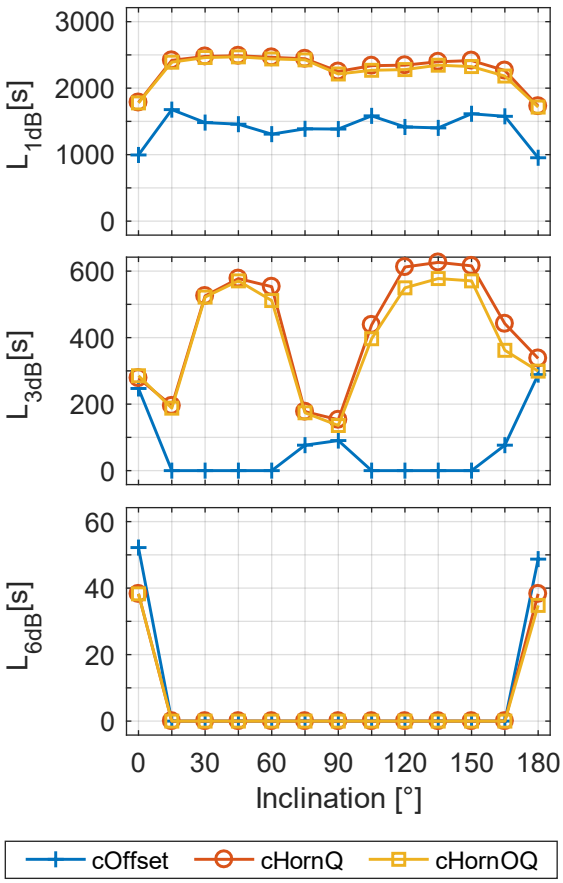

Figure 15: LOS of flight model, case 1

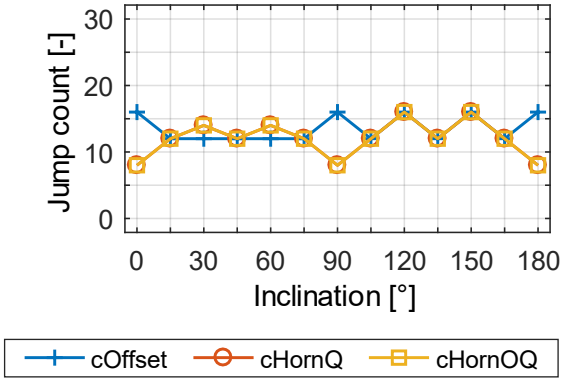

Figure 16: Total jump count of demonstrator, case 1

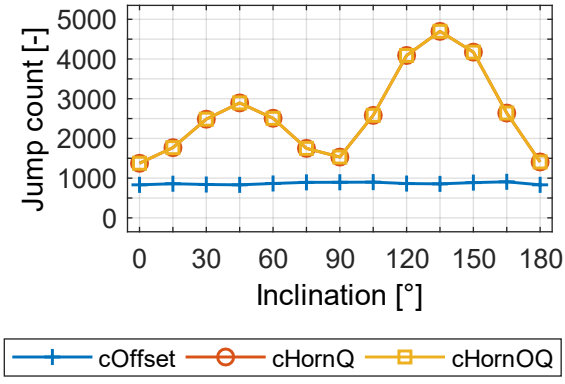

Figure 17: Total jump count of flight model, case 1

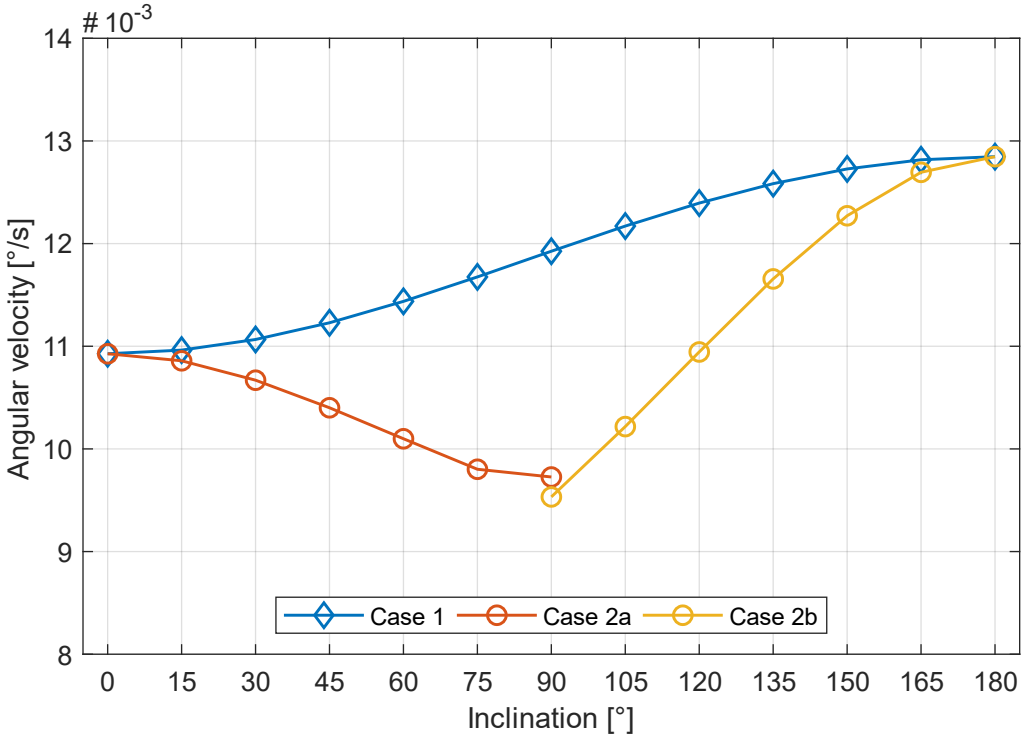

Figure 18: Maximum relative angular velocity

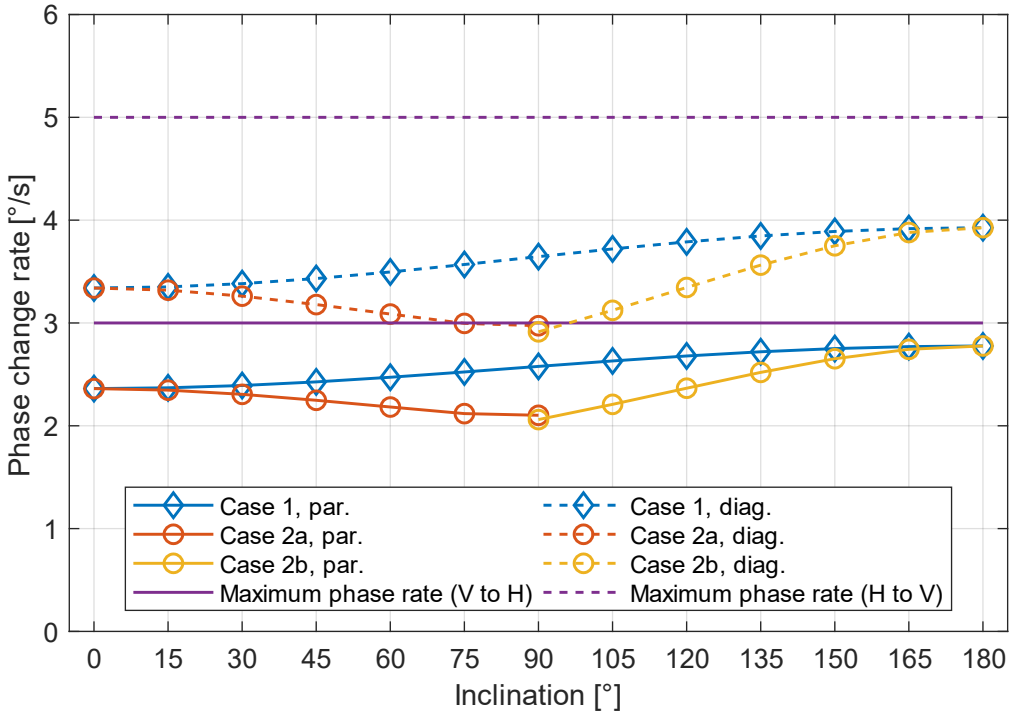

Figure 19: Maximum phase change rate

3.4 Mitigation Methods

3.4.1 Influence of the Maximum Phase Change Rate

One way to enhance the usability of the antenna array is the reduction of jump time by increasing the maximum phase change rate, for example through a different LC, or applying a larger field strength, of the electric biasing field, for steering. To study the effects of faster LC alignment, two different approaches were simulated. The first approach is to increase the phase change rate, but to keep the ratio of the positive and negative phase change rates constant. The second approach is to have equal phase change rates in both directions, which assumes a different geometry of the electric biasing field. Table 19 shows the four simulated phase change rates for these two approaches.

Table 19: Effects of phase change rates

No.	Constant ratio [°/s]		Equal rates [°/s]	
	V to H	H to V	V to H	H to V
1	3.0	5.0	5.0	5.0
2	4.5	7.5	7.5	7.5
3	6.0	10.0	10.0	10.0
4	9.0	15.0	15.0	15.0

Table 20 shows a comparison of the cases No. 1 to 4. For cHornQ and cHornOQ the $L_{1\mathrm{dB}}$ values for 0° inclination dropped from 1 785 s / 1 778 s to 696 s / 682 s for the constant ratio approach, and from 1 510 s to 508 s for the equal rates approach. Similar results can be seen for cOffset, but with smaller values. This behavior is expected, since faster phase shifters lower the time for a jump. The slow phase shifters for the constant ratio simulation increase the time compared to equal rates with the same maximum rate but does not lead to a drop below the next slower case with equal rates.

In contrast to the previous results, the $L_{6\mathrm{dB}}$ values for No. 1 to 3 of the equal rates approach (cOffset) are higher than the ones of the constant ratio approach. The reason for this behavior is that, for 0° inclination, the cOffset method causes two rows of LCPSs to jump at the same time, but into different directions. Therefore, with different phase change rates dependent on the direction, one of the rows passes the paraphase earlier than the other, resulting in a lower overall loss. For No. 4 (highest simulated phase change rate) the influences of the change rates predominate the advantage of the delayed paraphrase.

Table 20: $L_{1\mathrm{dB}}$ values at 0° inclination, case 1

No.	cOffset		cHornQ		cHornOQ	
	Const. ratio	Equal rates	Const. ratio	Equal rates	Const. ratio	Equal rates
1	995 s	745 s	1 785 s	1 510 s	1 778 s	1 510 s
2	727 s	536 s	1 374 s	1 099 s	1 371 s	1 099 s
3	571 s	404 s	1 037 s	772 s	1 047 s	772 s
4	411 s	289 s	696 s	508 s	682 s	508 s

In the previous chapter, the calculations show that the maximum positive phase change rate is lower than the one needed for a diagonal steering process for cHornQ and cHornOQ. Therefore, the constant ratio case was also simulated for an inclination angle of 45°. The simulation shows a drop of the $L_{3\mathrm{dB}}$ value from

578 s (cHornQ, No. 1) / 571 s (cHornOQ, No. 1) to 42 s (cHornOQ, No. 2) / 0 s (cHornQ, No. 2). This shows that these two methods can be used with the flight model if the phase change rate could be increased by 50 % from the current experimentally validated rate (also see Figure 19).

3.4.2 Optimization Strategy for the Jump Distribution over Time

Another way to decrease the losses is to distribute the jumps over time. The simulations in the previous chapters were all performed with the phase jumps starting at the ideal jump time (when crossing the maximum/minimum phase level, 'latest jump'). This is only one of many starting points for jumps in a range that can be seen in Figure 20 (left, green line). The earliest starting point of the time range is defined so that the actual jump would end at the first point after the ideal jump (purple line). Therefore, the range is dependent on the phase change rate and the curve progression of the phase.

When several phase ideal jumps occur simultaneously, one goal could be to distribute the real jumps equally within an available time range to especially avoid paraphases occurring at the same time. Therefore, it would be useful to stretch this range to have more space between the jumps. Since the LCPSs are designed longer than required for a 360° phase shift, this is a feasible option. For the simulation, 400° was chosen as a conservative assumption, although a larger phase shift might be possible at higher losses.

The influence of this larger phase range on the jump range is shown in Figure 20 (right) and is used in the following optimization of the jump distribution. In addition, it would also be possible to hold one LCPS at its maximum / minimum phase to avoid simultaneous paraphases (Weickhmann, Nathrath, *et al.*, 2013). This option is not regarded here, because it would add additional losses to the array.

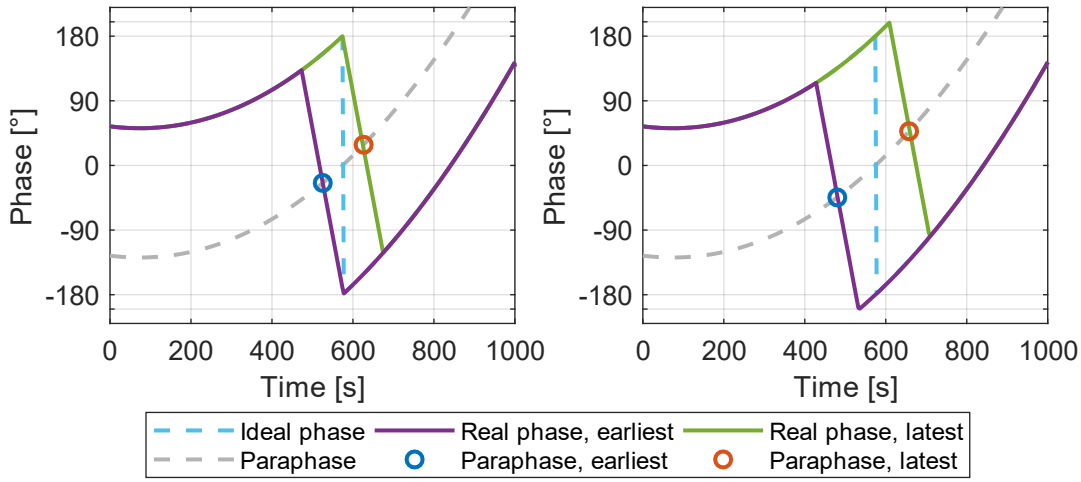

Figure 20: Possible jump range at 360° (±180°, left) and at 400° (±200°, right)

Case 1 with an inclination angle of 0° is used as an example for a worst case optimization. The jumps are distributed by their earliest and latest time of their paraphase, as it is marked by the blue and red circles in Figure 20. Figure 21 shows the sum of these paraphases of phase shifters with a 400° phase range over the entire array at their earliest (blue) and latest (red) time. Between 491 s and 1 646 s a gap between these two sums appears which allows for a distribution of the jumps between these time stamps. Since a linear fit (equal distribution) does not fit between the two curves over the whole time period, a parabolic fit with the following boundary conditions is created:

- Start with the earliest jump available
- End with the latest jump available
- Stay inside the gap of the two sums

The same procedure is applied to the second gap between 1830 s and 2985 s.

This parabolic function is used to distribute the jumps automatically to get a homogenous distribution over time. To distribute the jumps over time, a jump list is created. The jumps are ordered by their earliest paraphase available (earliest first). If there are several jumps with the same timestamp for the earliest paraphase they are ordered by their latest paraphase (earliest first). This ensures, that the jumps are performed within their desired timeframe for the jump.

The value of the parabolic function is checked at each timestep during the simulation. If the value of the parabolic function at the current time step is higher than the total jump count for this time step, the next jump in the list is performed and marked as such.

The yellow line in Figure 21 shows the sum of these distributed paraphases over time. It matches the parabolic fit within the gap of the earliest- and latest paraphase sums.

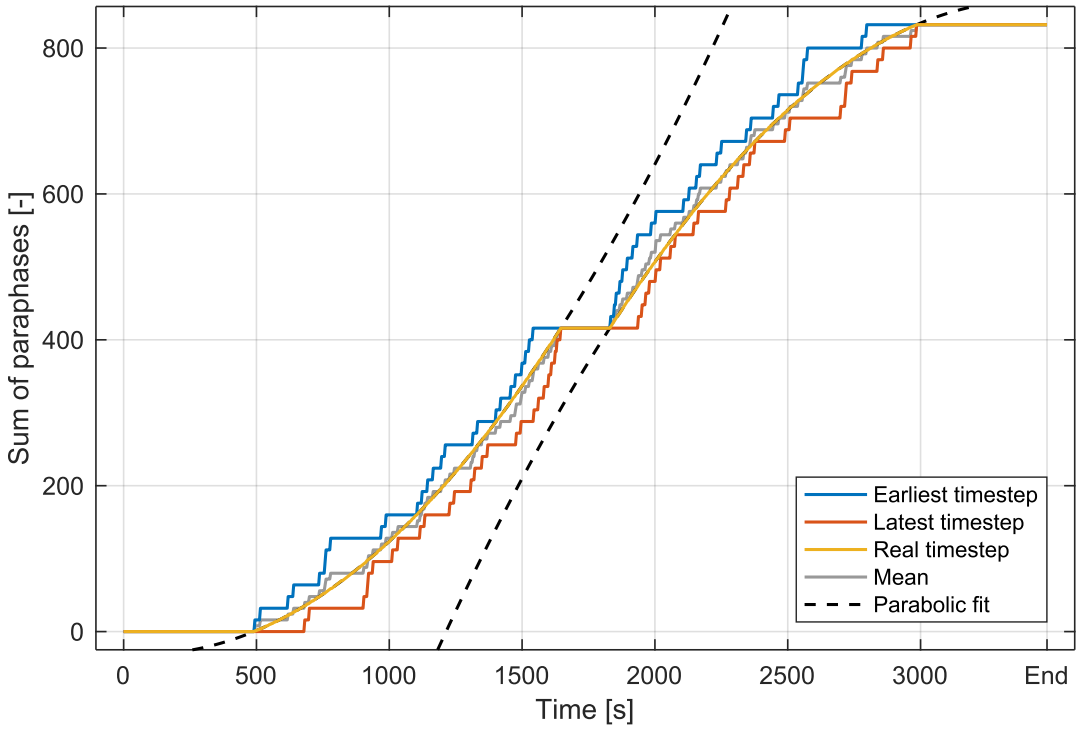

Figure 21: Sum of paraphases for earliest and latest timesteps, inclination 0°

3.4.3 Results of the Optimized Jump Distribution

Figure 22 and Figure 23 show the jump distribution for the non-optimized and the optimized distribution. The vertical blue lines mark the positions of the ideal jumps and the yellow and red areas mark the actual jumps. Red marks the jumps from V to H (3 °/s) and yellow the ones from H to V (5 °/s).

Figure 24 and Figure 25 show the gain of the flight model for case 1 at 0° inclination. The optimized jump distribution in Figure 25 has a maximum loss of about 2 dB which is an improvement compared to maximum losses of over 6 dB for the non-optimized jump distribution (Figure 24). However, the optimization also causes longer time periods of losses in the $L_{1\mathrm{dB}}$ region (1 719 s instead of 995 s).

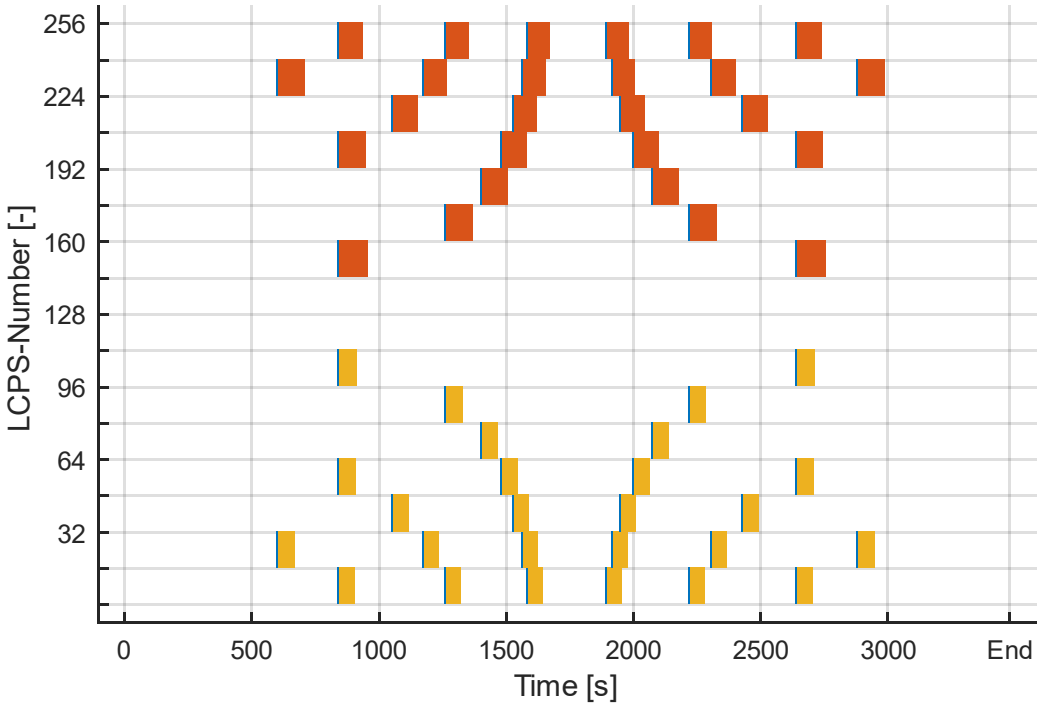

Figure 22: Regular jump distribution, inclination 0°

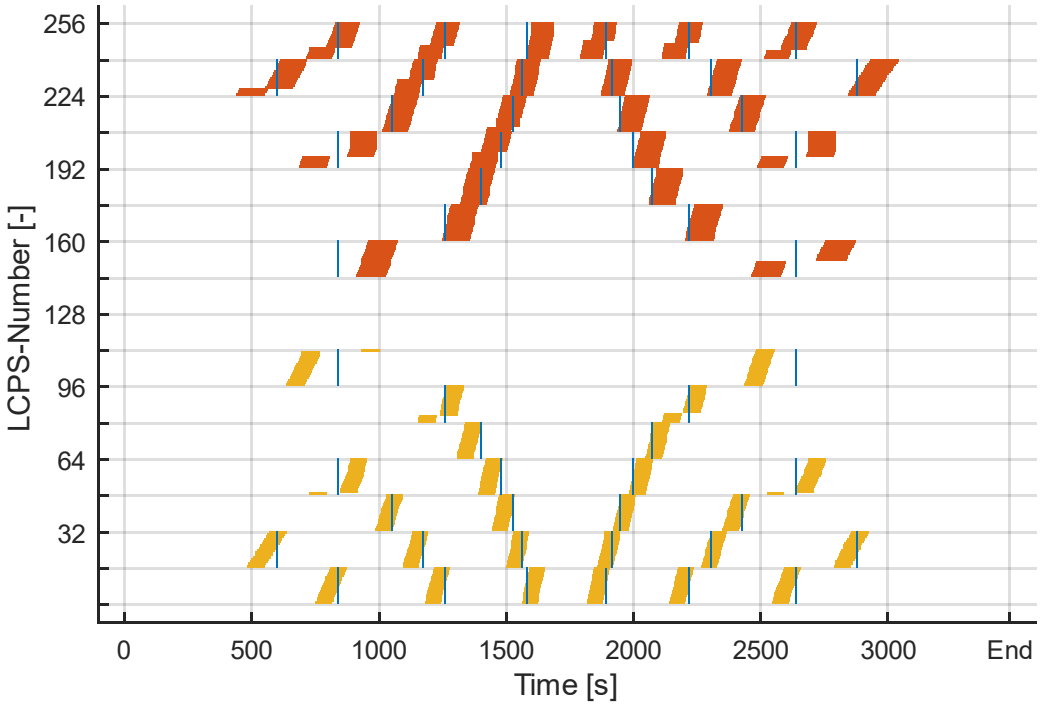

Figure 23: Optimized jump distribution, inclination 0°

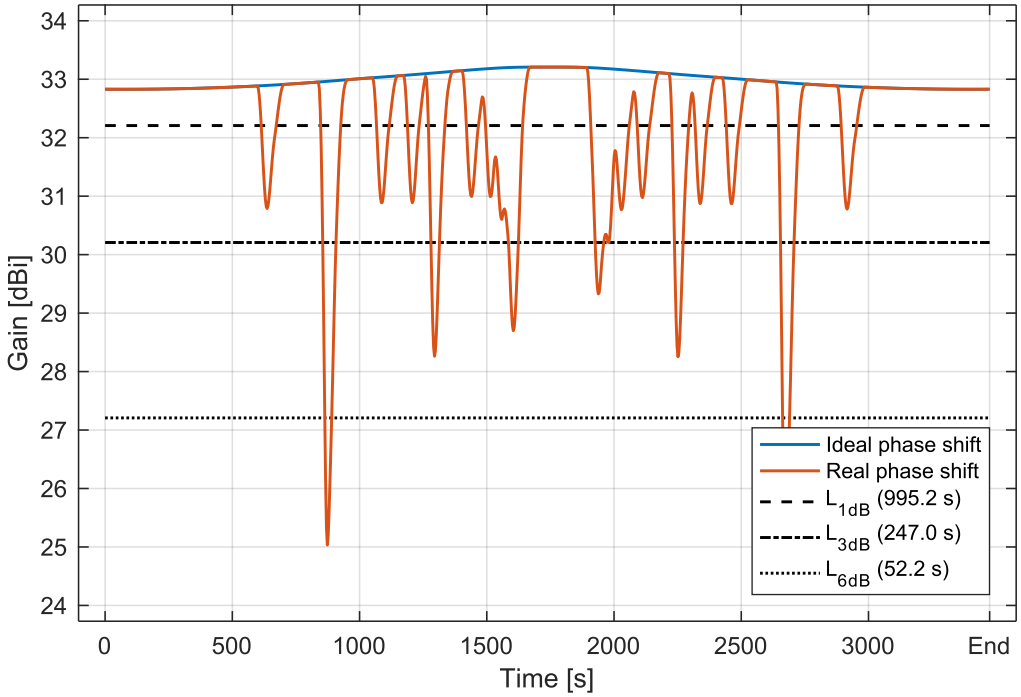

Figure 24: Gain with regular jump distribution

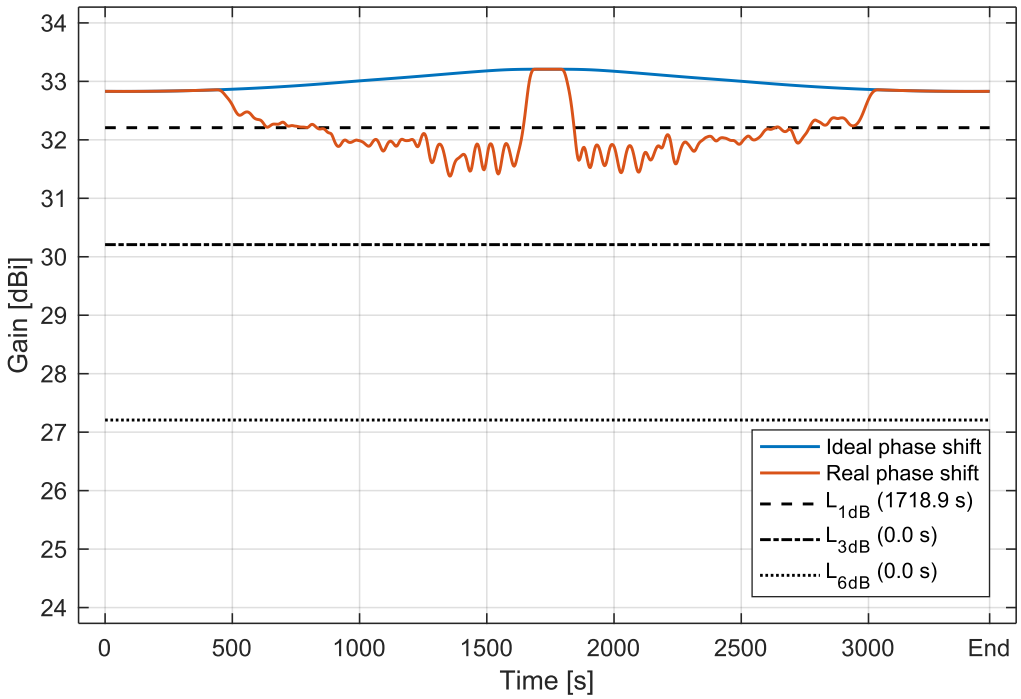

Figure 25: Gain with optimized jump distribution

3.5 Discussion

The optimization was performed on the cOffset method at an inclination angle of 0° (case 1) as a worst case scenario. Table 21 shows the results of this optimization. It was not possible to achieve an equal distribution since the jumps accumulate close to half time of the simulation, when the LEO satellite crosses boresight of the antenna ($\dot{p}$ at its maximum). Nevertheless, the drops in gain can be mitigated effectively, reducing the loss of gain from more than 6 dB to less than 2 dB. However, this improvement induces an increase in $L_{1\mathrm{dB}}$, because the gaps between severe losses in Figure 24 are now filled with jumps and therefore the value for $L_{1\mathrm{dB}}$ is now 1 719 s instead of only 995 s (see Figure 24 and Figure 25).

Table 21: Jump optimization at 0° inclination, case 1

	regular	optimized
L_{1dB}	995 s	1 719 s
L_{3dB}	247 s	0 s
L_{6dB}	52 s	0 s

If the mitigation option of trading fewer but more severe losses with longer but smaller losses is not possible for certain applications, than a possible alternative would be shorter periods of severe losses. Forcing as many LCPSs as possible to jump simultaneously will cause a total loss of signal for shorter periods but will then provide full antenna gain over the rest of the time. A first test of this method showed, that it is possible to reduce $L_{1\mathrm{dB}}$ from 995 s down to 695 s. Because of the large gradient of the gain-drops over time during these jumps, the $L_{1\mathrm{dB}}$ value is almost equal to $L_{3\mathrm{dB}}$ and $L_{6\mathrm{dB}}$.

4 Manufacturing of Electroplated Liquid Crystal Phase Shifters

The following chapter is an updated and extended version of the publication Tebbe et al. (2017).

Manufacturing and testing of liquid crystal phase shifters for an electronically steerable array

2017 IEEE Aerospace Conference, March 2017

This chapter describes the design and manufacturing process of the intended LCPS hardware for a space application. It is divided into three parts, the first part recaps the design process with several iterations, the second part shows the manufacturing process and describes the modifications that are established and in the third part alternative manufacturing methods are proposed and partially tested.

4.1 Design Process

The challenges in building a lightweight LCPS are to contain the LC despite thermal expansion, and to actively orient the LC with an adjustable electric field within the large quantity of required waveguides in the distribution network.

Containment is provided by various design iterations of an LC-cavity made of a polystyrene, *Rexolite® 1422*, known for its superior high frequency dielectric properties (C-Lec Plastics, 2015). The electric field is generated by two separate film electrodes on the two broad sides of the waveguide. Electric field generation, field strength and uniformity are optimized using multiple electrodes connected by a resistor network to minimize the required electric connections. During the development, several design iterations for both the LC-cavity and film electrodes, were build and tested.

4.1.1 LC-Cavity

1st generation LC-cavity: The first generation consisted of an LC-body which is open on the two broad sides of the long waveguide. The cavity is sealed with two glued-on 50 µm thin polyethylene terephthalate (PET) films, on which the original aluminum electrodes were vapor-deposited (Figure 26). The voltage-dividing resistor across the electrodes consisted of a screen-printed polymer resistor, series *ESL RS 12116* polymer resistive paste.

The electrode films could adjust with the thermal expansion of the LC, however, the sealing of the two films against the body was problematic, leading to LC leakage and air bubble intrusion with subsequent detrimental effects of RF performance. A contracting film, for example, created an air gap (Figure 26, Cross section – Top), which also reduced the possible total phase change, in addition to poor RF performance.

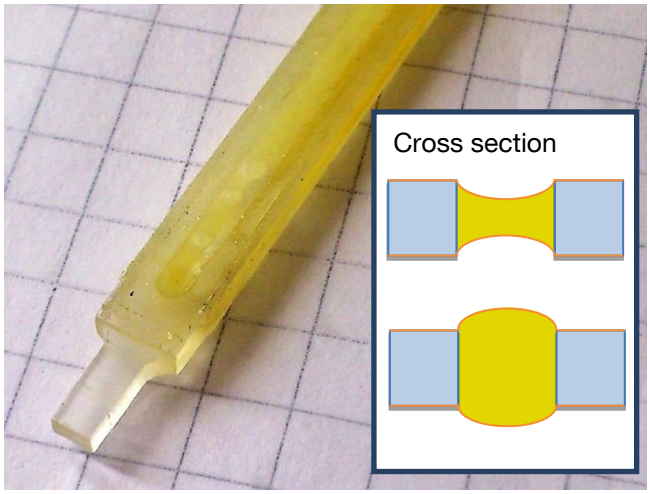

Figure 26: 1st generation LC-cavity

2nd generation LC-cavity: The second generation consisted of two polystyrene halves, glued together to create the LC-cavity (manufactured at *GEWO GmbH*). Polystyrene adhesive (*Rexolite*® adhesive) was used to create uniform material properties (C-Lec Plastics, 2015). The required minimal wall thickness of 0.2 mm against the waveguide surfaces was thicker than the 50 µm PET-film, but with defined and stable, yet non-expanding geometry. Two fill ports on opposing ends allowed for air-bubble free filling.

Figure 27 shows the LC-cavity with one of the fill ports. The blue lines mark the 'lid' that is glued into the 'body' to close the cavity. After an air-bubble free fill is achieved, the cavity is closed by gluing polystyrene pins into the orifices. This design resulted in pressurization of the LC-cavity during pin insertion and a poor glue joint due to LC-contamination of the polystyrene surfaces. This poor glue joint together with the pressurization is leading to leaks.

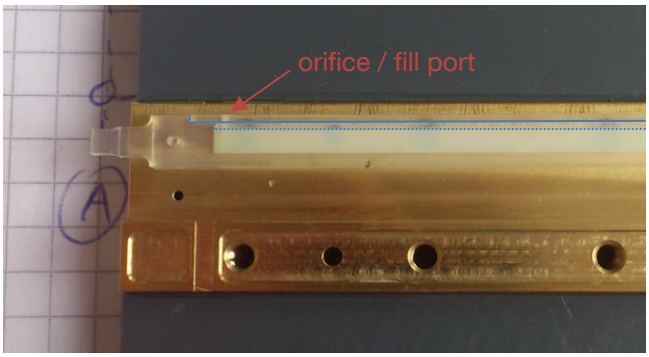

Figure 27: 2nd generation LC-cavity on split block (Weickhmann, Gaebler, *et al.*, 2013)

3rd generation LC-cavity: To avoid the pressurization of the LC-cavity during port sealing, the pins were inserted normal to the orifice axis (Figure 28, manufactured at *GEWO GmbH*). The orifice was sealed by a press fit, and the pin secured with polystyrene adhesive. With the orifice closure and pressurization solved, leakage through the joined polystyrene halves could be observed at the glue joints, which showed pin hole capillaries and flaws created during the curing of the polystyrene adhesive, sufficient in size to pass LC under thermal expansion.

Even moderate ambient temperature changes in the laboratory could result in structural failure of the LC-cavity due to the small wall thicknesses. Therefore, the 4th generation of LC-cavities had to accommodate thermal expansion even for ambient lab applications without extreme thermal excursions.

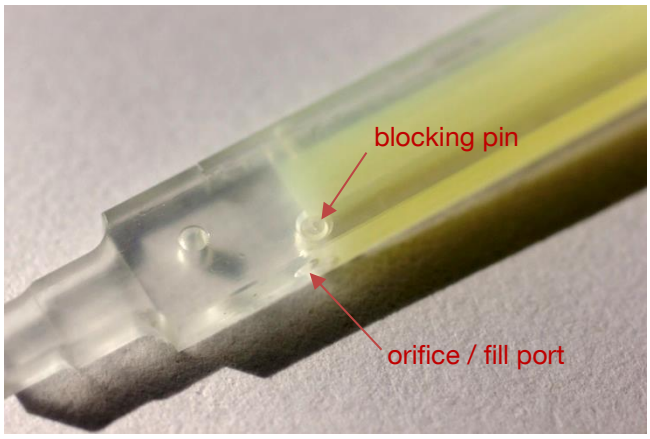

Figure 28: 3rd generation LC-cavity

4th generation LC-cavity: Thermal expansion can be addressed by an internal adjustable volume or an external expansion volume. Internal expansion could be accomplished with a closed-cell foam. The air-bubbles within the closed-cell foam, however, could diffuse into the LC, and again create unpredictable gas bubbles within the cavity, and thus affect RF performance. Therefore, a new design was developed that uses 'chimneys' to be able to fill the cavity from outside the waveguide and to also enable the use of external bellows (e.g., *Servometer*® - *MW Industries, Inc.*) to reduce pressurization due to thermal expansion.

Structural failure of the polystyrene glue joint was addressed by an improved 'Z'-shaped joint geometry with larger contact surface area. The polystyrene adhesive was replaced with a low viscosity two-part epoxy (*Zeiss Kleber 56*) to avoid pin-hole capillaries and to improve bonding strength. The very low-viscosity epoxy quickly and completely spreads by capillary action without the need for a larger gap required for the more viscous polystyrene adhesive. The low viscosity glue and capillary action also ensure that the epoxy only fills the capillary gap and does not enter the LC-cavity (Figure 29, manufactured at *GEWO GmbH*).

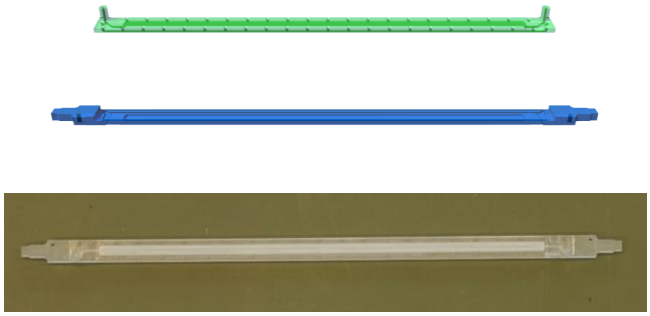

Figure 29: 4th generation LC-cavity (top: 'lid', middle: 'body', bottom: glued LC-cavity)

4.1.2 Film Electrode

1st generation film electrode: The first generation of film electrodes was manufactured at *TU Darmstadt*. The film is made out of 50 µm PET with aluminum striplines as electrodes (Figure 30).

However, the aluminum-coated PET film (*HVB Hoch-Vakuum Beschichtungs GmbH & Co. KG, Berlin*) used for the manufacturing of the electrodes had imperfections in the thin aluminum coating (< 200 nm). Furthermore, it is advantageous to use a material with higher resistivity for the striplines to suppress the stripline modes. Decreasing the thickness of the electrodes for higher resistance leads to electrode breaks.

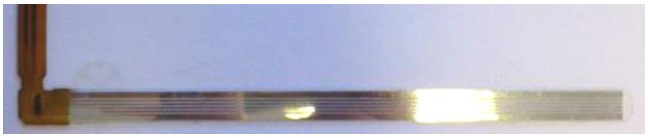

Figure 30: 1st generation film electrodes

2nd generation film electrode: The second generation of film electrodes was manufactured at *Cicor Microelectronics* (*Reinhardt Microtech GmbH*). The film material is 50 µm (2 mil) polyimide (PI, *Pyralux® AP* without copper) and the striplines are made out of 200 nm vapor deposited titanium. To ensure a correct placement on the LC-cavity, each film electrode has two alignment pin holes (Figure 31).

The striplines have been tested with various filter structures. The structure of the electrode lines is designed in order to suppress stripline mode propagation (RF signals propagating between waveguide wall and electrode line). This is achieved using stubs and stepped impedance filter structures along the electrode lines.

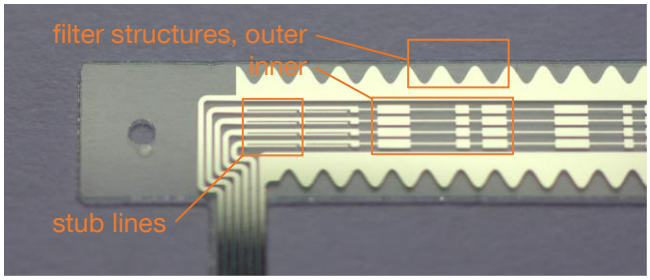

Figure 31: 2nd generation film electrode (Weickhmann, Nathrath, *et al.*, 2013)

3rd generation film electrode: The current film electrodes are manufactured in six different designs (*manufactured at Cicor Microelectronics / Reinhardt Microtech GmbH*). These designs can be broken down into three designs that are manufactured each with and without an inner filter structure (see Table 22). The first design consists of two pads for the electric field control and six for the monitoring. In the second design the two pads for the electric field control were replaced by two solder pads for wire attachment. The third design is similar to the second but rejects the six monitoring pads (see Figure 32).

The film electrodes are now glued onto the LC-cavity with a 50 µm pressure-sensitive adhesive to ensure reproducible geometry, and the alignment pin holes are excluded from the design.

Table 22: Film electrodes

No.	Electric field control	Monitoring	Inner filter structure
708-767	2 Pads	6 Pads	Yes
708-768	2 Pads	6 Pads	No
708-769	2 Wires	6 Pads	Yes
708-770	2 Wires	6 Pads	No
708-771	2 Wires	No	Yes
708-772	2 Wires	No	No

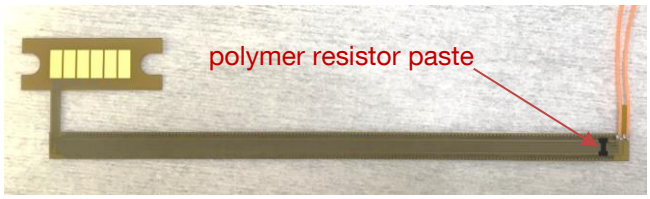

Figure 32: 3rd generation film electrode with soldered wires

4.2 Manufacturing Process

The manufacturing process is challenging and most of the manufactured LCPS were not functional. Several steps were added to the process and some changes were made to the process sequence to reduce the number of scrap parts.

4.2.1 Internal Structure of the Liquid Crystal Phase Shifter

Chapter 1.2.4.3 shows a simplified structure of the LCPS to explain the general functionality. In this chapter, the structure is shown in more detail with the different materials and geometries. Figure 33 shows the cross section of an electroplated LCPS. The thickness of the titanium striplines, the silicone sealing and the silver layer are not to scale since they would be invisible.

The LC is surrounded by a polystyrene body. On both broad sides of this body, two film electrodes are attached with adhesive. Surrounding this assembly is a silicone layer to seal it from the electroplating bath and a silver layer as the electrically conductive layer for the electroplating process. After the electroplating a copper layer provides mechanical stability and increases the wall thickness of the conductive layer.

The striplines are attached to the polyimide film and are pressed into the adhesive as a first electrical insulation layer.

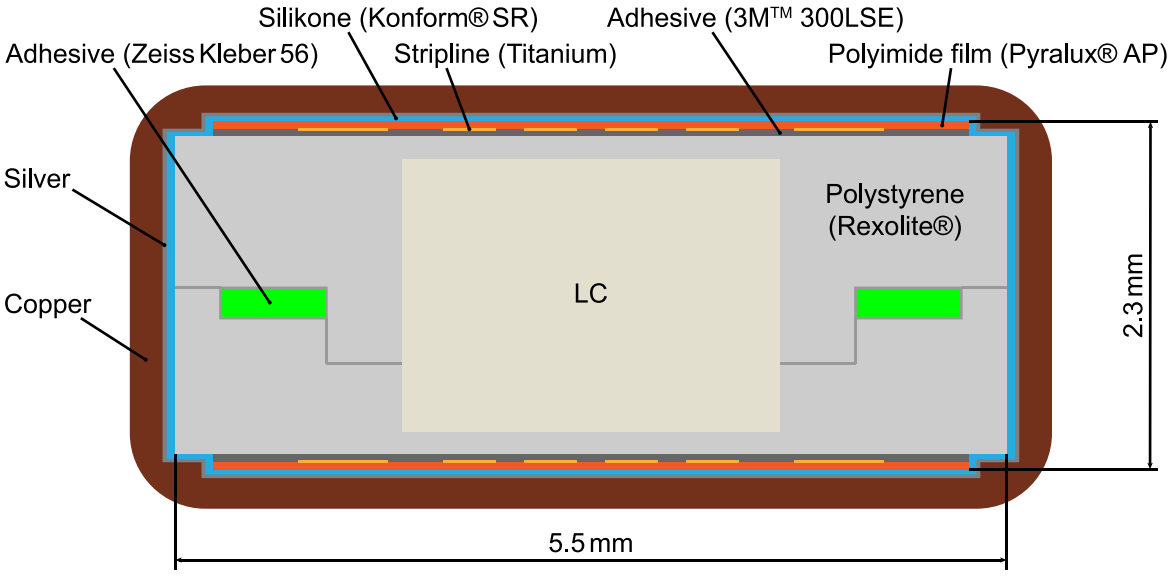

Figure 33: Cross section of the electroplated LCPS

4.2.2 Waveguide Core Assembly

LC-cavity: The two polystyrene body parts are milled separately and glued together with a low viscosity two-part epoxy (*Zeiss Kleber 56*, Figure 29). During the curing it is necessary to weigh the 'lid' down onto the 'body' to ensure that the glue does not lift the 'lid' and therefore change the dimensions of the LC-cavity. Final dimensional accuracy for use in the split block (split waveguide for a laboratory setup) should be to ±20 µm.

Film electrode: The titanium layer on the 50 µm film electrodes is etched in a printed circuit board (PCB) like process to get six striplines including optional filter structures and solder pads for wire attachment (Figure 32). The solder pads are later on covered with gold. Afterwards, these striplines are connected via a polymer resistor paste to create a resistor network.

For some of the film electrodes, wires instead of the film electrode itself are used as feedthrough. These polytetrafluoroethylene (PTFE) insulated 30 AWG (American Wire Gauge) wires are soldered to two gold-clad pads on the film electrode before the assembly (Figure 32).

Exposed contact areas on the wire and film where they are fed through the waveguide wall are insulated prior to attachment to the LC-cavity. Insulation is required against the waveguide walls as well as the penetrating and corrosive electroplating bath. The bath may both dissolve contacting metals as well as leave conductive residues / salts behind.

The insulation consists of a thin layer of spray-on silicone (*Konform® SR*: Chemtronics, 2018) and pressure sensitive adhesive tape to mechanically support the thin film.

Assembling: The LC-cavity is cleaned (ideally air plasma cleaning and surface activation) and laminated with a pressure-sensitive adhesive (*3M™ 300LSE*, 50 µm: 3M, 2006) on both sides where the film electrodes have to be attached. Film electrodes are applied onto the adhesive with the electrodes facing the polystyrene body, paying close attention to the alignment between LC-cavity and film electrode using a guide (Figure 34). Once adhered, it is not possible to remove the film electrode without destroying the electrode lines. Pressure has to be applied carefully to avoid damage to the thin titanium electrodes. Therefore, the assembled LCPS-core (LC-cavity + film electrodes) is placed into a mechanical press to apply pressure evenly onto the assembly for about 24 hours. Excess adhesive has to be carefully removed for a smooth galvanic surface at the film edges.

LCPS with wired electrodes have milled out provisions for the wire and solder, which will be sealed after the attachment of the film electrodes with *Zeiss Kleber 56* and polystyrene adhesive to obtain the waveguide geometry.

The prefabricated copper flanges are slid onto the LC-cavity and secured with a polystyrene pin. The transition between the copper flanges and the LC-cavity as well as the pins are sealed with glue (*Zeiss Kleber 56*) to avoid entry of electroplating solution. The prefabricated copper parts for fluid line attachments are glued around the two chimney orifices, used later on to fill the LC-cavity with LC (Figure 35).

To avoid the entry of the electroplating bath into the pressure-sensitive adhesive, the entire assembly is covered with a thin layer of silicone conformal coating spray. The copper parts and the external gold pads on the film electrode have to be covered beforehand to ensure electrical conductivity afterwards.

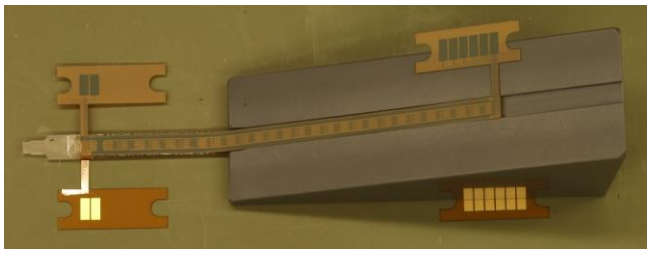

Figure 34: Attaching the film electrodes to the LC-cavity

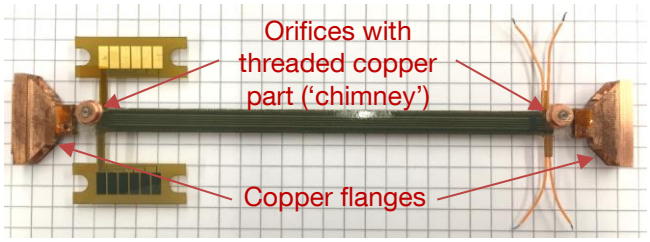

Figure 35: Assembly with flanges and chimneys

4.2.3 Waveguide Wall Manufacturing

Metallization for electroplating: Before being able to start the electroplating process, it is necessary to have a first conductive layer on top of the silicone layer.

Since this conductive layer will stay within the waveguide after the electroplating process it should be a homogeneous contiguous metallic layer with very low resistance.

Several layers of silver are sputter-coated onto the assembly. The desired thickness of this layer and the material were chosen to withstand the following corrosive manufacturing steps with some margin. Critical in this case is the necessary activation process of the pre-manufactured copper parts, where the oxide layers have to be removed with acid and also mechanically before the electroplating process can be started. A thin sputtered layer of copper would be removed in the process, while the silver withstands the process.

The parts of the assembly that should not be sputter-coated with silver are covered (external gold pads on the film electrode, chimneys and some parts of the flanges). A jig holding the phase shifters and providing appropriate masking was used to sputter-coat four phase shifters at a time (Figure 36).

Electroplating: The flanges on each end of the LCPS are sealed (foam + silicone on the inside) and the assembly was integrated into an electroplating jig made of acid resistant PVC (polyvinyl chloride) tubes and end plates to ensure the position and orientation of the flanges as well as the correct LCPS length (Figure 37).

The electroplating process starts with covering most parts of the flanges with wax. The rest of the flanges that will be exposed to the electroplating bath and the threaded copper parts for the chimneys are then activated with a mixture of sulfuric acid and hydrogen peroxide. In addition, some areas of the prefabricated copper parts with a thick oxide layer have to be treated with sandpaper.

Afterwards the uncoated external gold pads and cable ends have to be covered with rosin to avoid contact to the electroplating bath (Figure 37). After the electroplating process it can easily be dissolved with isopropyl alcohol without inducing any mechanical forces onto the fragile film electrodes.

Before the electroplating process starts, tubes are attached to the chimneys and the cavity is filled with water in case of the intrusion of electroplating bath. Both tubes from the two chimneys are attached to syringe bodies to avoid the buildup of pressure due to thermal expansion.

Once the desired copper thickness has been achieved (after about 16 hours in the electroplating bath), the rosin is dissolved, the wax cover on the flanges is removed, and the seals on both flanges are removed (Figure 38). The functionality, integrity, isolation, continuity and values of the resistor network are verified to detect potential shorts or corrosion-induced alterations in the electroplating process.

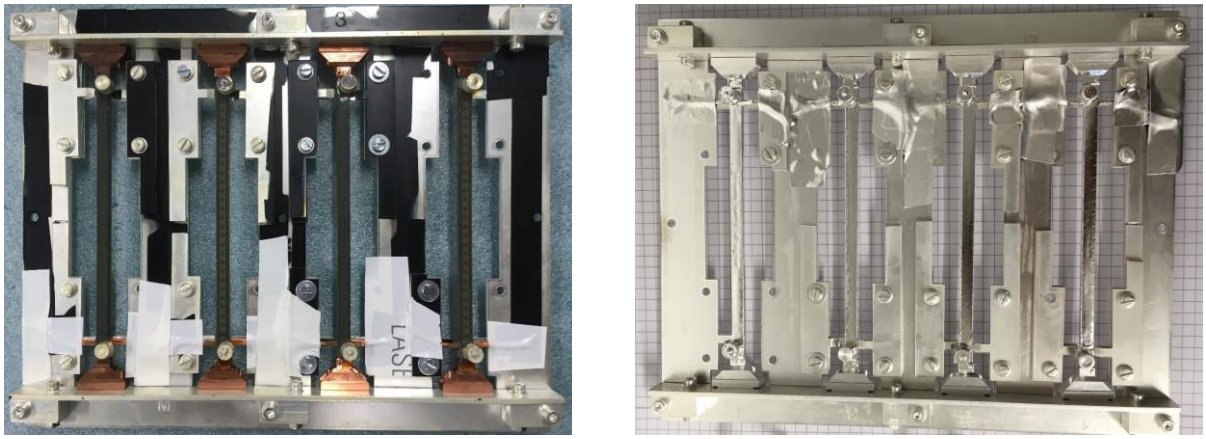

Figure 36: Cover jig with four assembled LCPS-cores before (left) and after (right) sputter-coating

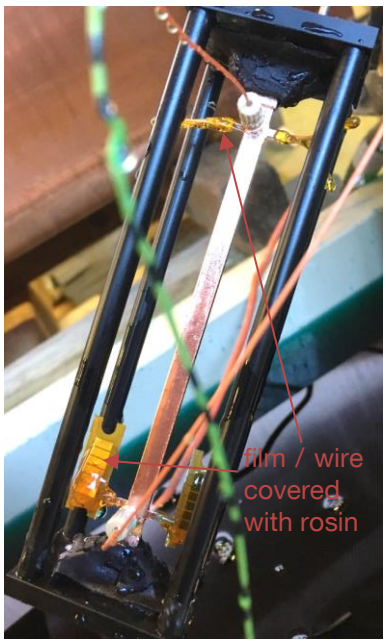

Figure 37: Phase shifter in the electroplating jig

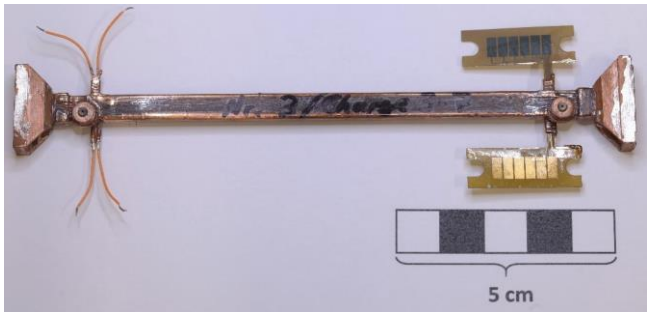

Figure 38: Electroplated LCPS

4.3 Alternative Manufacturing Processes

4.3.1 Sputtered Silver Wall

The influence of the electroplating process and of any potentially remaining residues on the RF-performance (scattering parameters) is unknown. Therefore, in addition to split block tests, a test body covered solely with silver, was also built (Figure 39).

Since one sputtered silver layer is about 80 nm to 120 nm thick (3 oscillations under the sputter source), the skin depth of the radio wave has to be calculated to ensure that appropriate effective conductivity is provided for the walls to shield and guide the RF signal with low loss (see Chapter 2.3). Table 23 shows the wall thickness needed for a 90 % decay for 23 GHz and 27.5 GHz.

The test body was cycled twelve times on both of the broader waveguide sides to achieve approximately 1 µm of silver thickness. The smaller sides receive less silver but are coated during all 24 cycles in total. The finished test body is shown in Figure 39 (infused in epoxy for mechanical stability).

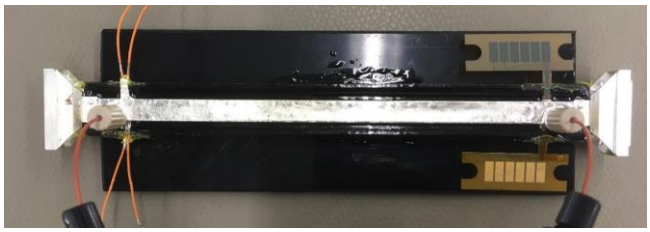

Figure 39: Test body, 1 µm silver

Table 23: Required wall thickness for 90 % decay

Material	Frequency	δ_S	Thickness for a 90 % decay
Silver	23.0 GHz	423.5 nm	975.2 nm
Silver	27.5 GHz	387.3 nm	891.8 nm
Copper	23.0 GHz	435.8 nm	1003.3 nm
Copper	27.5 GHz	398.5 nm	917.6 nm

4.3.2 Avoiding the Lead-Through of Electrodes

The necessity of biasing the electric field from outside the waveguide leads to film electrodes or cables that have to be fed through the waveguide wall. Those feedthroughs are difficult to seal against the electroplating bath.

Therefore, one solution to this problem is to attach the feedthrough after the electroplating process. To be able to access the solder pads of the film electrodes, the electrode lines have to be on the outside. This means that they have to be covered with an electric isolator before the part is sputter coated. The solder pads are covered with acrylonitrile butadiene styrene (ABS, Figure 40) before the electric isolator is applied. This later on helps to uncover the solder pads without destroying the film electrode.

After the sputter coating and the electroplating process, the copper on top of the ABS-blocks can be cut away and the ABS is dissolved with acetone to access the solder pads (Figure 41).

However, a first test with this method (batch 6) has not been successful because only one film electrode is functional after dissolving the ABS.

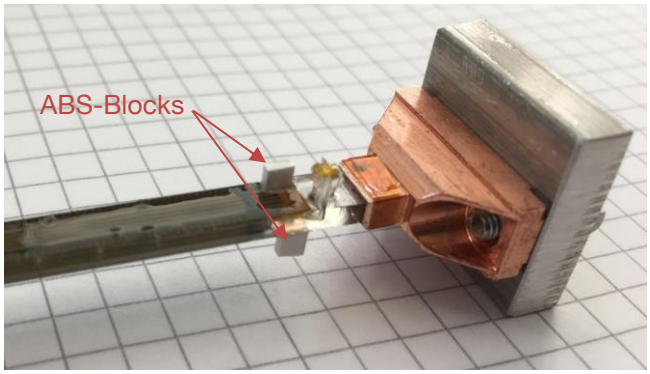

Figure 40: ABS-blocks for electrode lead-through (batch 6)

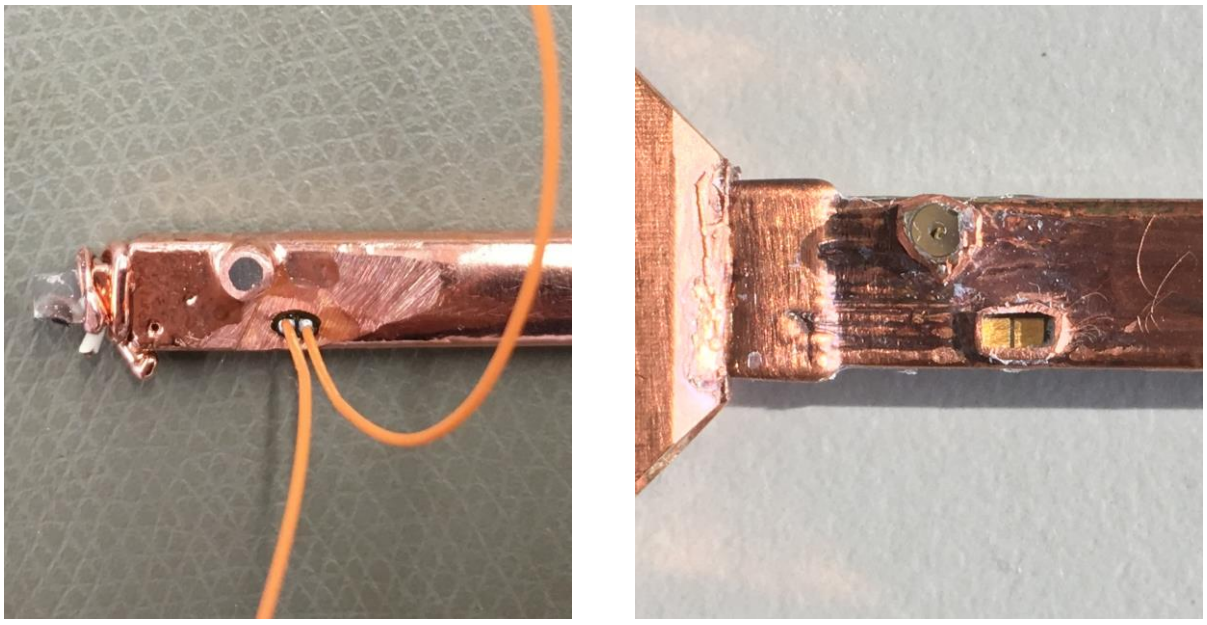

Figure 41: Soldered wires on test body (left) and batch 6 (right) after electroplating process

4.3.3 Avoiding Contact of the Electroplating Bath and the Film Electrodes

Instead of covering all parts with silicone coating to avoid the intrusion of electroplating bath it might be also possible to electroplate the copper onto a lost core (for instance ABS, Figure 42). This core can be dissolved leaving behind a flexible copper shell (Figure 43).

Since this shell is flexible, it can be compressed in one direction to expand in the other direction and therefore make room for the LCPS-core. If the shell is released, it will return to its former shape and therefore squeeze the LCPS-core. The flexibility is enhanced by changing the geometry of the cross-section to hexagonal (Figure 44).

The Flanges have to be attached afterwards, since they are not flexible enough. This attachment can also be done by electroplating, because now it is possible to dip one end of the LCPS into the electroplating bath instead of the entire LCPS. The electrodes therefore avoid getting into contact with the electroplating bath. Another option could also be soldered flanges.

Figure 42: ABS-Core with electroplated copper

Figure 43: Copper shells with 50 µm, 100 µm and 150 µm copper

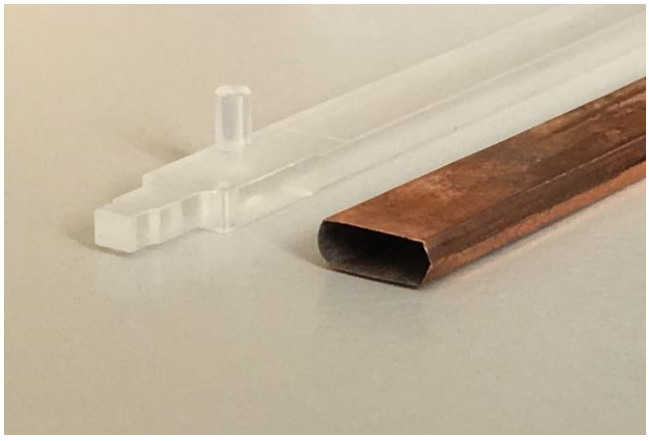

Figure 44: Flexible copper waveguide (50 µm)

5 RF Characterization of Liquid Crystal Phase Shifters

Since the target application is an ISL antenna on a GEO relay satellite, the performance of the LCPS has to meet the simulated phase velocities and phase ranges (≥360°, see Chapter 3). In Chapter 5.1 the experimental setups for the different LCPSs are described. Chapter 5.2 is a RF-comparison (scattering parameters) between the different manufacturing methods. The temperature dependency of the RF-properties of the LCPSs are shown in Chapter 5.3 and the calibration results are shown in Chapter 5.4. The discussion of the results can be found in Chapter 5.5.

5.1 Experimental Setup

For the characterization of the LCPSs two different ways to form the waveguide around the LCPS core are tested. The first one is a waveguide that is split into two halves and can be screwed together after the core is inserted (split block). This LCPS is fully functional but heavier and bulkier than the second option. The second way to form the waveguide is electroplating as described in Chapter 4.

The RF-parameters are measured with different network analyzers, *PNA* / *PNA-X* series (*Agilent Technologies* / *Keysight Technologies*) with semi rigid or phase stable coaxial cables and standard transitions from coaxial to waveguide (WR34 – waveguide rectangular, width 0.34 inch, height 0.17 inch). The calibration techniques used are SOLT (Short-Open-Load-Thru) and TRL (Thru-Reflect-Line) with reflect as standard. For the time dependent measurements with *GT3-23002* (campaign 3) a response calibration was used to avoid the time correction necessary for time-dependent measurements with a full two port calibration (SOLT) (see Chapter 5.1.3).

The control electronics hardware (see Chapter 1.2.4.4) is used to control the phase of the LCPS. The measurements at *TU Darmstadt* are performed with a similar hardware but with only one channel.

5.1.1 Comparison Measurements

The split block LCPS is fitted with two transitions to WR34 flanges. Therefore, standard coaxial to waveguide transitions can be used for the measurement. The calibration is performed for the WR34 flange of the coaxial to waveguide transition with standard calibration kits. This also means that the two transitions from WR34 to the split block are always included in the measured parameters. This setup is equal to the one used for the measurements under different temperatures. The electrode films used in this setup are 708-769-14 (top); 708-769-6 (bottom) with a resistance between the two outer striplines of 7.65 MΩ and 7.19 MΩ.

The measurement of the electroplated LCPS and the sputtered silver LCPS is similar to the split block measurements. The main differences are special waveguide transitions from WR34 to the flanges used in the electroplated LCPS (specially designed LISA-ES flanges, adapted to the restricted space).

5.1.2 Temperature Control and Measurement

The temperature dependent measurements are conducted in a modified split block. The split block is fitted with six holes for thermocouples (three in each halve) to measure a temperature close to the LCPS core without piercing the waveguide wall. Only four holes are equipped with thermocouples because the temperature data logger (*Omega - RDXL6SD*) only supports four thermocouples. Each thermocouple is inserted into the holes with thermal compound and the temperatures at each of the four thermocouples is measured every second. The exact positioning of the thermocouples can be found in Appendix E.

The temperature of the split block can be controlled with two resistance heaters glued to two aluminum plates that can be screwed onto each of the broad sides of the split block. A temperature controller uses a

PT100 thermistor (platinum thermistor with a resistance of 100 Ω at 0 °C) glued onto one of the resistance heaters to control the temperature. Figure 45 shows the split block with mounted heaters and PT100 thermistor. The assembly is surrounded by polyurethane foam as thermal insulation. Only the flanges are not insulated to enable the mounting of the transitions to WR34.

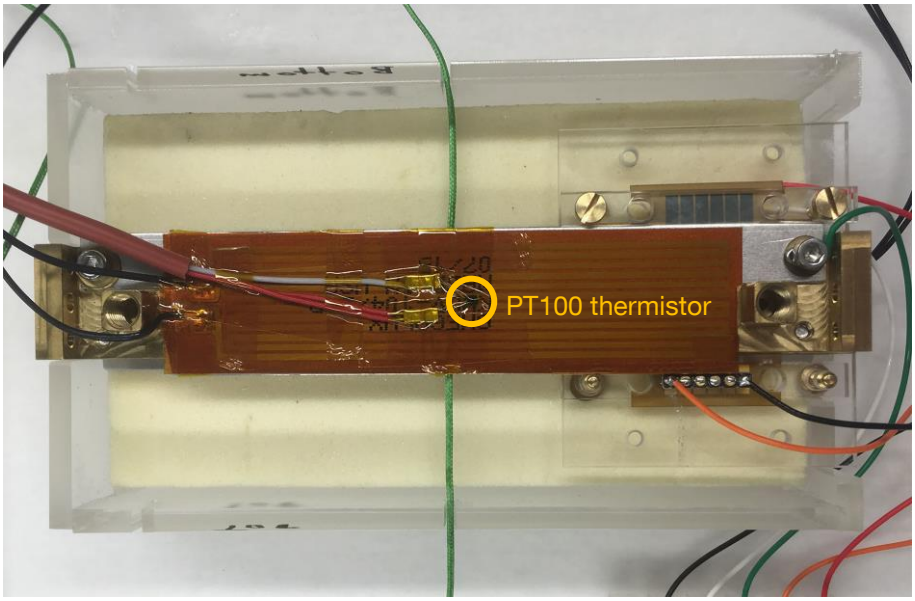

Figure 45: Setup for temperature dependent measurements

Since the temperature of the LC is the one of interest, a thermal simulation has been conducted to estimate the temperature of the LC relative to the temperatures at the measuring points. The result for the 80 °C case is shown in Table 24. This case has the highest temperatures and the widest temperature range.

In Appendix E the results of the simulation and the assumed boundary conditions are shown in more detail.

Table 24: Temperature range for the 80 °C case (simulation and campaign 2)

	Temperature of the liquid crystal		Temperature at the thermocouple positions			
	Min.	Max.	Bottom center side	Bottom center	Bottom end side	Top center
Simulation (stationary)	81.1 °C	84.0 °C	84.0 °C	84.0 °C	80.2 °C	84.0 °C
Measurement (Test 4, Test series 7, No. 1)	-	-	83.6 °C ±3.3 °C	83.4 °C ±3.3 °C	79.2 °C ±3.3 °C	83.4 °C ±3.3 °C
Measurement (Test 4, Test series 7, No. 7)	-	-	83.4 °C ±3.3 °C	83.2 °C ±3.3 °C	79.8 °C ±3.3 °C	83.3 °C ±3.3 °C
Measurement (Test 4, Test series 7, No. 2-6, min. range)	-	-	80.8 °C ±3.3 °C	80.6 °C ±3.3 °C	78.2 °C ±3.3 °C	80.7 °C ±3.3 °C
Measurement (Test 4, Test series 7, No. 2-6, max. range)	-	-	83.4 °C ±3.3 °C	83.2 °C ±3.3 °C	78.5 °C ±3.3 °C	83.3 °C ±3.3 °C

For the temperature dependency, the temperatures of all four thermocouples are recorded during the measurements with the network analyzer. In the evaluation of the data recorded by the network analyzer, only the temperatures with the correct timestamp are taken into account.

The measured temperatures of these four thermocouples are combined to a temperature range shown in the temperature dependent figures. The range is defined by the minimum temperature minus the maximum error and the maximum temperature plus the maximum error measured during the RF measurements. The error is a combination of the thermocouple error (Type K, Class 2, reference junction at 0 °C: ±2.5 °C in the desired temperature range) and the error of the data logger (±0.8 °C, *Omega - RDXL6SD*).

If the timespan of the measurement with the network analyzer comprises several temperature measurements, the maximum and minimum temperature of the entire timespan are taken.

5.1.3 Time-Dependent Measurements

The time-dependent measurements are realized through the *CW Time Sweep* function implemented in the *PNA* / *PNA-X* series network analyzers. This function uses the dwell time of the network analyzer to spread the measuring points over time (given as sweep time). Depending on the calibration method, the measurement on a two-port network analyzer must be performed in both directions (Port 1 -> Port 2, Port 1 <- Port 2) to calculate all the scattering parameters and phases.

If *Standard Sweep* is chosen, the network analyzer will measure one direction over the sweep time, change the direction and measure again. This accumulates to a measurement time of twice the sweep time. Since two measuring points of both directions are used to calculate corrections for some of the scattering parameters and phases, this type of measurement might be useless for the measurement of a time-dependent behavior (if all scattering parameters are needed).

The *Point Sweep* method forces the network analyzer to measure both directions successively. The measured points that are used to calculate one set of scattering parameters are therefore closer together (time-wise). Instead of measuring both directions directly after one another, the dwell time is used before each measurement and therefore the time sweeps are twice as long as given in the sweep time.

The calculated scattering parameters and phases are stored as if they were measured in the given sweep time which means that each time set that is saved as a *Touchstone* file has to be corrected according to the calibration method used for the measurement.

Figure 46 shows the measurement order of *CW Time Sweep* with the *Point Sweep* method and the table in this figure shows the timestamp and measurement order that is saved in the *Touchstone* file. It is assumed that the time used for each measurement is significantly shorter than the dwell time and therefore negligible.

The time dependent measurements with *GT3-23002* are performed with a response calibration. With this calibration, no correction is needed but only a limited set of scattering parameters and phases are available.

The time dependent behavior is measured at 23 GHz since this is the lowest frequency of interest and the LCPSs have the lowest phase range at this frequency.

Measurement sequence

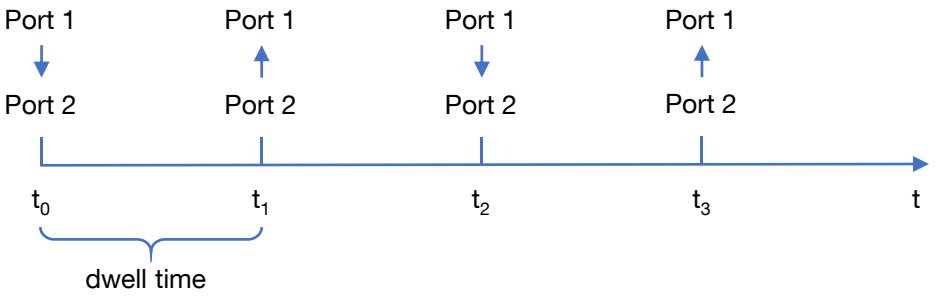

Touchstone file

Time	Measurement direction Port 1 -> Port 2	Measurement direction Port 2 -> Port 1
t_0	Port 1 -> Port 2 at t_0	Port 2 -> Port 1 at t_1
t_1	Port 1 -> Port 2 at t_2	Port 2 -> Port 1 at t_3

Figure 46: Measurement order for *CW Time Sweep* with *Point Sweep* method

5.2 Comparison of different Manufacturing Methods

Some measurements of the following chapter have been published in Tebbe et al. (2017).

Manufacturing and testing of liquid crystal phase shifters for an electronically steerable array

2017 IEEE Aerospace Conference, March 2017

The manufacturing method, especially the electroplating bore some uncertainties. For a better understanding of the influence of the electroplating process on the RF performance, a similarly prepared LCPS core assembly is tested without the electroplated copper layer. As described in Chapter 4.2, the LCPS core assemblies are silver sputtered before they are electroplated. For one LCPS (silver LCPS) the number of sputter cycles is increased to get a sufficient wall thickness for the RF wave (about 1 µm, see Chapter 4.3.1) without the electroplated copper. This LCPS was then covered with a two-component epoxy to get a mechanically stable LCPS that can be tested.

For both, the copper and the silver LCPS, electrode films with soldered wires and monitoring pads are chosen. The soldering pads lie within the waveguide walls.

The split block LCPS is the intended version for first measurements to get a better understanding of the different influence factors. The LCPS core assembly used for the split block has no soldered wires but is controlled through the monitoring pads.

5.2.1 Transmission

Figure 47 shows the transmission of the three different versions of the LCPSs with an electric biasing in the vertical (V) and the horizontal (H) direction. All measurements are conducted with the LC *GT5-26001*. The gray areas mark the intended frequency bands for ISLs (23.0 GHz to 23.5 GHz and 27.0 GHz to 27.5 GHz).

Between 22 GHz and 26 GHz, the transmission of the copper LCPS (blue) is undulating. In contrast to this frequency dependency, the silver LCPS (red) is almost constant in the same frequency range (about -4.0 dB for the vertical and -5.8 dB for the horizontal biasing field). From 26 GHz to 30 GHz both LCPSs show a similar, almost constant transmission. Above 30 GHz the transmission of the silver LCPS is decreasing whereas the copper LCPS shows an alternating dependency.

Between 22 GHz and 28 GHz, the split block LCPS (yellow) shows a similar behavior as the silver LCPS only at about -2.8 dB for the vertical and -4.2 dB for the horizontal biasing field. The transmission is slightly decreasing to lower frequencies. Above 28 GHz the transmission starts alternating and decreasing.

The difference in transmission between the two states of the biasing field is about 1.4 dB for the split block LCPS, about 1.6 dB for the copper LCPS and about 1.8 dB for the silver LCPS.

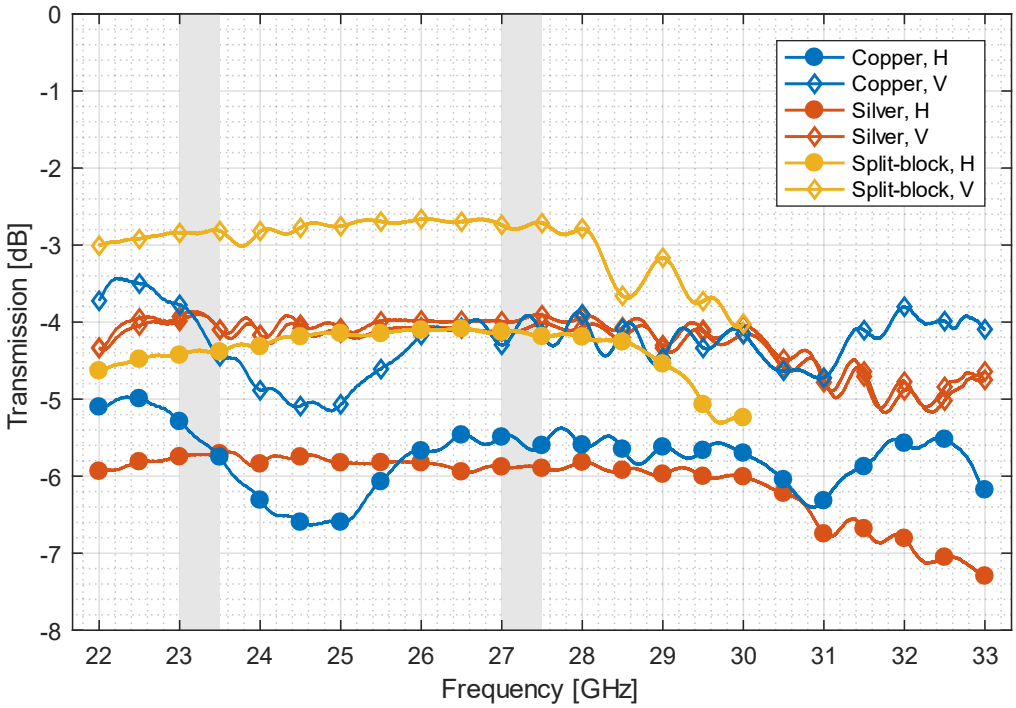

Figure 47: Comparison of the transmission, *GT5-26001*

Table 25 shows the transmission values for selected frequencies. The difference in transmission between the copper LCPS and the split block LCPS is between -0.9 dB and -1.6 dB (V) and -0.9 dB and -1.4 dB (H). For the silver LCPS the same comparison leads to: -1.1 dB to -1.3 dB (V) and -1.3 dB to -1.8 dB (H).

Table 25: Comparison of the transmission for select frequencies, *GT5-26001*

	23.0 GHz		23.5 GHz		27.0 GHz		27.5 GHz	
	V	**H**	**V**	**H**	**V**	**H**	**V**	**H**
Copper	-3.8 dB	-5.3 dB	-4.4 dB	-5.8 dB	-4.3 dB	-5.5 dB	-4.2 dB	-5.6 dB
Silver	-3.9 dB -4.0 dB	-5.8 dB	-4.1 dB -4.1 dB	-5.7 dB	-4.0 dB -4.1 dB	-5.9 dB	-3.9 dB -4.0 dB	-5.9 dB
Split block	-2.8 dB	-4.4 dB	-2.8 dB	-4.4 dB	-2.7 dB	-4.13 dB	-2.7 dB	-4.2 dB

5.2.2 Reflection

Figure 48 and Figure 49 show the reflection of the three LCPS versions for a vertical and a horizontal alignment of the biasing field.

For the vertical biasing field between 25.4 GHz and 28.4 GHz, the silver LCPS and the split block LCPS have a similar curve progression whereas the copper LCPS has higher maxima. The silver and the split block LCPSs show maximum reflection values below -20 dB in the frequency regions from 22.2 to 23.2 GHz and from 25.5 to 27.0 GHz. The absolute maxima within the measured frequency range are -9 dB at 28.5 GHz for the split block LCPS, -10.5 dB at 31.2 GHz for the silver LCPS and -10 dB at 28.2 GHz for the copper LCPS.

In the horizontal biasing case, the values of the copper LCPS are slightly lower (maximum -12.5 dB at 28.6 GHz). The absolute maximum for the silver LCPS is -12.5 dB at 31.1 GHz and for the split block LCPS it is -14 dB at 29.6 GHz.

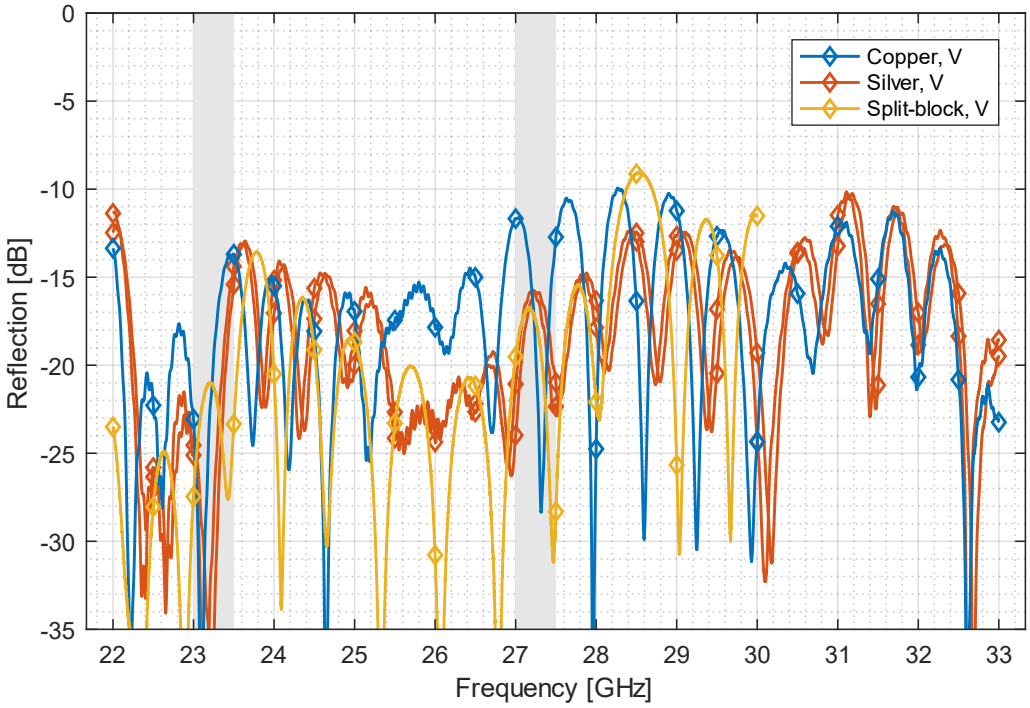

Figure 48: Comparison of the reflection, V, *GT5-26001*

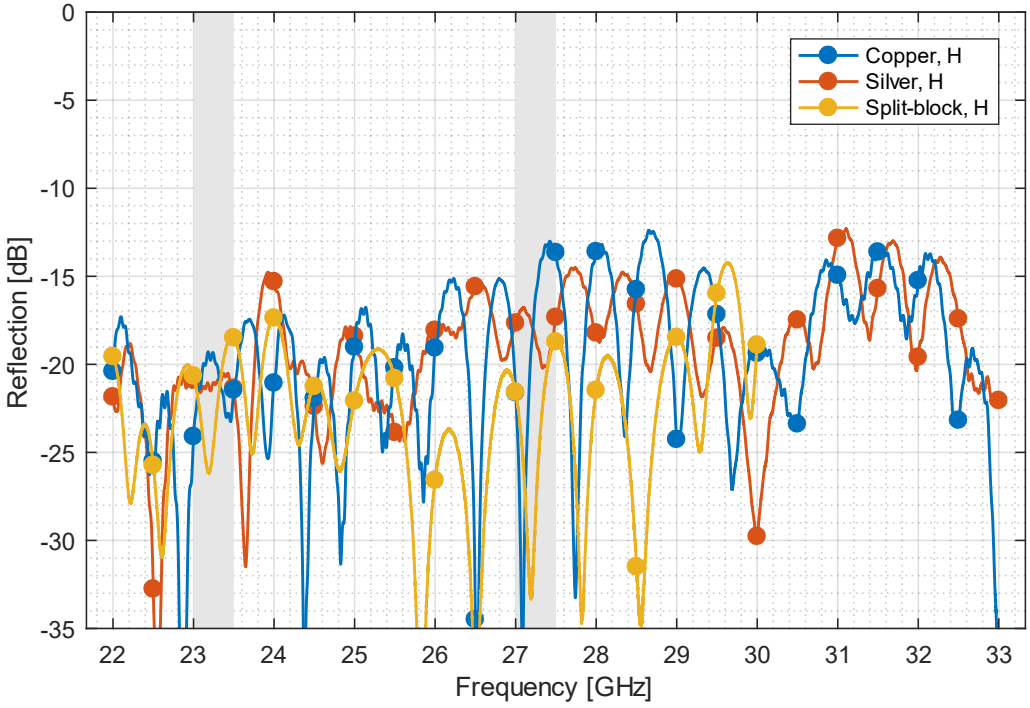

Figure 49: Comparison of the reflection, H, *GT5-26001*

5.3 Temperature Dependency

The temperature dependent measurements are conducted in three campaigns. The measurements are carried out in two days for campaign 1 & 3 and three days for campaign 2. In campaign 1 & 2 the LC *GT5-26001* is tested and in campaign 3 the LC *GT3-23002* is tested.

Campaign 2, day 1 is not shown in the following because the focus of these measurements is different (first phase over voltage tests).

The measurements for the 27 GHz to 27.5 GHz band are shown in Appendix F, except of the time-dependent behavior (measured at 23 GHz only).

5.3.1 Transmission

Figure 50 shows the transmission (S_{21}) of the LCPS (LC: *GT5-26001*) over temperature for the lower frequency band (23 GHz to 23.5 GHz). The blue markers show the transmission for a horizontal electric field for campaign 1. The red markers show the transmission for a vertical electric field for campaign 1. The yellow and violet markers show the same field orientations for campaign 2.

On day 2 of campaign 1, the LC was solidified. The LC was heated up in the test setup to about 100 °C. This process was supposed to get the LC back to the nematic state but was not sufficient. Higher temperatures would have been necessary but critical for some of the other materials used in the setup. The phase range is comparable to the one measured before the solidification, but the transmission and reflection are still affected. Therefore, the results from campaign 1 / day 2 are not representative.

Disregarding the measurements from campaign 1 / day 2, the transmission losses increase with temperature. For the horizontal case the transmission degrades with approximately 0.036 dB/K and for the vertical case the transmission degrades with 0.025 dB/K. Because of this difference, the transmission anisotropy increases with higher temperatures.

Figure 51 shows the transmission for the same frequency range than Figure 50, but the LCPS is filled with *GT3-23002* instead of *GT5-26001*. The green markers show the horizontal orientation of the electric field and the light blue markers show the vertical orientation.

This LC shows higher losses and the temperature dependency is also more distinctive. The transmission anisotropy is larger as is the variation of the transmission at constant temperatures. For the horizontal case the transmission degrades with approximately 0.053 dB/K and for the vertical case the transmission degrades with 0.030 dB/K. The transmission anisotropy increases with higher temperatures.

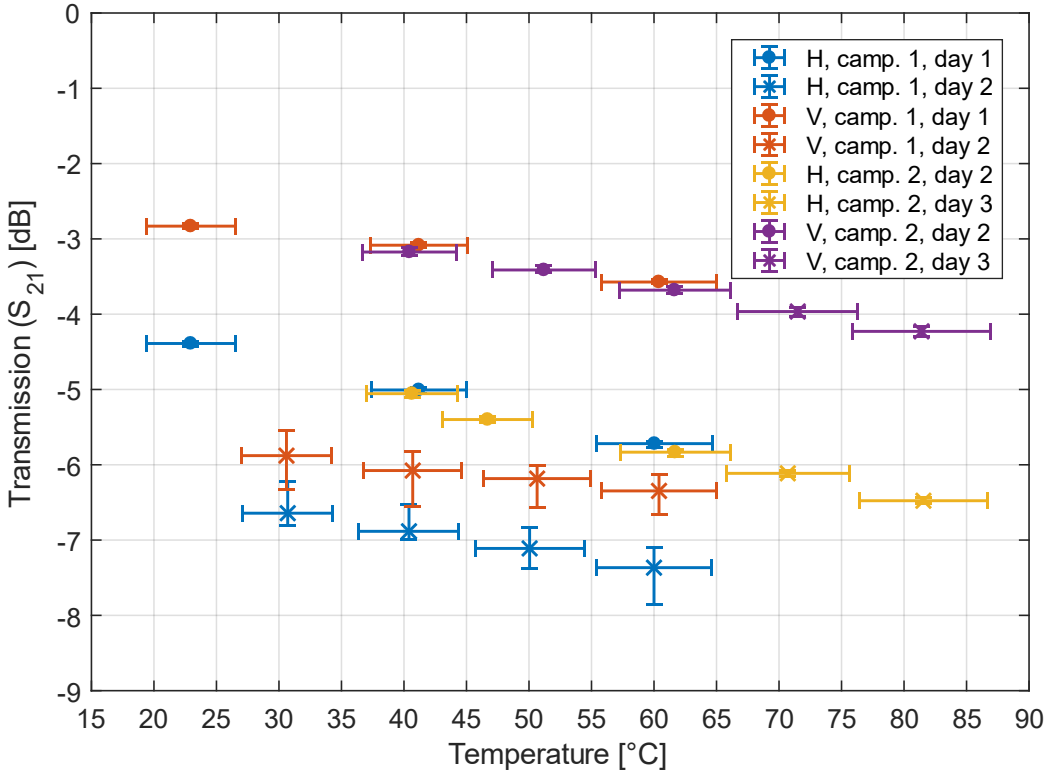

Figure 50: Transmission (S_{21}) over temperature, 23 to 23.5 GHz, *GT5-26001*

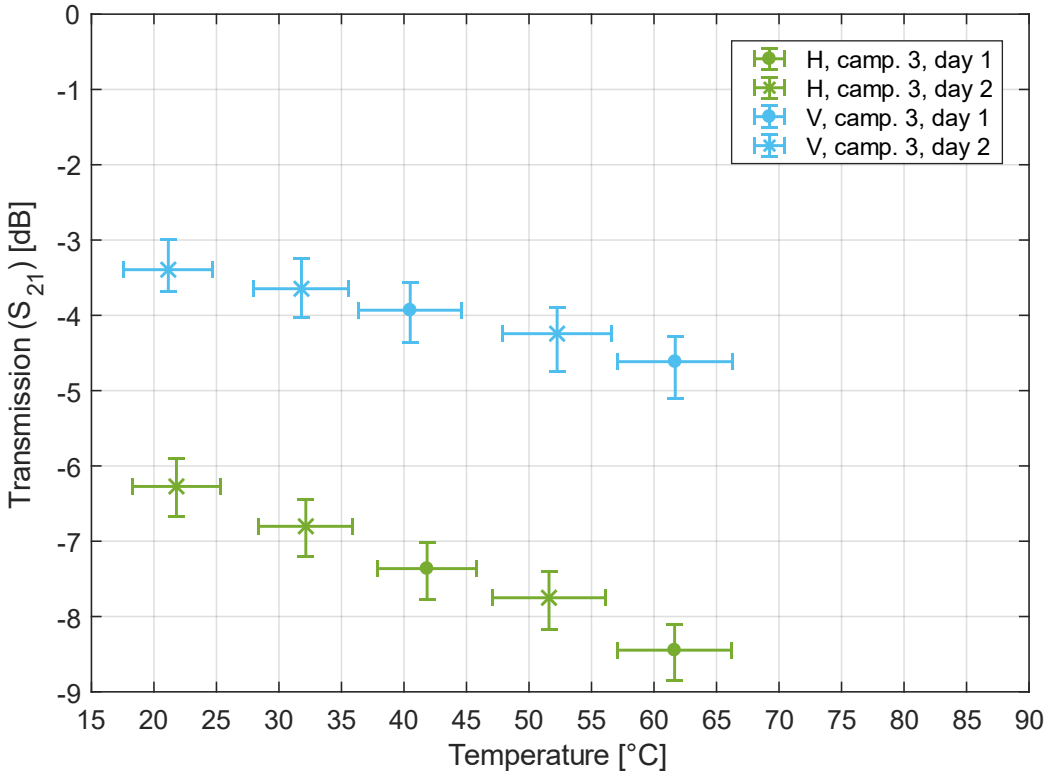

Figure 51: Transmission (S_{21}) over temperature, 23 to 23.5 GHz, *GT3-23002*

5.3.2 Reflection

Figure 52 shows the reflection (S_{11}) of the LCPS (LC: *GT5-26001*) over temperature for the lower frequency band (23 GHz to 23.5 GHz). Disregarding the measurements from campaign 1 / day 2 (see Chapter 5.3.1), the mean reflection level is almost constant over the temperatures measured. The spreading width of the reflection value increases for higher temperatures but also varies between different measurements at the same temperature. The maximum reflection level is below -15 dB at about 82 °C.

The reflection of *GT3-23002* is not measured because a different calibration method is used (response calibration) to simplify the time-dependent measurements. This calibration however does not include the calibration of the reflection measurements.

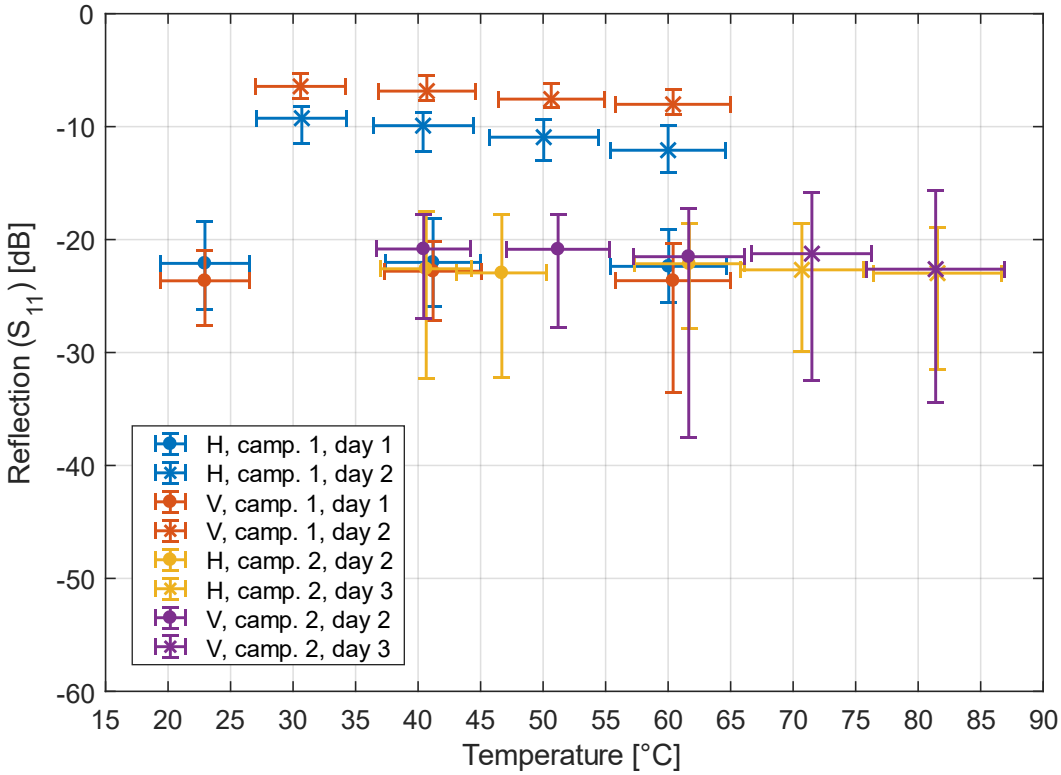

Figure 52: Reflection (S_{11}) over temperature, 23 to 23.5 GHz, *GT5-26001*

5.3.3 Phase shift

Figure 53 shows the differential phase over temperature for both LCs (*GT5-26001*: campaign 1 and 2, *GT3-23002*: campaign 3).

The variations in the measurements for *GT5-26001* and especially the low total phase shift (412.6°) for the measurement at around 20 °C can be explained with the slow reaction time at low temperatures. The measurement is optimized to measure the phase jumps and the time for each measurement is chosen to cover the fast bit of the jump and a minimum of 360° phase change. The entire phase range of an LCPS is only of interest for a static application where each LCPS can settle over a long period of time. The values for campaign 1 day 2 show the differential phase after the solidification (see Chapter 5.3.1).

For *GT5-26001* the differential phase is above or close to 400° whereas the *GT3-23001* LC only accomplishes 360° at 20 °C. Both LCs show a temperature dependent differential phase with decreasing values for higher temperatures.

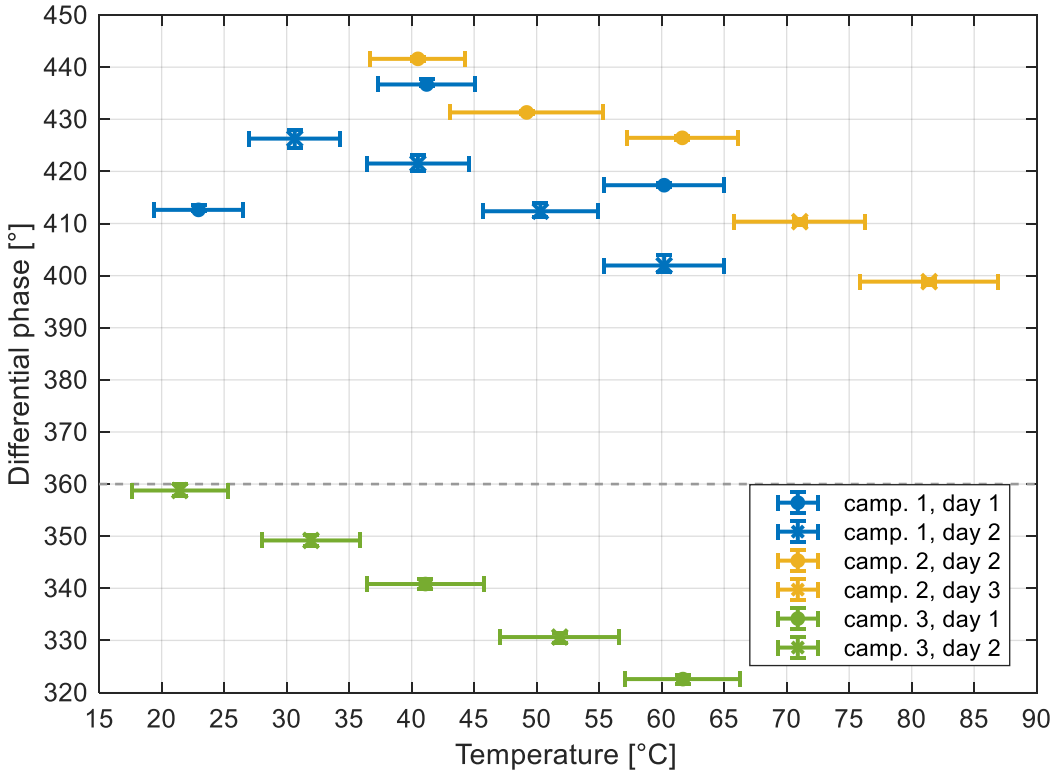

Figure 53: Differential phase over temperature, 23 to 23.5 GHz, *GT5-26001* (camp. 1 & 2) and *GT3-23002* (camp. 3)

Figure 54 shows the relative phase over temperature for both LCs (*GT5-26001*: campaign 1 and 2, *GT3-23002*: campaign 3). Each campaign has one reference measurement that is symmetric around the 0° phase level. For campaign 1 & 3 the reference measurement is at about 20 °C and for campaign 2 it is the measurement at 40 °C (Campaign 1 day 2 - after the solidification, see Chapter 5.3.1).

Especially for campaign 2 & 3 the temperature dependency for small phase shifts is different to the dependency for large phase shifts. For campaign 1 this is not as obvious because of the low total phase shift at 20 °C.

The increase of the phase to higher temperatures of the large phase shift in campaign 2 is approximately 0.27 °/K and the increase of the small phase is approximately 1.30 °/K. In campaign 3 the increase of the

phase to higher temperatures of large phase is approximately 0.11 °/K and of the small phase approximately 1.02 °/K. Because of this anisotropy, the total phase shift decreases and the middle phase / phase level increases.

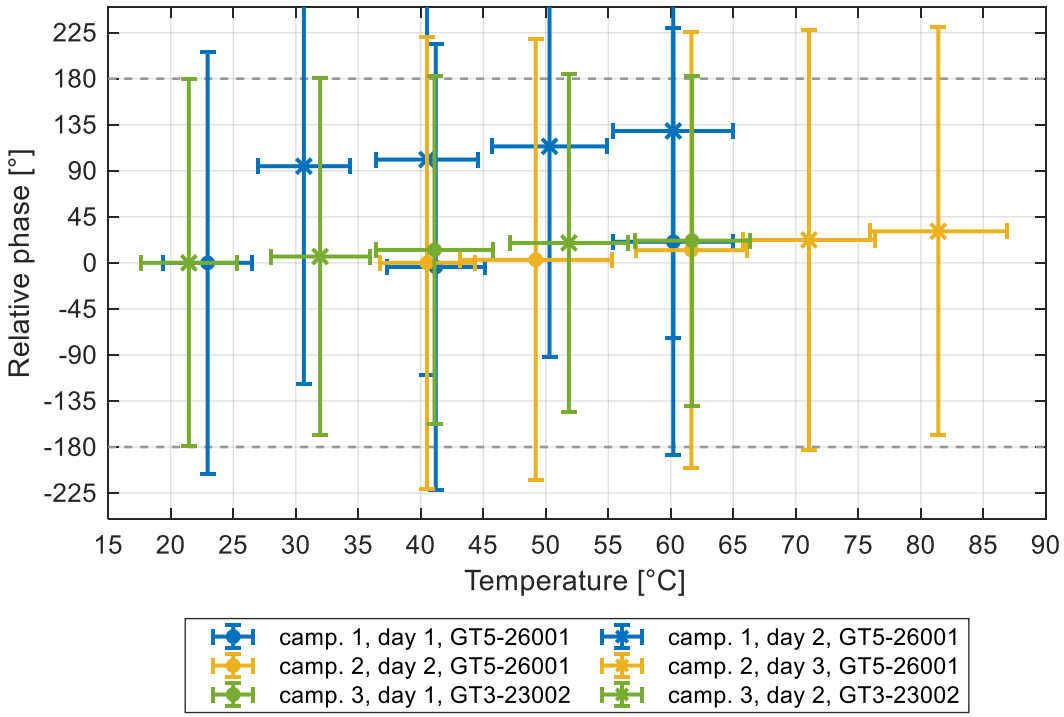

Figure 54: Relative phase over temperature, 23 GHz, *GT5-26001* and *GT3-23002*

5.3.4 Figure of Merit

Figure 55 shows the figure of merit for both LCs (*GT5-26001*: campaign 1 & 2, *GT3-23002*: campaign 3) for the frequency band from 23 GHz to 23.5 GHz (see Appendix G for comparison with other LCPSs).

The figure of merit for *GT5-26001* (again without campaign 1 / day 2) is between 94 °/dB at 20 °C and 62 °/dB at 80 °C. The figure of merit for *GT3-23002* is between 57 °/dB at 20 °C and 38 °/dB at 60 °C but shows larger variations.

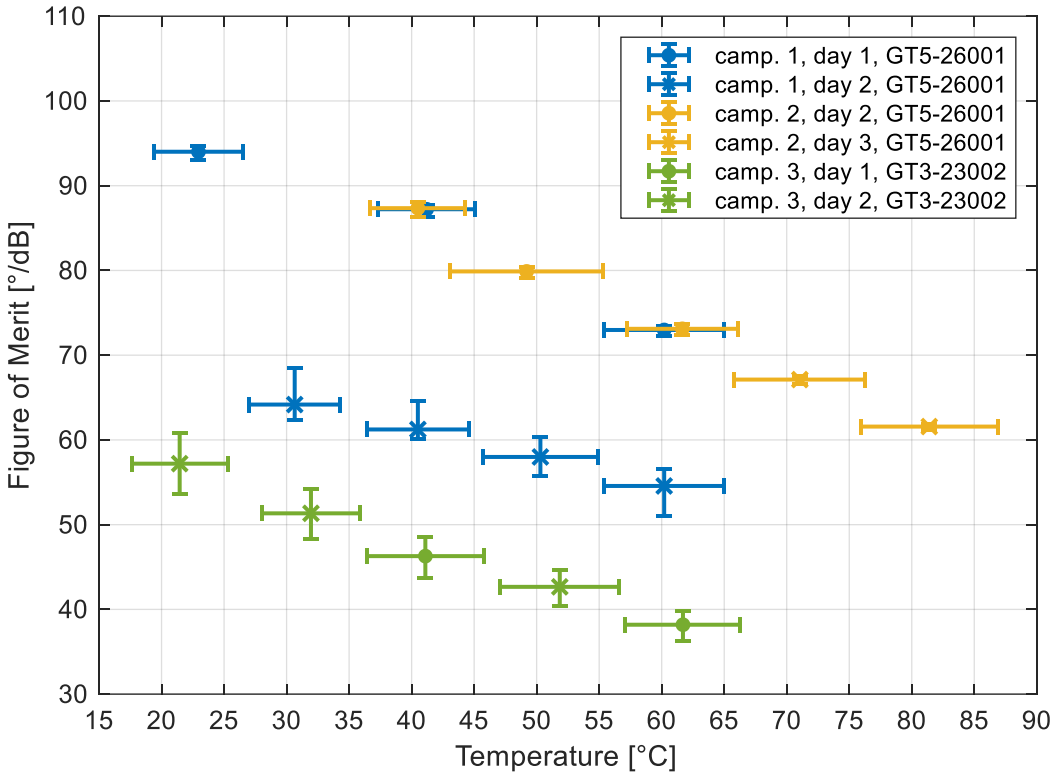

Figure 55: Figure of Merit over temperature, 23 to 23.5 GHz, *GT5-26001* and *GT3-23002*

5.3.5 Time-Dependent Behavior

Figure 56 shows the maximum phase change rate for a phase jump from the vertical to the horizontal orientation of the LC and Figure 57 shows the maximum phase change rate for a phase jump from the horizontal to the vertical orientation of the LC over temperature for 23 GHz.

For both LCs the maximum phase change rate increases with temperature but the phase change rate of *GT3-23002* is significantly higher and the value at 20 °C is about the same as the value at 60 °C for *GT5-26001*.

The maximum phase change rate for *GT5-26001* increases by a factor of 12 from 20 °C (9 °/s) to 80 °C (111 °/s) for H to V and by a factor of 11 for V to H (4 °/s to 42 °/s). From 20 °C to 60 °C the factor is 6.5 for both directions. For *GT3-23002* the factor is 3.5 from 20 °C (29 °/s; 76 °/s) to 60 °C (103 °/s; 261 °/s) for both directions.

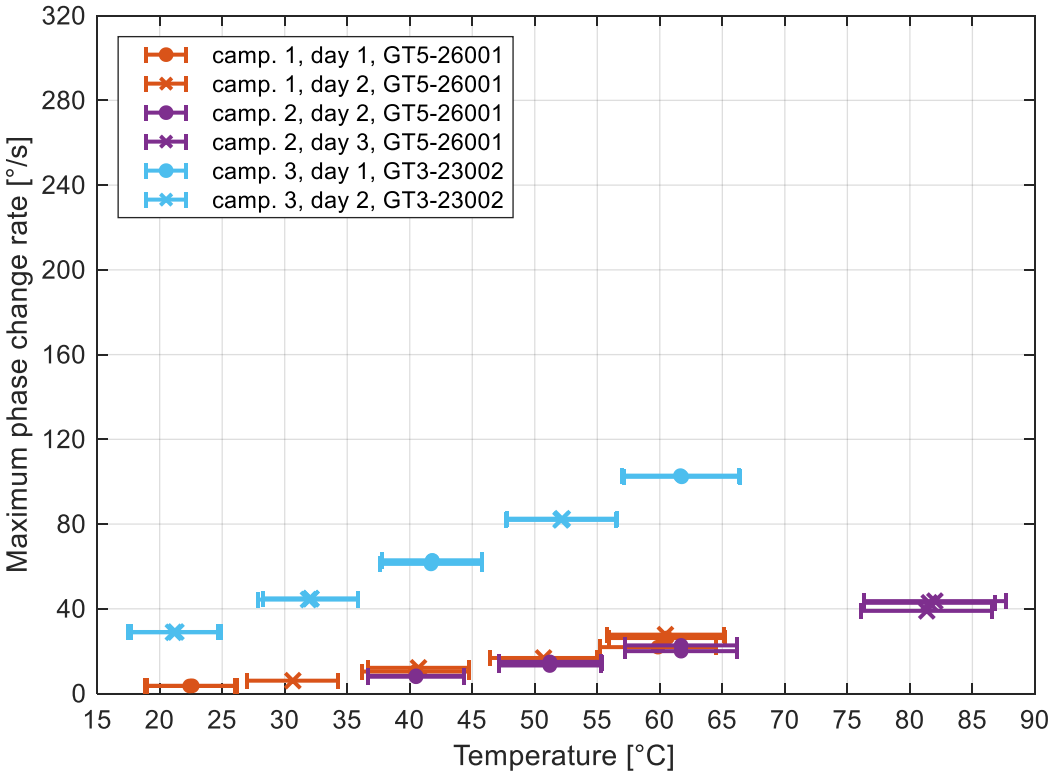

Figure 56: Maximum phase change rate (V to H) over temperature, 23 GHz

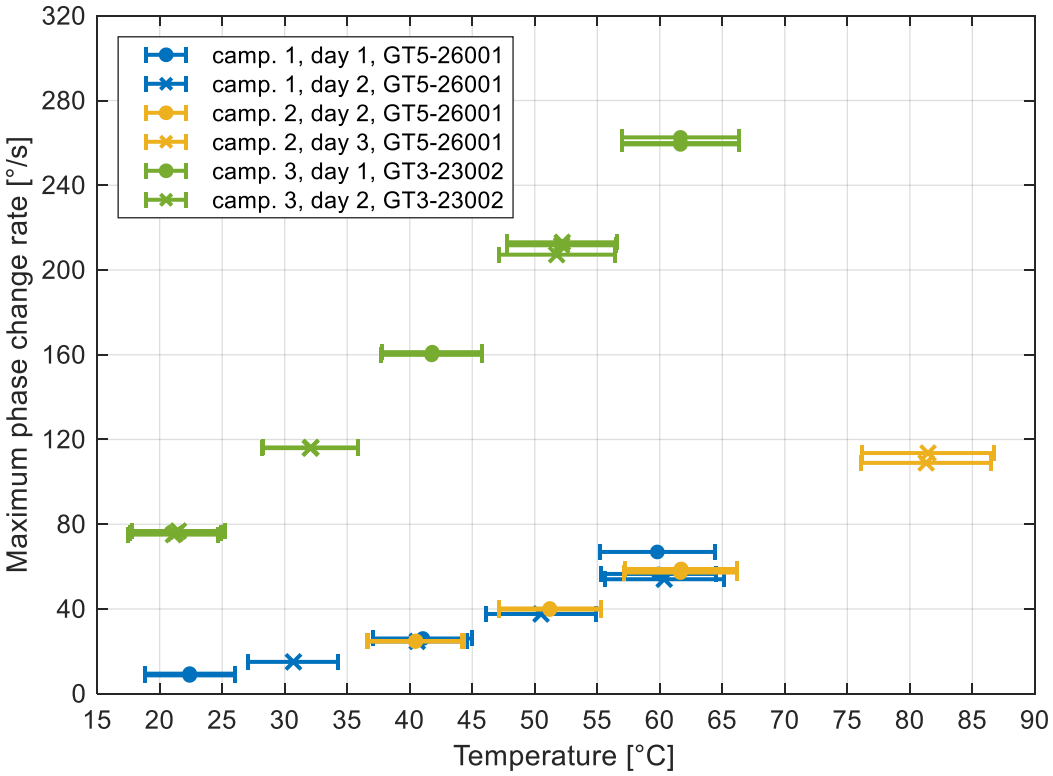

Figure 57: Maximum phase change rate (H to V) over temperature, 23 GHz

Figure 58 shows the minimal phase jump time for a 360° phase change over temperature. This figure shows the data only for *GT5-26001* because when the LCPS is filled with *GT3-23002* it reaches 360° only for 20 °C. The plotted value is the integral over the largest phase change rates over time until 360° phase change is reached.

The minimal phase jump time decreases from 20 °C to 80 °C by a factor of about 9 and the time for the slow direction (V to H) is about twice as long as for the fast direction (H to V).

The complete phase variation with time can be found in Appendix H.

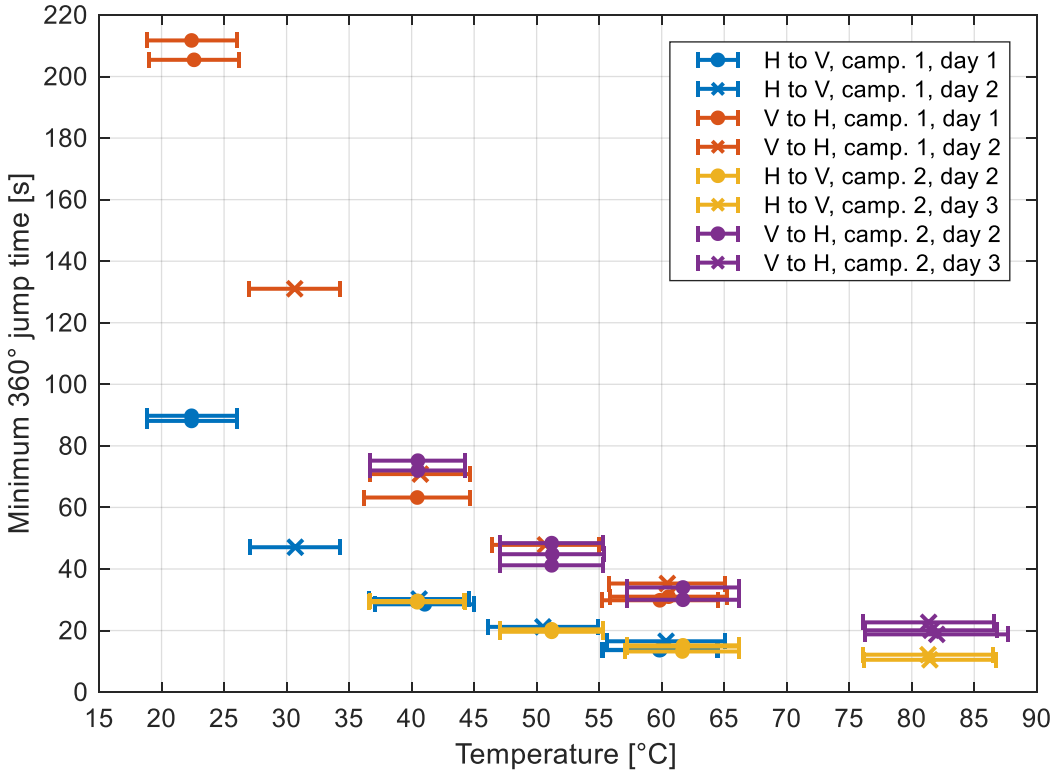

Figure 58: Minimal jump time for 360° over temperature, 23 GHz, *GT5-26001*

5.4 Phase over Voltage

The phase over voltage measurement is the calibration for the LCPS. Since the phase cannot be measured within the antenna array, this curve is used to adjust the desired phase for each LCPS.

This measurement is only performed with *GT3-23002* because of the solidification problem with *GT5-26001*. The phase over voltage measurement and the 4x1 array measurements take some time and a solidification, and a possible change in the behavior of LCPS is not desirable.

The measurement does not provide an absolute phase through the device under test. By measuring the phase over several frequencies, the network analyzer can calculate phases in a range larger than 360° but the absolute phase is still unknown.

Because the measurement does not provide an absolute phase it is important to start the measurement for each LCPS with the same orientation of the electric field. This ensures, that the relative phases between the four LCPSs are correct, since it is improbable that the phases of the four LCPSs will vary more than 360° for the same LC alignment / biasing field orientation.

For the use in the antenna array, only the relative phases between the LCPSs are relevant. The 'zero' level of the phase can thereby be set by the user.

The phase measurements are conducted between 22 GHz and 30 GHz with steps of 1 MHz. Since the measurements of the 4x1 array are performed at 23 GHz only the measured phases at this frequency are used to steer the antenna. However, it would be possible to get a phase over voltage over frequency look-up table, to calculate the desired voltages for the LCPSs.

In addition to these measurements, the electric biasing field of the two electrode films is also simulated in *COMSOL Multiphysics®*. This simulation helped to define the voltages for the first phase over voltage measurements and could further be used to refine the phase over voltage curve without the necessity of further, time consuming measurements. A description of this model can be found in Appendix I.

The aim of this simulation is to reproduce the progression of the phase over voltage curve without a complex simulation to calculate the phase directly. Therefore, a simplified model of the cross-section is used to get the electric biasing field distribution for several commanded voltages.

The influence of the changing field distribution on the phase change is assessed by integrating the change of the relative permittivity within the area of the LC (area integral). In theory, the permittivity of the LC can be simplified by an elliptic model with the extreme states as the major axis and minor axis ($\varepsilon_{\parallel}$ and $\varepsilon_{\perp}$, see Chapter 2.2). With this LC model and the direction of the electrical biasing field from the simulation, a first estimation of the phase over voltage curve progression can be calculated.

In addition, this integral can be improved by taking more influences into account. One option is for instance the distribution of the electric field strength of the TE wave that is influenced by the LC or the gradient of the biasing field.

The integration of the field direction itself is performed in *MATLAB*.

5.4.1 Measurement Results

Figure 59 shows the relative phase over the commanded voltage for all four LCPSs.

The LCPSs are fitted with two different types of electric films. Two are fitted with electrode films that are lead through the waveguide wall to the outside where cables are soldered to pads on the electrode films to connect them to the power supply (marked with 'el. film'). The other two LCPSs are fitted with electrode films that have soldering pads within the waveguide. Two cables for each film are soldered to these pads and lead through the waveguide wall (marked with 'cable').

The 'zero' level in the plot is chosen to be in the middle between the lowest maximum phase (blue curve on the left) and the highest minimum phase (green curve on the right) measured for all four LCPSs. This level is used in the first measurement campaign with the 4x1 array. With this level, the range of all LCPSs is limited to less than ±180°.

For the second measurement campaign with the 4x1 array, the 'zero' level was shifted (+9.5°) to enable a phase shift of ±180° at the phase shifters mounted at the borders of the array (LCPS 1 and 4). The phase shifters mounted at the inner positions are thereby limited to a range smaller than 360° which does not affect the array performance in the desired steering range.

Three of the four LCPSs show a similar behavior over the commanded voltage, only LCPS 3 has an offset and a rising phase from -164 V to -130 V. The split block used for LCPS 3 is also used in the temperature dependent measurements (where a similar behavior occurred), but the electrode films and the body with LC cavity is changed between these two measurements.

The commanded voltage of +164 V corresponds to a vertical (V) electric field and -164 V corresponds to a horizontal (H) electric field.

Figure 60 shows the phase change per commanded voltage over the commanded voltage for each LCPS. Since the step size of the power supply is 1 V this graph shows the phase step for each commanded voltage. The maximum phase step size is about 2.5°.

Figure 61 shows the transmission (S_{21} / S_{12}) over the commanded voltage. The two LCPSs with the lead through of the electrode film show lower losses than the two LCPSs with soldering pads on the inside of the waveguide.

Figure 62 shows the reflection (S_{11} / S_{22}) over the commanded voltage. The reflection is below -20 dB for most of the LCPSs except for LCPS 3, where S_{22} is slightly above -20 dB for commanded voltages between -164 V and -70 V.

The progression of the transmission over voltage is inverse to the relative phase over voltage. The behavior of the transmission over the relative phase is linear (the transmission degrades to higher relative phases).

The phase over voltage behavior for 27.5 GHz is shown in Appendix J.

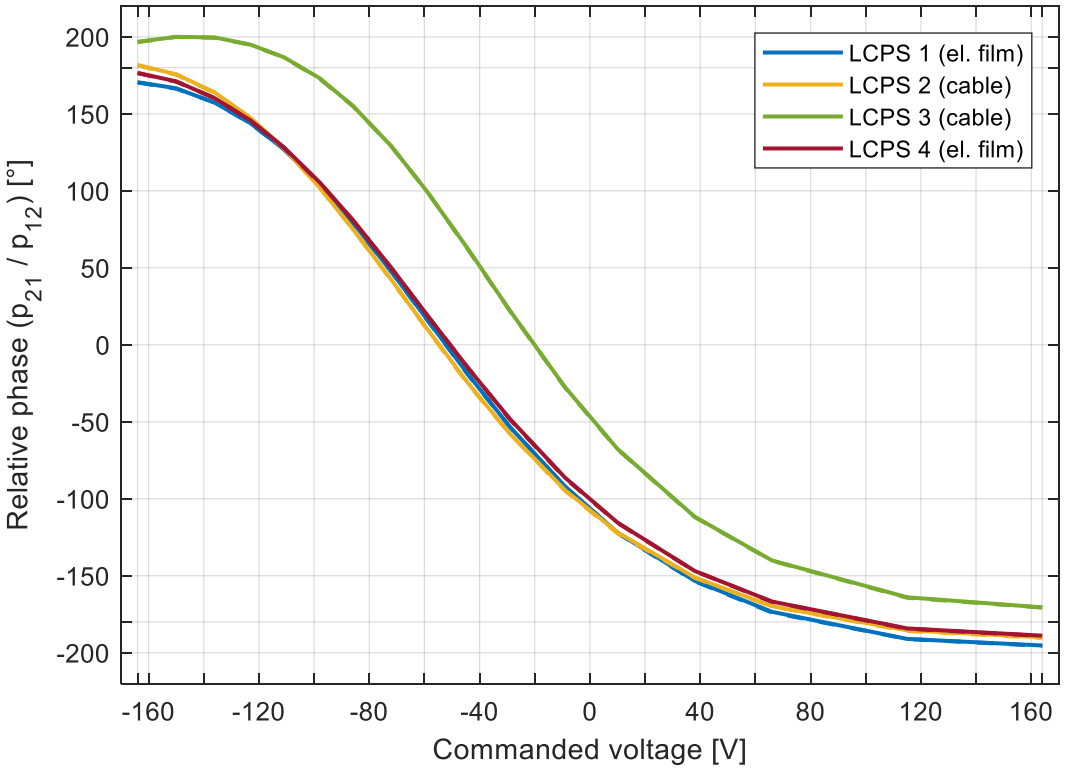

Figure 59:Phase over voltage (p_{21} – solid, p_{12} – dashed), 23 GHz, *GT3-23002*

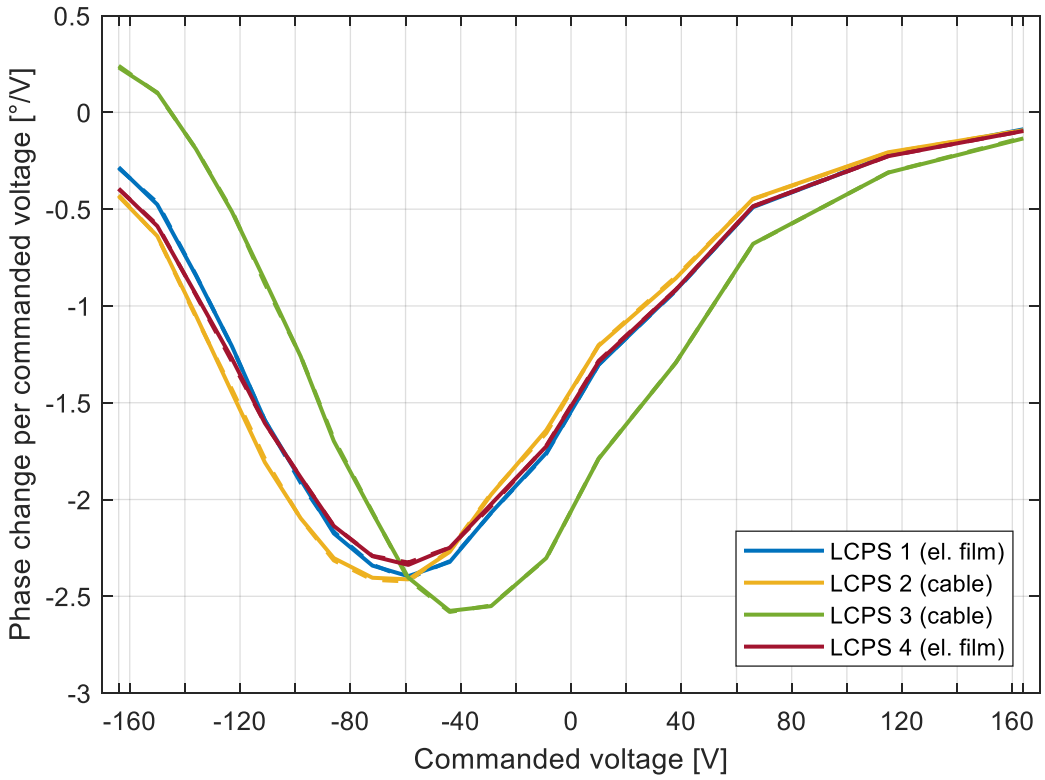

Figure 60: Phase change per commanded voltage (p_{21}/U– solid, p_{12}/U– dashed), 23 GHz, *GT3-23002*

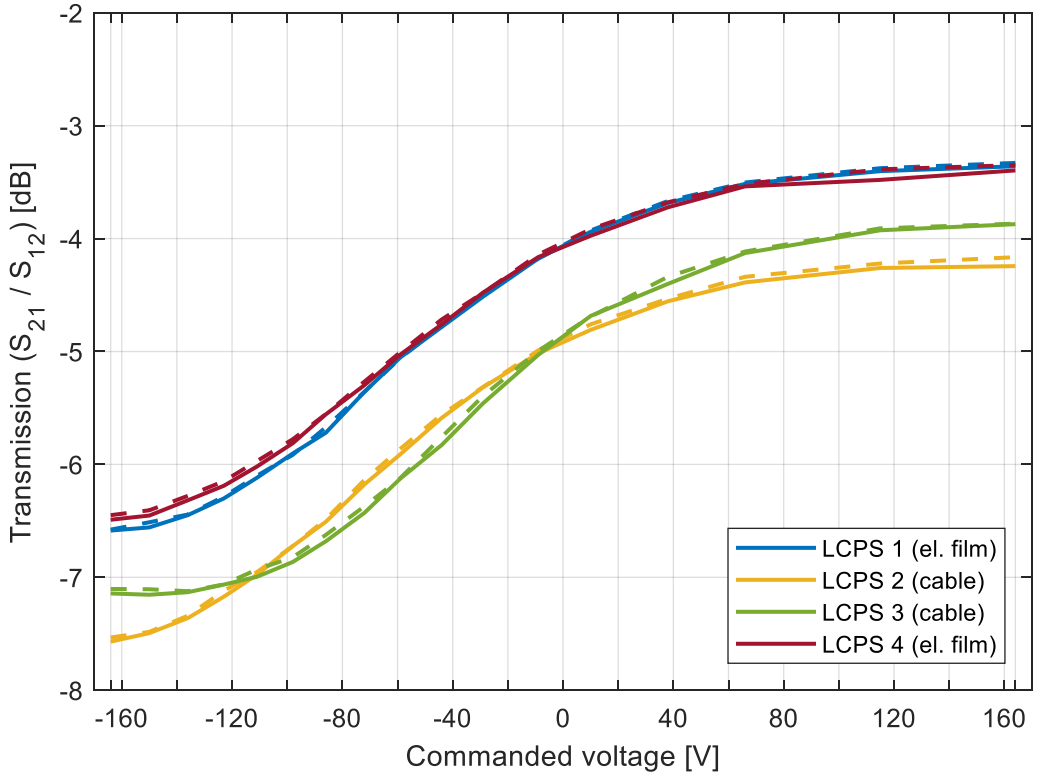

Figure 61: Transmission over commanded voltage (S_{21} – solid, S_{12} – dashed), 23 GHz, *GT3-23002*

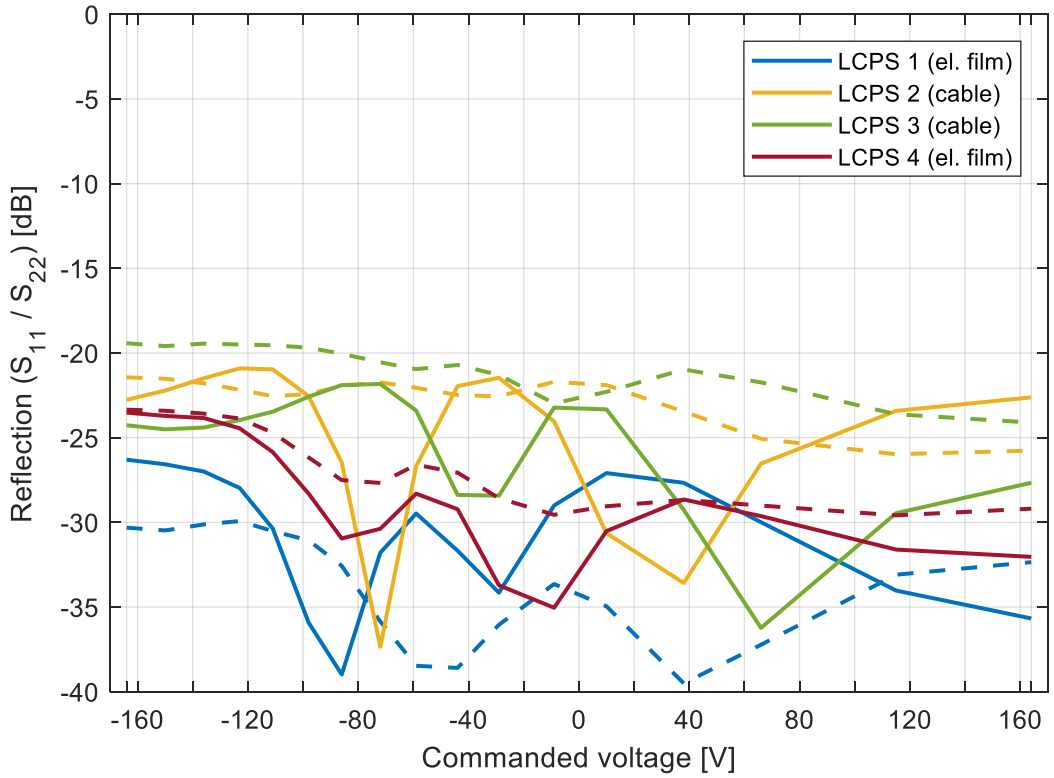

Figure 62: Reflection over commanded voltage (S_{11} – solid, S_{22} – dashed), 23 GHz, *GT3-23002*

5.4.2 Simulation Results

Figure 63 shows the electric biasing field within the LC cavity. The black lines are equipotential lines to illustrate the distortion of the electric field towards the top and the bottom of the LCPS. In the center of the cavity the gradient of the field has an angle of about 45° relative to the vertical.

This state illustrates that the electric biasing field and the hereby oriented liquid crystals have no homogeneous orientation for all commanded voltages.

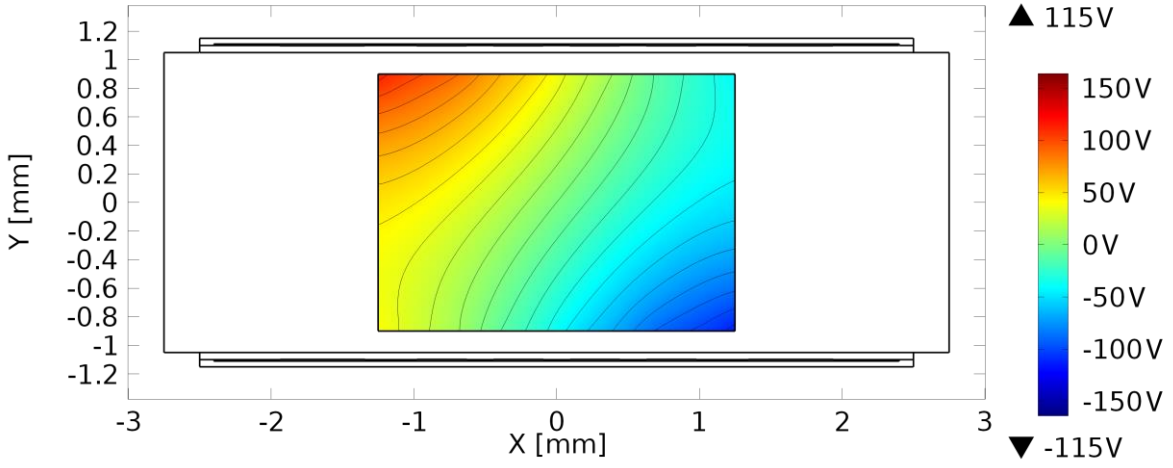

Figure 63: Electric field directions for an electric field angle of 45° in the center

Figure 64 shows normalized values over the commanded voltage. For the LCPSs the normalized value is the relative phase of each phase shifter. The phases are normalized by the maximum and minimum value of each phase shifter. Method 1 & 2 are two surface integrals within the simulated LC cavity. Both are also normalized with their maximum and minimum values.

Since the simulation uses a finite number of triangles the surface integral is approximated by a sum. The director of the LC is rotated according to the direction of the field to get the correct permittivity from the tensor (see equation (2-14)). For method 1 & 2, the y-component (see Figure 9) is multiplied with the normalized area of each cell and these products are then summed up over the area of the LC cavity. In method 2 the product for each cell is extended with the sinusoidal distribution ($[0, \pi]$) along the x-direction of the waveguide (see Chapter 2.3).

In *COMSOL Multiphysics*® the permittivity of the LC is set constant, therefore the influence of the tensor on the biasing field (electric displacement) is disregarded. The surface integral (sum) is calculated in *MATLAB.*

The curve progressions for method 1 & 2 are almost identical. The progressions of these two curves and the curves of LCPS 1, 2 and 4 are also similar. The maximum deviation between method 2 and each of the three LCPSs is 0.02 for LCPS 1, 0.05 for LCPS 2 and 0.03 for LCPS 4.

LCPS 3 is not regarded because of its abnormal behavior (see Chapter 5.4.1).

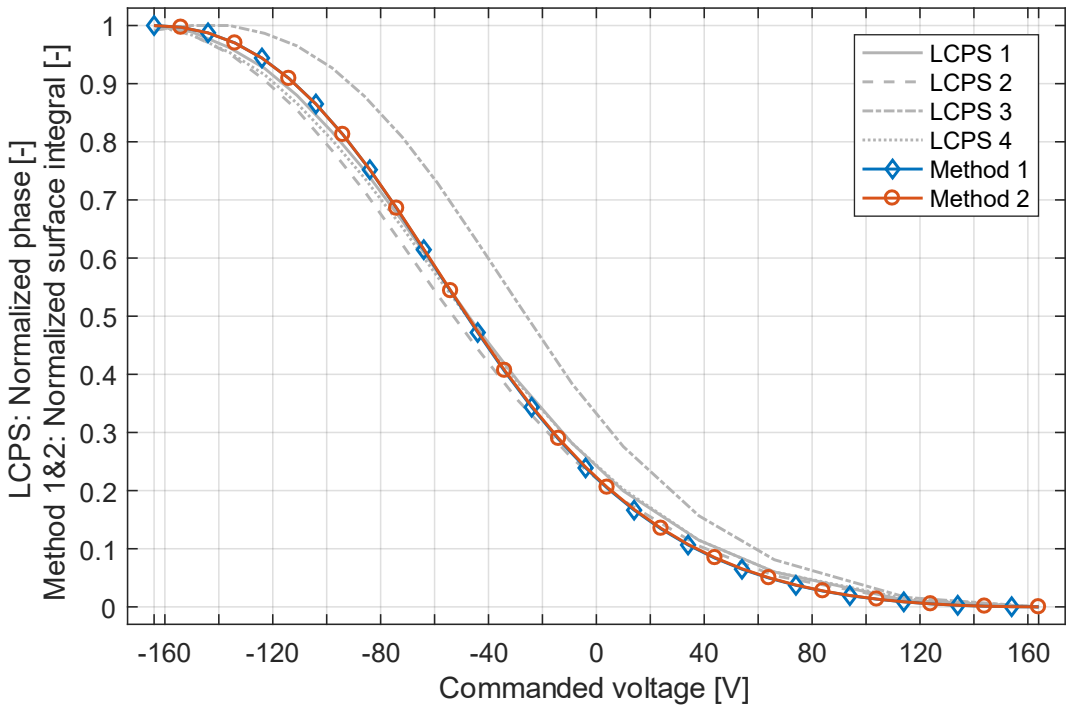

Figure 64: Normalized phase (23 GHz, *GT3-23002*) / normalized surface integral over commanded voltage

5.5 Discussion

5.5.1 Manufacturing Techniques

The transmission for the copper and silver LCPS is about -0.9 dB to -1.8 dB below the transmission level of the split block. Besides the differences of the material of the waveguide wall, there are some other differences between the split block LCPS and the two others (copper and silver LCPS):

- Different flanges
    - Copper & silver LCPS: copper flanges + copper (electroplated) waveguide transition to WR34
    - Split block LCPS: built in flanges + aluminum waveguide transition to WR34
- Different electrode films
    - Copper & silver LCPS: electrode films with soldered cables within the waveguide walls
    - Split block LCPS: electrode films without soldered cables within the waveguide walls (uses the monitoring pads to control the electric biasing field)
- Different surface and geometry of the core
    - Copper & silver LCPS: prepared for the electroplating bath and therefore the core is sealed with silicone spray
    - Split block LCPS: no sealing

Figure 65 shows the transmission values over the frequency of all four split block LCPSs measured during the calibration (phase over voltage). Two of the LCPSs are equipped with electrode films that have soldered cables within the waveguide walls (LCPS 2 & 3), the other two do not have soldered cables (LCPS 1 & 4). This measurement cannot be compared directly to the one in Chapter 5.2.1, since it is performed with a different LC (*GT3-23002* instead of *GT5-26001*). The general trend of the two LCPSs with soldered cables is, that they both have higher losses compared to the ones without cables. The behavior of LCPS 2 is significantly different to the behavior of LCPS 3. It is likely that this is not only an effect of different soldering points within the waveguide since the difference in transmission between LCPS 1 & 4 and LCPS 3 is partially smaller than between LCPS 3 and LCPS 2. Therefore, LCPS 2 is not taken into account in the following discussion.

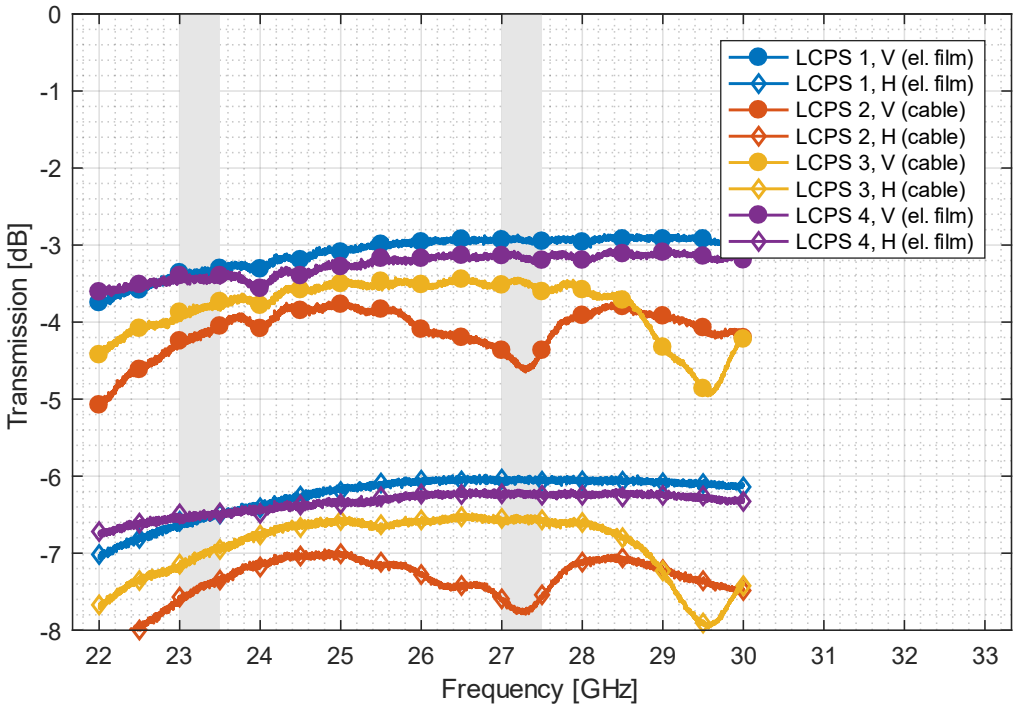

Figure 65: Influence of the soldered cables on the transmission, *GT3-23002*

Table 26 shows the transmission values for select frequencies. The differences between the two LCPSs without cables (LCPS 1 & 4) and LCPS 3 are between -0.3 dB and -0.7 dB. If this difference can be traced back to the soldered cables solely, there is still an offset between the manufacturing methods (-0.2 dB to -1.4 dB) that cannot be explained by the soldered cables.

Table 26: Comparison of the transmission for select frequencies, *GT3-23002*

	23.0 GHz		23.5 GHz		27.0 GHz		27.5 GHz	
	V	**H**	**V**	**H**	**V**	**H**	**V**	**H**
LCPS 1	-3.4 dB	-6.6 dB	-3.3 dB	-6.5 dB	-2.9 dB	-6.0 dB	-2.9 dB	-6.1 dB
LCPS 2	-4.3 dB	-7.6 dB	-4.1 dB	-7.4 dB	-4.4 dB	-7.6 dB	-4.4 dB	-7.6 dB
LCPS 3	-3.9 dB	-7.2 dB	-3.8 dB	-6.9 dB	-3.5 dB	-6.6 dB	-3.6 dB	-6.6 dB
LCPS 4	-3.4 dB	-6.5 dB	-3.5 dB	-6.5 dB	-3.1 dB	-6.2 dB	-3.2 dB	-6.2 dB

The additional losses might be induced by the silicone sealing and by residues of the electroplating bath. For the silver LCPS the electroplating bath can be excluded as an option, but in addition the thin silver wall and the conductivity between the silver wall and the copper flanges might play a role.

Not all the different causes of the additional losses can be quantified separately but together they add up to more than 0.9 dB. The undulating behavior of the copper LCPS compared to the almost constant behavior of the silver and the split block LCPS could be an effect of residues of the electroplating bath.

For the reflection measurements, the influence of the silicone sealing, the residues of the electroplating bath and the soldering points cannot be separated from one another. There are differences between the different manufacturing techniques for some frequencies, but over the measured frequency range this effect is not as definite. The most significant difference between the manufacturing techniques can be seen between

25.4 GHz and 28.4 GHz in the vertical biasing case where the reflections of the copper LCPS are significantly higher. Therefore, this might be an effect of residues from the electroplating bath.

For the horizontal biasing, the copper and the silver LCPS show higher reflections between 25.8 GHz and 29.6 GHz, whereby the copper LCPS shows even more reflections than the silver LCPS. Both, soldering points and electroplating bath could play a role.

Manufacturing inaccuracies could also cause differences between the LCPSs especially for the reflection because the absolute values are considerably smaller than the transmission values.

The current manufacturing technique of the copper LCPS with the option of soldered wires for the control of the electric biasing field causes higher losses than the split block solution that is only intended as a testing option for the laboratory. Therefore, an alternative solution to manufacture the LCPSs should be taken into account.

5.5.2 Temperature Dependency

For both LCs the transmission decreases with higher temperatures and the anisotropy between the two extreme states (H and V) increases. Assuming that the LC causes this behavior solely, the loss tangent $\tan\delta$ of the LC is the parameter of interest.

In Penirschke et al. (2004) and Mueller, Penirschke, et al. (2005) two different methods are used to measure the loss tangent $\tan\delta$ at different temperatures for two LCs, *K15* and *MDA-03-2838* (called 'novel mixture' in: Penirschke *et al.*, 2004). Since the nematic phase for *K15* only exists between 20.0 °C and 34.9 °C, the behavior of *MDA-03-2838* (nematic phase from -7 °C to +115 °C, at least) might be closer to the LCs investigated in this study.

Table 27 shows the temperature dependency of *MDA-03-2838*. A similar table in Mueller, Penirschke, et al. (2005) shows values that are not entirely plausible. Therefore, the values are taken from the graphs. Due to the fluctuations of $\tan\delta_\perp$ for the coaxial transmission line measurement around 23 GHz, the values are taken at 20 GHz.

The loss tangent $\tan\delta$ shows a temperature dependency for both extreme states (parallel and perpendicular). For the parallel alignment of the LC $\tan\delta_\parallel$ shows less temperature dependency ($\tan\delta_\parallel/T$) than the loss tangent for the perpendicular alignment $\tan\delta_\perp$ ($\tan\delta_\perp/T$).

Table 27: Temperature dependency of *MDA-03-2838*
Modified from Mueller et al. (2005) and Penirschke et al. (2004)

Temperature	Method	$\varepsilon_{r,\parallel}$	$\tan\delta_\parallel$	$\varepsilon_{r,\perp}$	$\tan\delta_\perp$	$\tan\delta_\parallel/T$	$\tan\delta_\perp/T$
26 °C	Resonator (at 35 GHz)	3.11	0.005	2.28	0.013	$2.6\cdot10^{-4}\,\frac{1}{\mathrm{K}}$	$3.1\cdot10^{-4}\,\frac{1}{\mathrm{K}}$
80 °C	Resonator (at 35 GHz)	2.85	0.019	2.24	0.030		
26 °C	Coaxial transmission line (approx. 20.0 GHz)	3.34	0.009	2.71	0.019	$1.7\cdot10^{-4}\,\frac{1}{\mathrm{K}}$	$3.0\cdot10^{-4}\,\frac{1}{\mathrm{K}}$
80 °C	Coaxial transmission line (approx. 20.0 GHz)	3.15	0.018	2.63	0.035		

The tendency for a higher temperature dependency in the perpendicular alignment compared to the dependency in the parallel alignment matches the measurements in this work. The temperature dependency of the horizontal (H) case (where the perpendicular alignment is dominant) is also higher than the dependency in the vertical (V) case (where the parallel alignment is dominant).

The measured maximum reflection increases slightly with increasing temperatures but the variations between the measurements is larger than the temperature dependency.

The differential phase shift decreases with larger temperatures. In Mueller, Penirschke, et al. (2005) it is shown that the phase shift per millimeter length for *MDA-03-2838* is also decreasing with rising temperatures (above 20 °C). In Table 27 the relative permittivity decreases with rising temperatures. The decrease depends on the orientation. For a parallel orientation the decrease is larger than for a perpendicular orientation. This is in accordance with the measured temperature dependency of the phase. Large phases experience a smaller effect. A large phase is accomplished with a horizontal (H) biasing field which corresponds with a perpendicular alignment of the LC.

The maximum figure of merit that is measured with *GT5-26001* is 94 °/dB. The same LCPS type (split block waveguide with LC-cavity) in different design stages has been measured before. A first prototype with a PTFE cavity showed a figure of merit of 100 °/dB for electric biasing at 28 GHz (lowest frequency that was measured, LC unknown, see Gaebler, Goelden, et al. (2009)). A measurement with the 2nd generation LC-cavity with 2nd generation film electrodes showed a figure of merit of 114 °/dB at 23 GHz for an electric biasing and a differential phase shift of 460° (LC: *TUD-026,* see Weickhmann, Gaebler, et al. (2013) and Weickhmann, Nathrath, et al. (2013), LC: *TUD-126* see Jost, Weickhmann, et al. (2015)). The 3rd generation LC-cavity with 3rd generation film electrodes shows the same result with 114 °/dB at 23 GHz with electric biasing and a differential phase shift of 450° (film electrodes: 708-612, LC: *GT5-26001*, see Weickhmann (2017)). The maximum insertion loss thereby is 4.0 dB compared to the 4.4 dB for the vertical (V) case in Figure 50 (at about 20 °C). The differential phase of 450° is larger than the 413° in Figure 53 (at about 20 °C). The difference in the differential phase, as mentioned in Chapter 5.3.3, can be explained in part with the holding time at the two extreme states. Due to the slow reaction time of *GT5-26001*, especially close to both extreme states, the chosen period is not sufficient to get a good estimate of the total differential phase shift potential. However, the differential phase shift that can be used in an application, especially for a dynamic steering process, is smaller than the total differential phase shift.

Further figure of merits of LCPSs with different designs can be found in Appendix G.

The phase change rate and the minimum 360° phase jump time have a strong temperature dependency. Both directions (V to H and H to V) are equally influenced by the temperature and the difference of the values for both directions are thereby only dependent on the strength of the electric biasing field.

The difference of the factor between the maximum phase change rate (factor 12 from 20 °C to 80 °C) and the minimum jump time for 360° (factor 9 from 20 °C to 80 °C) can be explained with a decreased differential phase for higher temperatures. Since the minimum jump time is always integrated over 360° a decrease in differential phase leads to an integral that gets closer to the extreme states of the phase shifter (maximum and minimum phase shift) where the reaction time is significantly slower. In principle, this could lead to an increase of the minimum 360° jump time when the differential phase gets close to 360°. The maximum phase change rate is still increasing for higher temperatures (assuming that the nematic phase still exists).

The strong temperature dependency of the maximum phase change rate and the jump time for 360° can be explained by the temperature dependent friction torque which is dependent on the rotational viscosity γ_1 (equation (2-17)). Since the rotational viscosity is temperature dependent, the friction torque and with that the reaction time of the LC changes over temperature. Figure 66 shows the rotational viscosity over temperature for different LC mixtures. The progression over the temperature is similar to the change in the maximum phase change rate over temperature.

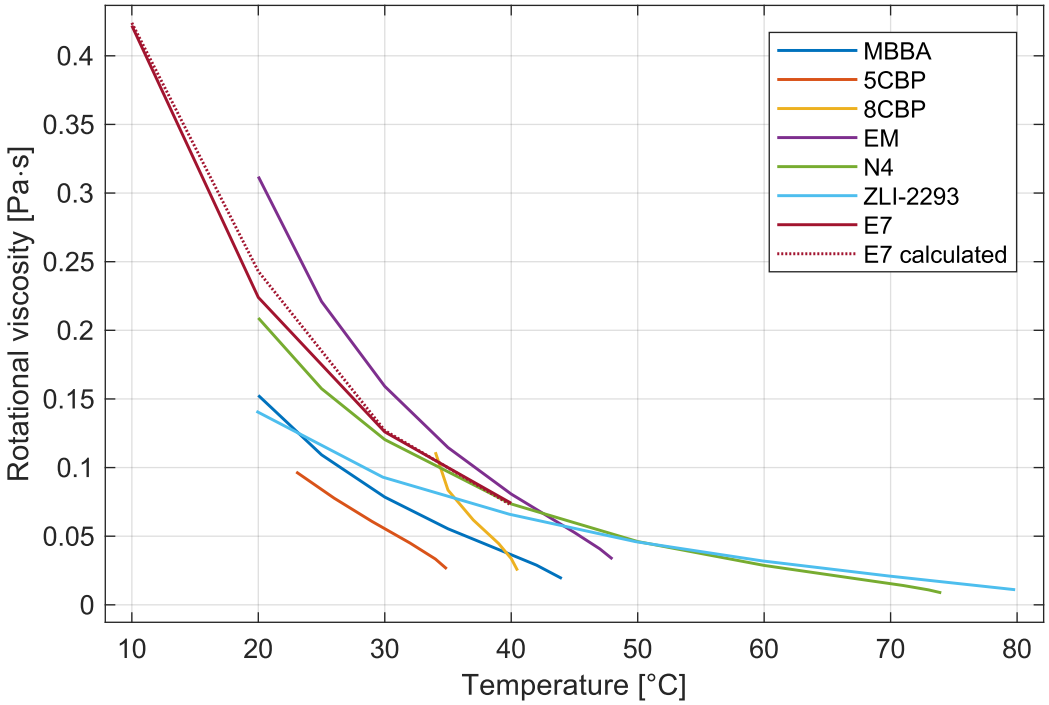

Figure 66: Rotational viscosity over temperature for different LCs
Data extracted from Kneppe, Schneider and Sharma (1982), Imai et al. (1994) and Kim et al. (2011)

Since the phase change rate of *GT3-23002* at about 20 °C and *GT5-26001* at about 60 °C are almost equal, it is likely that the rotational viscosity for both LCs is about the same.

The fact that the phase change rate can be manipulated by the temperature can be used to optimize the LC behavior for a given scenario. If the scenario is more stationary, the LC can be at lower temperatures (but still in a nematic state) with a wider phase range and lower losses. For a dynamic tracking scenario, the LC can be heated up to the desired temperature accepting the higher losses and lower phase range.

For such applications a phase over voltage calibration has to be conducted for several temperatures to get a two-dimensional look up table for each LCPS.

5.5.3 Phase over Voltage

The phase over voltage measurements show the variation of transmission, reflection and phase for different commanded voltages.

The inverse behavior of transmission over voltage compared to relative phase over voltage can be explained with the inverse behavior of the relative permittivity and the loss tangent (*GT3-23002* at 19 GHz). A rising relative permittivity leads to a decrease in the loss tangent and therefore to a better transmission. Since it also leads to a decrease in the relative phase, lower transmission losses occur at lower relative phase angles.

The phase progression over the commanded voltages is similar for LCPS 1, 2 and 4. The reason for the offset of LCPS 3 is not known for sure. LCPS 3 is the split block that was used to perform the temperature dependent measurements, where this behavior (especially the maximum phase close to -140 V instead of -164 V) could also be seen. One possible reason for this behavior is, that the mechanical process to create the holes for the thermocouples slightly changed the geometry and that both halves do not fit as intended. It is unlikely that the LC-cavity or the film electrodes play a role in this behavior, since the LC-

cavity and the film electrodes were exchanged between the temperature dependent measurements and the phase over voltage measurements.

The phase change per commanded voltage shows the maximum phase change that is induced by a change in the commanded voltage. Since the step size of the power supply is 1 V, the maximum phase step for a single step at the power supply is 2.5° at 23 GHz. This corresponds with a difference in the time delay of 0.3 ps or a propagation distance of 90.5 µm in free space (vacuum) which is 0.7 % of the wavelength. Therefore, the error caused by the step size should be negligible.

The progression of the phase over voltage can be simulated with a maximum error of 0.05. Several effects are not regarded and could lead to this error:

- Effects of the biasing field at the ends of the film electrodes (3D phase shifter instead of cross section)
- Effect of manufacturing errors such as an offset from the center line of one or both film electrodes or fluctuations in the resistance between the electrode lines (resistor network)

The effects of these errors on the performance seems to be limited, since the overall offset compared to the entire range of the phase shifter is small.

Besides the before mentioned effects that are disregarded, a further improvement could probably be achieved by including the influence of variations in the relative permittivity on the group velocity. Therefore, the change of the relative permittivity within the waveguide (as a combination of several relative relative permittivities) has to be calculated.

6 Characterization of a 4x1 Array with Liquid Crystal Phase Shifters

The measurements of the 4x1 horn antenna array are conducted in the CCR at the University of Applied Sciences Munich. The antenna is mounted on a turntable within the quiet zone of the compact range. In this zone the horn antenna array experiences far field conditions of the transmitting antenna. Figure 67 shows the compensated compact range with the two RF mirrors on the left, the transmitting horn in the back, behind the RF shielding held by ropes (middle of the picture), and the 4x1 horn antenna array on the right (on the turntable). The transmitting horn is linear polarized, therefore two measurements (vertical and horizontal polarization) have to be performed to calculate the circular polarization levels of the LISA-ES array. Two measurement campaigns were conducted whereby some of the measurements are repeated.

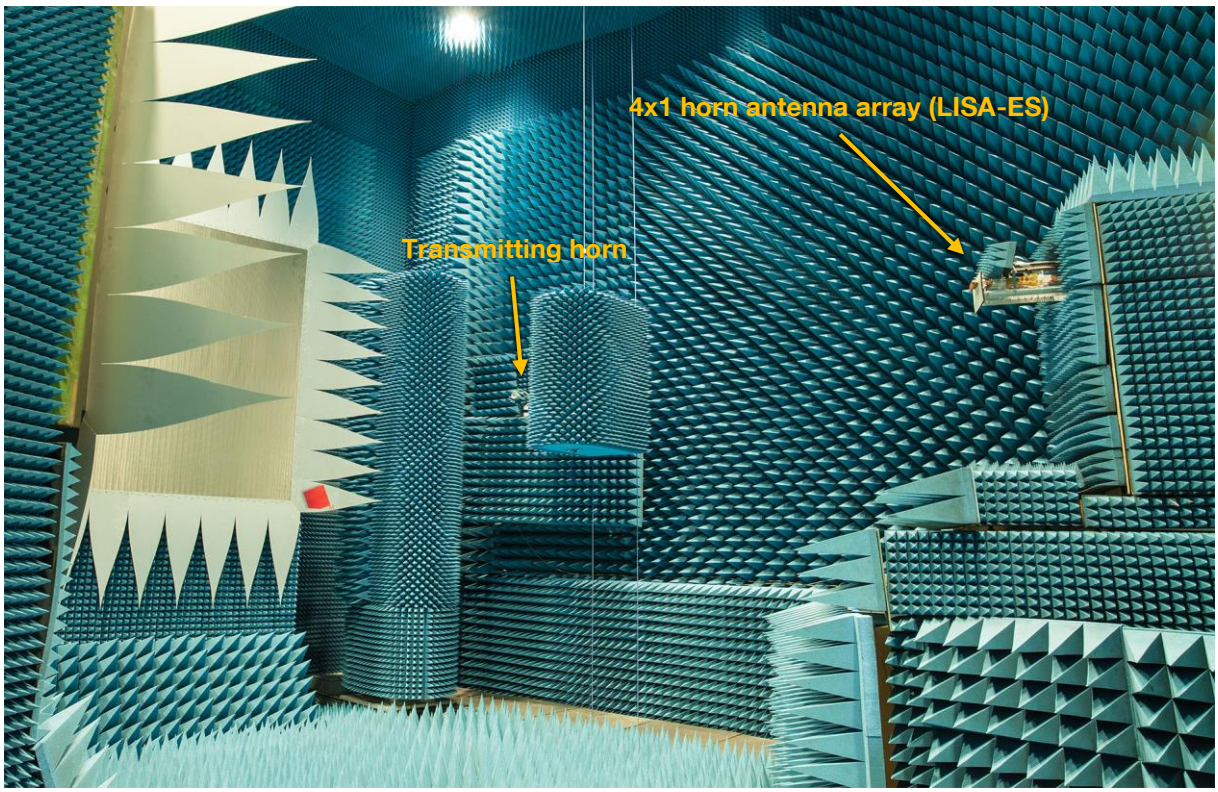

Figure 67: 4x1 array mounted in the CCR at the University of Applied Sciences Munich

In Chapter 6.1 the experimental setup of the antenna and the control setup for the interaction with the turntable within the CCR are described. The results of the static measurements are shown in Chapter 6.2 followed by the discussion. Chapter 6.3 shows the results of dynamic measurements. These results are compared with a simulation that is conducted with the simulation tool introduced in Chapter 3. The results of these measurements and the simulation are also discussed in Chapter 6.3.

6.1 Experimental Setup

The experimental setup consists of the CCR with a turntable, the antenna array and control electronics hardware, the control software that communicates with the power supply and a tick counting box that tracks the position of the turntable and communicates with the control software.

6.1.1 Hardware Setup of the Antenna

The original LISA-ES antenna array is designed for the integration with electroplated LCPSs. The waveguide cross section is nonstandard, and the flanges are designed to meet the compact design restrictions of the 4x4 array. Since only one electroplated LCPS is fully functional, the demonstration of the horn antenna array with LCPSs is performed with split block LCPSs. Four split blocks are built for measurements of the performance and comparative measurements. Since these four split blocks are used for the horn antenna array demonstration, measurements are limited to a 4x1 array. This limits the resulting gain, but the general performance can still be demonstrated.

The 4x1 horn antenna array is mounted on an acrylic glass structure to ensure the relative positioning of the horns, split blocks and waveguide distribution network. Each split block is fitted with two waveguide transitions to allow the attachment to the small flanges of the horns and waveguide distribution network.

Figure 68 shows the assembled horn antenna array with the waveguide distribution network and waveguide transition to WR34 (right). Each LCPS is attached to five cables (1x ground, 2x fixed voltage, 2x variable voltage) to control the phase. The LC is filled into each LCPS through tubes with an outer diameter of 0.6 mm. The two tubes used for each LCPS (filling and bleeding) are connected after the filling process. The connecting tube has a larger diameter and is flexible to allow for thermal expansion of the LC.

For campaign 2 the LCPSs were refilled with LC since, at least for one LCPS, the air bubble from the expansion tube was shifted into the LC cavity.

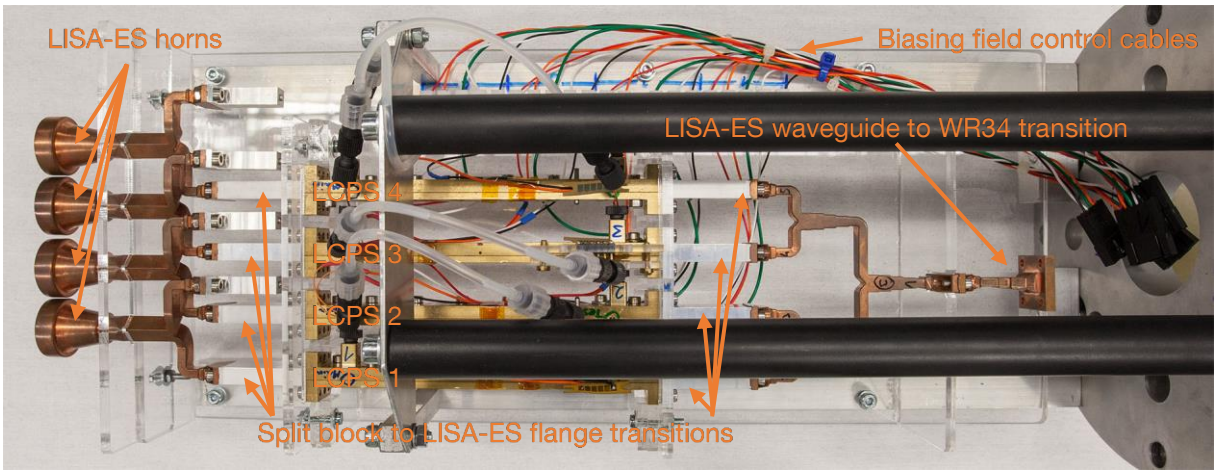

Figure 68: 4x1 horn antenna array with waveguide distribution network

For the measurements in the CCR, the assembly on the acrylic glass structure is mounted to a flange used for the installation on the turntable (right side in Figure 68). The cables to control the LCPSs and the rigid cable for the RF signal (waveguide to coaxial transition and rigid cable are not mounted in Figure 68) are fed through the hole in the middle of this flange.

The control cables of each LCPS can be extended through the flange and are then connected to one of the channels of the control electronics hardware (see Chapter 1.2.4.4).

6.1.2 Software and Control Setup

As mentioned in Chapter 1.2.4.4 the basic software with some extensions was developed during the project.

The already implemented extensions to the software were not used for the array measurements since the array size changed from 4x4 to 4x1 and the use of the software together with the LCPS hardware showed the demand for different functions.

For the measurements in the compact range the basic software is extended with functions that aim to easily manipulate the phases of a 4x1 array and allows for fast and easy sanity checks. The phase of each LCPS is calculated with the data from a calibration table and the phase offset for each LCPS can be manipulated independently of the phase calculation. This is used in campaign 2, where the offset is shifted by +9.5° to allow a 360° phase change at the two outer LCPSs. This shift allows to measure the desired steering range of ±11° whereas campaign 1 is limited to ±9°. The pivot point can be adjusted and each of the LCPSs can be forced to go into paraphase for testing.

The software is extended to communicate with a microcontroller that counts the ticks send by the turntable. This allows the automatic adjustment of the main lobe of the array to constantly point in one direction while the turntable is moving.

Figure 69 shows the automatic scan tab of the software. The manual scan tab is similar but allows to insert a steering angle by hand and does not use the tick count box to adjust the angle.

Figure 70 shows the control circuit for the automatic steering. The tick counter uses an interrupt to count each tick and adds them together with respect to the given direction. The control software retrieves this relative position (default update frequency 10 Hz) and calculates the phases for each LCPS to countersteer the motion of the turntable.

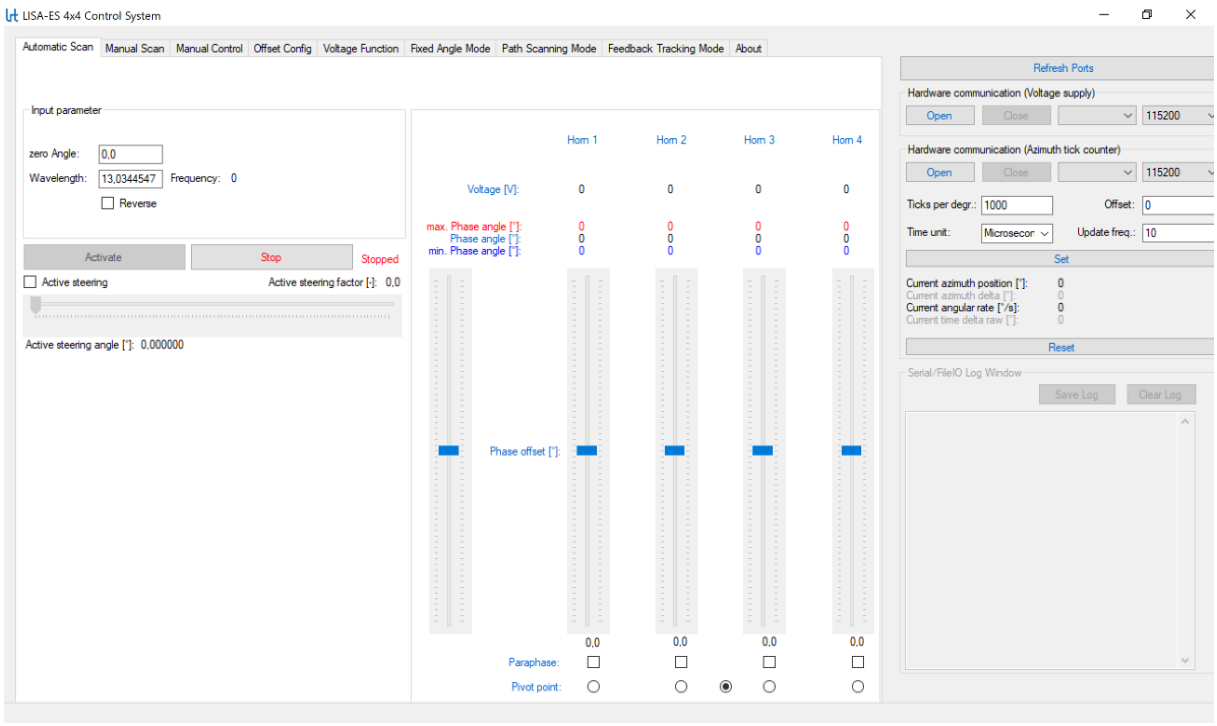

Figure 69: Control software for the antenna, automatic scan

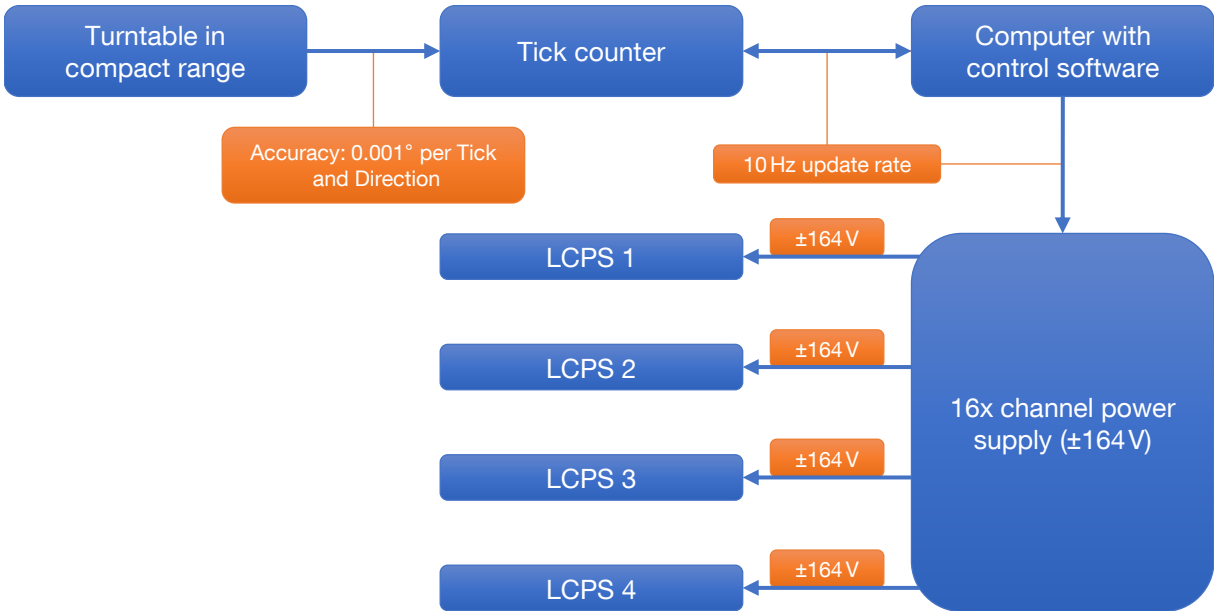

Figure 70: Automatic phase control circuit

6.2 Static Measurements

The static measurements comprise the measurement of the antenna pattern within the array plane for several steering angles (polar and cross-polar at 23 GHz), the gain measurement for the boresight alignment, to be able to subtract the influence of the working section, and the measurements of two patterns (0° and -9°) with several frequencies between 21.5 GHz and 24.5 GHz.

6.2.1 Results

Figure 71 shows the array patterns (polar) from -90° to 0° azimuth angle for several steering angles (campaign 2). Between 0° and -11° the main lobes of the array can be seen. From -40° to -18° the grating lobes show an increasing gain that would continue to the level of the main lobes for larger steering angles. The first grating lobe has an offset of slightly more than 30° to the main lobe which is in accordance with the calculations (Chapter 1.2.4.2).

The cross-polar is more than 29 dB below the gain in the desired steering direction and about 23 dB below the maximum gain of the main lobes within the measured azimuth range.

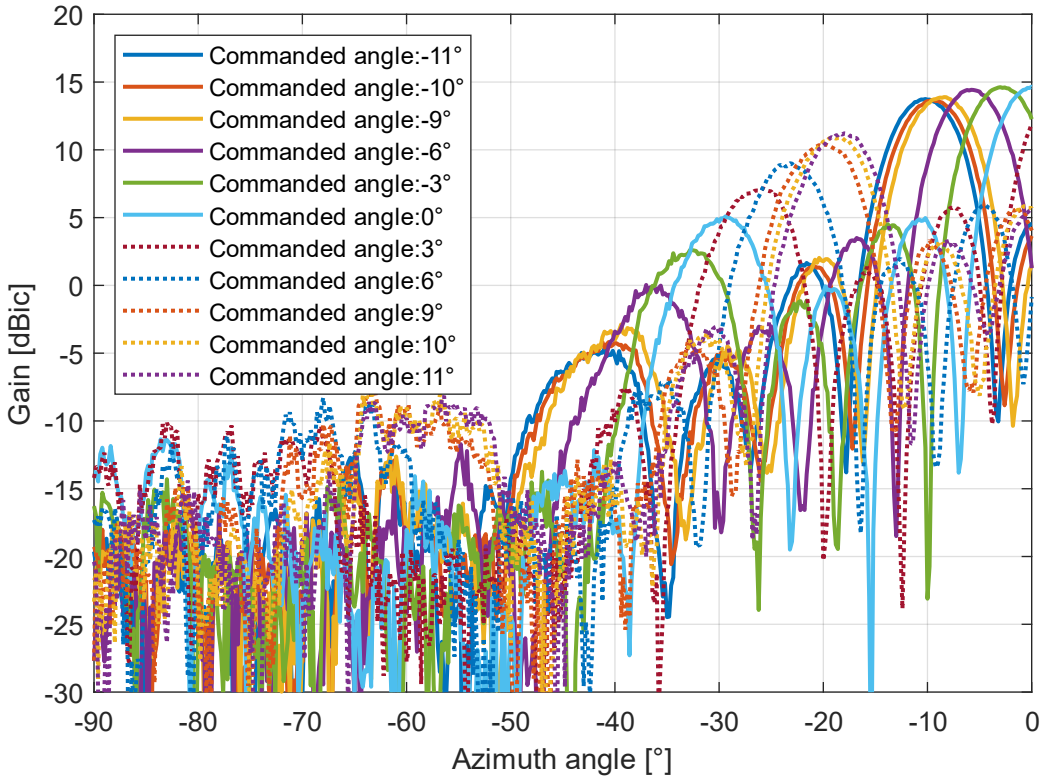

Figure 71: Pattern polar, 23 GHz, *GT3-23002*

To evaluate the steering accuracy, the measured angle has to be compared to the commanded angle. The measured angle is determined by two different methods. The first method uses the angle of the maximum value. The deviation thereby has to be a multiple of the step size used in the measurements (0.5° in campaign 1 and 0.2° in campaign 2). The second method uses the 3 dB beam width. To get the values 3 dB below the maximum level, the data points close to this level are linearly interpolated. The center point between the two interpolated values on the left and on the right side of the main lobe represents the steered angle. The advantage of this method is that the steeper slopes on both sides of the main lobe are used and the influence of measurement errors is therefore lessened.

Figure 72 shows the difference between the commanded and the measured angles. The blue markers show the deviation of the maximum gain ('Max') value and the red markers show the deviation of the center point at the 3 dB beam width level ('3dB-BW').

The dotted gray lines mark a deviation of ±0.5°. Most of the markers stay within these lines except for some of the markers of campaign 2 in the range between -9° and -11°, with a maximum deviation of 0.81° (7 %) from the desired angle.

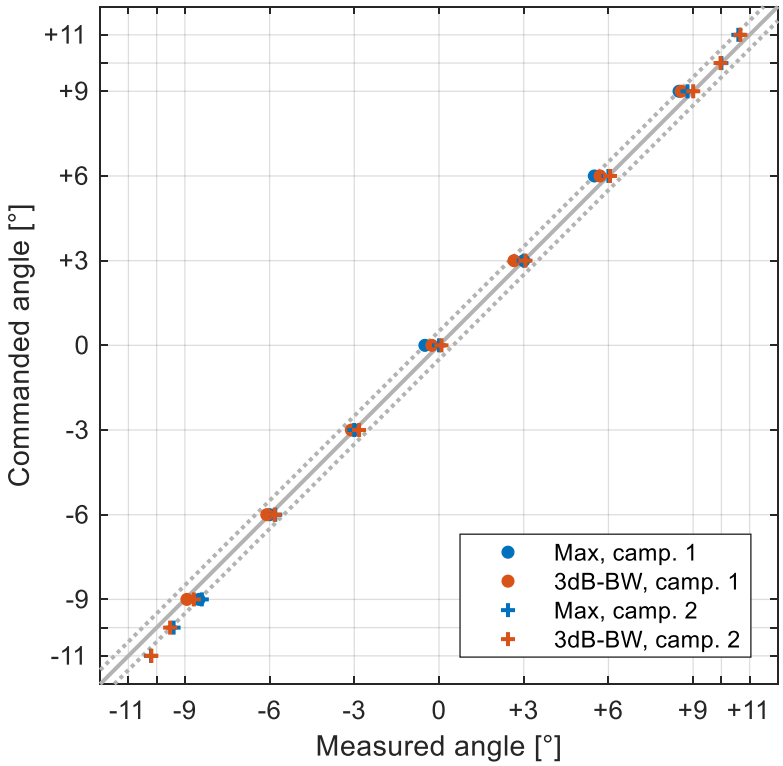

Figure 72: Commanded versus measured angle, 23 GHz, *GT3-23002*

Figure 73 shows the patterns for frequencies between 21.5 and 24.5 GHz at a steering angle of -9°. The calibration used for each phase shifter and thereby the adjusted phase is valid only for 23 GHz. The gain varies in a range of about 2.5 dB.

The deviation of the steering angle in this frequency range is shown in Figure 74. The maximum offset of the maximum value is 1°, whereby the measurement step size is 0.5° (campaign 1). The values calculated at the 3 dB beam width level ('3dB-BW') show a maximum deviation of less than 0.5°.

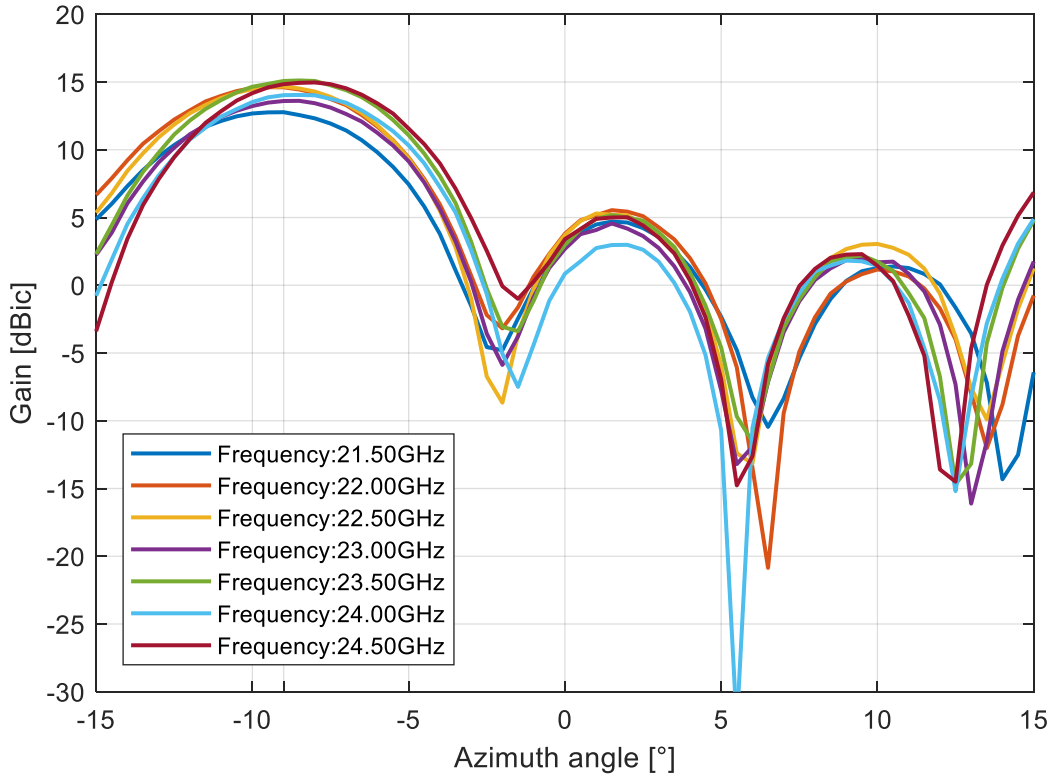

Figure 73: Frequency sweep for a desired angle of -9°, *GT3-23002*

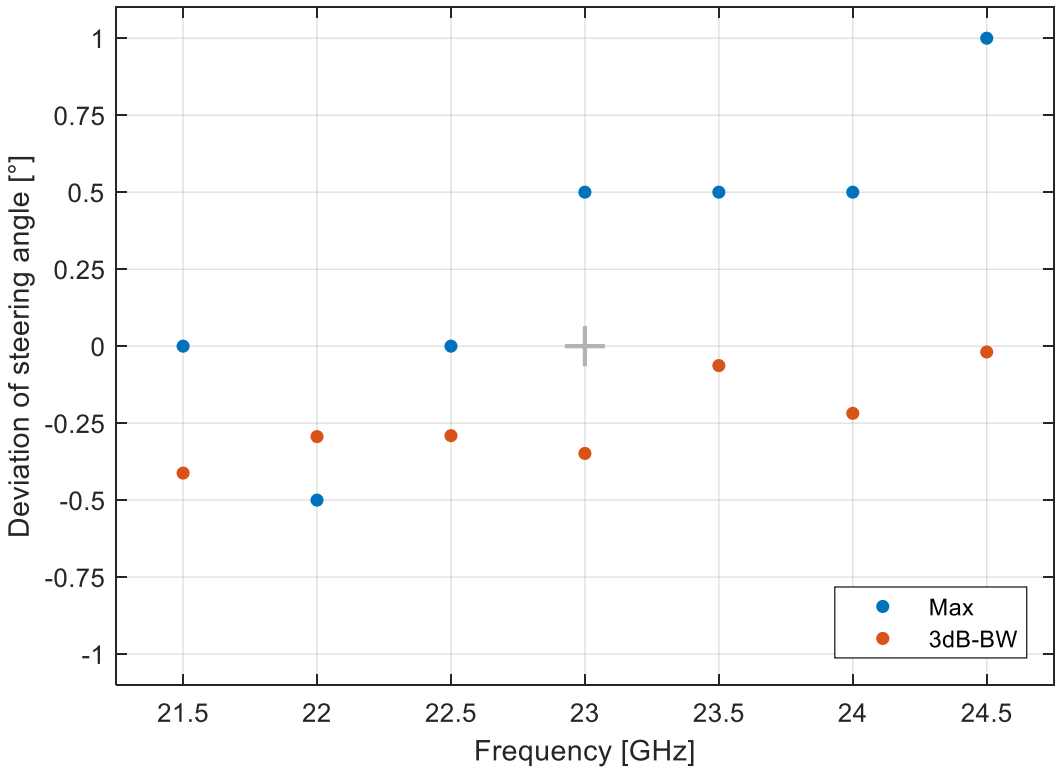

Figure 74: Deviation of the steering angle over frequency, desired angle -9°, *GT3-23002*

Figure 75 shows the pattern for a steering angle of -10° (where the jump occurs) as a reference and the disturbed patterns due to individual paraphases at each of the outer LCPSs (LCPS 1 and LCPS 4) and paraphases at both.

The disturbed patterns with individual paraphases are similar to each other and show a decrease in gain between 6 dB and 8 dB compared to the maximum level of the nominal pattern for a steering angle of -10°. A paraphase at both phase shifters results in a decrease of more than 20 dB.

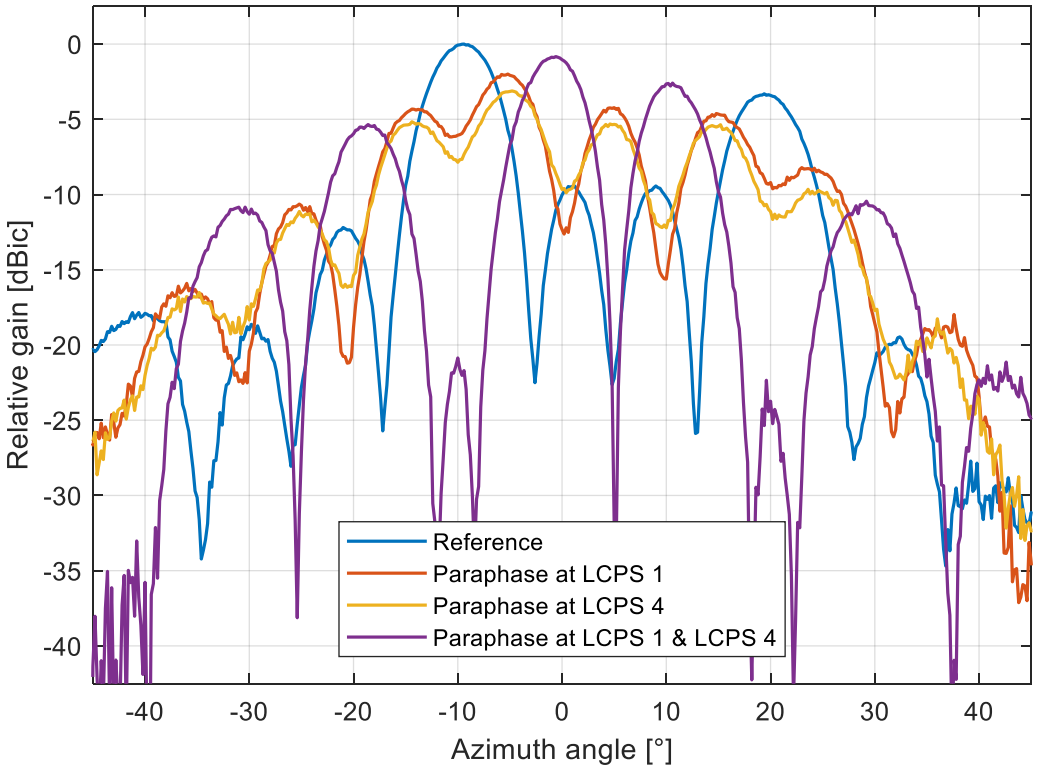

Figure 75: Pattern polar with phase errors for a desired angle of -10°, *GT3-23002*

6.2.2 Discussion

The decrease in gain of the main lobe for an increased offset of the main lobe to the boresight position is caused by the element patterns (horn pattern). According to equation (2-5) the first grating lobe is to be expected at an offset of 31.42° which is close to the offset in Figure 71 (slightly more than 30°).

The maximum gain of the 4x1 horn array is 14.4 dBic. With a simulated gain of 15.1 dBic (at 23.2 GHz, early design calculations by *NTP GmbH*) for each radiating element, the gain of the 4x1 horn array without LCPSs and distribution network is expected to be 21.1 dBic. The difference of 6.7 dB are losses mainly caused by the LCPSs with the LC *GT3-23002*. The transmission losses of the LCPSs for a 0° steering angle are between 5 dB and 6 dB.

The cross-polar level is 23 dB below the maximum polar level (28 dB within the desired steering range). A simulation during the design process of the horn (by *NTP GmbH*) showed a 28.5 dB decoupling of the cross-polar and the polar. This parameter is dependent on the horn design (septum) and the relative alignment of the horns within the array and not on the LCPSs performance.

The steering accuracy is clearly within a range of ±1° at a 3 dB beam width of about 6.5°. The accuracy of the steering is dependent on the accuracy and resolution of the calibration (phase over voltage measurement, Chapter 5.4) and the interpolation method (linear). In addition, the temperature has to be

constant or additional, temperature dependent calibrations have to be provided. It is not expected that the minimum step size of 1 V has an effect on the performance (see Chapter 5.5.3).

The frequency sweep shows that high bandwidths (in this case 3 GHz) are possible with this type of phase shifter. The percentage of the maximum loss caused by beam squint (frequency-dependent deviation from the maximum of the main lobe) due to different frequencies is 0.22 dB (at 24.27 GHz) whereas the gain varies within 2.5 dB (measured at a steering angle of -9°).

The effect of paraphases is severe, as expected from the simulations in Chapter 3, but larger numbers of array elements and LCPSs with a phase range of more than 360° could soften these effects.

Theoretically, the gain at the steering angle of -10° should be at -∞ dB for two horns / LCPSs in paraphase, since the signals radiated from the two horns at paraphase and the two horns at nominal phase should extinguish each other. Inaccuracies in the phase level of each phase shifter, differences in the transmission losses and in the alignment and positioning of the horns could be the reason for the deviation from the theory.

These results show, that the design is feasible for a static application with the need for high data rates. For a lager array, the steering accuracy could still be improved to enable an accurate shaping of spot beams. The transmission losses within the LCPSs reduce the gain of the array significantly. This has to be improved to make the technology attractive for applications.

6.3 Dynamic Measurements

The measurements of the dynamic steering are performed at three rotation rates of the turntable, 0.66 °/s, 0.17 °/s and 0.10 °/s. Where 0.10 °/s is the slowest rate of the turntable. The rates are constant, except for the run-up of the motor which is negligible at the rates measured. The maximum phase change rates (at LCPS 1 & 4)for these angular rates are 11.93 °/s, 3.07 °/s and 1.81 °/s (except for the phase jumps).

The expected steering rates for an application on a GEO satellite (see Chapter 3.3) are at about 0.013 °/s for a LEO satellite (altitude 1 500 km) in a retrograde equatorial orbit and 0.012 °/s for a LEO satellite in a polar orbit. The maximum phase change rate depends on the orientation of the array elements relative to the movement plane. For a rectangular array with the pivot point in the center of the array, the absolute maximum phase change rate occurs for a movement plane that is parallel to the diagonal of the array. In this case, the LCPSs at the two corners within the movement plane will experience the maximum phase change rate. The maximum phase change rate for a movement plane parallel to one of the main axes of the array occurs at LCPSs that are mounted at the borders that are orthogonal to the movement plane.

For a full-size array with 16x16 horns the maximum phase change rates at the maximum angular rate for a LEO satellite in a retrograde equatorial orbit are 1.662 °/s (diagonal case) and 1.175 °/s (parallel case). For a polar orbit these rates are slightly lessened to 1.534 °/s (diagonal case) and 1.085 °/s (parallel case). These cases will only occur, if the LEO satellite passes the antenna at boresight (steering angle equal to zero). For all other steering angles, the angular rates are reduced.

Due to the linear polarization of the transmitting horn of the CCR, each measurement is performed twice because the LISA-ES antenna is circular polarized. This assumes, that the behavior over time of each LCPS is replicable.

6.3.1 Results

Figure 76 shows the measurement results for all three angular rates of the antenna beam. The gain is given relative to the maximum gain measured in the static pattern at 0°. Except for the 0.66 °/s case, the antenna is able to track the target and reach a gain close to the maximum gain measured in static pattern measurements. For the 0.66 °/s case the antenna is not able to ensure the gain level between the jumps. Only between -11° and -10° and at about -2° the desired level is reached.

The tracks are recorded from -11° to +11° (-13° to +13° for 0.1 °/s), so the impact of the jumps that ideally occur at about ±10° is protracted to larger angles.

Figure 77 shows the same plot only for the 0.10 °/s case. In addition to the azimuth angle, the time of the measurement is also shown. The impact of both jumps on the gain lasts for about 20 s. During the jump time the gain drops rapidly to about -6 dB below the static gain level at these angles, in accordance with equation (3-1) and one LCPS in paraphase. After this first drop, the gain rises and drops again, but with a slower rate. The second drop is at about the same gain level than the first. The rise from the second drop to the normal level is slowed down towards the end.

Figure 78 shows the result of an array that is simulated with the *MATLAB* tool introduced in Chapter 3. The horn patterns are simplified with a cosine pattern, the phase change rates are taken from a jump measurement performed with a split block LCPS at room temperature and the LC *GT3-23002* (not constant as in Chapter 3). The change from a constant phase change rate to a more realistic one results in a time dependent behavior that has a similar progression during the jump of the two phase shifters compared to the measurement in Figure 77.

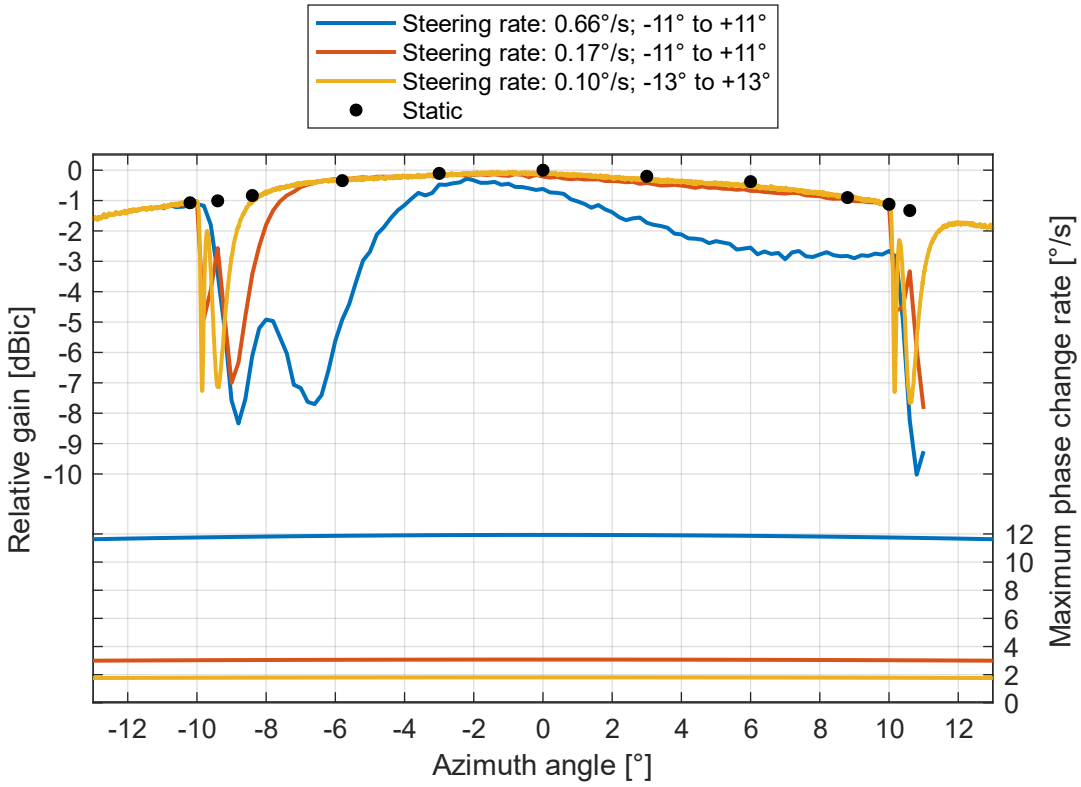

Figure 76: Relative gain for different steering rates, 23 GHz, *GT3-23002*

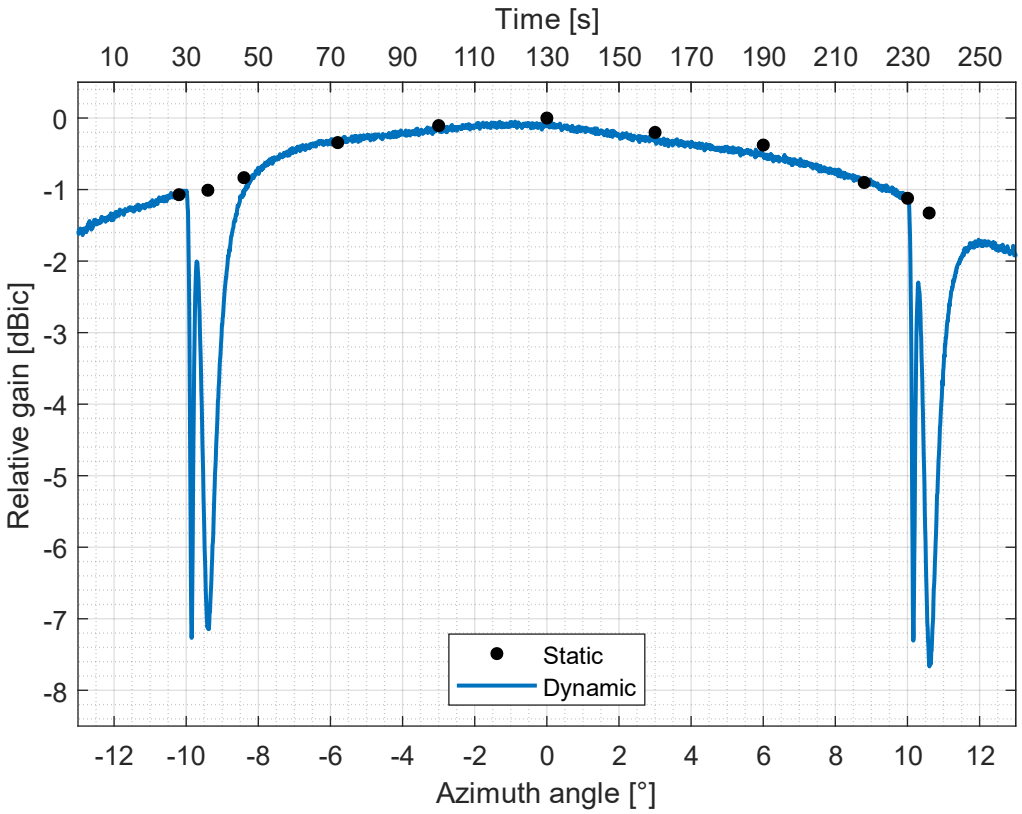

Figure 77: Relative gain over azimuth angle / time, steering rate 0.10 °/s, 23 GHz, *GT3-23002*

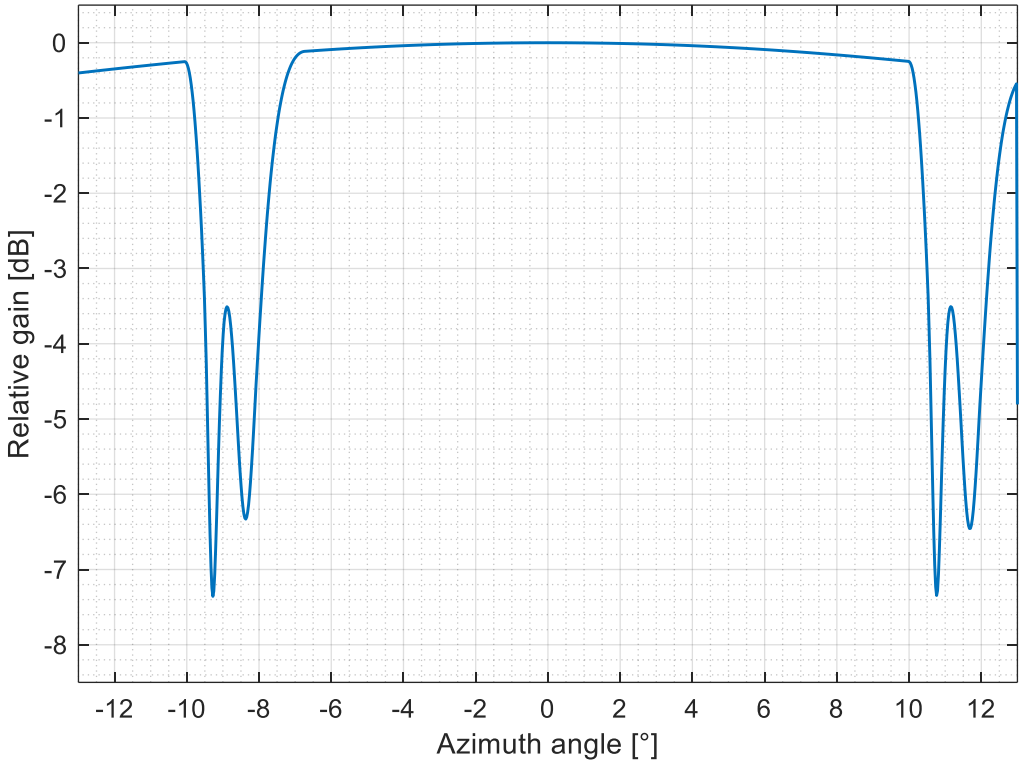

Figure 78: Simulated relative gain over azimuth angle / time, steering rate 0.10 °/s, 23 GHz

6.3.2 Discussion

The antenna is able to track the target at the angular rates that are necessary for a GEO application. The impact of the jumps is relatively short because of the faster LC *GT3-23002* (compared to *GT5-26001*). During the dynamic tracking, two of the phase shifters are performing a jump. One is jumping in the fast direction (H to V) and the other one in the slow direction (V to H). The superposition of these two jumps produces the gain progression over time. The first drop is mainly caused by the fast phase shifter that steers through the paraphase (-6 dB). This phase shifter has almost finished the entire 360° jump before the phase error of the slower phase shifter has an impact. This leads to the temporal rise of the gain. The two phase shifters that have to perform the jump are operated close to their maximum phase range. Therefore, the phase shifters approach the saturation level at the end of each jump which causes a lower phase change rate and delays the adjustment to the desired phase.

Assuming a constant rate for the entire jump time of 20 s (0.1 °/s case), the performance of these phase shifters is comparable to phase shifters with a constant phase change rate of 18 °/s, which is faster than the simulated +5 °/s and -3 °/s (see Chapter 3, where *GT5-26001* is assumed).

The simulation shows a similar behavior to the measurement, but the phase shift in both directions seems to be slower than the measured one in the array. The transition from the jump region to the subsequent region of normal performance is more gradual in the measurement. Reasons for this behavior could be slightly different measurement conditions such as higher temperatures or updated directions of the electric biasing field during the steering process compared to a single command without an oncoming phase.

Since the effect of the ‘faster’ and ‘slower’ steering direction of the phase shifters is larger than expected, it might be desirable to start the jump of the ‘slower’ phase shifter earlier so that the paraphases of both phase shifters occur at the same time (as proposed in Chapter 3.5). This would shorten the time of very high losses and therefore might extend the usable communication time for an antenna with only four array elements.

For arrays with a larger number of array elements, the impact of one or two paraphases at the same time is smaller and therefore, it might be desirable to spread these jumps over time (see Chapter 3).

7 Conclusion and Outlook

The goal of this thesis is to examine the feasibility of LCPSs based on a waveguide design with regard to the application in a passive phased array antenna on a GEO relay satellite mission.

Several steps were necessary to validate the feasibility. A simulation was conducted to evaluate the influence of phase jumps on the overall array performance. The manufacturing process was established to build a functional integrated copper LCPS. Different LCPSs designs were measured to determine the relevant characteristics for the intended application. A 4x1 horn antenna array with calibrated LCPSs was tested in a CCR to validate the functionality of the LCPSs as well as the overall system performance.

The results of these steps can be concluded as follows:

1) The simulation of a possible flight model of the antenna tracking a LEO satellite from a GEO relay satellite showed that single phase shifters in paraphase do not cause severe losses. There are only a few orbits that could cause severe losses (≥6 dB) due to simultaneous jumps of entire rows of LCPSs. For one of these cases it is shown that phase shifters with a slightly improved phase range (400°) allow to distribute the jumps such that the losses do not exceed 2 dB.

This shows that the jumps are not necessarily a criterion for exclusion of such an antenna, and the losses can be handled to minimize the influence.

Furthermore, different control methods have been analyzed which differ in the number of jumps and in the jump direction. For antennas with a large anisotropy in the phase change rates of both jump directions, it might be of interest to avoid one jump direction. This could be accomplished by a combination of the two methods cHornQ and cHornOQ. The disadvantage of this method is a doubling of the maximum phase change rate that is necessary for the nominal tracking (at the horn opposite to the one with the fixed phase).

2) The preceding designs are reviewed to learn from the errors identified up to that point and further optimize the manufacturing process. Over several batches of manufactured phase shifters, a manufacturing process was established that lead to an integrated functional electroplated LCPS. The entire process consists of several major steps such as core assembly, sputter coating and electroplating. Several sub-steps have been added and the process sequence has been changed to reach this goal of a functional copper LCPS. At the end, the process assurance of the core assembly and the sputter process could be improved significantly. The number of scrap parts after the electroplating exceeded the number of functioning parts and thus it is recommended to rethink the entire manufacturing process.

The most critical point of the manufacturing process is the electroplating in combination with the film electrodes. The suggestion is to split the process to avoid the contact of electroplating bath and film electrodes completely and, as a side effect, also drop the additional sealing. In addition, novel additive manufacturing methods could also be used to build the body in one piece and avoid the adhesive between the two body parts within the waveguide.

The performance of the integrated LCPS is worse than the performance of the LCPS in a split block design. Several causes in combination lead to this performance drop such as soldered cables within the waveguide, additional sealing of the core and possibly also residues of the electroplating bath.

3) The temperature-dependent measurements show a linear dependency of the transmission losses with higher losses at higher temperatures. The reflection does not show a significant change over temperature. The relative phase changes differently for large and small phase shifts. For large phase

shifts, the phase increases only slightly with rising temperatures. For small phases, the increase is stronger and in the investigated temperature range, this increase is linear. This results in a decrease of the phase range which can result in a significant change of the antenna tracking range or additional losses if the range drops below 360°. Both, the increase of the transmission losses and the decrease in phase range result in a decrease of the figure of merit.

For the time dependent behavior, higher temperatures lead to a lower rotational viscosity and thus to a faster reaction / phase change. This means that a relatively slow LC with improved RF performance can be heated up if fast phase changes are necessary. For a stationary use, the temperature can be decreased to reduce the losses. The significant increase of the phase change rate enables tracking applications also for LCs with a large rotational viscosity at room temperature. Thereby, it is important to not only increase the phase change rate but also regard the decrease in phase range since the phase change rate is significantly lower if the phase shifter is used close to its phase limits. This has to be taken into account in the design of the LCPS.

4) The method of calibrating the LCPSs and to steer the antenna without a closed feedback loop with a phase measurement seems to be sufficient for the intended application. However, the long-term stability of the calibration has to be shown when a qualifiable design for a space application is available. Thereby, the phase change from nematic to isotropic and back or a solidification of the LC might be critical but realistic for extreme hot or cold cases in space. In the case of a solidification, it might be desirable to be able to increase the temperature to the clearing point of the LC (isotropic phase) to ensure a homogeneous nematic phase after the LC has cooled down.

The measurements of the 4x1 array show a good static performance with a maximum deviation of 0.81° at a steering angle of -11°. The grating lobes are in accordance with the calculated position at ±30° (23 GHz). The cross-polar is more than 25 dB below the maximum gain in the desired steering range. The measurements at frequencies of ±1.5 GHz of the center frequency (23 GHz) showed a maximum deviation of the beam of less than 0.5° (3dB-BW method) at a steering angle of -9°. This shows that these LCPSs are not very sensitive to changing frequencies which allows the transmission of high bandwidth signals. The measured decrease in gain due to paraphases in one or two LCPSs is as expected from the simulation. It shows that the signal power is spread to other directions which can be seen as multiple beams which could also be used to track multiple objects with reduced gain. The dynamic measurements show a good tracking accuracy since the gain of the static measurements is reached. The signal collapses only during the jumps of the two outer LCPSs. A simulation using measured phase velocities during the jump shows a similar behavior and validates the implemented simulation method.

The largest impediment for an application is the transmission loss. Despite several design changes, the losses are still too high for the use in a passive array. Unless this problem is solved, the technology is not desirable for the planned application. If the transmission loss can be reduced (e.g., new LC, new core design), it is appropriate to rethink the manufacturing process.

If the transmission loss cannot be reduced significantly, an LCPS application is limited to AESAs, where the loss of components before (transmitting case) the HPA is not as critical. In this case the use of a different design of the LCPS, e.g., Strip-Line, is more likely.

It can be assumed that the efficiency of SSPAs in K/Ka-band will increase. A trend towards AESAs can be expected. Even smaller TWTAs can be an option in active arrays if the number of elements can be kept relatively small (AFR, IPA) and the element spacing is not too small.

A strong competitor for phase shifting technologies in AESAs is digital beamforming. This technology is especially interesting, because a true time delay can be implemented. The development in this technology for frequencies in the K/Ka-band will increase due to the new *5G* mobile services.

This work showed the general feasibility of LCPSs based on a waveguide design for PESAs in a GEO application. Especially the achievable bandwidth is an advantage compared to other technologies. For the intended application on a GEO satellite, further developments are necessary.

7.1 References

3M (2006) 'Transferklebebänder ohne Träger Serie 300 LSE', pp. 1–5.

Acikel, B. *et al.* (2001) 'Phase shifters using (Ba,Sr)TiO3 thin films on sapphire and glass substrates', in *IEEE MTT-S International Microwave Symposium*. IEEE, pp. 1191–1194. doi: 10.1109/MWSYM.2001.967105.

Acikel, B. *et al.* (2002a) 'A new high performance phase shifter using BaxSr1-xTiO3 thin films', *IEEE Microwave and Wireless Components Letters*, 12(7), pp. 237–239. doi: 10.1109/LMWC.2002.801129.

Acikel, B. *et al.* (2002b) 'A new X-band 180° high performance phase shifter using (Ba, Sr)TiO3 thin films', in *IEEE MTT-S International Microwave Symposium*. IEEE, pp. 1467–1469. doi: 10.1109/MWSYM.2002.1012132.

Ackerman, E. *et al.* (1992) 'Integrated 6-bit photonic true-time-delay unit for lightweight 3-6 GHz radar beamformer', in *1992 IEEE Microwave Symposium Digest MTT-S*. IEEE, pp. 681–684. doi: 10.1109/MWSYM.1992.188075.

Airbus (2014) 'X-band for mission critical communications'. Stevenage: AIRBUS DS Satellite Communications, p. 24.

Anderson, B. L. and Liddle, C. D. (2002) 'Optical true time delay for phased-array antennas: demonstration of a quadratic White cell', *Applied Optics*, 41(23), p. 4912. doi: 10.1364/AO.41.004912.

Angeletti, P. and Lisi, M. (2008) 'A survey of multiport power amplifiers applications for flexible satellite antennas and payloads', in *The 14th Ka and Broadband Communications Conference*.

Anzalchi, J. *et al.* (2017) 'Optical beamforming based on microwave photonic signal processing', *International Conference on Space Optics 2016*, (October), p. 75. doi: 10.1117/12.2296094.

Aoki, S. *et al.* (1982) 'The new definition of Universal Time', *Astronomy and Astrophysics*, 105(2), pp. 359–361. Available at: http://adsabs.harvard.edu/full/1982a&a...105..359a.

Asmar, S. W. and Matousek, S. (2016) 'Mars Cube One (MarCO) shifting the paradigm in relay deep space operation', in *SpaceOps Conference*. Reston, Virginia: American Institute of Aeronautics and Astronautics, pp. 1–7. doi: 10.2514/6.2016-2483.

Atwater, H. A. (1985) 'Circuit design of the loaded-line phase shifter', *IEEE Transactions on Microwave Theory and Techniques*, 33(7), pp. 626–634. doi: 10.1109/TMTT.1985.1133038.

Avant, R. *et al.* (1992) 'STGT multiple access beamforming system modelling and analysis', in *MILCOM 92 Conference Record*. IEEE, pp. 1028–1034. doi: 10.1109/MILCOM.1992.243953.

Backus, D. L. (1965) 'Electronically steerable antennas for spacecraft-to-spacecraft communications', *Navigation*, 12(3), pp. 227–251. doi: 10.1002/j.2161-4296.1965.tb02139.x.

Begovich, N. A. *et al.* (1966) *Microwave scanning antennas. volume III : array systems*. Edited by R. C. Hansen. New York and London: Academic Press.

Berghmans, F. *et al.* (1996) 'Radiation effects on nematic liquid crystal devices', in Taylor, E. W. (ed.), pp. 2–11. doi: 10.1117/12.254035.

Bildik, S. *et al.* (2011) 'Reconfigurable liquid crystal reflectarray with extended tunable phase range', in *41st European Microwave Conference*, pp. 404–407. doi: 10.23919/EuMC.2011.6101792.

Bildik, S. *et al.* (2015) 'Reconfigurable folded reflectarray antenna based upon liquid crystal technology', *IEEE Transactions on Antennas and Propagation*, 63(1), pp. 122–132. doi: 10.1109/TAP.2014.2367491.

Bulja, S. *et al.* (2010) 'Measurement of dielectric properties of nematic liquid crystals at millimeter wavelength', *IEEE Transactions on Microwave Theory and Techniques*, 58(12), pp. 3493–3501. doi: 10.1109/TMTT.2010.2054332.

C-Lec Plastics (2015) *Rexolite*, *C-Lec Plastics Inc.* Available at: http://www.rexolite.com/ (Accessed: 22 January 2018).

Campbell, C. F. *et al.* (2012) 'A K-band 5W doherty amplifier MMIC utilizing 0.15µm GaN on SiC HEMT technology', in *IEEE Compound Semiconductor Integrated Circuit Symposium*. IEEE, pp. 1–4. doi: 10.1109/CSICS.2012.6340057.

Campbell, C. F. *et al.* (2013) 'High efficiency Ka-band gallium nitride power amplifier MMICs', in *IEEE International Conference on Microwaves, Communications, Antennas and Electronic Systems*. IEEE, pp. 1–5. doi: 10.1109/COMCAS.2013.6685246.

Carr, E. F. (1969) 'Influence of electric fields on the molecular alignment in the liquid crystal p-(anisalamino)-phenyl acetate', *Molecular Crystals*, 7(1), pp. 253–268. doi: 10.1080/15421406908084876.

Chemtronics (2018) *Conformal Coatings*, *Chemtronics*. Available at: https://www.chemtronics.com/conformal-coatings (Accessed: 22 January 2018).

Chen, Y. *et al.* (2004) 'Reconfigurable true-time delay for wideband phased-array antennas', in Jabbour, G. E. and Rantala, J. T. (eds) *Emerging Optoelectronic Applications*, p. 125. doi: 10.1117/12.549229.

Christodoulou, C. G. *et al.* (2012) 'Reconfigurable antennas for wireless and space applications', *Proceedings of the IEEE*, 100(7), pp. 2250–2261. doi: 10.1109/JPROC.2012.2188249.

Collin, R. E. (1992) *Foundations for microwave engineering*. 2nd edn. John Wiley & Sons, Inc.

Collings, P. J. (1990) *Liquid crystals - nature's delicate phase of matter*. Bristol: Adam Hilger imprint by IOP Publishing Ltd.

Cook, K. L. B. (2010) 'Current wideband MILSATCOM infrastructure and the future of bandwidth availability', *IEEE Aerospace and Electronic Systems Magazine*, 25(12), pp. 23–28. doi: 10.1109/MAES.2010.5638785.

Cooley, M. (2015) 'Phased array fed reflector (PAFR) antenna architectures for space-based sensors', in *2015 IEEE Aerospace Conference*. IEEE, pp. 1–11. doi: 10.1109/AERO.2015.7118963.

Darbandi, A. *et al.* (2008) 'Flexible S-band SSPA for space application', in *2008 NASA/ESA Conference on Adaptive Hardware and Systems*. IEEE, pp. 70–76. doi: 10.1109/AHS.2008.47.

Davis, S. R. *et al.* (2013) 'Next-generation photonic true time delay devices as enabled by a new electro-optic architecture', in Pham, K. D. et al. (eds) *Sensors and Systems for Space Applications VI*. doi: 10.1117/12.2015302.

Deng, G. J. *et al.* (2017) 'A novel high power X-band ferrite phase shifter', *Review of Scientific Instruments*, 88(1), pp. 014705-1–8. doi: 10.1063/1.4974105.

Deo, P. *et al.* (2013) 'Liquid crystal based patch antenna array for 60 GHz applications', in *IEEE Radio and Wireless Symposium*, pp. 127–129. doi: 10.1109/RWS.2013.6486663.

Deschamps, J., Trusler, J. P. M. and Jackson, G. (2008) 'Vapor pressure and density of thermotropic liquid crystals: MBBA, 5CB, and novel fluorinated mesogens', *The Journal of Physical Chemistry B*, 112(13), pp. 3918–3926. doi: 10.1021/jp711211w.

Deuling, H. J. (1972) 'Deformation of Nematic Liquid Crystals in an Electric Field', *Molecular Crystals and Liquid Crystals*, 19(2), pp. 123–131. doi: 10.1080/15421407208083858.

DeWalt, S. A., Miller, K. B. and Stockley, J. E. (2004) 'Nematic liquid crystal spatial light modulator's response to total-dose irradiation', in Taylor, E. W. (ed.) *Photonics for Space Environments IX*. doi: 10.1117/12.558731.

Dionne, G. F., Oates, D. E. and Temme, D. H. (1995) 'YBCO/ferrite low-loss microwave phase shifter', *IEEE Transactions on Appiled Superconductivity*, 5(2), pp. 2083–2086. doi: 10.1109/77.402993.

Dixit, L. and Pourush, P. K. S. (2000) 'Radiation characteristics of switchable ferrite microstrip array antenna', *IEE Proceedings - Microwaves, Antennas and Propagation*, 147(2), p. 151. doi: 10.1049/ip-map:20000038.

Dixit, S. and Manohar, R. (2015) 'Gamma radiation-induced transformational change in IR spectrum of EBHA nematic liquid crystal', *International Journal of Advanced Research in Engineering and Technology*, 6(3), pp. 1–6.

Dolfi, D. *et al.* (1993) 'Liquid crystal microwave phase shifter', *Electronics Letters*, 29(10), pp. 926–928. doi: 10.1049/el:19930618.

Doyle, D. *et al.* (2016) 'Environmental concerns with liquid-crystal-based printed reflectarrays in space', *IEEE Antennas and Wireless Propagation Letters*, 15, pp. 1919–1922. doi: 10.1109/LAWP.2016.2538085.

Ellinger, F., Vogt, R. and Bachtold, W. (2001) 'Ultra compact, low loss, varactor tuned phase shifter MMIC at C-band', *IEEE Microwave and Wireless Components Letters*, 11(3), pp. 104–105. doi: 10.1109/7260.915615.

Esman, R. D. *et al.* (1993) 'Fiber-optic prism true time-delay antenna feed', *IEEE Photonics Technology Letters*, 5(11), pp. 1347–1349. doi: 10.1109/68.250065.

Fenech, H. *et al.* (2015) 'Eutelsat Quantum: a game changer', in *33rd AIAA International Communications Satellite Systems Conference and Exhibition*. Reston, Virginia: American Institute of Aeronautics and Astronautics. doi: 10.2514/6.2015-4318.

Follmann, R. *et al.* (2013) 'Liquida-Sky - a tunable liquid crystal filter for space applications', in *IEEE-APS Topical Conference on Antennas and Propagation in Wireless Communications*. IEEE, pp. 90–93. doi: 10.1109/APWC.2013.6624872.

Franc, A.-L. *et al.* (2013) 'Compact and broadband millimeter-wave electrically tunable phase shifter combining slow-wave effect with liquid crystal technology', *IEEE Transactions on Microwave Theory and Techniques*, 61(11), pp. 3905–3915. doi: 10.1109/TMTT.2013.2282288.

Franc, A. L. *et al.* (2013) 'Compact and broadband millimeter-wave electrically tunable phase shifter combining slow-wave effect with liquid crystal technology', *IEEE Transactions on Microwave Theory and Techniques*, 61(11), pp. 3905–3915. doi: 10.1109/TMTT.2013.2282288.

Frankel, M. Y. *et al.* (1998) 'Practical optical beamforming networks', *Optical and Quantum Electronics*, 30(11/12), pp. 1033–1050. doi: 10.1023/A:1006950928457.

Friesicke, C. *et al.* (2013) 'A linear 4W power amplifier at K-band using 250nm AlGaN/GaN HEMTs', in *8th European Microwave Integrated Circuits Conference*, pp. 157–160. Available at: http://www.scopus.com/inward/record.url?eid=2-s2.0-84893485258&partnerID=tZOtx3y1.

Fujii, K. (2015) 'Low cost Ka-band 7W GaAs PHEMT based HPA with GaN PHEMT equivalent performance', in *IEEE Radio Frequency Integrated Circuits Symposium*. IEEE, pp. 207–210. doi: 10.1109/RFIC.2015.7337741.

Gabriel, T. *et al.* (2016) 'Steerable Ka-band dual reflector antenna', in *German Microwave Conference*. IEEE, pp. 329–332. doi: 10.1109/GEMIC.2016.7461623.

Gaebler, A. *et al.* (2008a) 'Efficiency considerations of tuneable liquid crystal microwave devices', in *German Microwave Conference*, pp. 271–274.

Gaebler, A. *et al.* (2008b) 'Modeling of electrically tunable transmission line phase shifter based on liquid crystal', in *IEEE Antennas and Propagation Society International Symposium*. IEEE, pp. 1–4. doi: 10.1109/APS.2008.4619963.

Gaebler, A., Goelden, F., *et al.* (2009) 'Investigation of high performance transmission line phase shifters based on liquid crystal', in *European Microwave Conference*, pp. 594–597. doi: 10.23919/EUMC.2009.5295928.

Gaebler, A., Moessinger, A., *et al.* (2009) 'Liquid crystal-reconfigurable antenna concepts for space applications at microwave and millimeter waves', *International Journal of Antennas and Propagation*, 2009, pp. 1–7. doi: 10.1155/2009/876989.

Gaebler, A. (2015) *Synthese steuerbarer Hochfrequenzschaltungen und Analyse flüssigkristall-basierter Leitungsphasenschieber in Gruppenantennen für Satellitenanwendungen im Ka-Band*, *PhD , Thesis, Technical University of Darmstadt*. Technische Universität Darmstadt.

Gatti, N. (2015) 'Ku-band downlink reconfigurable active antenna for Quantum mission', in *33rd AIAA International Communications Satellite Systems Conference and Exhibition*. Reston, Virginia: American Institute of Aeronautics and Astronautics, pp. 1–5. doi: 10.2514/6.2015-4326.

de Gennes, P.-G. and Prost, J. (1995) *The physics of liquid crystals*. 2nd edn.

Goelden, F. *et al.* (2006) 'IP3 measurements of liquid crystals at microwave frequencies', in *European Microwave Conference*. IEEE, pp. 971–974. doi: 10.1109/EUMC.2006.281084.

Goelden, F. *et al.* (2008) 'Liquid-crystal varactors with fast switching times for microwave applications', *Electronics Letters*, 44(7), p. 480. doi: 10.1049/el:20080161.

Goelden, F. *et al.* (2009) 'Tunable liquid crystal phase shifter for microwave frequencies', *Electronics Letters*, 45(13), p. 686. doi: 10.1049/el.2009.1168.

Graham, A. *et al.* (1996) 'Preliminary space environment tests of nematic liquid crystals', *Photonics for Space Environments IV*. Edited by E. W. Taylor, 2811, pp. 46–50. doi: 10.1117/12.254054.

Gruler, H. and Meier, G. (1973) 'Investigations on the elastic constants of the nematic homologous series of 4,4′-Di(n-Alkoxy) Azoxybenzene', *Molecular Crystals and Liquid Crystals*, 23(3–4), pp. 261–270. doi: 10.1080/15421407308083376.

Gruler, H., Scheffer, T. J. and Meier, G. (1972) 'Elastic constants of nematic liquid crystals', *Zeitschrift für Naturforschung A*, 27(6), pp. 966–976. doi: 10.1515/zna-1972-0613.

Harder, J. *et al.* (2009) 'A compact, light-weight high data-rate antenna system for remote-sensing orbiters and space exploration', *Acta Astronautica*. Elsevier, 65(11–12), pp. 1738–1744. doi: 10.1016/j.actaastro.2009.05.001.

Heath, R. R. and Tumlinson, J. H. (1986) 'Correlation of retention times on liquid crystal capillary column with reported vapor pressures and half-lives of compounds used in pheromone formulations', *Journal of Chemical Ecology*, 12(11), pp. 2081–2088.

Helfrich, W. (1973) 'Electric alignment of liquid crystal', *Molecular Crystals and Liquid Crystals*, 21(3–4), pp. 187–209. doi: 10.1080/15421407308083319.

Hiro, K. and Wada, T. (2011) 'Phase diagram of thermotropic liquid crystal including negative pressure region generated in metal Berthelot tube', *Solid State Phenomena*, 181–182, pp. 22–25. doi: 10.4028/www.scientific.net/SSP.181-182.22.

Hodges, R. E., Radway, M. J., *et al.* (2015) 'ISARA - integrated solar array and reflectarray CubeSat deployable Ka-band antenna', in *IEEE International Symposium on Antennas and Propagation & USNC/URSI National Radio Science Meeting*. IEEE, pp. 2141–2142. doi: 10.1109/APS.2015.7305460.

Hodges, R. E., Hoppe, D. J., *et al.* (2015) 'Novel deployable reflectarray antennas for CubeSat communications', in *IEEE MTT-S International Microwave Symposium*. IEEE, pp. 1–4. doi: 10.1109/MWSYM.2015.7167153.

Hodges, R. E. *et al.* (2017) 'A deployable high-gain antenna bound for mars: developing a new folded-panel reflectarray for the first CubeSat mission to mars.', *IEEE Antennas and Propagation Magazine*, 59(2), pp. 39–49. doi: 10.1109/MAP.2017.2655561.

Hu, W. *et al.* (2007) 'Liquid-crystal-based reflectarray antenna with electronically switchable monopulse patterns', *Electronics Letters*, 43(14), p. 744. doi: 10.1049/el:20071098.

Hu, W. *et al.* (2008) 'Design and measurement of reconfigurable millimeter wave reflectarray cells with nematic liquid crystal', *IEEE Transactions on Antennas and Propagation*, 56(10), pp. 3112–3117. doi: 10.1109/TAP.2008.929460.

Hu, W. (2011) *Analysis and design of tunable phase shifters for considerations of time domain constrains*. Technische Universitaet Darmstadt.

Huang, J. and Encinar, J. A. (2007) *Reflectarray antennas*. Hoboken, NJ, USA: John Wiley & Sons, Inc. doi: 10.1002/9780470178775.

IEEE Aerospace & Electronic Systems Society (2002) 'IEEE Standard Letter Designations for Radar-Frequency Bands'. The Institute of Electrical and Electronics Engineers, Inc. doi: 10.1109/IEEESTD.2003.94224.

Imai, M. *et al.* (1994) 'Method for determination of rotational viscosity in nematic liquid crystals', *Japanese Journal of Applied Physics*, 33(Part 2, No. 1B), pp. L119–L121. doi: 10.1143/JJAP.33.L119.

Jacomb-Hood, A. and Lier, E. (2000) 'Multibeam active phased arrays for communications satellites', *IEEE Microwave Magazine*, 1(4), pp. 40–47. doi: 10.1109/6668.893245.

Jakoby, R. *et al.* (2004) 'Nonlinear dielectrics for tunable microwave components', in *15th International Conference on Microwaves, Radar and Wireless Communications*. IEEE, pp. 369–378. doi: 10.1109/MIKON.2004.1357043.

Jost, M. *et al.* (2013) 'Liquid crystal based low-loss phase shifter for W-band frequencies', *Electronics Letters*, 49(23), pp. 1460–1462. doi: 10.1049/el.2013.2830.

Jost, M., Strunck, S., *et al.* (2015) 'Continuously tuneable liquid crystal based stripline phase shifter realised in LTCC technology', in *European Microwave Conference*. IEEE, pp. 1260–1263. doi: 10.1109/EuMC.2015.7345999.

Jost, M., Weickhmann, C., *et al.* (2015) 'Tuneable hollow waveguide devices for space applications based on liquid crystal', in *SBMO/IEEE MTT-S International Microwave and Optoelectronics Conference*. IEEE, pp. 1–5. doi: 10.1109/IMOC.2015.7369046.

Kampinsky, A. and Kummer, W. H. (1970) 'Phased array antennas for applications on spacecraft', in *Phased Array Antenna Symposium*. Farmingdale, N. Y.: NASA Center for Aerospace Information.

Kaper, V., Harris, S. and Kessler, K. (2017) *Ku- and K-band GaN High Power Amplifier MMICs*. Andover United States. Available at: https://de.scribd.com/document/368483358/Raytheon-MmW-GaN-MMIC.

Karabey, O. H. *et al.* (2011) 'Methods for improving the tuning efficiency of liquid crystal based tunable phase shifters', in *European Microwave Integrated Circuits Conference*, pp. 494–497. Available at: http://ieeexplore.ieee.org/xpls/abs_all.jsp?arnumber=6102814.

Karabey, O. H. *et al.* (2012) 'A 2-D electronically steered phased-array antenna with 2x2 elements in LC display technology', *IEEE Transactions on Microwave Theory and Techniques*, 60(5), pp. 1297–1306. doi: 10.1109/TMTT.2012.2187919.

Katz, A. *et al.* (2017) 'High-efficiency high-power linearized L-band SSPA for navigational satellites', in *IEEE MTT-S International Microwave Symposium*. IEEE, pp. 1834–1837. doi: 10.1109/MWSYM.2017.8059009.

Kim, J.-S. *et al.* (2011) 'Rotational viscosity calculation method for liquid crystal mixture using molecular dynamics', *Journal of Information Display*, 12(3), pp. 135–139. doi: 10.1080/15980316.2011.593903.

Klesh, A. and Krajewski, J. (2015) 'MarCO: CubeSats to mars in 2016', in *29th Annual AIAA/USU Small Satellite Conference*, pp. 1–7.

Kneppe, H., Schneider, F. and Sharma, N. K. (1982) 'Rotational viscosity γ1 of nematic liquid crystals', *The Journal of Chemical Physics*, 77(6), pp. 3203–3208. doi: 10.1063/1.444195.

Koul, S. K. and Bhat, B. (1991) *Microwave and millimeter wave phase shifters (volume 1): dielectric and ferrite phase shifters*. Artech House Antennas and Propagation Library.

Koul, S. K. and Bhat, B. (1992) *Microwave and millimeter wave phase shifters (volume 2): semiconductor and delay line phase shifters*. Artech House Antennas and Propagation Library.

Kozilek, H. *et al.* (2013) 'Micro vibration improvement of a stepper actuated mechanism', in *Conference proceedings of the 15th European Space Mechanisms & Tribology Symposium*, pp. 25–27. Available at: http://www.esmats.eu/noordwijk/index.php.

Kuki, T., Fujikake, H. and Nomoto, T. (2002) 'Microwave variable delay line using dual-frequency switching-mode liquid crystal', *IEEE Transactions on Microwave Theory and Techniques*, 50(11), pp. 2604–2609. doi: 10.1109/TMTT.2002.804510.

Kumar, R. *et al.* (2005) 'Wideband gapfiller satellite (WGS) system', in *IEEE Aerospace Conference*. IEEE, pp. 1410–1417. doi: 10.1109/AERO.2005.1559431.

Lane, S. A. *et al.* (2009) 'Radiation testing of liquid crystal optical devices for space laser communication', *Optical Engineering*, 48(11), p. 114002. doi: 10.1117/1.3265710.

Liu, L. and Langley, R. J. (2008) 'Liquid crystal tunable microstrip patch antenna', *Electronics Letters*, 44(20), p. 1179. doi: 10.1049/el:20081995.

Lundin, R. and Stoll, E. (2006) 'Coverage time variation in a near-earth data relay satellite system', in *57th International Astronautical Congress*. Reston, Virigina: American Institute of Aeronautics and Astronautics, pp. 3–8. doi: 10.2514/6.IAC-06-B3.1.01.

Maier, W. and Saupe, A. (1958) 'Eine einfache molekulare Theorie des nematischen kristallinflüssigen Zustandes', *Zeitschrift für Naturforschung A*, 13(7), pp. 564–566. doi: 10.1515/zna-1958-0716.

Maier, W. and Saupe, A. (1959) 'Eine einfache molekular-statistische Theorie der nematischen kristallinflüssigen Phase. Teil I', *Zeitschrift für Naturforschung A*, 14(10), p. 287. doi: 10.1515/zna-1959-1005.

Maier, W. and Saupe, A. (1960) 'Eine einfache molekular-statistische Theorie der nematischen kristallinflüssigen Phase. Teil II', *Zeitschrift für Naturforschung A*, 15(4), pp. 1–6. doi: 10.1515/zna-1960-0401.

Marin, R. *et al.* (2007) '77 GHz reconfigurable reflectarray with nematic liquid crystal', in *2nd European Conference on Antennas and Propagation*. Institution of Engineering and Technology, pp. 9–9. doi: 10.1049/ic.2007.0940.

Martin, N. *et al.* (2003) 'Improvement of an inverted microstrip line-based microwave tunable phase-shifter using liquid crystal', in *33rd European Microwave Conference Proceedings*. IEEE, p. 1417–1420 Vol.3. doi: 10.1109/EUMC.2003.177754.

Masanobu, Y. *et al.* (2007) 'Ka-band Active Phased Array Antenna', *Journal of the National Institute of Information and Communications Technology*, 54(4), pp. 53–59.

McManamon, P. F. *et al.* (1996) 'Optical phased array technology', *Proceedings of the IEEE*, 84(2), pp. 268–298. doi: 10.1109/5.482231.

Meier, G. and Saupe, A. (1966) 'Dielectric relaxation in nematic liquid crystals', *Molecular Crystals and Liquid Crystals*, 1(4), pp. 515–525. doi: 10.1080/15421406608083290.

Meijerink, A. *et al.* (2007) 'Optical beam forming for phased-array antennas', *Fotonica Magazine*, 31(4), pp. 5–9.

Metzen, P. L. (2000) 'Globalstar satellite phased array antennas', in *IEEE International Conference on Phased Array Systems and Technology Proceedings*. IEEE, pp. 207–210. doi: 10.1109/PAST.2000.858941.

Milligan, T. A. (2005) *Modern antenna design*. 2nd edn. Hoboken, NJ, USA: John Wiley & Sons, Inc. doi: 10.1002/0471720615.

Miranda, F. A. *et al.* (2000) 'Design and development of ferroelectric tunable microwave components for Ku- and K-band satellite communication systems', *IEEE Transactions on Microwave Theory and Techniques*, 48(7), pp. 1181–1189. doi: 10.1109/22.853458.

Moessinger, A. *et al.* (2006) 'Electronically reconfigurable reflectarrays with nematic liquid crystals', *ELECTRONICS LETTERS*, 42(16).

Moessinger, A. *et al.* (2010) 'Compact tunable Ka-band phase shifter based on liquid crystals', in *IEEE MTT-S International Microwave Symposium*. IEEE, pp. 1020–1023. doi: 10.1109/MWSYM.2010.5517405.

Mueller, S., Penirschke, A., *et al.* (2005) 'Broad-band microwave characterization of liquid crystals using a temperature-controlled coaxial transmission line', *IEEE Transactions on Microwave Theory and Techniques*, 53(6), pp. 1937–1945. doi: 10.1109/TMTT.2005.848842.

Mueller, S., Felber, C., *et al.* (2005) 'Passive tunable liquid crystal finline phase shifter for millimeter waves', in *European Microwave Conference*. IEEE, doi: 10.1109/EUMC.2005.1608852.

Muller, S. *et al.* (2004) 'Tunable passive phase shifter for microwave applications using highly anisotropic liquid crystals', in *IEEE MTT-S International Microwave Symposium Digest*. IEEE, pp. 1151–1154. doi: 10.1109/MWSYM.2004.1339190.

Ng, W. *et al.* (1991) 'The first demonstration of an optically steered microwave phased array antenna using true-time-delay', *Journal of Lightwave Technology*, 9(9), pp. 1124–1131. doi: 10.1109/50.85809.

Nicol, E. F., Mangus, B. J. and Grebliunas, J. R. (2008) 'TWTA versus SSPA: analysis update of the Boeing fleet on-orbit reliability data', in *IEEE International Vacuum Electronics Conference*. IEEE, pp. 169–170. doi: 10.1109/IVELEC.2008.4556435.

Noh, Y. S. and Yom, I. B. (2016) 'A linear GaN high power amplifier MMIC for Ka-band satellite communications', *IEEE Microwave and Wireless Components Letters*, 26(8), pp. 619–621. doi: 10.1109/LMWC.2016.2585553.

Oates, D. E. *et al.* (1997) 'Superconductor ferrite phase shifters and circulators', *IEEE Transactions on Appiled Superconductivity*, 7(2), pp. 2347–2350. doi: 10.1109/77.621710.

Ohira, T. (1997) 'Megalithic microwave signal processing for phased-array beamforming and steering', *IEEE Transactions on Microwave Theory and Techniques*, 45(12 PART 2), pp. 2324–2332. doi: 10.1109/22.643837.

Parker, D. and Zimmermann, D. C. (2002a) 'Phased arrays-part II: implementations, applications, and future trends', *IEEE Transactions on Microwave Theory and Techniques*, 50(3), pp. 688–698. doi: 10.1109/22.989954.

Parker, D. and Zimmermann, D. C. (2002b) 'Phased arrays - part 1: theory and architectures', *IEEE Transactions on Microwave Theory and Techniques*, 50(3), pp. 678–687. doi: 10.1109/22.989953.

Penirschke, A. *et al.* (2004) 'Cavity perturbation method for characterization of liquid crystals up to 35GHz', in *34th European Microwave Conference*, pp. 545–548.

Perez-Palomino, G. *et al.* (2013) 'Design and experimental validation of liquid crystal-based reconfigurable reflectarray elements with improved bandwidth in F-band', *IEEE Transactions on Antennas and Propagation*, 61(4), pp. 1704–1713. doi: 10.1109/TAP.2013.2242833.

Perez-Palomino, G. *et al.* (2015) 'Design and demonstration of an electronically scanned reflectarray antenna at 100 GHz using multiresonant cells based on liquid crystals', *IEEE Transactions on Antennas and Propagation*, 63(8), pp. 3722–3727. doi: 10.1109/TAP.2015.2434421.

Pillans, B. *et al.* (1999) 'Ka-Band RF MEMS Phase Shifters', *IEEE Microwave and Guided Wave Letters*, 9(12), pp. 520–522. doi: 10.1109/75.819418.

Pillans, B. *et al.* (2000) 'Ka-band RF MEMS phase shifters for phased array applications', in *IEEE Radio Frequency Integrated Circuits Symposium Digest of Papers*. IEEE, pp. 195–199. doi: 10.1109/RFIC.2000.854447.

Polifke, W. and Kopitz, J. (2005) *Wärmeübertragung*. 1st edn. Pearson Studium.

Pozar, D. (2011) *Microwave engineering*. 4th edn. Edited by A. Melhorn. John Wiley & Sons, Inc.

Ramo, S., Whinnery, J. R. and Van Duzer, T. (1994) *Fields and waves in communication electronics*. 3rd edn. Edited by S. Elliot. New York, Chichester, Brisbane, Toronto, Singapore: John Wiley & Sons, Inc.

Rebeiz, G. M., Tan, G.-L. and Hayden, J. S. (2002) 'RF MEMS phase shifters: design and applications', *IEEE Microwave Magazine*, 3(2), pp. 72–81. doi: 10.1109/MMW.2002.1004054.

Roederer, A. G. (2005) 'Antennas for space: some recent european developments and trends', in *18th International Conference on Applied Electromagnetics and Communications*. IEEE, doi: 10.1109/ICECOM.2005.204908.

Rohwer, A. B. *et al.* (2010) 'Iridium main mission antennas - a phased array success story and mission update', in *IEEE International Symposium on Phased Array Systems and Technology*. IEEE, pp. 504–511. doi: 10.1109/ARRAY.2010.5613319.

Romanofsky, R. R. *et al.* (2000) 'K-band phased array antennas based on Ba 0.60 Sr 0.40 TiO3 thin-film phase shifters', *IEEE Transactions on Microwave Theory and Techniques*, 48(12), pp. 2504–2510. doi: 10.1109/22.899005.

Romanofsky, R. R. (2007) *Array phase shifters: theory and technology*, *NASA*.

Romanofsky, R. R. and Qureshi, A. H. (2000) 'A model for ferroelectric phase shifters', *IEEE Transactions on Magnetics*, 36(5), pp. 3491–3494. doi: 10.1109/20.908870.

Romanofsky, R. R. and Toonen, R. C. (2018) 'Past, present and future of ferroelectric and multiferroic thin films for array antennas', *Multidimensional Systems and Signal Processing*. Springer US, 29(2), pp. 475–487. doi: 10.1007/s11045-016-0449-5.

Roper, D. H. *et al.* (2003) 'WGS phased arrays support next generation dod satcom capability', in *IEEE International Symposium on Phased Array Systems and Technology*. IEEE, pp. 82–87. doi: 10.1109/PAST.2003.1256961.

Rotman, R., Tur, M. and Yaron, L. (2016) 'True time delay in phased arrays', *Proceedings of the IEEE*, 104(3), pp. 504–518. doi: 10.1109/JPROC.2016.2515122.

Rutledge, D. and Muha, M. (1982) 'Imaging antenna arrays', *IEEE Transactions on Antennas and Propagation*, 30(4), pp. 535–540. doi: 10.1109/TAP.1982.1142856.

Sanadgol, B., Holzwarth, S. and Kassner, J. (2009) '30 GHz liquid crystal phased array', in *Loughborough Antennas & Propagation Conference*. IEEE, pp. 589–592. doi: 10.1109/LAPC.2009.5352427.

Schneider, M., Hartwanger, C. and Wolf, H. (2011) 'Antennas for multiple spot beam satellites', *CEAS Space Journal*, 2(1–4), pp. 59–66. doi: 10.1007/s12567-011-0012-z.

Schwartz, L. *et al.* (1970) 'Data relay satellite phased array', in *3rd Communications Satellite Systems Conference*. Reston, Virigina: American Institute of Aeronautics and Astronautics, doi: 10.2514/6.1970-424.

Schwartz, L. and Smith, J. (1975) 'Adaptive ground implemented phased array (AGIPA) for the tracking and data relay satellite system (TDRSS)', in *Antennas and Propagation Society International Symposium*. Institute of Electrical and Electronics Engineers, pp. 213–216. doi: 10.1109/APS.1975.1147439.

Sharma, A. *et al.* (2017) 'High efficiency 25 Watt GaN X-band SSPA for deep space missions', in *IEEE Aerospace Conference*. IEEE, doi: 10.1109/AERO.2017.7943723.

Simons, R. N. *et al.* (2010) 'High-efficiency K-band space traveling-wave tube amplifier for near-earth high data rate communications', in *IEEE MTT-S International Microwave Symposium*. IEEE, pp. 1–1. doi: 10.1109/MWSYM.2010.5516163.

Soref, R. A. (1996) 'Fiber grating prism for true time delay beamsteering', *Fiber and Integrated Optics*, 15(4), pp. 325–333. doi: 10.1080/01468039608202279.

Spearing, R. E. (1973) 'Adaptive ground implemented phase array', in *Significant Accomplishments in Technology*. United States, pp. 103–108.

Srivastava, A. and Singh, S. (2004) 'Elastic constants of nematic liquid crystals of uniaxial symmetry', *Journal of Physics: Condensed Matter*, 16(41), pp. 7169–7182. doi: 10.1088/0953-8984/16/41/001.

Stirland, S. J. and Brain, J. R. (2006) 'Mobile antenna developments in EADS Astrium', in *First European Conference on Antennas and Propagation*. IEEE, doi: 10.1109/EUCAP.2006.4584956.

Stirland, S., Scouarnec, D. and Wolf, H. (2013) 'Current status and future trends in satellite telecommunications antennas', in *Loughborough Antennas & Propagation Conference*. IEEE, pp. 14–17. doi: 10.1109/LAPC.2013.6711842.

Stockley, J. *et al.* (2006) 'In situ measurement of liquid crystal spatial light modulators' beam steering characteristics during gamma irradiation', *Proceedings Volume 6308, Photonics for Space Environments XI*, 630805(August 2006). doi: 10.1117/12.683616.

Stoll, E. *et al.* (2009) 'On-orbit servicing', *IEEE Robotics & Automation Magazine*, 16(4), pp. 29–33. doi: 10.1109/MRA.2009.934819.

Stoll, E. *et al.* (2012) 'The future role of relay satellites for orbital telerobotics', *Advances in Space Research*, 50(7), pp. 864–880. doi: 10.1016/j.asr.2012.05.014.

Strauss, R. (1994) 'Reliability of SSPA's and TWTA's', *IEEE Transactions on Electron Devices*, 41(4), pp. 625–626. doi: 10.1109/16.278524.

Strunck, S. *et al.* (2013) 'Continuously tunable phase shifters for phased arrays based on liquid crystal technology', in *IEEE International Symposium on Phased Array Systems and Technology*. IEEE, pp. 82–88. doi: 10.1109/ARRAY.2013.6731805.

Strunck, S. *et al.* (2015) 'Reliability study of a tunable Ka-band SIW-phase shifter based on liquid crystal in LTCC-technology', *International Journal of Microwave and Wireless Technologies*, 7(05), pp. 521–527. doi: 10.1017/S175907871400083X.

Suzuki, Y. *et al.* (2000) 'Onboard large scale MMIC beam forming network for ETS-VIII', in *18th International Communications Satellite Systems Conference and Exhibit*. Reston, Virigina: American Institute of Aeronautics and Astronautics, pp. 9–13. doi: 10.2514/6.2000-1193.

Suzuki, Y., Imaizumi, Y. and Ohata, K. (2008) 'In-orbit Testing of the Beam Forming Network on Engineering Test Satellite VIII', *NTT Technical Review*. NTT, pp. 1–5.

Tanaka, M. *et al.* (1994) 'Development of multibeam phased array antenna on ets-vi for s-band intersatellite communications', *Electronics and Communications in Japan (Part I: Communications)*, 77(1), pp. 117–129. doi: 10.1002/ecja.4410770112.

Tanaka, M. *et al.* (1997) 'Antenna pattern measurement of S-band active phased array on ETS-VI', *Electronics and Communications in Japan (Part I: Communications)*, 80(4), pp. 29–38. doi: 10.1002/(SICI)1520-6424(199704)80:4<29::AID-ECJA4>3.0.CO;2-3.

Tanaka, M. *et al.* (1998) 'On-orbit measurement of phased arrays in satellites by rotating element electric field vector method', *Electronics and Communications in Japan (Part I: Communications)*, 81(1), pp. 1–13. doi: 10.1002/(SICI)1520-6424(199801)81:1<1::AID-ECJA1>3.0.CO;2-S.

Tebbe, M. *et al.* (2016) 'Simulation of an electronically steerable horn antenna array with liquid crystal phase shifters', in *IEEE Aerospace Conference*, doi: 10.1109/AERO.2016.7500660.

Tebbe, M. *et al.* (2017) 'Manufacturing and testing of liquid crystal phase shifters for an electronically steerable array', in *IEEE Aerospace Conference*, doi: 10.1109/AERO.2017.7943661.

Teles, J., Samii, M. V. and Doll, C. E. (1995) 'Overview of TDRSS', *Advances in Space Research*, 16(12), pp. 67–76. doi: 10.1016/0273-1177(95)98783-K.

Thales (2012a) 'Ku-band space traveling wave tubes'. Thales Group.

Thales (2012b) 'L & S-band space traveling wave tubes'. Thales Group.

Thales (2012c) 'X-band space traveling wave tubes'. Thales Group.

Thales (2013) 'K & KA-band space TWTs'. Thales Group.

Van Trees, H. L. (2002) *Optimum array processing*. New York, USA: John Wiley & Sons, Inc. doi: 10.1002/0471221104.

Uber, C. F. *et al.* (2008) 'Radiation testing of liquid crystal optical phase shifters for space survivability', in *IEEE Military Communications Conference*. IEEE, doi: 10.1109/MILCOM.2008.4753053.

Vallado, D. A. (2013) *Fundamentals of astrodynamics and applications*. 4th edn. Edited by J. Wertz. Microcosm Press Space Technology Library.

Vélu, G. *et al.* (2007) 'A 360° BST phase shifter with moderate bias voltage at 30 GHz', *IEEE Transactions on Microwave Theory and Techniques*, 55(2), pp. 438–444. doi: 10.1109/TMTT.2006.889319.

De Vleeschouwer, H. *et al.* (2001) 'Long-term ion transport in nematic liquid crystal displays', *Japanese Journal of Applied Physics*, 40(Part 1, No. 5A), pp. 3272–3276. doi: 10.1143/JJAP.40.3272.

Wallis, R. E. and Cheng, S. (2001) 'Phased-array antenna system for the MESSENGER deep space mission', in *IEEE Aerospace Conference Proceedings*, p. 49. doi: 10.1109/AERO.2001.931694.

Weekley, J. M. and Mangus, B. J. (2005) 'TWTA versus SSPA: a comparison of on-orbit reliability data', *IEEE Transactions on Electron Devices*, 52(5), pp. 650–652. doi: 10.1109/TED.2005.845864.

Weickhmann, C., Nathrath, N., *et al.* (2013) 'A light-weight tunable liquid crystal phase shifter for an efficient phased array antenna', in *European Microwave Conference*, pp. 428–431.

Weickhmann, C., Gaebler, A., *et al.* (2013) 'Recent measurements of compact electronically tunable liquid crystal phase shifter in rectangular waveguide topology', *Electronics Letters*, 49(21), pp. 1345–1347. doi: 10.1049/el.2013.2281.

Weickhmann, C. (2017) *Liquid crystals towards terahertz : characterisation and tunable waveguide phase shifters for millimetre-wave and terahertz beamsteering antennas*, *PhD , Thesis, Technical University of Darmstadt*. Technische Universität Darmstadt.

Weil, C., Mueller, S., Scheele, P., Kryvoshapka, Y., *et al.* (2003) 'Ferroelectric- and liquid crystal-tunable microwave phase shifters', in *33rd European Microwave Conference*. IEEE, pp. 1431–1434. doi: 10.1109/EUMA.2003.340890.

Weil, C., Mueller, S., Scheele, P., Best, P., *et al.* (2003) 'Highly-anisotropic liquid-crystal mixtures for tunable microwave devices', *Electronics Letters*, 39(24), p. 1732. doi: 10.1049/el:20031150.

Weil, C., Luessem, G. and Jakoby, R. (2002) 'Tunable inverted-microstrip phase shifter device using nematic liquid crystals', in *IEEE MTT-S International Microwave Symposium Digest*. IEEE, pp. 367–371. doi: 10.1109/MWSYM.2002.1011632.

Wilde, M. *et al.* (2015) 'Impact of space-to-ground video transmission constraints on teleoperated final approach and docking', *Journal of Aerospace Information Systems*, 12(7), pp. 441–454. doi: 10.2514/1.I010288.

Woehrle, C. D. *et al.* (2016) 'Space radiation environment testing of liquid crystal phase shifter devices', *IEEE Antennas and Wireless Propagation Letters*, 15, pp. 1923–1926. doi: 10.1109/LAWP.2015.2511058.

Wolf, H. *et al.* (2014) 'Satellite multibeam antennas at airbus defence and space: state of the art and trends', in *The 8th European Conference on Antennas and Propagation (EuCAP 2014)*. IEEE, pp. 182–185. doi: 10.1109/EuCAP.2014.6901722.

Yang, X. *et al.* (2013) 'Compact and low loss phase shifter with low bias field using partially magnetized ferrite', *IEEE Transactions on Magnetics*, 49(7), pp. 3882–3885. doi: 10.1109/TMAG.2013.2244860.

Yüceer, M. (2012) 'Emerging technologies for communication satellite payloads', *Progress in Aerospace Sciences*, 50, pp. 27–34. doi: 10.1016/j.paerosci.2011.11.001.

7.2 List of Publications

Tebbe, M. *et al.* (2016) 'Simulation of an electronically steerable horn antenna array with liquid crystal phase shifters', in *IEEE Aerospace Conference*, doi: 10.1109/AERO.2016.7500660.

Tebbe, M. *et al.* (2017) 'Manufacturing and testing of liquid crystal phase shifters for an electronically steerable array', in *IEEE Aerospace Conference*, doi: 10.1109/AERO.2017.7943661.

Tebbe, M. *et al.* (2017) 'Satellite visibility map for emergency services applications', in *International Astronautical Congress*.

Tebbe, M. and Strauss, G. (2018) 'Measurement of the dynamic pattern of an electronically steerable phased antenna array with circular polarization in Ka-band', in *AMTA 2018 Proceedings*.

Hoehn, A. *et al.* (2017) 'LISA ES – evaluating liquid crystals as phase shifters in a direct radiating horn array antenna (ISL Ka-band)', in *ESA Antenna Workshop*.

Hoehn, A. *et al.* (2017) 'Novel copper-galvanic electroforming manufacturing technologies for the LISA high gain antenna systems and related Ka-Band RF components', in *ESA Antenna Workshop*.

Nathrath, N. *et al.* (2017) 'The electroplated lightweight inter-satellite antenna (LISA) system for Ka-band with low loss, dual polarization, waveguide rotary joint', in *ESA Antenna Workshop*.

Appendix A List of Figures and Tables

A.1 List of Figures

A.2 List of Tables

Appendix B Relative Angular Velocities

Figure 79, Figure 80 and Figure 81 show the relative angular velocities of the line of sight in the body frame of the GEO satellite. The differences between the curves in Figure 79 are solely caused by the motion of the GEO satellite, which causes the difference in relative motion between the two satellites. For Figure 80 and Figure 81, the situation, compared to Figure 79, is a bit different, because the inclination angle causes differences in the distance between the two satellites, which also has an effect on the angular velocity. The differences between Figure 80 and Figure 81 are again caused by the GEO satellites motion and the distance variation between LEO and GEO satellite.

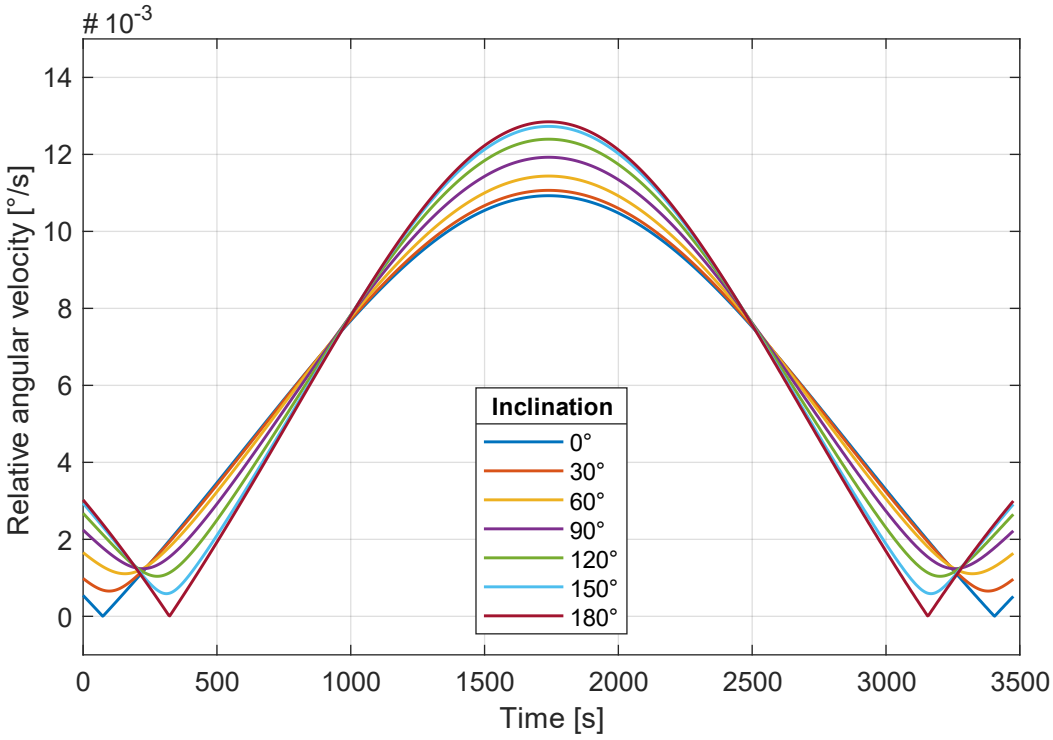

Figure 79: Relative angular velocity, case 1

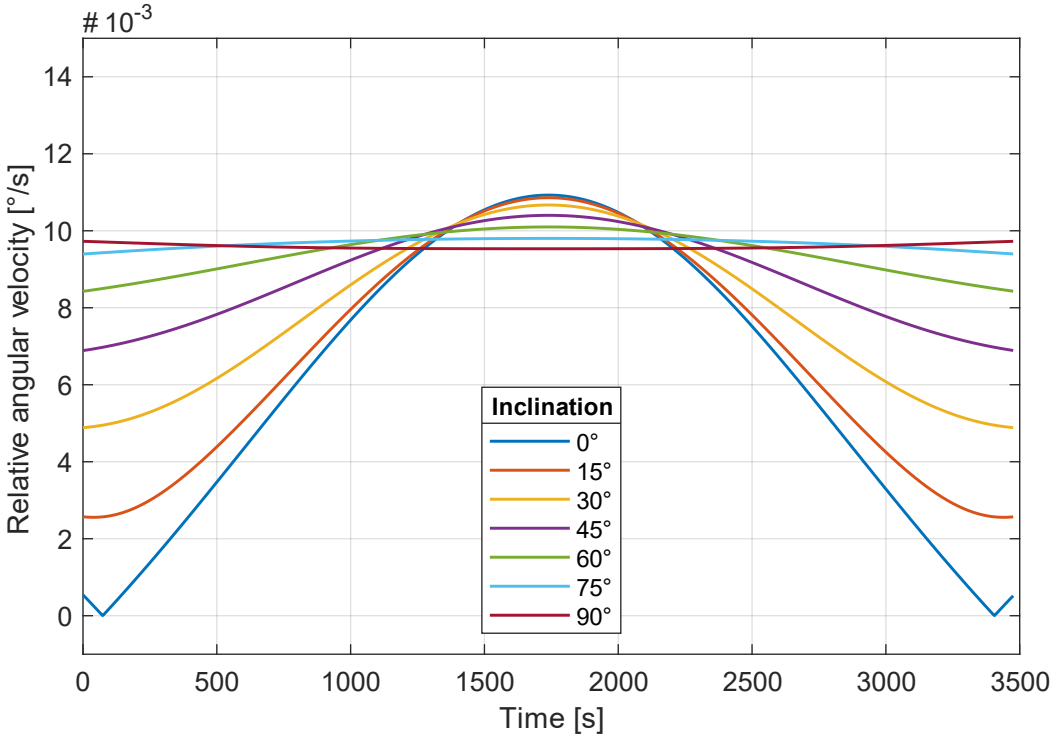

Figure 80: Relative angular velocity, case 2a

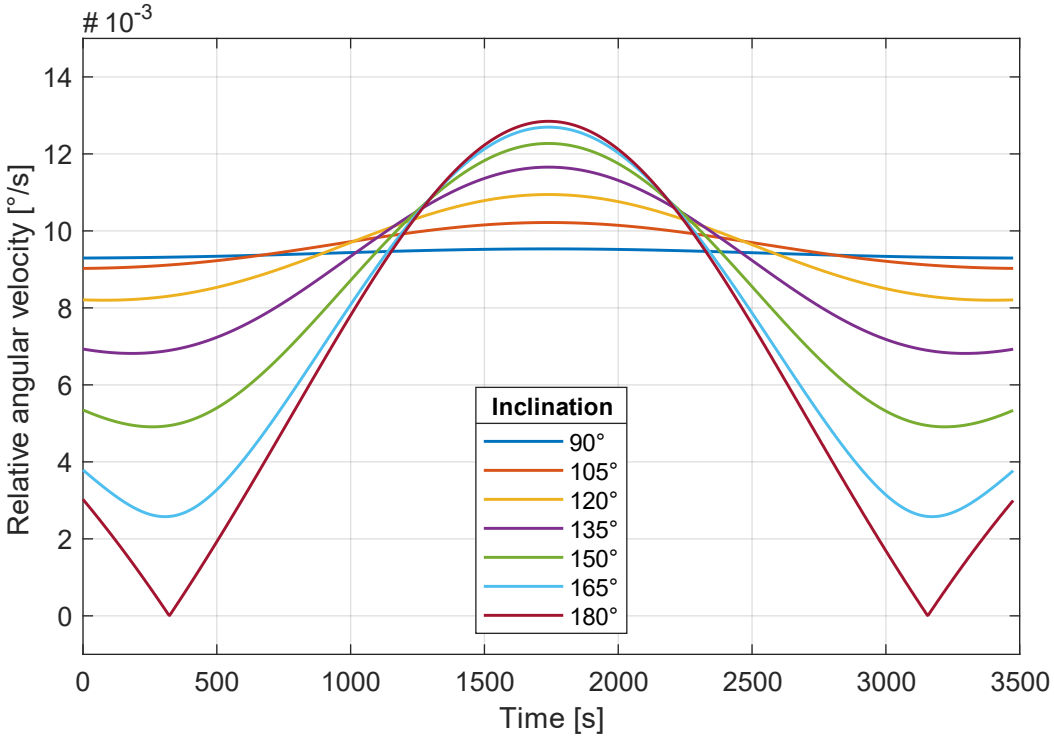

Figure 81: Relative angular velocity, case 2b

Appendix C Simulation of Case 2a&b

Figure 82, Figure 83, Figure 84 and Figure 85 show the LOS and the total jump count of case 2a and 2b. Though both cases are very similar, the plots are not symmetrical. In case 2a, the LEO satellite starts on the left-hand side of the GEO satellite and ends at the right-hand side with the line of sight of the GEO satellite oriented towards earth. In case 2b, it is the other way around. Thereby, the GEO satellite causes an asymmetry because its flight direction is always the same.

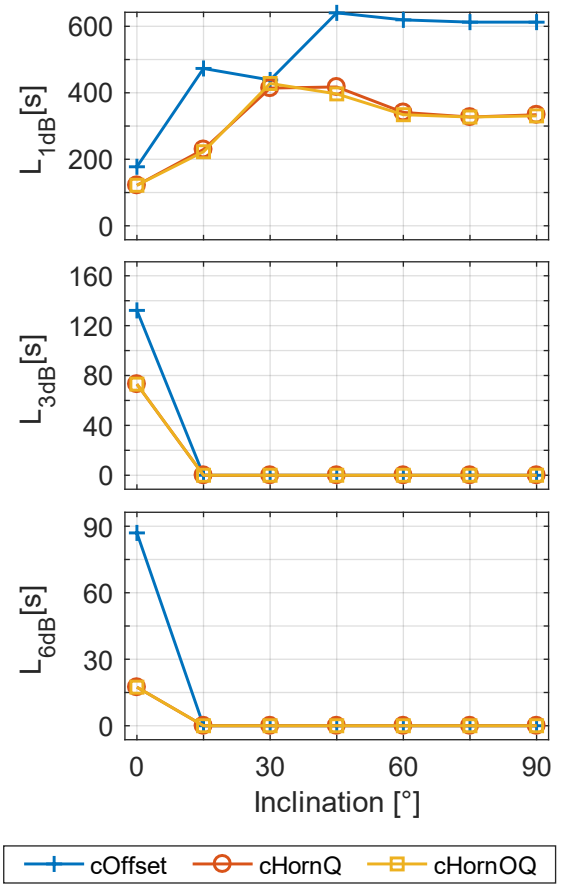

Figure 82: LOS of demonstrator array, case 2a

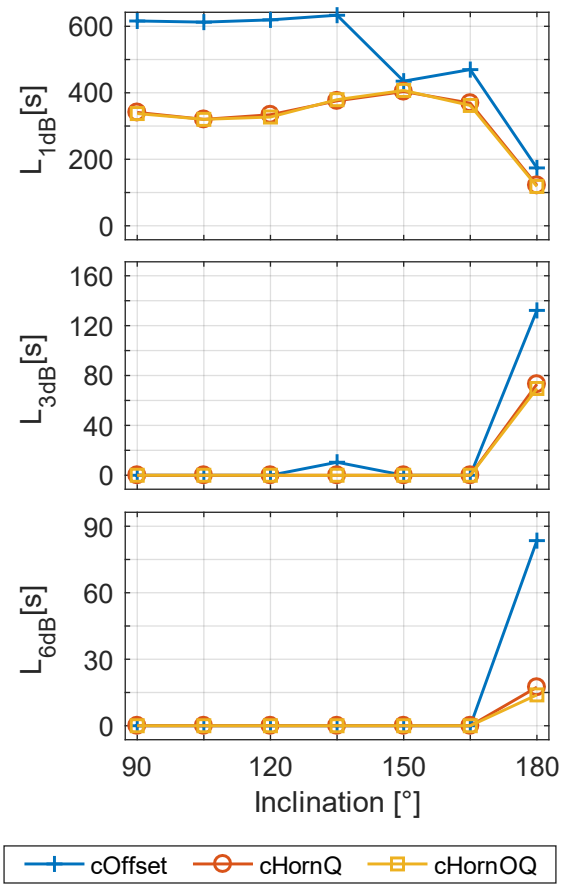

Figure 83: LOS of demonstrator array, case 2b

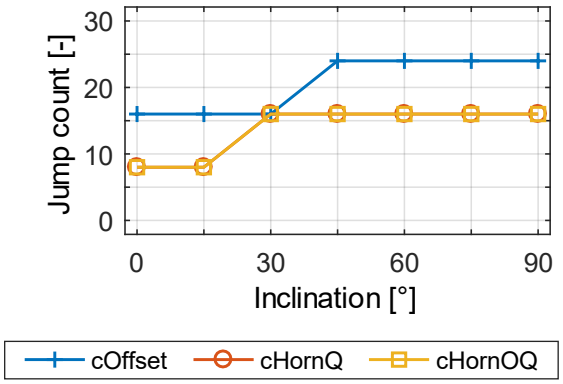

Figure 84: Total jump count, case 2a

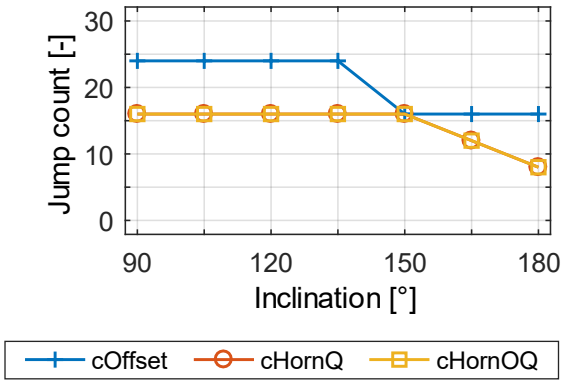

Figure 85: Total jump count, case 2b

Figure 86, Figure 87, Figure 88 and Figure 89 show the LOS and total jump counts of the flight model (case 2a&b). Because of the motion of the GEO satellite, the curves of both cases are not symmetrical. The differences are less obvious compared to the demonstrator array since the horn count is larger and therefore jumps of solitary LCPS's have a lesser effect on the antenna performance.

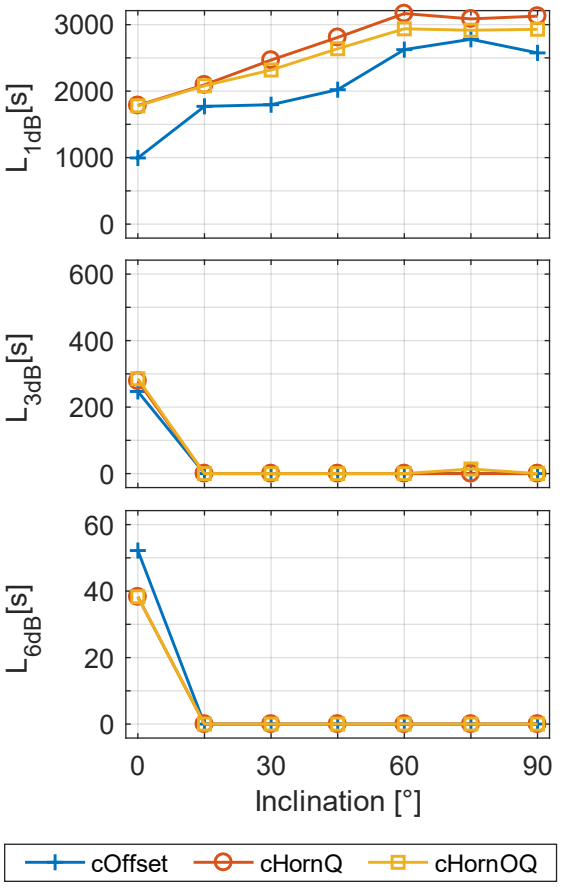

Figure 86: LOS of flight model, case 2a

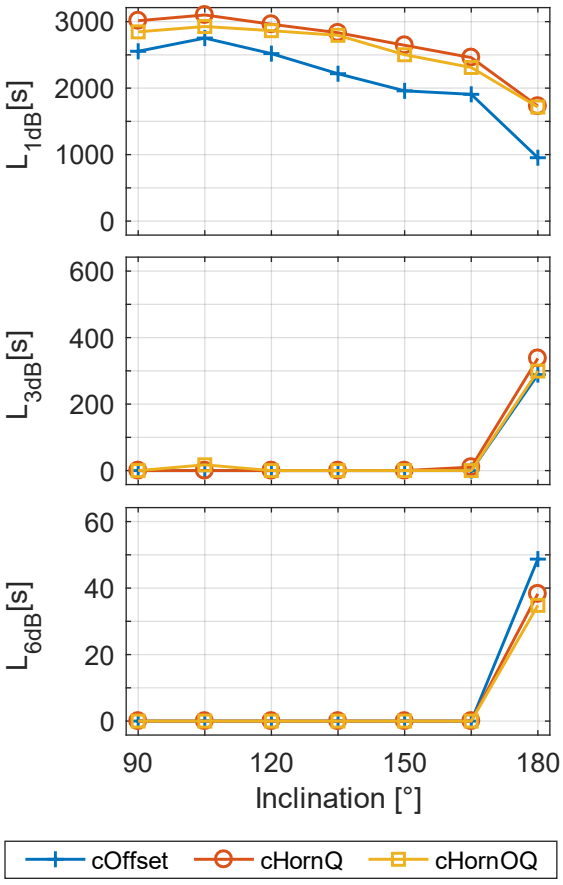

Figure 87: LOS of flight model, case 2b

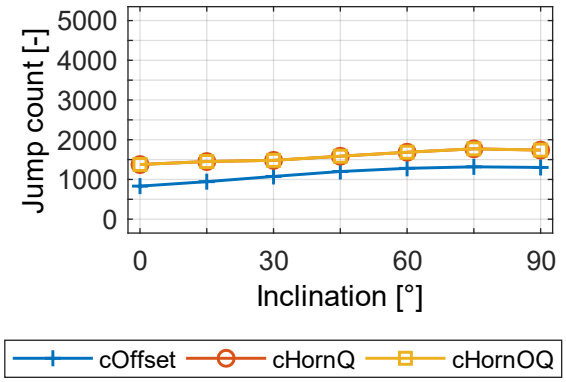

Figure 88: Total jump count of flight model, case 2a

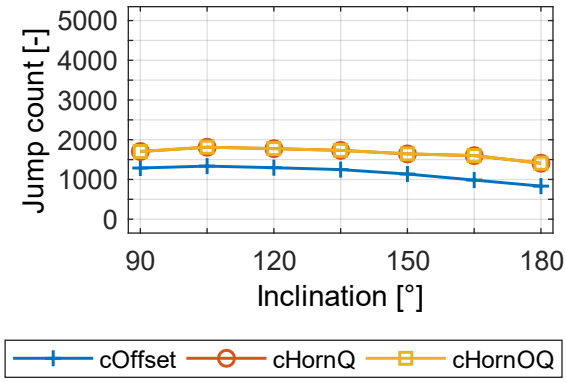

Figure 89: Total jump count of flight model, case 2b

Appendix D Electroplated Liquid Crystal Phase Shifters

List of all manufactured electroplated liquid crystal phase shifters within the scope of this work:

Batch	**Body** (Batch-No.)	**Film electrode, top** (Batch-Type-No.)	**Film electrode, bottom** (Batch-Type-No.)	**Sputtered**	**Electroplated**	**Functional**
1	1-12?	708-767-?	708-767-?	+	+	-
1	1-7?	708-768-?	708-768-?	+	+	-
1	Full	708-771-?	708-771-?	+	+	-
1	Full	708-772-?	708-772-?	+	+	-
2	2-2	708-767-10	708-767-9	+	+	-
2	1-13	708-767-8	708-767-7	+	+	-
2	2-1	708-768-8	708-768-5	+	+	-
2	2-3	708-768-10	708-768-9	+	+	-
3	2-6	708-767-14	708-767-13	+	-	-
3	2-7	708-768-16	708-768-15	+	+	-
3	3-1	708-769-3	708-769-1	+	-	-
3	1-10	708-768-4	708-768-3	+	-	-
4	3-2	708-769-4	708-769-2	+	+	-
4	3-4	708-771-3	708-771-2	+	-	-
4	3-5	708-770-5	708-770-1	+	+	-
4	3-3	708-772-1	708-772-2	+	+	-
5	3-7	708-770-8	708-770-3	+	+	+
5	3-8	708-771-14	708-771-11	+	+	-
5	2-8	708-770-11	708-770-10	+ 1 µm silver	-	+
5	2-9	708-769-10	708-769-9	+	+	-
6	1-0	708-772-?	708-772-?	+	+	-

Some phase shifter cores and film electrodes were sorted out due to manufacturing errors such as missing electric contact between the electrode lines or problems during the core assembly. Those parts are not listed in this table. The electroplated liquid crystal phase shifters have a mass of about 19 g (without LC).

The first batch includes two bodies without cavity (‘Full’). They are used to test the process without losing one of the bodies with a LC cavity.

Batch 6 consists of one LCPS only, because it is a test for a different mounting of the film electrodes. Normally the stripline side of the polyimide film is glued onto the body. In this batch the striplines are on

the outside of the assembled core and silicone spray is used for the electric isolation. The idea is to avoid any lead through of striplines or wiring during the electroplating process. Instead, the two soldering pads inside the waveguide are covered with ABS blocks. After the electroplating process, the copper around these blocks can be grinded down to a level where the ABS blocks are visible without damaging the film electrodes. The ABS blocks can now be dissolved to uncover the soldering pads.

Appendix E Temperature Controlled LCPS Setup

Figure 90 shows the six holes for the thermocouples. The positions of the thermocouples are named ‘top center’ (TC), ‘bottom center’ (BC), ‘bottom center side’ (BCS), ‘top center side’ (TCS), ‘top end side’ (TES) and ‘bottom end side’ (BES). The data logger only supports four thermocouples (TC, BC, BCS, BES), two holes have not been used (TCS, TES). The ‘top’ and ‘bottom’ refer to the ‘top’ and ‘bottom’ half of the split block.

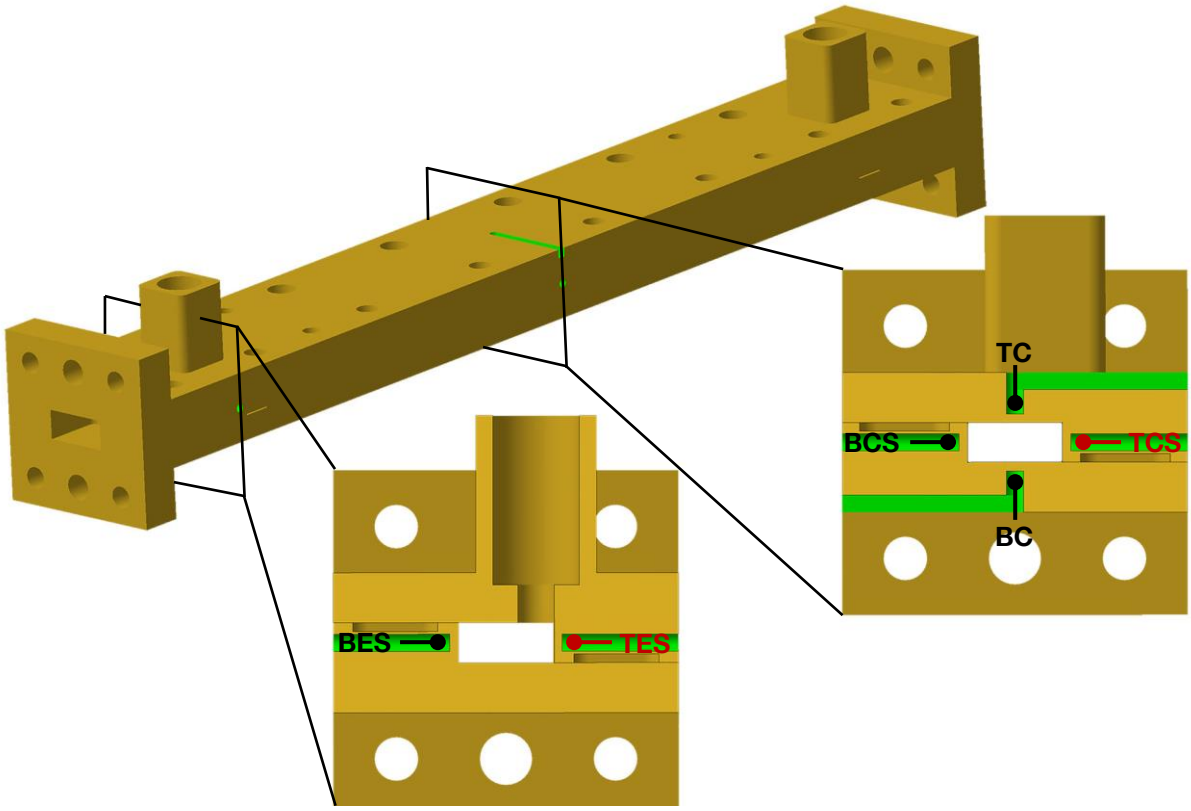

Figure 90: Holes for thermocouples

Figure 91 and Figure 92 show cross sections of the LCPS with the simulated temperature distribution. The simulation is performed in *COMSOL Multiphysics 5.0*. The temperature is close to 357.15 K at the heaters and 293.15 K at the boundaries of the insulation. The simulation is stationary with a proportional regulator that keeps the heaters at a temperature close to 357.15 K. The model consists of halve the LCPS (split in length) with a symmetry boundary condition. It consists of 1 922 541 elements with a minimum element quality of 0.09018 and an average element quality of 0.7563.

The white lines are isotherms from 293.15 K to 357.15 K with a spacing of 4 K. The heat flux at the flange is set to 7000 W/m^2 to get similar temperatures at the positions of the thermocouples (Polifke and Kopitz, 2005, p. 39).

Figure 93 shows the assembled LCPS setup. The green wires are the connection wires of the thermocouples at the positions shown in Figure 90. The thermocouples inserted from the upper part of the picture are the ones in the bottom half of the split block (BC, BCS, BES) and the only one coming from the lower part of the picture is the one in the upper half of the split block (TC). The red wire is connected with

the PT100 thermistor that is used to regulate the temperature of the heaters and the black wires are connected to the heaters. The remaining wires at the lower right side are used to control the LCPS. The calibration level of the network analyzer is marked with the yellow lines.

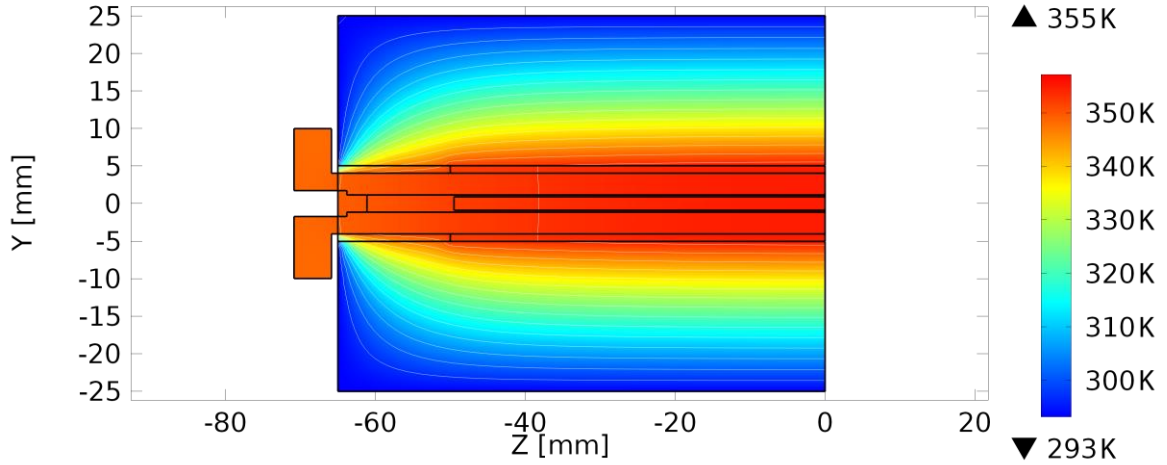

Figure 91: Temperature simulation, cross section, side view

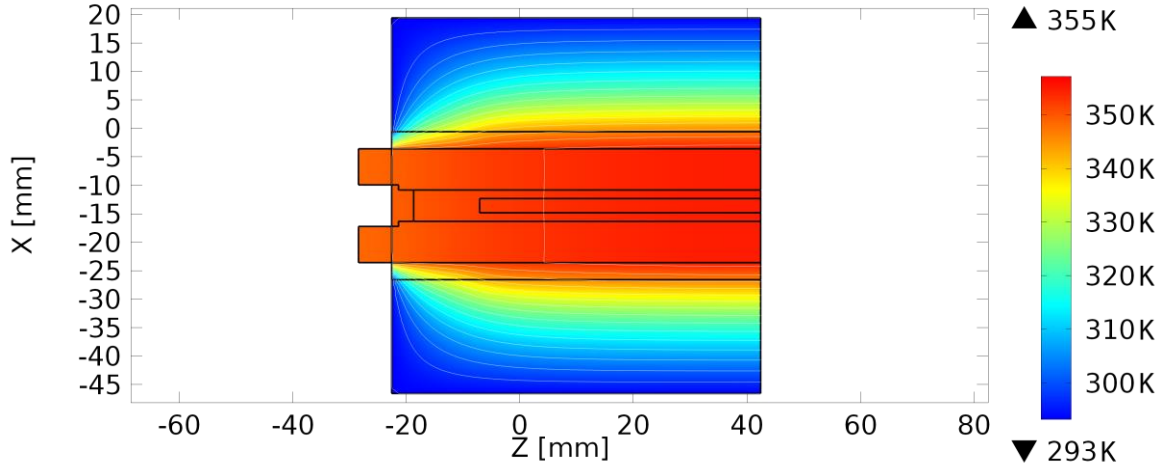

Figure 92: Temperature simulation, cross section, top view

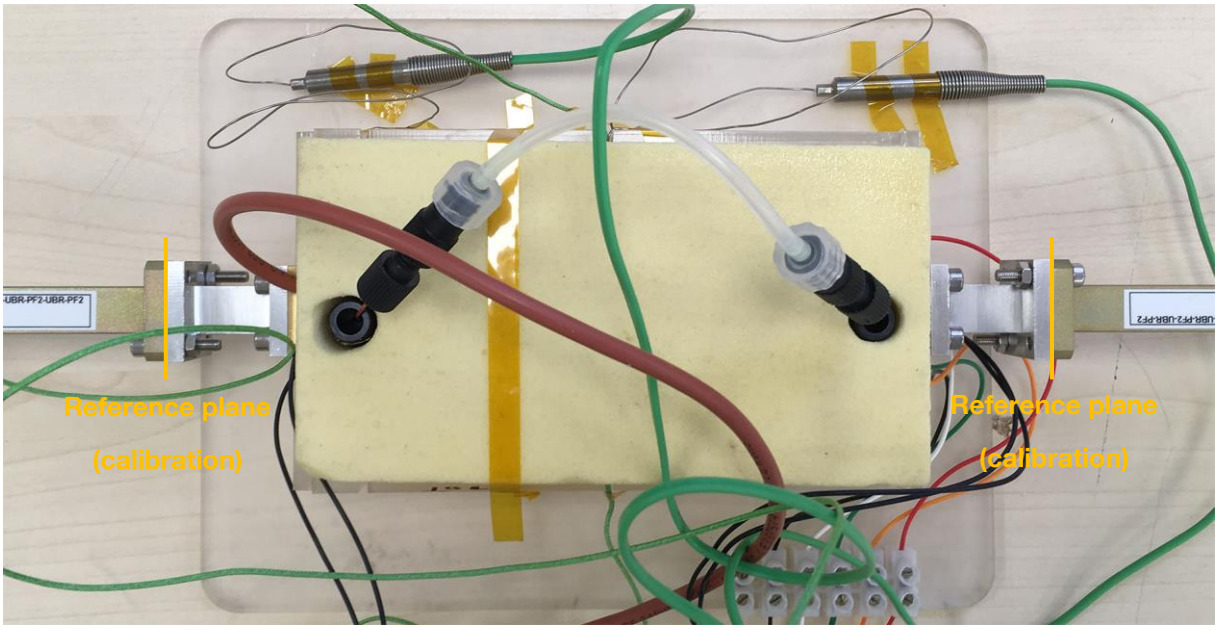

Figure 93: Assembly with insulation

Appendix F Temperature Dependency at 27 GHz

Figure 94 shows the transmission (S_{21}) of the LCPS (LC: *GT5-26001*) over temperature for 27 GHz to 27.5 GHz. The blue markers show the transmission for a vertical (H) electric field for the first campaign. The red markers show the transition for a horizontal (V) electric field for the first campaign. The yellow and violet markers show the same field orientations for the second campaign.

Compared to the measurement between 23 GHz and 23.5 GHz (Figure 50), the offset of the measurements from campaign 1 / day 2 compared to the other measurements is significantly lower.

The effect of the higher frequency is stronger for the horizontal (H) case than for the vertical (V) case. The transmission for the vertical case is about 0.1 dB higher and the transmission for the horizontal case is about 0.25 dB higher.

The temperature dependency is equal to Figure 50.

Figure 95 shows the transmission for the same frequency range than Figure 94, but the LCPS is filled with *GT3-23002* instead of *GT5-26001*. The green markers show the horizontal (H) orientation of the electric field and the light blue markers show the vertical (V) orientation.

The effect of the higher frequency is equal to the effect with *GT5-26001*.

Figure 96 shows the reflection (S_{11}) of the LCPS (LC: *GT5-26001*) over temperature for the upper frequency band (27 GHz to 27.5 GHz). The behavior is different to the one at the lower frequency band, but unevenly. For some measurements the reflection is up to 5 dB higher, but for others it is even lower.

As for the transmission, the offset of the measurements from campaign 1 / day 2 is also less, but the reflection is still slightly higher than the measured reflections on the other days.

Figure 97 shows the differential phase over temperature for both LCs at the higher frequency band. The total phase shift is increased with higher frequencies. This effect is higher for *GT5-26001*. The phase range of *GT5-26001* is about 18° higher and for *GT3-23002* about 13° higher.

Figure 98 shows the relative phase over temperature for both LCs at 27 GHz. The higher frequency effects both extreme states (maximum and minimum phase) of the phase. The effect on the maximum phase is higher as can be seen for higher temperatures.

Therefore, the increase of the medium phase level for higher temperatures is stronger with higher frequencies.

Figure 99 shows the figure of merit over temperature for both LCs for the frequency band from 27 GHz to 27.5 GHz. The overall level is higher compared to the lower frequency band. For *GT5-26001* the difference is between about 10 °/dB at 20 °C and 6 °/dB at 80 °C. For *GT3-23002* the difference is less (between 5 °/dB at 20 °C and 4 °/dB at 80 °C).

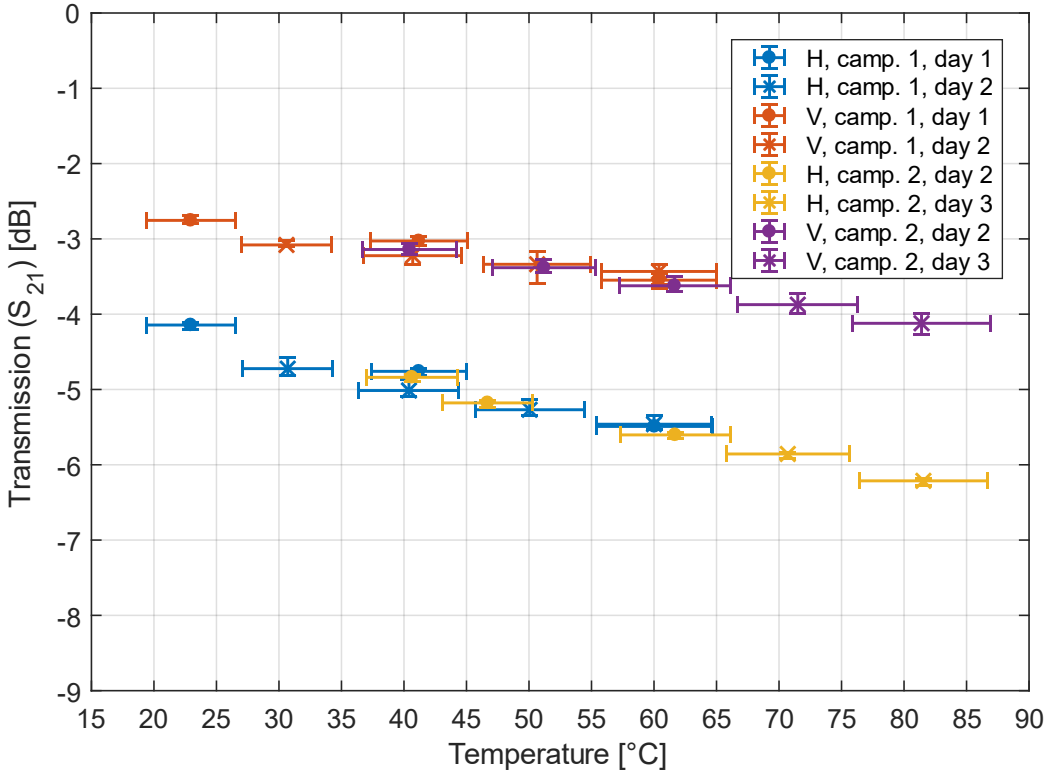

Figure 94: Transmission (S_{21}) over temperature, 27 to 27.5 GHz, *GT5-26001*

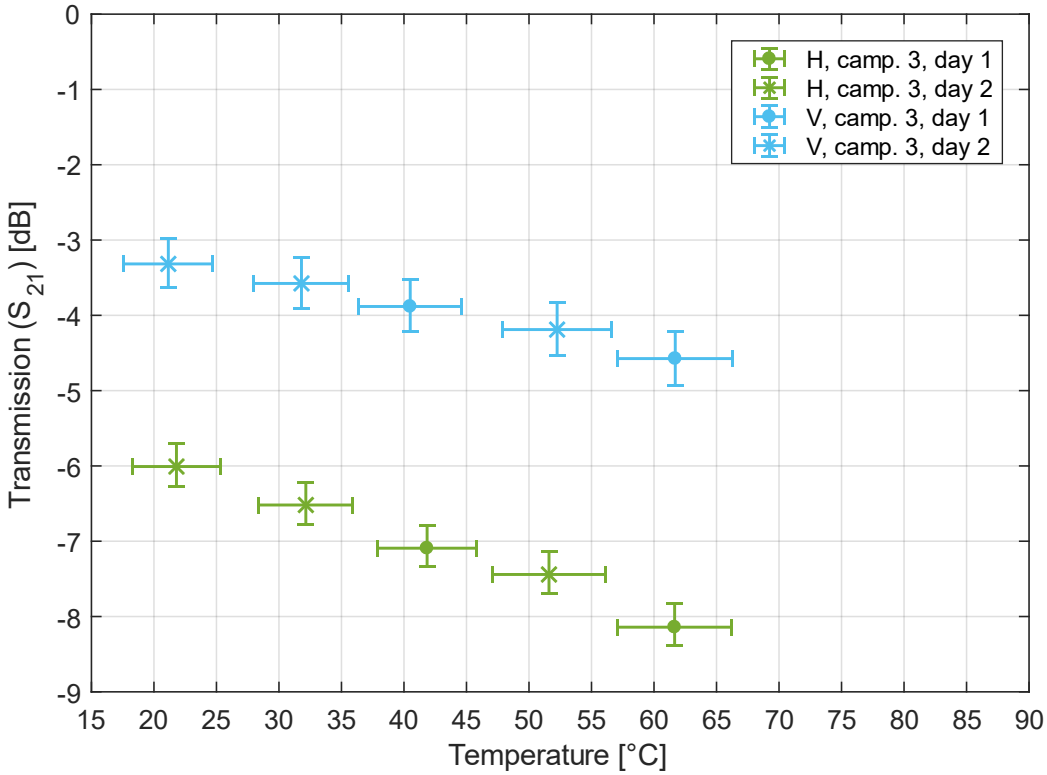

Figure 95: Transmission (S_{21}) over temperature, 27 to 27.5 GHz, *GT3-23002*

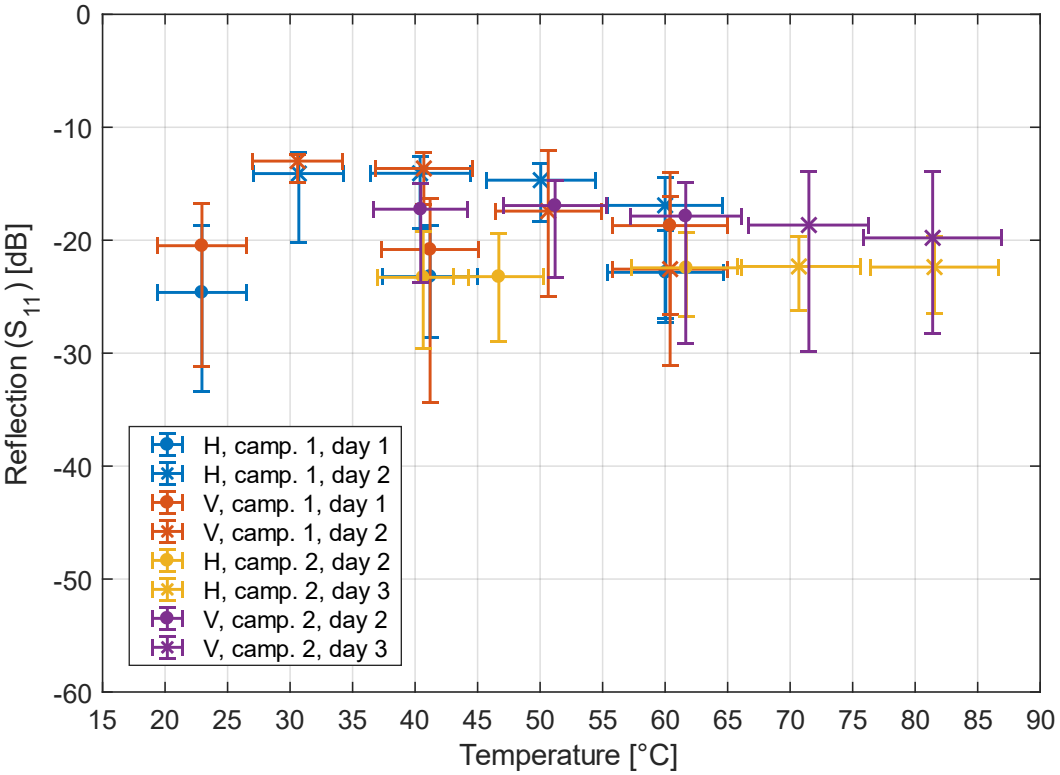

Figure 96: Reflection (S_{11}) over temperature, 27 to 27.5 GHz, *GT5-26001*

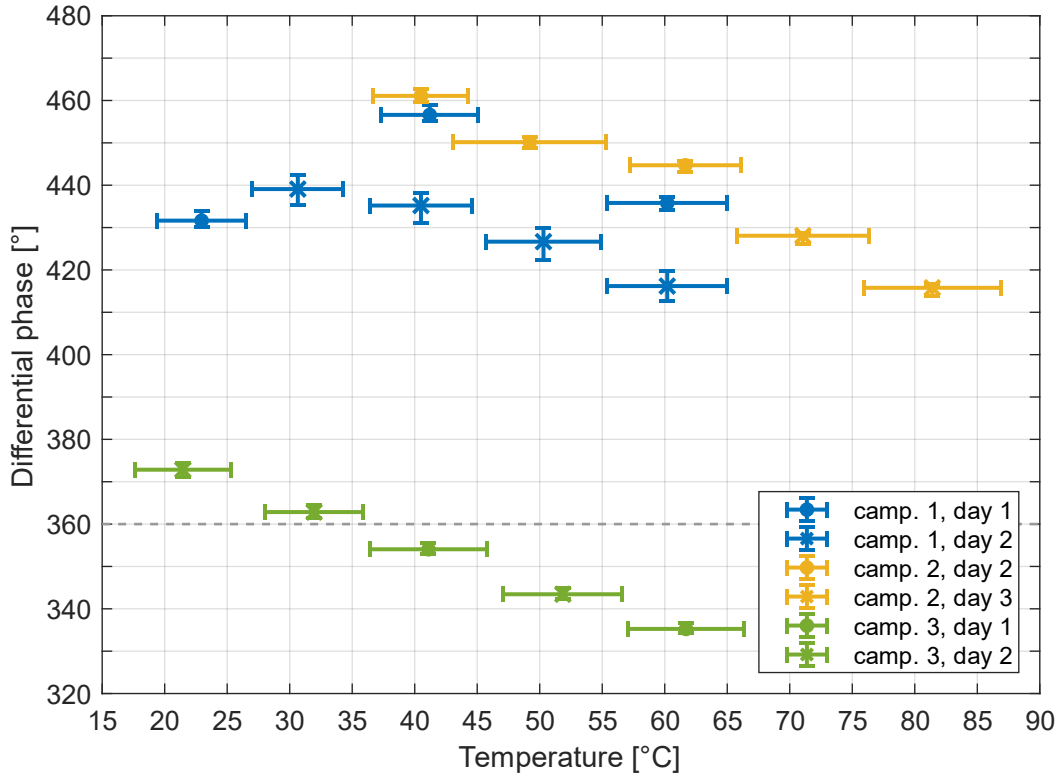

Figure 97: Differential phase over temperature, 27 to 27.5 GHz
***GT5-26001* (camp. 1 & 2) and *GT3-23002* (camp. 3)**

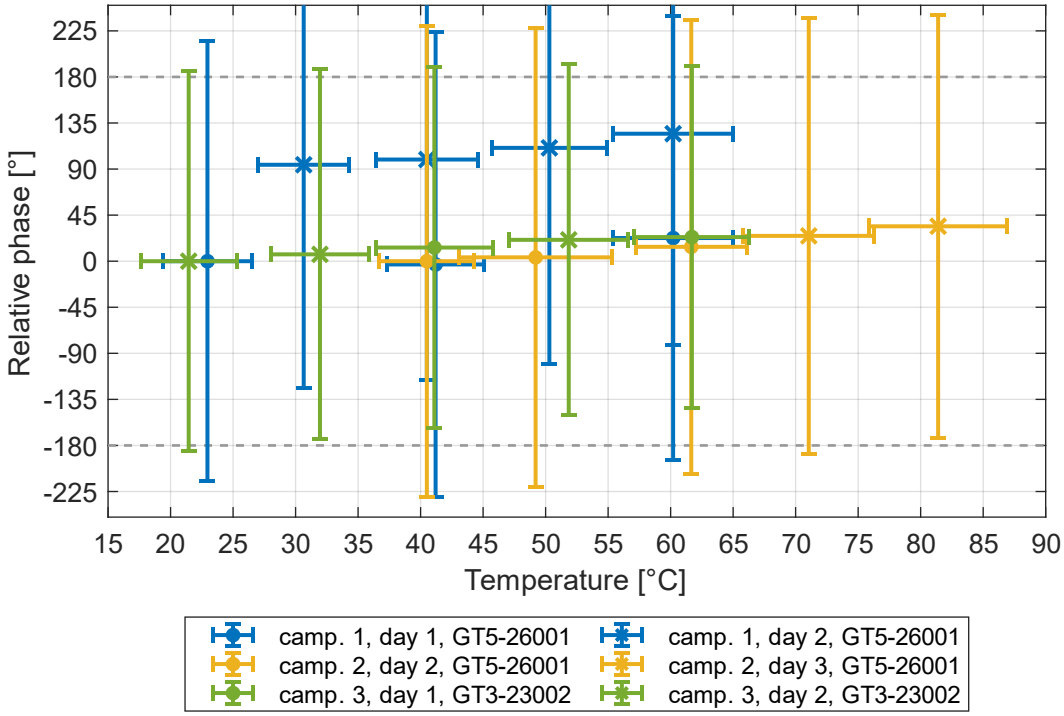

Figure 98: Relative phase over temperature, 27 GHz, *GT5-26001* and *GT3-23002*

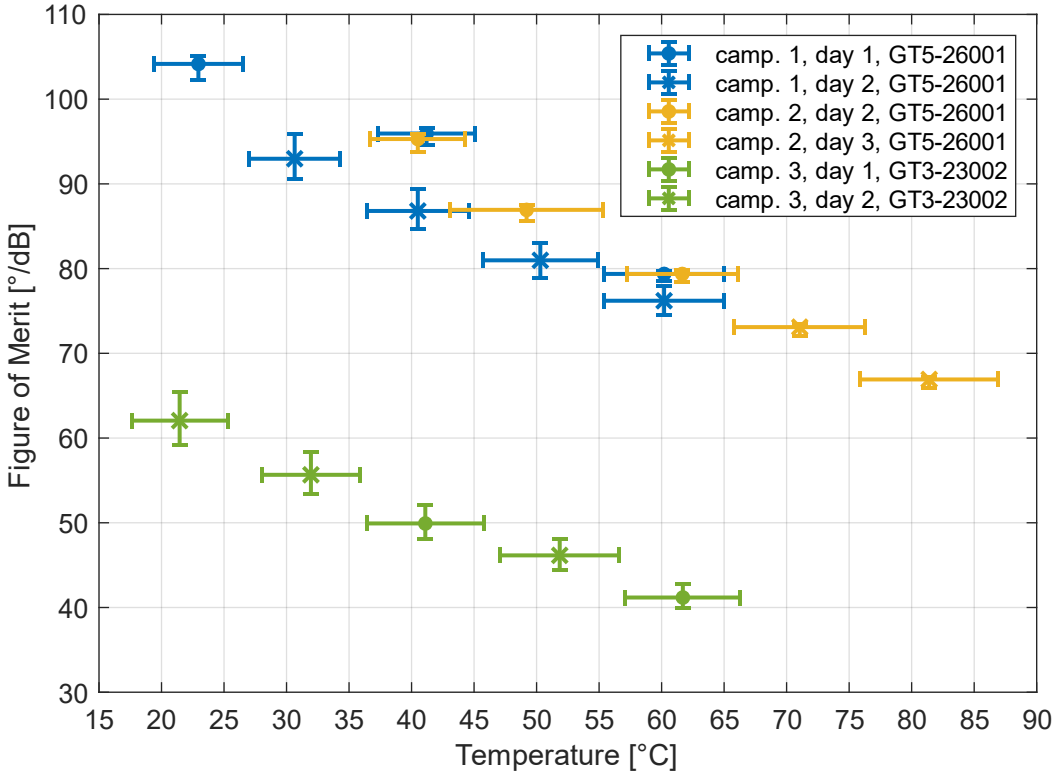

Figure 99: Figure of Merit over temperature, 27 to 27.5 GHz, *GT5-26001* and *GT3-23002*

Appendix G Figure of Merit for different LCPSs

Table 28 shows the figure of merit for different phase shifter designs based on LC.

Table 28: Figure of merit for different LCPSs

Figure of Merit	LC	Frequency	Topology	Publication	Comment
41 °/dB	*TUD-566*	28 GHz	SIW / LTCC	(Strunck *et al.*, 2015)	
100 °/dB	?	28 GHz	Waveguide / split block	(Gaebler, Goelden, *et al.*, 2009)	Electric biasing
111 °/dB	*n. m. IMSL 1*	23 GHz	IMSL	(Muller *et al.*, 2004)	
81 °/dB	*n. m. IMSL 2*	23 GHz			
21 °/dB	*K15*	23 GHz			
9-11.5 °/dB	*K15*	18 GHz	IMSL	(Weil, Luessem and Jakoby, 2002)	
30.6 °/dB	?	34.32 GHz	IMSL	(Moessinger *et al.*, 2010)	Average IL
51-100 °/dB	?	45 GHz	S-CPW	(A. L. Franc *et al.*, 2013)	
14.5-19 °/dB	?	20 GHz	IMSL	(Martin *et al.*, 2003)	
19.55 °/dB	*E7*	30 GHz	CPW (coplanar waveguide)	(Bulja *et al.*, 2010)	
13.94 °/dB	*K15*				
18.97 °/dB	*E44*				
19.93 °/dB	*E63*				
15.59 °/dB	*MDA-00-3506*				
105-120 °/dB	*GT5-26001*	23 GHz	Waveguide / split block	(Weickhmann, 2017)	Electric biasing
4 °/dB	*K15*	26.5 GHz	Finline	(Mueller, Felber, *et al.*, 2005)	
50-72 °/dB	*MDA-03-2838*				
110 °/dB	?	33 GHz	Waveguide / split block	(Gaebler, 2015)	Electric biasing
113 °/dB	*TUD-026*	23 GHz	Waveguide / split block	(Weickhmann, Nathrath, *et al.*, 2013)23	Electric biasing
20 °/dB 110 °/dB	*K15* *Mixture 'C'*	24 GHz	IMSL	(Weil, Mueller, Scheele, Best, *et al.*, 2003)	
115 °/dB	*TUD-126*	23 GHz	Waveguide / split block	(Jost, Weickhmann, *et al.*, 2015)	
62 °/dB	*LC mixture 1*	18 GHz	IMSL	(Karabey *et al.*, 2011)	
15 °/dB	*GT3-23001*	23 GHz	SL / LTCC	(Jost, Strunck, *et al.*, 2015)	
15 °/dB	*K15*	25 GHz	IMSL / LTCC	(Gaebler, Moessinger, *et al.*, 2009)	

Appendix H Time Courses of Phase Jumps at different Temperatures

Figure 100 and Figure 101 show the relative phase over time for a phase jump (instant change of the electric biasing field from V to H or H to V) at different temperatures. The temperatures are rounded to the nearest ten.

The phase change is performed faster for higher temperatures and with this, the convergence to the limit is also faster. The temperature dependency of this effect is higher for lower temperatures and the overall phase range degrades with increasing temperatures.

Figure 102 and Figure 103 show the time derivative of the relative phase (phase velocity or phase change rate) over time for a phase jump. The difference between the two jump directions (V to H and H to V) is clearly visible (about 2.5 times faster for H to V). The phase velocity changes very fast at the beginning (almost instantaneously). After this jump the phase velocity increases to its maximum and the following decrease of the phase velocity is slower than the increase.

For a phase shifting application where phase jumps of 360° are necessary, one goal is to decrease the time of this jump. An increase of the temperature leads to higher phase velocities, but this effect is partly counteracted by the decrease of the phase range. Through the decrease of the phase range, the LCPS has to work close to its phase limits to accomplish a 360° phase jump. Since the phase velocity close to the limits gets slower, the effect of faster jumps because of higher phase velocities at higher temperatures is partly counteracted.

One way to avoid this problem would be to increase the phase range (longer phase shifter) to avoid the limits of the LCPS at a desired temperature. However, this would also lead to increased losses.

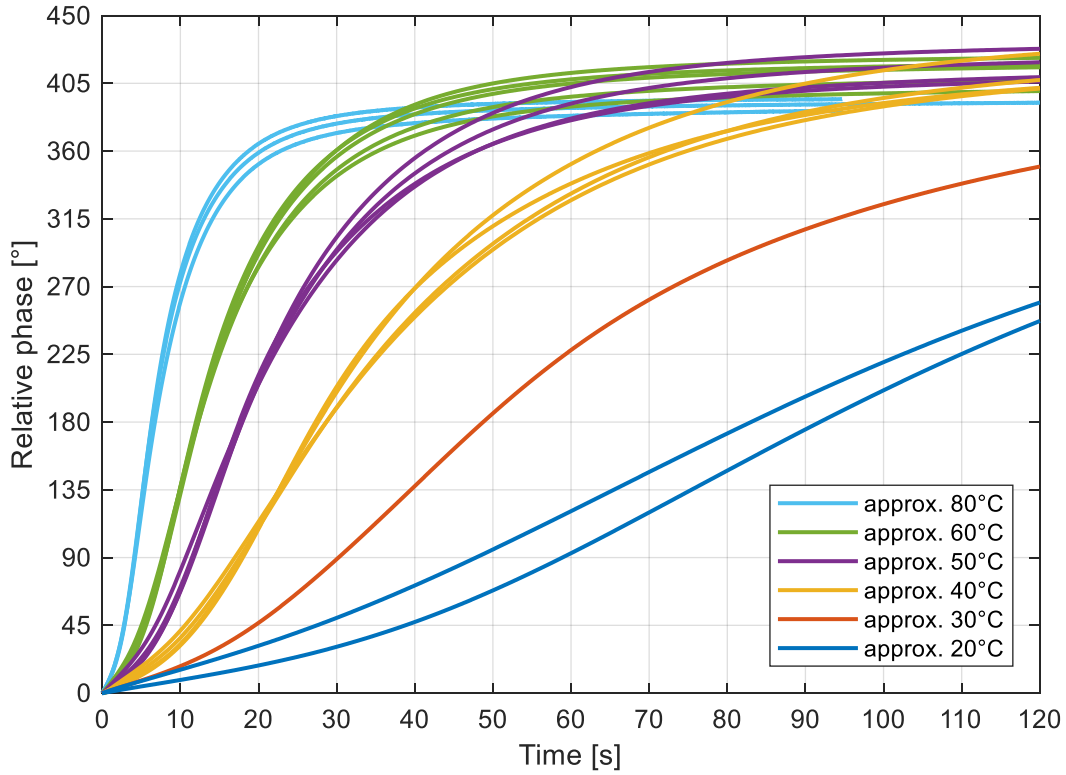

Figure 100: Relative phase over time (V to H), 23 GHz, *GT5-26001*

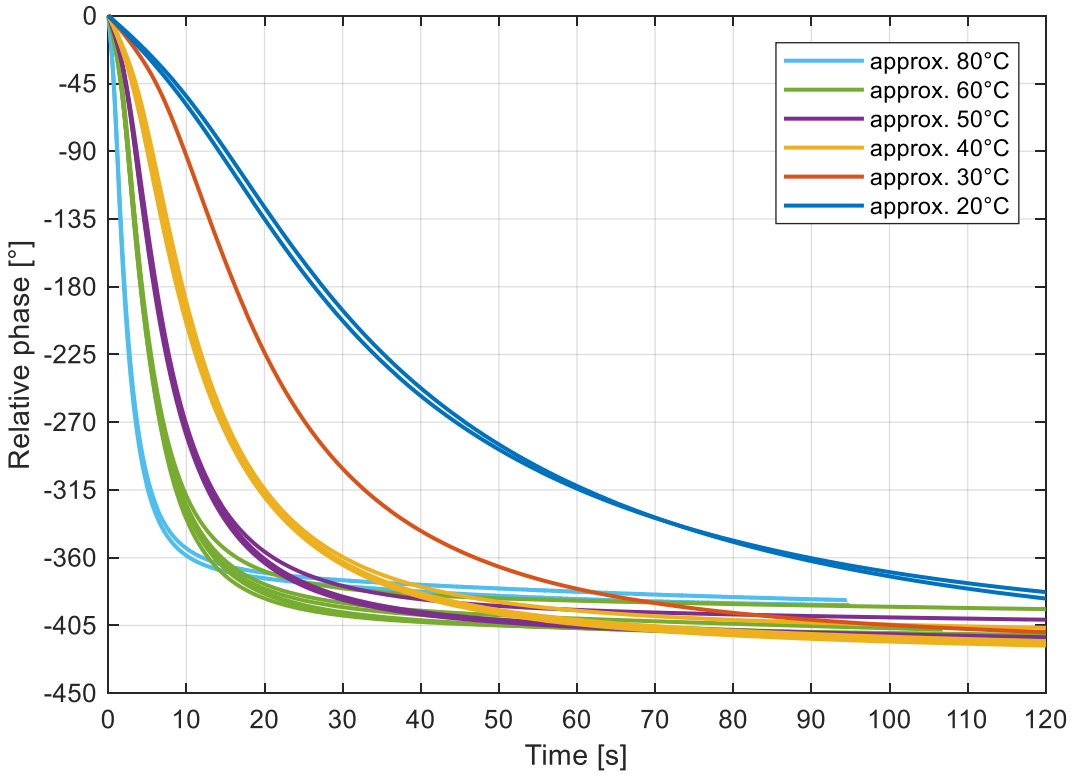

Figure 101: Relative phase over time (H to V), 23 GHz, *GT5-26001*

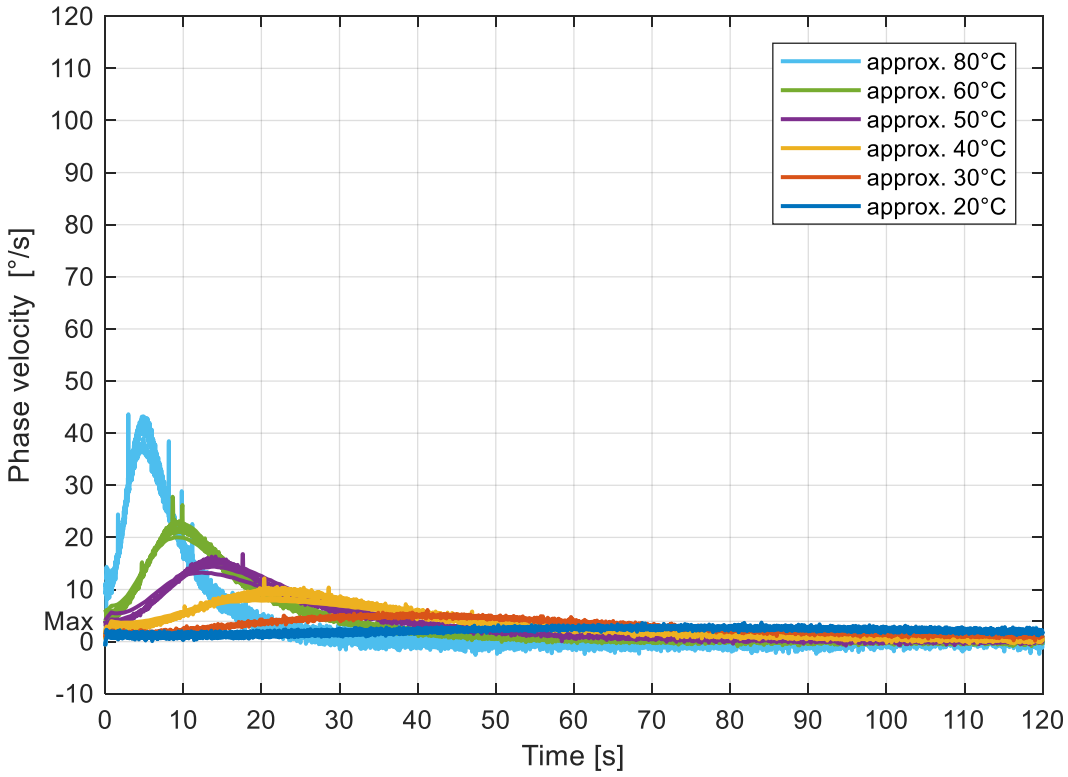

Figure 102: Phase velocity over time (V to H), 23 GHz, *GT5-26001*

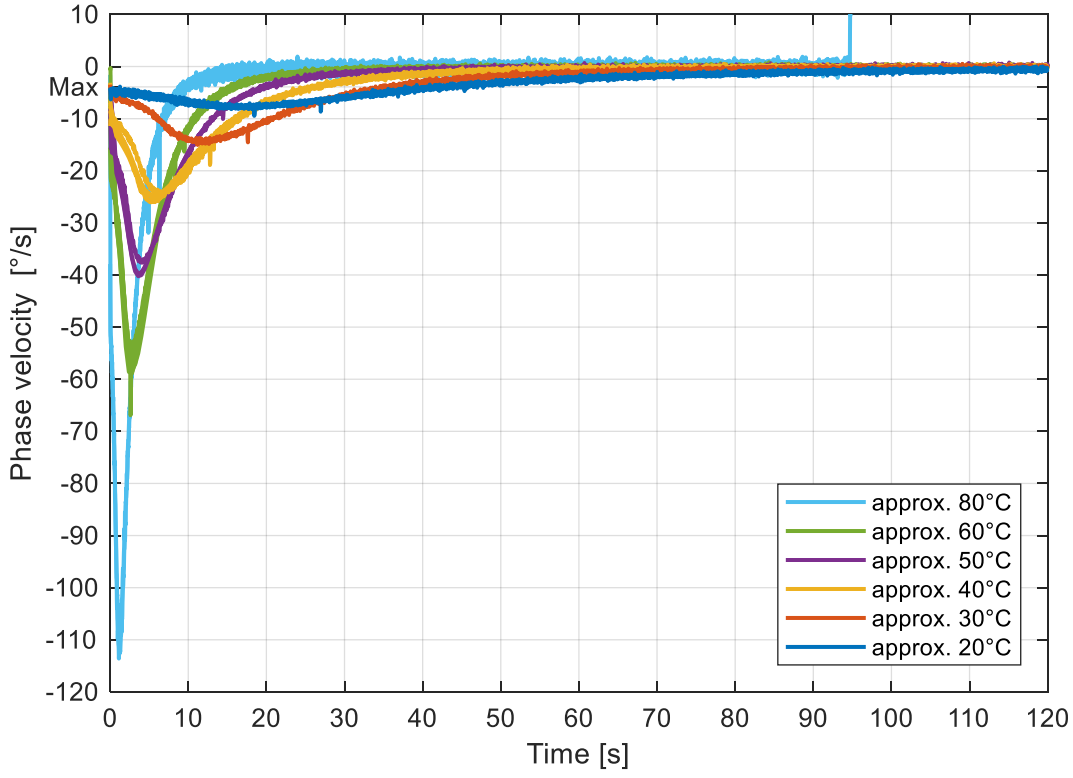

Figure 103: Phase velocity over time (H to V), 23 GHz, *GT5-26001*

Appendix I Simulation of the Electric Biasing Field (Model)

The model is build out of 5 different materials, whereby the geometry is equal to a cross-section of the CAD (computer aided design) model. The voltages for each stripline are calculated relative to the voltages on the electrodes on the far left and far right side of each film electrode and are spread equally. The contribution of the resistor paste to the static field is not taken into account, since in the actual LCPS the paste is only used at one end of each film electrode. In longitudinal direction of the LCPS, the resistor paste stretches over about 0.8 mm in contrast to the 99 mm extension of the LC cavity.

The simulation model consists of 123 326 elements (Figure 104) with a minimum element quality of 0.22 and an average element quality of 0.95.

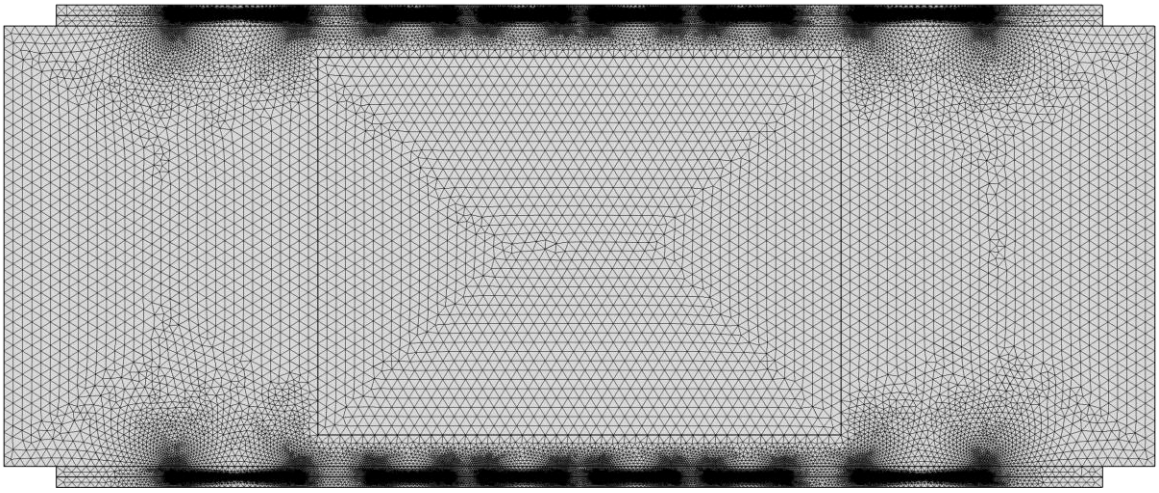

Figure 104: Mashed model of the LCPS cross section

Appendix J Phase over Voltage at 27.5 GHz

Figure 105 shows the phase over voltage for 27.5 GHz. The progression is similar to the one at 23 GHz with a slight increase in the total phase range.

Figure 106 shows the phase change per commanded voltage at 27.5 GHz. The minimum value is slightly lower than at 23 GHz since the total phase range is increased.

Figure 107 shows the transmission over the commanded voltage at 27.5 GHz. Compared to the transmission at 23 GHz the level for LCPS 1, 3 and 4 is shifted to lower losses by about 0.4 dB.

Figure 108 shows the reflection over the commanded voltage at 27.5 GHz. It is similar to the reflection at 23 GHz but between 20 V and 164 V the reflection level is significantly higher.

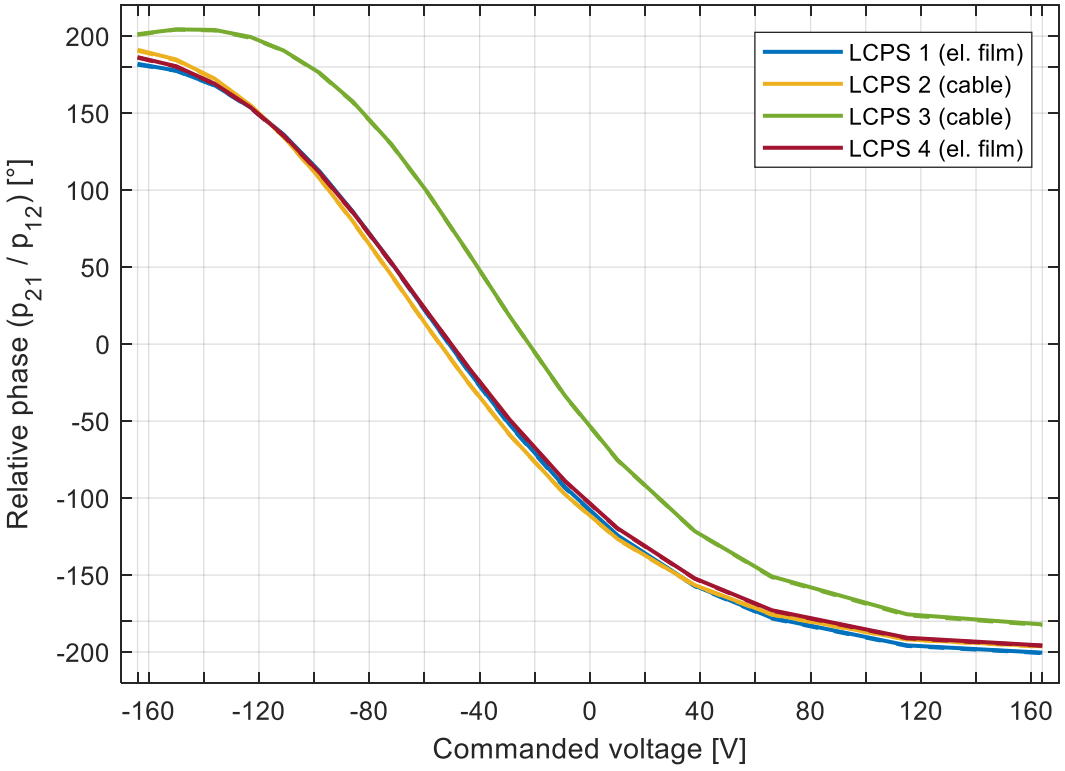

Figure 105: Phase over voltage, 27.5 GHz, *GT3-23002*

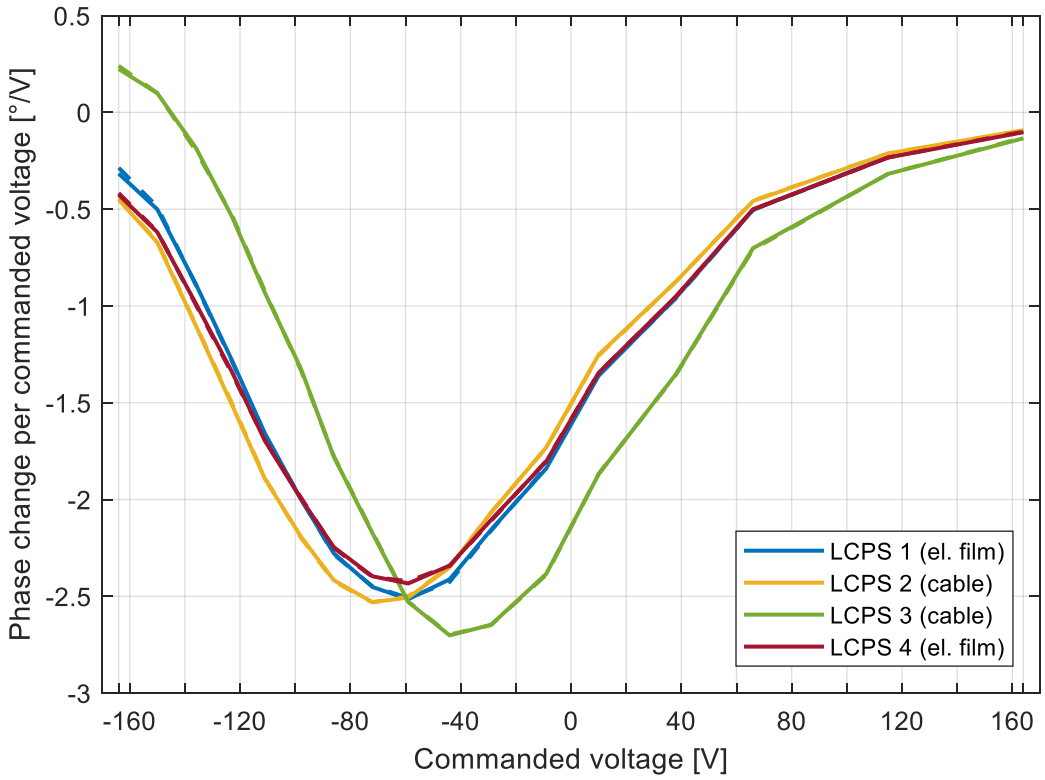

Figure 106: Phase change per commanded voltage, 27.5 GHz, *GT3-23002*

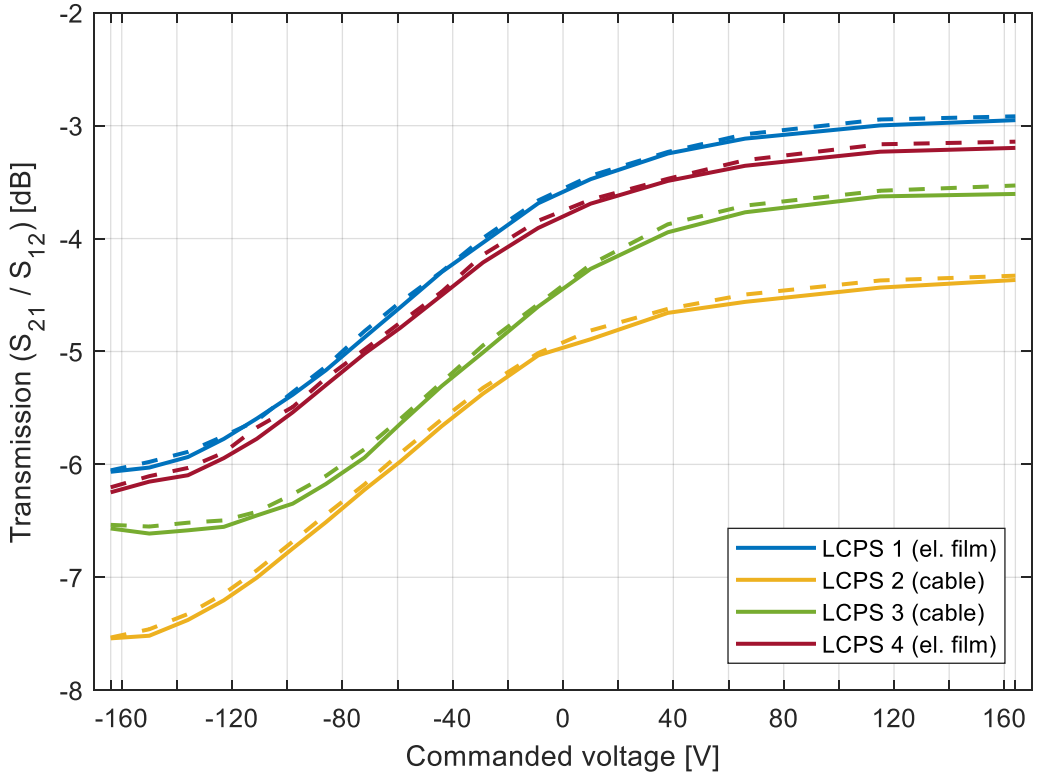

Figure 107: Transmission over commanded voltage, 27.5 GHz, *GT3-23002*

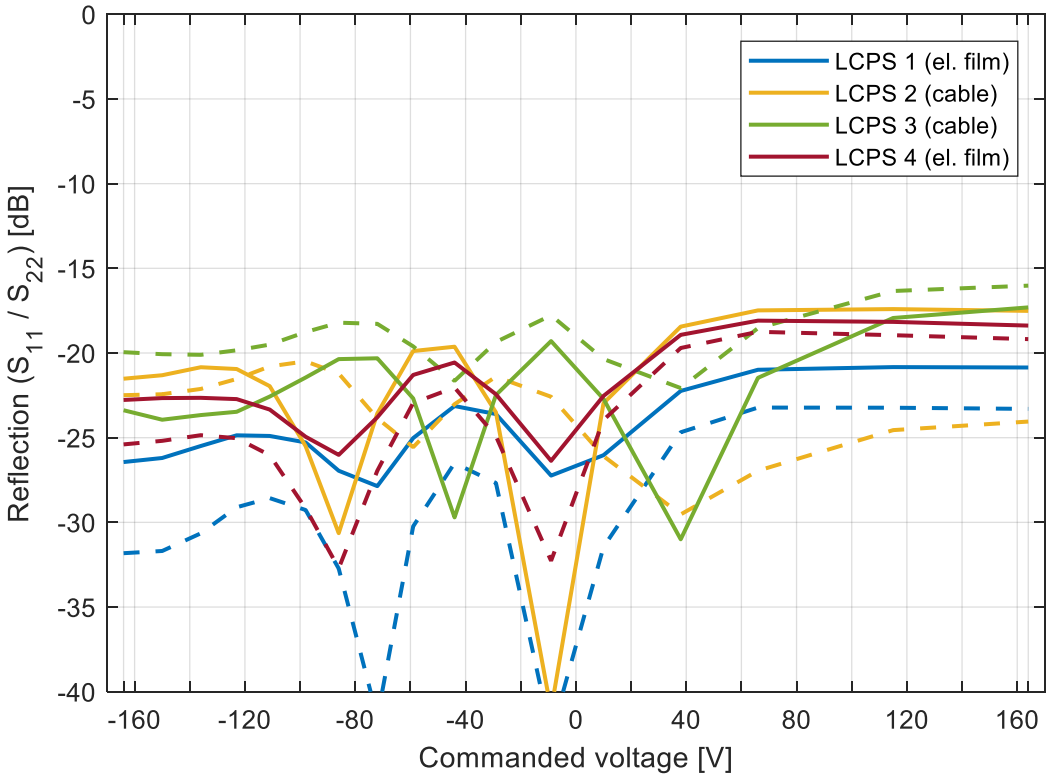

Figure 108: Reflection over voltage (S_{22} – dashed line, 27.5 GHz), *GT3-23002*